CONFINEMENT INDUCED STRUCTURAL EVOLUTION OF CALCIUM- AND MAGNESIUM-CARBONATES IN ALUMINA AND ARCHITECTED SILICEOUS NANOCHANNELS

A Dissertation

Presented to the Faculty of the Graduate School

of Cornell University

In Partial Fulfillment of the Requirements for the Degree of

Doctor of Philosophy

by

Akanksh Mamidala

August 2025

CONFINEMENT INDUCED STRUCTURAL EVOLUTION OF CALCIUM- AND MAGNESIUM-CARBONATES IN ALUMINA AND ARCHITECTED SILICEOUS NANOCHANNELS

Akanksh Mamidala, Ph. D.

Cornell University 2025

Probing the mechanism of carbon mineralization in confined nanochannels provides insights into the nucleation and growth of carbonate crystals along with the preferential formation and stabilization providing implications to biomineralization, carbon sequestration and material synthesis. In the given thesis, the focus is specifically on the evolution of calcium- and magnesium-carbonate crystallization in confined volumes under the variation of solid interface from alumina to silica. Parameters like pore size, surface wettability, electrostatic charges and reaction temperature are altered to delineate the pre-nucleation behavior through MD simulations, phase transition pathway and the interfacial water behavior through experimental analysis. Results from these studies indicate that magnesium carbonate loaded in anodic alumina membrane proceeded via the transition and stabilization of hydrated phases before transitioning to stable magnesite phase with confinement significantly influencing both kinetic pathway and polymorph selectivity. Classical MD simulations revealed that hydrophilic alumina membrane stabilized the hydrated coordination shell around Mg^{2+} whereas hydrophobicity led to clatharate-like water structure. Extending this study with silica nanochannel solid interface investigates the formation and stabilization of nesquehonite ($MgCO_3.\ 3H_2O$) and hydromagnesite ($Mg_5(CO_3)_4(OH)_2.\ 4H_2O$) in hydrophilic and hydrophobic environments while a pronounced reduction in water mobility in silica nanoconfinement is observed through quasi-elastic neutron scattering. Transitioning to

calcium carbonate mineralization in nanoconfined alumina and silica solid interface depicts the transition from hydrated phases to metastable to stable calcite phase. In alumina interface, calcite is stabilized while silica interface promotes the stabilization of metastable vaterite and aragonite for a brief period with transition to calcite. MD simulations investigated the local density of bicarbonate, nitrate and water ions around Ca^{2+} giving a probabilistic idea of forming anhydrous phases over hydrated phases in nanoconfinement. To further mimic the geological conditions, reactive surface driven mineralization was explored through calcium silicate nanochannels. The reactive hosts accelerate the formation of vaterite and aragonite via silica dissolution and interfacial reaction mechanism, establishing temporal control over phase stabilization. Collectively, the thesis provides insights into the nucleation and diffusion pathways of carbonate mineralization in nanoconfinement providing a rational to develop models for geochemical transport in porous media.

BIOGRAPHICAL SKETCH

Akanksh Mamidala pursued his doctoral research in the department of Civil and Environmental Engineering, with a concentration in Environmental Processes. His research focused on understanding the confinement induced structural evolution of calcium and magnesium carbonate within engineered nanopores advancing applications in carbon sequestration and biomineralization. During his doctoral tenure, he presented his work in conferences such as AGU, ISRD-RCN workshop and ACS Fall meeting while contributing to interdisciplinary projects addressing sustainability, mineral recovery and carbon capture technologies. Prior to joining Cornell, Akanksh earned his bachelor's degree in Chemical Engineering, where he developed a strong foundation in chemical engineering fundamental principles. Beyond research, Akanksh has actively mentored graduate students, collaborating with multidisciplinary teams. He is passionate about scientific communications and the translation of fundamental research into real-world applications. Upon completing his PhD, he aims to continue working in the field of chemical and environmental engineering, scaling technologies for carbon management and sustainable mineral systems.

Dedicating to all those who stood by me through the late nights, last minute edits, and chaos-you know who you are. I would also like to thank me- for believing in me, even when the path was uncertain and for rising each day to try again.

ACKNOWLEDGMENTS

I gratefully acknowledge the invaluable support and guidance provided by Dr. Greeshma Gadikota. Her knowledge, wisdom, and expertise made this journey highly enjoyable and provided a unique perspective towards research and in my personal growth. My sincere thanks to Damian Helbling and Nicole Fernandez for serving on my committee and providing guidance on courses related to quantitative and computational aspects of the environmental science and engineering which was very helpful for my research. I would like to thank all members from Gadikota Research Group for the stimulating discussions, technical help and the camaraderie that made long hours in lab both productive and enjoyable. Special thanks to the staff at CCMR and CNF for their support with experimental facilities and instruments. I would also like to thank the staff and instrument scientist at ORNL for helping me in performing neutron scattering studies. Last but not the least, I would be remiss in not acknowledging the consistent and thoughtful support of my parents, sibling, and grandfather which was crucial for the successful completion of my doctoral program at Cornell University.

TABLE OF CONTENTS

LIST OF FIGURES

LIST OF SUPPLEMENTARY FIGURES

LIST OF TABLES

LIST OF SUPPLEMENTARY TABLES

CHAPTER 1

Background, Motivation and Introduction

The fundamental aspect of living organism functioning, encompassing vital role in human health, nutrition, and environmental management to industrial and natural processes revolves around the interaction of metal ions and minerals contributing to physiological, geological and environmental studies. Specifically, these metal ions, by virtue of their inherent chemical properties, participate in a diverse array of biological processes, often serving as essential factors for enzyme functioning and structural components of proteins. [1] The bioavailability of these metal ions, coupled with their redox potentials, coordination flexibility, valency, and ligand affinity dictates the workings of the metals for biological processes, influencing everything from catalysis to electron transfer, redox sensing and signaling. [2] Furthermore, these metal ions aid in the functioning of the nerve cells, muscle cells, the brain, heart and the transport of oxygen while stabilizing nucleotide bases and regulating the DNA transcription. [3–5] Understanding these factors governing metal ion chemistry in natural aqueous systems from kinetics to thermodynamics, is crucial in deciphering their role in biological systems. [6]

In particular, the internalization process involving abundant metal ions like Na^+, K^+, Ca^{2+}, Mg^{2+}, and Fe^{2+}/Fe^{3+} is pivotal in the functioning of various biological processes. [4] Critical body functions like neurotransmission, muscle contraction and heart function are clearly influenced by the difference between the concentration of Na^+ and K^+ ions in the extracellular and intracellular fluids, [4,7,8] while Ca^{2+} acts as an important source in bones and teeth and acts as a electrolyte controlling the constriction and dilation of

blood vessels, Mg^{2+} regulating the biochemical reactions by being the cofactor for more than 300 enzymes aiding in protein, DNA, RNA, and antioxidant glutathione synthesis, [4,9,10] and Fe^{2+}/Fe^{3+} regulating the oxygen transport and storage through globin-heme proteins. [11,12] Although, these metal ions play a vital role in regulating the biological system, the current focus is specifically on Ca^{2+} and Mg^{2+} ions due to their involvement in the natural process of biomineralization. Biomineralization involves the formation of mineralized tissues with hierarchal structures including bones and teeth in vertebrates that heavily rely on the controlled deposition of Ca^{2+} and Mg^{2+} in organic matrices. [13–15] Calcium ions play a vital role in formation of skeletal tissue as hydroxyapatite ($Ca_{10}(PO_4)_6(OH)_2$) crystals, contributing to their rigidity and mechanical strength. [16] Magnesium ions, on the other hand, acts as the main component of the bone improving its growth and regeneration. Further, Mg^{2+} control the crystallization of collagen while inhibiting its calcification. [17,18] Given these fundamental roles to both structural and regulatory functions in biomineralization, understanding their behavior and role in biological transport of Ca^{2+} and Mg^{2+} is crucial for advancing in the fields of bone tissue engineering, pathological calcification studies, and development of biomimetic materials.

Biomineralization showcases the nature's ability to form complex crystal structures at ambient conditions, whose mechanisms have been typically classifying into biologically controlled mineralization and biologically induced mineralization. [19] Biologically controlled mineralization dictates the nucleation, growth, morphology and crystal orientation of the mineral phase while biologically induced mineralization occurs as a result of metabolic activities of microorganisms altering the surrounding environment,

leading to crystal precipitation and crystallization. [20,21] Typically, the underlying formation of precipitate minerals by biomineralizing organisms occurs in small phospholipid bilayer compartments, which are universally representing confined volume systems. [22,23] These confinements play a crucial role in influencing the reaction pathways, kinetics and the resulting mineral phase facilitating and stabilizing certain crystal phases. [24] Prior studies investigated that spatial constraint influences biomineralization of amorphous calcium carbonate in collagen fibrils through electrostatic interactions and capillary forces promoting the crystallization of calcite nanoparticles, [25] while the recombinant protein rGST-Hic 12 attained from the mantle of Hyriopsis cumingii accelerate the calcium carbonate deposition and promote the conversion of calcite to vaterite during pearl biomineralization, [26] highly ordered single crystal aragonite are preferentially formed in the nacre layers of molluscan layers which can be attributed to the role of dipole-dipole interactions between the assembled units, [27] and microbial mats possessing filamentous cyanobacteria create ideal precipitation conditions for nesquehonite ($MgCO_3 . 3H_2O$), dypingite ($Mg_5(CO_3)_4(OH)_2 . 5H_2O$) and aragonite. [28] Delving into these biomineral formations provides insights into the stabilizing nature of the confining template and their role in regulating the natural biological processes. Based on the mechanisms involved, it is important to note that the carbonation mechanism in nanochannels is also observed in natural geological conditions having applications in CO_2 sequestration and the observed interfacial interaction between the solid-fluid interface are visibly transferrable. This concept of carbonate crystallization in subsurface geological conditions is attributed to the phenomena of carbon mineralization.

Carbon mineralization is a thermodynamically downhill pathway to store atmospheric CO_2 for a large timeframe by using suitable and globally available feedstock. [29] Among these precursors Ca- and Mg-based resources are considered most promising due to their availability and resource-bearing capacity. [29–31] Pathways with lower thermodynamic limitations should be considered among which CO_2 mineralization in mafic and ultramafic rocks consisting of silicates of calcium and magnesium enable stable and safe storage forming water-insoluble minerals like calcite ($CaCO_3$), dolomite ($CaMg(CO_3)_2$) or magnesite ($MgCO_3$). [32] These mafic and ultramafic rocks constitute ~70% of the oceanic floor and ~5% of the continental surface but account for about ~30% of the atmospheric CO_2 capture. Specifically, hydrothermally active mafic rocks can naturally store >100 kg CO_2 m^{-3} depicting an overall storage capacity of 100,000-250,000 Gt CO_2, which is larger than the current emissions. [31] Based on the promising sequestration capacity within subsurface environments, studies have focused on understanding the natural precipitation/crystallization pathways in bulk fluids using geological conditions of high temperatures and high pressures. But, these naturally available subsurface lithologies are rich in confined nanopores which play a key role in the fate and transport of water and ions aiding to carbonate growth in bulk. These mineralization mechanisms differ in confined nanochannels and the major difference is in the estimation of the time scales of carbon mineralization in nanochannels with respect to bulk fluids. For example, the solubility and adsorption behavior of solutes such as metal ions and gases is considerably different in nanoscale confinement compared to in bulk fluids. [33–35] Furthermore, the growth of carbonates in silica nanochannels influences the crystal morphology, orientation, and nucleation rates. [23] Furthermore, within confinement, the

volume of the confined media and the interaction between the crystals will determine the nature of crystal growth. [23] To understand these effects, engineering a homogenous pathway and achieving predictive growth of carbonates within reactive and unreactive silica interfaces helps us understand the mechanisms involved and in controlling the morphology and phase formation of the carbonate particles.

This research effort focuses on understanding and developing mechanistic insights into carbonate growth in abundant alumina and siliceous nanopores and determining the preferential formation of the carbonate phases. The reactivity of amorphous, and Ca-bearing silicate nanochannels and their role on influencing the chemistry and evolution of carbonates will be examined. Furthermore, the influence of interfacial water on carbonate nucleation and crystallization behavior is investigated. In this context, the following chapters are explored:

- Develop approaches to understand the evolution of Mg-carbonate phases in large pore size nanochannels.
- Direct the formation and evolution of Mg-carbonate polymorphism in Alumina vs Silica confined hosts in various physicochemical conditions.
- Probe the nucleation and crystallization of calcium carbonate in alumina vs siliceous nanopores and explore the nucleation mechanism of carbonates in confinement.
- Determine the influence of reactive silica interfaces on calcium carbonate formation and the temporal evolution on the phase formation and stabilization.

Within the following thesis, the second chapter (objective 1) focuses on investigating the evolution of magnesium carbonate phases in 200 nm alumina membrane by varying the surface wettability and reaction temperature. A combination of experiments and

molecular dynamics simulations are employed to understand the phase behavior and the coordination environment. The third chapter (objective 2) delineates the crystallization behavior of magnesium carbonate in alumina vs silica nanochannels and in much smaller nanopores along with controlled surface wettability and reaction temperature. The study investigates the kinetics of each phase and the dimensionality of growth along with quasi elastic neutron scattering to examine the dynamics of confined water in the presence of magnesium carbonate. The fourth chapter (objective 3) explores the nucleation and growth of calcium carbonate in alumina and silica nanochannels of varying pore sizes, temperature and surface properties. Experimental approach investigates the phase transition pathway while simulations reveal the pre-nucleation and coordination environment of Ca^{2+} ions. The fifth chapter (objective 4) introduces reactive calcium silicate nanochannels to study the formation of calcium carbonate through interfacial interactions while investigating the effect of temporal evolution on phase formation and stabilization. The overview of the entire thesis along with the respective objectives is indicated in **Figure 1**.

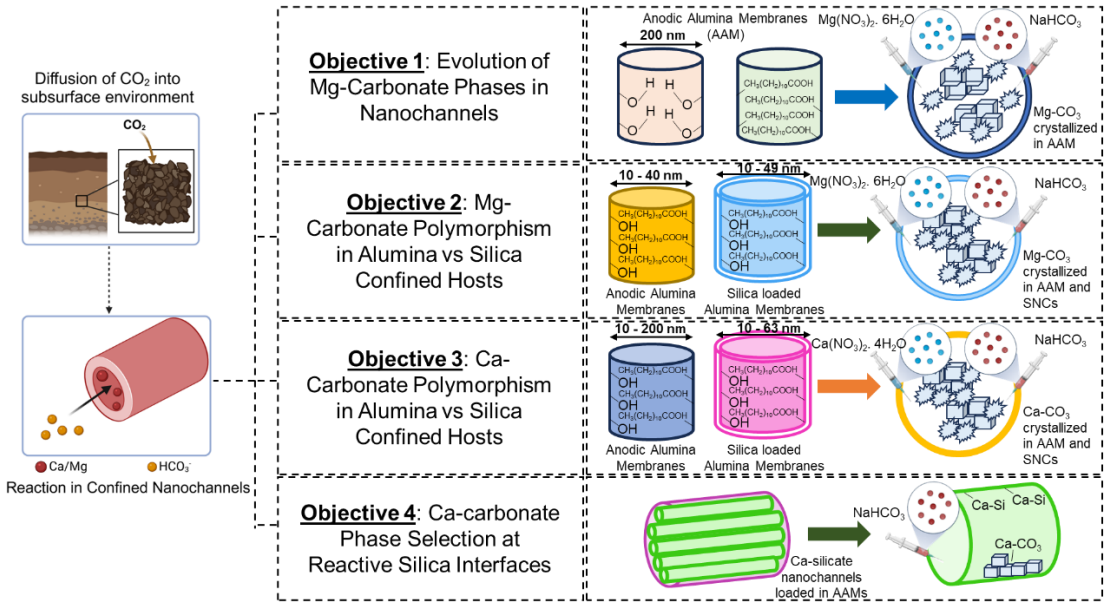

Figure 1 Schematic representation of the research focusing on structural evolution of calcium and magnesium carbonate in nanoconfined reactive/unreactive systems

References

1. Chen, A. Y. *et al.* Targeting metalloenzymes for therapeutic intervention. *Chemical Reviews* vol. 119 Preprint at https://doi.org/10.1021/acs.chemrev.8b00201 (2019).

2. Bhagi-Damodaran, A. & Lu, Y. The Periodic Table's Impact on Bioinorganic Chemistry and Biology's Selective Use of Metal Ions. in *Structure and Bonding* vol. 179 (2019).

3. Moustakas, M. The role of metal ions in biology, biochemistry and medicine. *Materials* vol. 14 Preprint at https://doi.org/10.3390/ma14030549 (2021).

4. Zheng, X., Cheng, W., Ji, C., Zhang, J. & Yin, M. Detection of metal ions in biological systems: A review. *Reviews in Analytical Chemistry* vol. 39 Preprint at https://doi.org/10.1515/revac-2020-0118 (2020).

5. Theophanides, T. Metal ions in biological system. *Int J Quantum Chem* 26, 933–941 (1984).

6. Williams, P. A. Solutions in the 'big laboratory': Toward a model for metals at the Earth's surface. in *Pure and Applied Chemistry* vol. 77 (2005).

7. Blaustein, M. P. & Lederer, W. J. Sodium/calcium exchange: Its physiological implications. *Physiological Reviews* vol. 79 Preprint at https://doi.org/10.1152/physrev.1999.79.3.763 (1999).

8. Hille, B. Ionic channels in excitable membranes. Current problems and biophysical approaches. *Biophys J* 22, (1978).

9. Saris, N. E. L., Mervaala, E., Karppanen, H., Khawaja, J. A. & Lewenstam, A. Magnesium: An update on physiological, clinical and analytical aspects. *Clinica Chimica Acta* vol. 294 Preprint at https://doi.org/10.1016/S0009-8981(99)00258-2 (2000).

10. Gröber, U., Schmidt, J. & Kisters, K. Magnesium in prevention and therapy. *Nutrients* vol. 7 Preprint at https://doi.org/10.3390/nu7095388 (2015).

11. Andrews, N. C. Iron homeostasis: Insights from genetics and animal models. *Nature Reviews Genetics* vol. 1 Preprint at https://doi.org/10.1038/35042073 (2000).

12. Hentze, M. W., Muckenthaler, M. U., Galy, B. & Camaschella, C. Two to Tango: Regulation of Mammalian Iron Metabolism. *Cell* vol. 142 Preprint at https://doi.org/10.1016/j.cell.2010.06.028 (2010).

13. Addadi, L. & Weiner, S. Biomineralization: Mineral formation by organisms. *Phys Scr* 89, (2014).

14. Tang, S., Dong, Z., Ke, X., Luo, J. & Li, J. Advances in biomineralization-inspired materials for hard tissue repair. *International Journal of Oral Science* vol. 13 Preprint at https://doi.org/10.1038/s41368-021-00147-z (2021).

15. Lowenstam, H. A. & Weiner, S. *On Biomineralization*. (Oxford University Press, 1989). doi:10.1093/oso/9780195049770.001.0001.

16. Boskey, A. L. Mineralization of bones and teeth. *Elements* 3, (2007).

17. Zhang, J. *et al.* Dual Function of Magnesium in Bone Biomineralization. *Adv Healthc Mater* 8, (2019).

18. Meldrum, F. C. & Cölfen, H. Controlling mineral morphologies and structures in biological and synthetic systems. *Chemical Reviews* vol. 108 Preprint at https://doi.org/10.1021/cr8002856 (2008).

19. Dhami, N. K., Reddy, M. S. & Mukherjee, M. S. Biomineralization of calcium carbonates and their engineered applications: A review. *Frontiers in Microbiology* vol. 4 Preprint at https://doi.org/10.3389/fmicb.2013.00314 (2013).

20. Hoffmann, T. D., Reeksting, B. J. & Gebhard, S. Bacteria-induced mineral precipitation: A mechanistic review. *Microbiology (United Kingdom)* 167, (2021).

21. Qin, W. *et al.* Microbe-Mediated Extracellular and Intracellular Mineralization: Environmental, Industrial, and Biotechnological Applications. *Advanced Materials* vol. 32 Preprint at https://doi.org/10.1002/adma.201907833 (2020).

22. Tester, C. C., Wu, C. H., Weigand, S. & Joester, D. Precipitation of ACC in liposomes - A model for biomineralization in confined volumes. *Faraday Discuss* 159, (2012).

23. Meldrum, F. C. & O'Shaughnessy, C. Crystallization in Confinement. *Advanced Materials* vol. 32 Preprint at https://doi.org/10.1002/adma.202001068 (2020).

24. DeJong, J. T., Mortensen, B. M., Martinez, B. C. & Nelson, D. C. Bio-mediated soil improvement. *Ecol Eng* 36, (2010).

25. Ping, H. *et al.* Confinement controlled mineralization of calcium carbonate within collagen fibrils. *J Mater Chem B* 4, (2016).

26. Luo, W., Jiang, R., Ren, G. & Jin, C. Hic12, a novel acidic matrix protein promotes the transformation of calcite into vaterite in Hyriopsis cumingii. *Comp Biochem Physiol B Biochem Mol Biol* 261, (2022).

27. Zhou, G. T., Yao, Q. Z., Ni, J. & Jin, G. Formation of aragonite mesocrystals and implication for biomineralization. *American Mineralogist* 94, (2009).

28. Power, I. M., Wilson, S., Thom, J. M., Dipple, G. M. & Southam, G. Biologically induced mineralization of dypingite by cyanobacteria from an alkaline wetland near Atlin, British Columbia, Canada. *Geochem Trans* 8, (2007).

29. Santos, H. S. *et al.* Mechanisms of Mg carbonates precipitation and implications for CO2 capture and utilization/storage. *Inorganic Chemistry Frontiers* Preprint at https://doi.org/10.1039/d2qi02482a (2023).

30. Gadikota, G. Carbon mineralization pathways for carbon capture, storage and utilization. *Communications Chemistry* vol. 4 Preprint at https://doi.org/10.1038/s42004-021-00461-x (2021).

31. Snæbjörnsdóttir, S. *et al.* Carbon dioxide storage through mineral carbonation. *Nature Reviews Earth and Environment* vol. 1 Preprint at https://doi.org/10.1038/s43017-019-0011-8 (2020).

32. Lamérand, C., Shirokova, L. S., Bénézeth, P., Rols, J. L. & Pokrovsky, O. S. Carbon sequestration potential of Mg carbonate and silicate biomineralization in the presence of cyanobacterium Synechococcus. *Chem Geol* 599, (2022).

33. Queralt-Martín, M. *et al.* Biphasic concentration patterns in ionic transport under nanoconfinement revealed in steady-state and time-dependent properties. *Journal of Chemical Physics* 158, (2023).

34. Xue, M., Qiu, H., Shen, C., Zhang, Z. & Guo, W. Ion Hydration under Nanoscale Confinement: Dimensionality and Scale Effects. *Journal of Physical Chemistry Letters* 13, (2022).

35. Gadikota, G., Dazas, B., Rother, G., Cheshire, M. C. & Bourg, I. C. Hydrophobic Solvation of Gases (CO2, CH4, H2, Noble Gases) in Clay Interlayer Nanopores. *Journal of Physical Chemistry C* 121, (2017).

CHAPTER 2

Non-Monotonic Evolution of Hydrated and Anhydrous Mg-Carbonate Phases in 200 nm Alumina Pores with Hydrophobic and Hydrophilic Surfaces

1. Introduction

The present era has witnessed a record level in the anthropogenic emissions associated with human activities making it imperative to act toward reducing these emissions. Carbon dioxide is the most abundant greenhouse gas and has strong ability to absorb infrared radiation, resulting in the rise of global temperature. [1] These human-made emissions contribute to changes in weather patterns, and surge in floods, drought, hurricanes, and heatwaves. To mitigate the harmful consequences caused by CO_2, it is crucial to develop smart and cost-effective carbon capture and sequestration (CCS) techniques with *in situ* mineralization. Carbon mineralization is a thermodynamically downhill process that converts CO_2 into stable carbonate minerals [2] using abundantly available alkaline earth metals. [3] Common alkali metals like calcium and magnesium react with CO_2 to form stable mineral carbonates in chemically bound form [4–6] offering an environment friendly pathway for permanent storage. [7]

Although gigatons of CO_2 are stored in subsurface environments, the kinetics of carbonate formation is decelerated due to its slow diffusion in the gas-solid system, resulting in timescales spanning over thousands of years. [8] The natural kinetics is also influenced by temperature, mineral composition, and the presence of other carbon sources [9] in ultramafic rocks and silicate minerals like olivine ($(Mg,Fe)_2SiO_4$), labradorite ($Ca_{0.6}Na_{0.4}Al_{1.6}Si_{2.4}O_8$) [10], anorthite ($CaAl_2Si_2O_8$) and basalt. [11] Given the complexity of the carbonation process, it is crucial to understand the fundamental

mechanism, the kinetics involved, and the effect of various earth-abundant minerals in this event to aid in desired carbon management.

The subsurface environments in many host lithologies (*e.g.* basalt, sandstone, shale) are abundant in confined nanopores that are highly reactive with CO_2 to form mineral carbonates. [12] These nanopores make up over 90% of the mineral surface area [13] and play a pivotal role in the transport of water and ions. [14] Interpreting the behavior of fluids in nanoconfinement is crucial as the fluids display characteristics largely different from what is exhibited in bulk. Fluids in confinement exhibit nanoscale effects, quantum effects, distorted phase effects, pressure effects, stability effects, and dielectric anomalies. [15–17] Additionally, concepts like Gibbs surface thermodynamics, surface tension, Laplace equations, Young's modulus, and the second law of thermodynamics break down at nanoscale. [18] Nanoconfinements are also known to induce long-lived metastable states, preferential adsorption of components, and unique phase transitions. [18]

Getting insights into the nucleation pathway of carbonate crystallization and the anomalies observed in confinement is crucial in developing accurate reactive models to predict the behavior of carbonates in natural systems along with improved control and manipulation of crystallization in engineered systems. [19] The conventional nucleation theory is derived from classical nucleation theory [20] which assumes the formation of a critical nucleus followed by the growth of the crystal. This aids in understanding the concept of phase-change kinetics in passive fluids. [21] On the other hand, non-classical nucleation theory is built on a two-step process involving an intermediate meta-stable phase prior to the formation of a stable nucleus. [21,22] The emergence of a stable nucleus

follows the decomposition of the amorphous phase and structural oscillation between the crystalline and amorphous phases. [22,23] Non-classical nucleation theory emphasizes the role of smaller clusters, amorphous phases, and oligomers during the growth process. [24] Ostwald ripening is one of the non-classical mechanisms where small particles dissolve and join the assembly of large particles that are more stable. [25] Under a temperature gradient in two-alloy systems, Ostwald ripening leads to a faster growth rate and particle migration [26] with a diffusive kinetics. [27] Another approach that involves the alignment of atomic lattices to form a single crystal [28] is termed as "oriental attachment", particularly considered in the generation of hierarchal structures. [29] Oriental attachment allows the unifying and mediating behavior of a large number of 1D, 2D, and 3D crystals [30] and thus removes the liquid interface lowering the energy of the system. [28]

The geological media is rich in calcium- and magnesium-based minerals which are promising materials for carbon mineralization. Carbonate minerals like calcite, magnesite, and dolomite are abundant in geological surfaces, with dolomite alone constituting 50% of the carbonate reservoir. [15] Numerous studies have been performed over the years to understand the crystal growth and nucleation mechanism of $CaCO_3$ ranging from confined nanoscales to bulk fluids. These comprise of the formation of stable calcite within silica nanochannels [30], the synthesis of single crystals of oriented aragonite in track-etched membranes [31], and the precipitation and transformation of amorphous calcium carbonate (ACC) into stable calcite within unfunctionalized glass surface. [32] However, a large knowledge gap resides on the mechanism of magnesium carbonate precipitation and phase evolution. Magnesite ($MgCO_3$), the most stable form

of magnesium carbonate is seen to form at elevated temperatures and pressure. In a study by Farhang et al., [33] thermally activated serpentine was reacted with bicarbonate solution at a temperature of 185 °C and a pressure of 140 bar of CO_2 to crystallize magnesite. In contrast, precipitation of magnesium carbonate has been investigated at room temperature with the aid of carboxylate microspheres over 70 days, and magnesite was observed to form on the sphere surface. [34] Reports involving nanoconfinement effects indicated that magnesium carbonate was found to adsorb 5 monolayers of water and displayed anomalous activation energy of 36±6 kJ/mol in 1 nm confinement similar to that of Ca^{2+} (calcite, 44 kJ/mol). [12] Although these studies explain the formation of stable magnesite in bulk and confinement, the gap lies in understanding several important phenomena such as the mechanism of nucleation, crystallization, and kinetics of multiple phases of magnesium carbonate at different temperatures, the mechanism behind magnesium modifying carbonate growth by inhibiting calcite crystallization in dolomite reservoirs, and the concept behind formation of hydrated magnesium carbonate crystals in nanoconfinement. [35–37] Bridging these gaps would help develop technologies to manufacture high-quality single crystals, enable the synthesis of hydrated magnesium carbonate with desired morphology, and develop magnesium alloys with high strength and ductility by varying the crystal structure for various industrial applications. [38,39]

Magnesium carbonate crystallizes into its hydrated forms at ambient conditions and plays a vital role in carbon biomineralization and geological processes. Metastable hydrated states are observed due to the presence of a stable hydration shell where each Mg^{2+} ion coordinates with six water molecules in an octahedral geometry. Hydrated

forms like barringtonite ($MgCO_3$. $2H_2O$), nesquehonite ($MgCO_3$. $3H_2O$), lansfordite ($MgCO_3$. $5H_2O$), hydromagnesite ($Mg_5(CO_3)_4(OH)_2$. $5H_2O$) and artinite ($Mg_2(CO_3)(OH)_2$. $3H_2O$) phases are observed in low-temperature hydrothermal environments that are rich in magnesium oxides and hydroxides. [40] Studies have been carried out on the precipitation of $MgCO_3$. $3H_2O$ and $Mg_5(CO_3)_4(OH)_2$. $5H_2O$ using thermally activated serpentine and CO_2 pressure of 80 PSI, with $MgCO_3$. $3H_2O$ forming at reaction temperatures below 50 °C and $Mg_5(CO_3)_4(OH)_2$. $5H_2O$ forming above 60 °C. [41] The transformation pathway of magnesium carbonate from metastable states into stable carbonates in bulk solutions was reported by Rheinheimer et al., [42] as, Lansfordite → Nesquehonite → Dypingite → Hydromagnesite → Magnesite and the transformation of Artinite → Pokrovskite. The major mineral phases observed after precipitation of magnesium carbonate in bulk and confinement are shown in **Table 1**.

Table 1 A list of majorly possible mineral phases in Mg-CO3 system

Mineral phase observed	**Chemical formula**
Magnesite	$MgCO_3$
Barringtonite	$MgCO_3$. $2H_2O$
Nesquehonite	$MgCO_3$. $3H_2O$
Artinite	$Mg_2(CO_3)(OH)_2$. $3H_2O$
Hydromagnesite	$Mg_5(CO_3)_4(OH)_2$. $4H_2O$
Lansfordite	$MgCO_3$. $5H_2O$
Dypingite	$Mg_5(CO_3)_4(OH)_2 \cdot 5H_2O$
Shelkovite	$Mg_7(CO_3)_5(OH)_4$. $24\ H_2O$
Pokrovskite	$Mg_2(CO_3)(OH)_2$. $0.5\ H_2O$

Giorgiosite	$Mg_5(CO_3)_4(OH)_2 \cdot 5\text{-}6H_2O$

Another key characteristic that influences evaporative dynamics and crystallite formation is surface wettability which promotes heterogenous nucleation from solution phase, allowing the design of surfaces to promote or inhibit precipitation. [43] Wettability in nanoconfinement explicitly modifies the dielectric response of water, resulting in a tunable polarity. [44] Hydrophobic surfaces show significant effects on particle adhesion [45] and display drag reduction effects, which can influence atomization performance. [46] Switching the surface to hydrophilic enhances heat transfer and water transport improving thermal-evaporation performance [47] and promoting water accumulation inside nanopores. [48] The extent of surface wettability is crucial in the organization of biomacromolecules, designing bio nano-devices, and in packaging industries etc. [49]

Therefore, the present study aims to explore the behavior of carbonate growth in nanoconfinement while tuning the surface wettability and multiple physicochemical conditions. To be specific, this work focuses on precipitating magnesium carbonate in 200 nm anodic alumina membranes (AAMs) loaded using an aspiration setup. Magnesium carbonate is precipitated using 0.8 M $Mg(NO_3)_2.\ 6H_2O$ and 0.4 M $NaHCO_3$ in a 2:1 molar ratio. Formation of different phases of magnesium carbonate, their growth, and variation with time and temperature in nanoconfinement are investigated. By changing the surface wettability, the impact of hydrophobicity on the evolution of phase formation and crystal growth are also explored. **Figure 2(a)** provides a schematic of the anodic alumina membrane. This study provides a holistic view into the role of

Mg^{2+} ions for storing atmospheric CO_2 via the mineralization pathway in nanoconfined pores that replicates the natural geological phenomena.

To gain an atomic-level insights into the mineralization in nanoconfinement, the current study utilized Molecular Dynamics (MD) as an efficient numerical simulation technique. Apart from predicting the time evolution of an ensemble of particles by solving Newton's equations of motion, MD simulation provides intricate details of atomic level interactions present in the system. With the advent of various force field parameters, it has become increasingly convenient to study systems involving complex chemistry and physics. This work employed classical MD simulation on systems containing hydrophilic and hydrophobic alumina surfaces in presence of solutions containing the ionic species required for magnesium carbonate crystallization in the experiment. However, due to the classical nature of the dynamics, the present simulation results focus mainly on the pre-nucleated coordination environment of the Mg^{2+} ions. It is important to note that density functional theory and Car-Parrinello method-based study by Tommaso et al. predicted the first coordination sphere of hydrated Mg^{2+} ion in bulk to be composed of six water molecules, whereas in case of solvated magnesium carbonate or magnesium bicarbonate, the most stable monomers were found to be of the forms $Mg[\eta^1\text{-}CO_3](H_2O)_4$ and $Mg[\eta^1\text{-}HCO_3](H_2O)_4^+$ respectively. [50] Besides, *ab-initio* MD studies by Rowley et al. found the coordination number of Mg^{2+} with respect to water as 6 with a discrete coordination sphere at 2.1 Å and an octahedral structure. [51] Since water in close contact with metal oxide surfaces (interfacial water) such as those of alumina is known to exhibit preferential orientation and delayed dynamics compared to bulk water, [52] the spatial arrangement of water molecules, if not the coordination

number around Mg^{2+}, is also anticipated to be affected. However, Tavani et al. observed that controlled exposure of MgO surface to water vapor at ambient pressure and 50 °C temperature, the surface Mg^{2+} ions still tend to form hexa-hydrated octahedral ($[Mg(H_2O)_6]^{2+}$) complex of magnesium similar to bulk conditions. [53] To the best of our knowledge, as the coordination behavior of Mg^{2+} ions in contact with amorphous alumina surfaces is not reported in literature, the simulations in the present study impart several useful details in this regard such as the coordination environment of the magnesium ions in the interface along with its direct comparison with bulk phase, wettability of the alumina surfaces in terms of hydrogen bonding with water, and estimates of the non-bonding interaction between alumina membrane and the ions. As a schematic representation of the computational studies, **Figure 2(b)** depicts the radial distribution function of Mg^{2+} ions with respect to bicarbonate oxygens as a function of radial distance in the interfacial and bulk fluid. An idea of the coordination environment of Mg^{2+} can be obtained from the snapshots included.

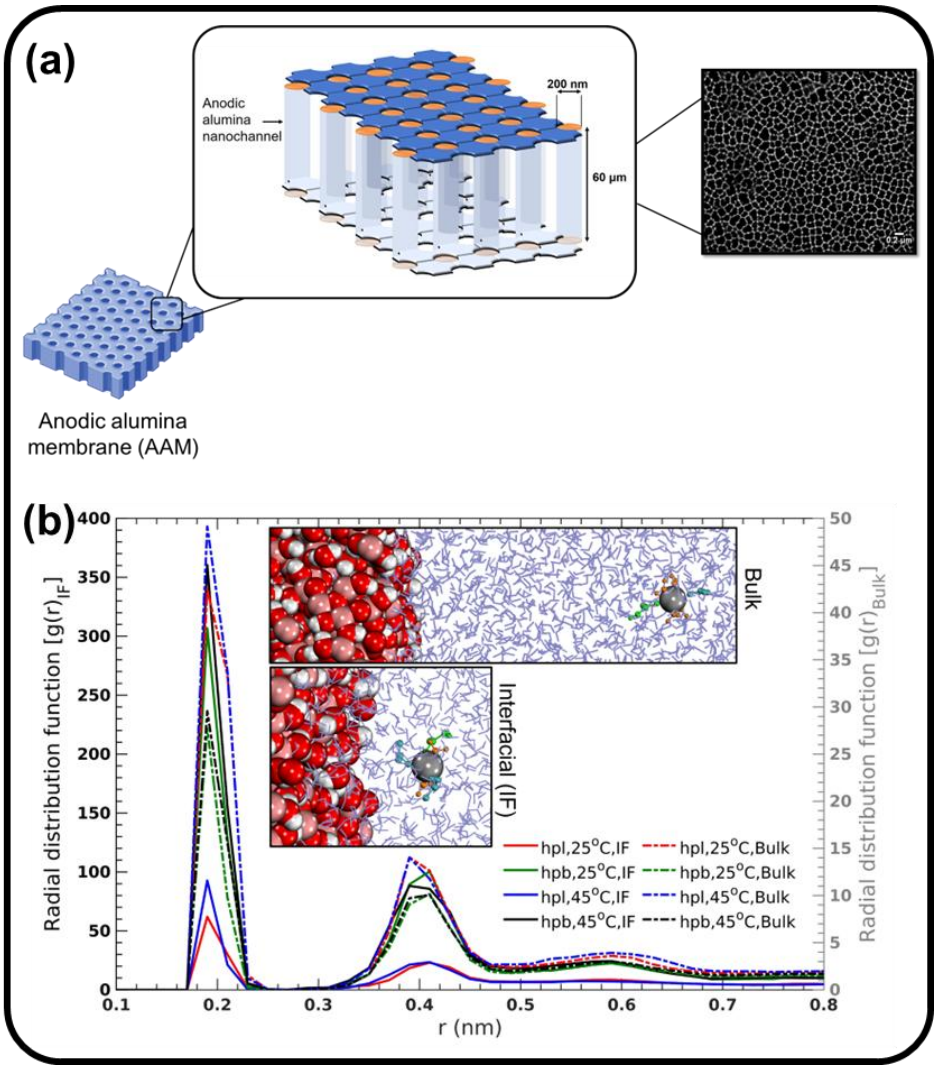

Figure 2 (a) Schematic representation of anodic alumina membrane (AAM) along with the pore diameter and height of the nanochannel and the corresponding snapshot as viewed using a scanning electron microscope, (b) radial distribution function of bicarbonate oxygens with respect to Mg^{2+} ions in the interfacial (IF) and bulk regions of the simulation cell at temperatures of 25 °C and 45 °C. 'hpl' and 'hpb' correspond to hydrophilic and hydrophobic alumina membrane respectively. Snapshots of a randomly selected Mg^{2+} along with the chemical entities in its first coordination sphere are provided as insets. Grey, Mauve, red, and white vdW spheres represent Mg^{2+}, Aluminum, Oxygen, and Hydrogen respectively. Water is shown as blue lines whereas orange, green, and cyan CPK representation correspond to water, bicarbonate, and nitrate ions respectively in the first coordination sphere of the chosen Mg^{2+}. A detailed insight into the g(r) profiles can be obtained from Figure 11.

2. Experiments and Methodology

2.1 *Materials*

Anodic alumina membranes (AAM) having a diameter of 25 mm, a length of 60 μm, and a pore size of 0.2 μm with trade name Cytiva Whatman™ Anodisc™, was used as the membrane. Laboratory grade magnesium nitrate hexahydrate ($Mg(NO_3)_2.\ 6H_2O$) (Sigma Aldrich, ACS reagent 99%) and sodium bicarbonate ($NaHCO_3$) (Fischer Scientific, ACS reagent 99%) powder were used for precipitating magnesium carbonate. To incorporate hydrophobicity, lauric acid ($C_{12}H_{24}O_2$) (Sigma Aldrich, FCC, FG, ≥ 98%), and anhydrous ethanol (C_2H_5OH) (Fischer Scientific, 96% v/v) were used. All chemicals were purchased from commercial vendors and used as received without any further purification. Deionized (DI) water (18.2 MΩ.cm) from the Milli-Q Q-POD® system was used in all experiments. The aspiration setup having a 25 mm filter funnel and a capacity of 50 mL was purchased from Cytiva and was used without any modification.

2.2. *Loading of Magnesium Carbonate in Hydrophilic Nanoconfinement*

An anodic alumina membrane with a well-defined pore size distribution of 0.2 μm and a diameter of 25 mm was utilized for precipitating magnesium carbonate in confinement. An aspiration setup was employed to load the magnesium-rich solution within the nanopores as shown in **Figure 3**. To examine the growth of magnesium carbonate, 0.8 M $Mg(NO_3)_2.\ 6H_2O$ and 0.4 M $NaHCO_3$ solutions were prepared and loaded. 0.2 mL of the prepared solution was passed through the pores with the aid of aspiration and this process was repeated 5 times. After loading, the membranes were placed at 25 °C for the reaction to proceed. To investigate the influence of temperature

on carbonate crystallization, the loaded membranes were immediately placed in a vacuum oven (Thermo Scientific Lindberg Blue M) at 45 °C for 15 minutes and the rest of the aging was then performed at 25 °C to prevent any fluid loss due to evaporation and simultaneously affect the crystal phase growth and speciation.

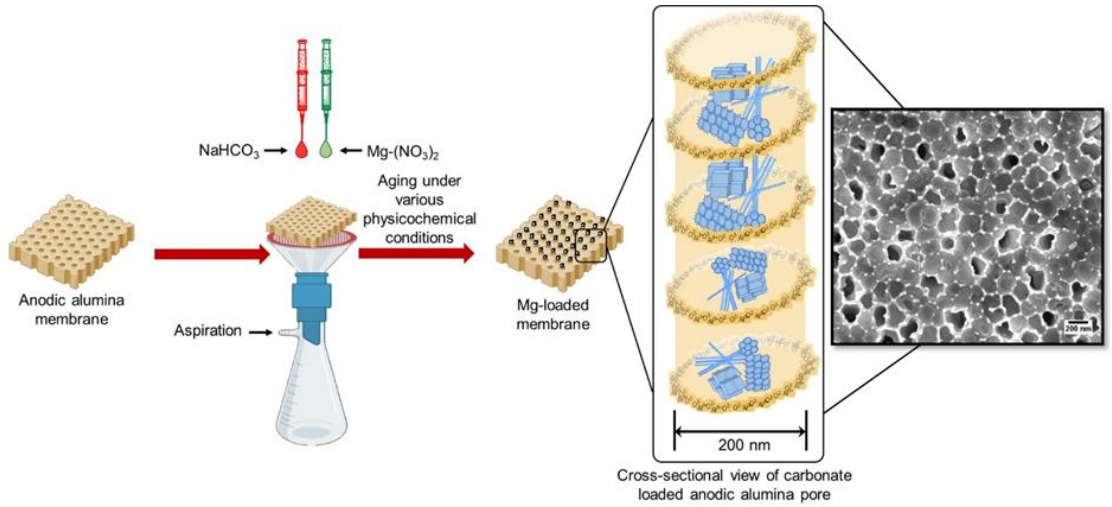

Figure 3 Schematic of the aspiration setup and the process of loading Mg-CO3 solution in the anodic alumina membrane along with a snapshot of the Mg-loaded pores as viewed using a scanning electron microscope. A cross-sectional view of the magnesium loaded alumina pore is provided to highlight the formation of different hydrated and non-hydrated phases of magnesium carbonate in the nanochannel.

2.3. *Variation in Surface Wettability and Sample Characterization*

For understanding the growth of magnesium carbonate in hydrophobic confined nanopores, surface modification of anodic alumina membrane was required. Therefore, the following methodology was adapted with slight modifications. [54] The purchased membrane is first rinsed with ethanol and water and dried at 85 °C for 30 minutes. Thereafter, the membranes were immersed in a solution of lauric acid in ethanol (20 g/L) for 15 minutes at 50 °C and stirred at 120 rpm. The surface-modified membranes were again rinsed with ethanol and DI water and dried at 85 °C for 30 minutes. This

surface-altering process replaces the hydroxide moieties attached to the aluminum ion with lauric acid as shown in **Figure 4(a)**. A contact angle measurer was used to confirm the surface wettability of both hydrophilic and hydrophobic membranes. Contact angle measurement was performed using Ramé-Hart Contact Angle Goniometer 500 having a volume step of 10 μL and delay time of 4000 milliseconds. During the measurement, the syringe volume was set at 250 μL with a volume step of 10 μL, and about 20 μL of water was dropped onto the membrane. The hydrophobic AAMs were then placed in an aspiration setup similar to the one shown in **Figure 3** and magnesium carbonate was loaded. The concentrations and the loading process are the same as described above for the hydrophilic surface. All the experiments were carried out in triplicates simultaneously to attain error bars as the crystal formation is sensitive to minute changes in atmospheric conditions.

The crystallite formation for both hydrophilic and hydrophobic membranes was determined using an X-ray diffractometer (Bruker D8 Advance ECO Powder diffractometer) having a Cu Kα radiation, operating voltage of 40 kV, and current of 25 mA. The XRD pattern was obtained in the range of $2\theta = 7°$ to 80° after 6, 24, 48, 72, and 96 hours of loading. To determine the morphological changes and to confirm the growth of magnesium carbonate in confined pores, the membranes were imaged using a scanning electron microscope (Zeiss Gemini 500) with an accelerating voltage of 3 kV.

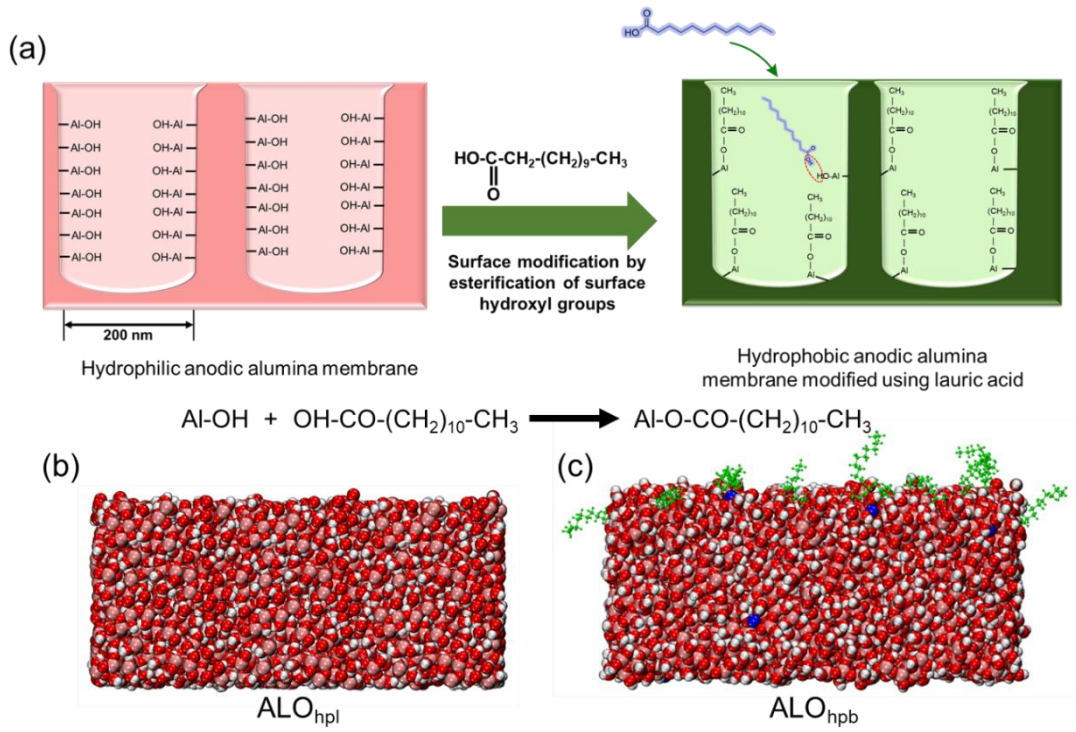

Figure 4 (a) Process schematic of the surface wettability modification of anodic alumina membrane from hydrophilic to hydrophobic using lauric acid indicating the surface reaction. Snapshots of the (b) hydrophilic (ALOhpl) and (c) hydrophobic (ALOhpb) alumina membranes as used in MD simulations. Mauve, blue, red, and white vdW spheres represent Aluminum, Sodium, Oxygen, and Hydrogen respectively. The lauric acid fragments in (c) are represented as green CPK chains.

2.4. *Molecular Dynamics Simulation Methodology*

2.4.1. *Modeling of the Hydrophilic (ALO_{hpl}) and Hydrophobic (ALO_{hpb}) Alumina Membrane*

Metal oxide surfaces exposed to water, often offer a useful alternative of the corresponding cylindrical confinements as large as 200 nm while suitably mimicking the interfacial water properties. [52,55,56] Therefore, several approaches exist for modeling amorphous metal oxide surfaces. [57–60] For example, Adiga et al. [61,62] obtained bulk amorphous alumina sample by placing Al and O atoms in the stoichiometric ratio of Al_2O_3 in an orthorhombic supercell of the hexagonal α-alumina lattice and heating the

system to a temperature of 5000 K followed by cooling. Further, to obtain the hydroxylated alumina surface, a specific number of Al atoms were replaced by H atoms in the bulk amorphous sample followed by removal of one O for every Al atom that was replaced by H atom. [61,62] Besides, *ab-initio* study of water adsorption on alumina reported 1-2 and 1-4 dissociations of water in the vicinity of alumina (0001) surface giving rise to hydroxylated alumina surfaces. [63] In line with these approaches, coordinates of the Corundum unit cell were obtained from Crystallography Open Database (COD ID: 1000017) with the cell parameters a= 4.761 Å, b= 4.761 Å, c= 12.994 Å, α= 90°, β= 90°, and γ= 90° for modeling the amorphous alumina membrane in this study. [64] The unit cell was partially hydroxylated to account for the presence of hydroxyl functionalities in the anodic alumina membrane used in the experiment. [65] A (4×4×1) supercell was built by replicating the unit cell in space. ClayFF parameters were used to describe the bonding and non-bonding potentials in the alumina membrane. [66] Hydroxyl moieties as described by the ClayFF parameters were added to neutralize the charge on the unit cell. [67,68] The resultant hydroxylated supercell was energy minimized using Steepest descent algorithm for 50,000 steps and subjected to equilibration in the NVT ensemble with simulated annealing in order to obtain an amorphous anodic alumina membrane. System temperature was raised from 298 K to 1500 K with a ramp rate of 0.05 K/ps. This was followed by relaxing the system back to 298 K with the same ramp rate. Fast cooling prevents reorganization of the atoms in the alumina membrane thus ensures the formation of a completely amorphous structure. The resultant system was equilibrated at 298 K for another 12 ns. The amorphous membrane thus obtained was used to generate a larger slab by constructing a (3×2×2)

supercell (**Figure 4(b)**). Henceforth, this supercell is termed as ALO_{hpl} with ~ 8 OH/nm^2 exposed on the surface. [69] Dimensions of ALO_{hpl} along x, y, and z axes are ~ 8 nm, ~ 4 nm, and ~ 4 nm respectively.

On the other hand, to model the hydrophobic alumina membrane, ALO_{hpl} was used as the initial structure. 12 Lauric acid (LAU) fragments were attached to the membrane surface by creating ester linkage between surface hydroxyl group on ALO_{hpl} and -COOH on LAU using Gaussview. [54,70] 12 chains of LAU were sufficient to cover ALO_{hpl} with a hydrophobic layer and were found to impart high hydrophobic character to the surface, as noticed through hydrogen bonding between the solid surface and interfacial water (**Figure 5(a)**). The net charge on the functionalized membrane was neutralized by adding 12 Na^+ and 12 OH^-. The resultant system was energy minimized using Steepest descent algorithm and equilibrated in NVT ensemble for 10 ns with position restraint on the membrane and LAU. [71] To allow the LAU fragments achieve their equilibrium configurations, the resultant structure was equilibrated for another 5 ns in NVT ensemble keeping all but LAU frozen. The resultant membrane (**Figure 4(c)**) is called ALO_{hpb} henceforth. It is to be noted that addition of Na^+ for charge neutralization in ALO_{hpb} has negligible effects on the fate of the simulation as the concentration of Na^+ present in the membrane is insignificant compared to the concentration of Na^+ in the aqueous medium. Moreover, Na^+ is the best ion candidate to be added as it is a part of the salt present in the ($Mg(NO_3)_2$ + $NaHCO_3$) system and has an inherent tendency of adsorption on alumina surface due to the presence of surface OH groups. [72] The detailed modelling workflow for ALO_{hpl} and ALO_{hpb} can be found in **Figure SI3**.

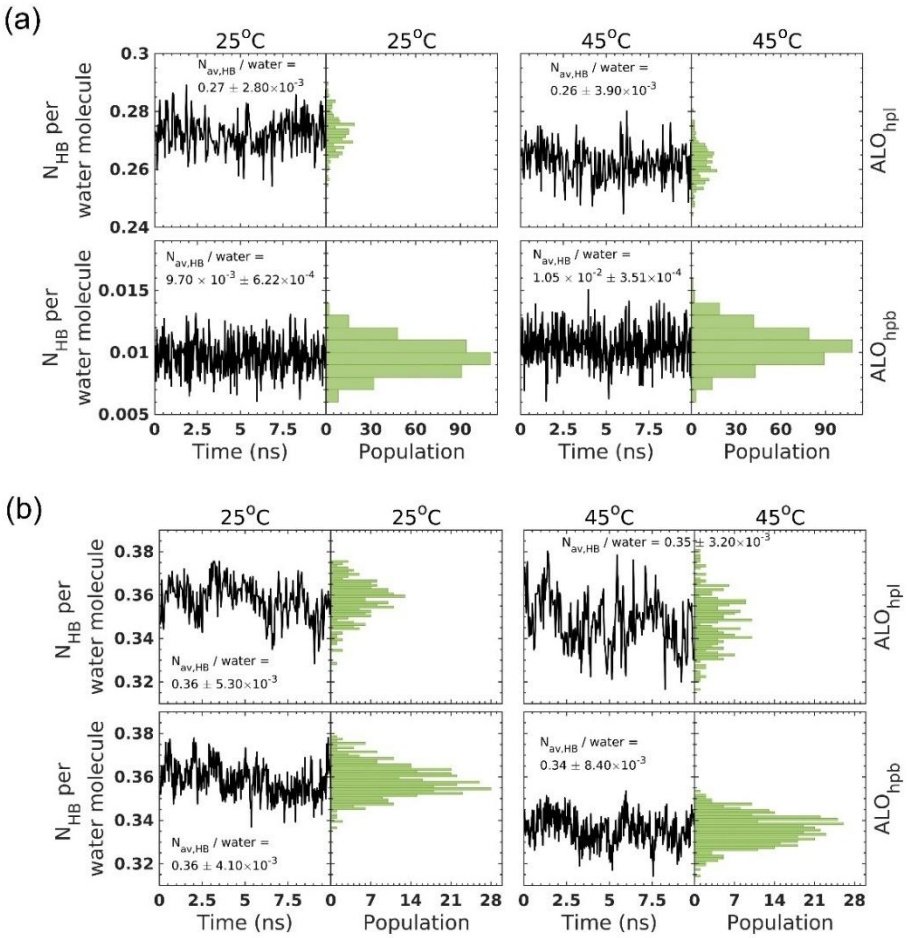

Figure 5 Time evolution of the number of hydrogen bonds (NHB) per water molecule (a) between water and the alumina membrane (ALOhpl and ALOhpb) in the interfacial region and (b) between the water molecules themselves in the bulk region at temperatures 25 °C and 45 °C. The data is averaged over the three concordant simulations in each case during the last 10 ns of the simulation trajectory as described in section 2.4.2. The right-hand panel corresponding to each subplot represents the histogram of the corresponding N_{HB}. Average number of hydrogen bonds in each case along with the standard deviation is mentioned adjacent to the timeline profiles.

2.4.2. *Construction of Simulation Cell, Force Field Parameters, and MD simulations*

In order to model the aqueous solution in presence of the alumina membrane, SPC/E water [73,74] was used to build a solvent layer of length 10 nm along the normal direction of the membrane surface (i.e. z axis) of ALO_{hpl} and ALO_{hpb}. Na^+, Mg^{2+}, NO_3^-, and

HCO_3^- ions were added as per the concentrations used in the experiments i.e. 0.4 M of $NaHCO_3$ and 0.8 M of $Mg(NO_3)_2$. As a result, the aqueous solution was composed of ~11000 water molecules, 84 Na^+, 168 Mg^{2+}, 336 NO_3^-, and 84 HCO_3^- ions in case of ALO_{hpl} whereas there were ~ 21000 water molecules, 184 Na^+, 369 Mg^{2+}, 184 HCO_3^-, and 738 NO_3^- ions in case of ALO_{hpb}. Snapshots of the systems constructed are provided in **Figure SI4**. Both the systems were energy minimized using Steepest descent algorithm for 50,000 steps followed by equilibration for 10 ns in NVT ensemble. Statistics were then accumulated from additional production runs of 40 ns in NPT ensemble. A timestep of 2 and 1 fs was used in all the simulations involving hydrophilic and hydrophobic alumina membrane respectively. Position restraint with force constant 1000 kJ mol^{-1} nm^{-2} was applied on the contents of the alumina membrane along the three spatial dimensions to keep the membrane position fixed in space yet allowing the constituents atoms to vibrate. [71] The simulations involving ALO_{hpl} and ALO_{hpb} were both carried out in triplicates with different random number seeds to avoid configurational bias and measure the standard deviations in different physical attributes. The force field (FF) parameters for Mg^{2+} and NO_3^- were obtained from OPLS-AA [75,76] and those for Na^+, HCO_3^-, and LAU were collected from CHARMM36. [77–79] It is important to note that mixing FF parameters from OPLS-AA and CHARMM36 in a simulation may not be advisable yet allowed to the extent of observing the correct dynamical evolution of a class of physical attributes that are aligned with the experimental results. [80] Our results from simulations as discussed later are found to be in good agreement with previous literature reports as well as provide right basis for the experimental observations in this case. All the simulations were carried out using

GROMACS 2024. [81] 3D Periodic boundary condition was applied in all the simulation cells. All bonds involving hydrogen were converted to rigid holonomic constraints using LINCS algorithm. Velocity Verlet algorithm was applied to solve Newton's equations of motion. A cut-off distance of 9 Å was used to calculate the electrostatic and van der Waals (vdW) interactions. [73] Particle Mesh Ewald (PME) method was applied to solve the long-range electrostatics. V-rescale thermostat was used for temperature coupling with time constant for coupling as 0.1 ps and a reference temperature of 298 K. [82] Exponential relaxation pressure coupling was implemented with a time constant of 2 ps, reference pressure of 1.0 bar, and a compressibility of 4.5×10^{-5} bar^{-1}. gmx tools, [81] VMD, [83] and MATLAB R2023b were used to analyze the results. VMD was used for visualization of the simulation trajectories and MATLAB R2023b was used for plotting.

3. Results and Discussions

3.1. *Wettability and Crystallinity of Anodic Alumina Membrane*

The purchased AAM is hydrophilic, displaying a strong affinity toward water. To modify the surface wettability of the AAM to that of hydrophobic, lauric acid in ethanol solution was used. Incorporating lauric acid into alumina pores reduces the surface energy, [84] modifies the surface tension, [85] and increases the contact angle. The contact angles measured were 23.6°, and 24.3° for the left side (α) and right side (α') of the droplet respectively for the hydrophilic membrane and 92.2°, and 95.5° for the left side (θ), and right side (θ') of the droplet respectively for the hydrophobic membrane as shown in **Figure 6**. Successful conversion of hydrophilic to hydrophobic membrane was confirmed by the mean contact angles of 23.9° and 93.9° for hydrophilic and

hydrophobic AAM respectively. To confirm this in terms of the *in-silico* modeling, hydrogen bonds between the alumina surface and water were calculated from MD simulations. **Figure 5(a)** shows the evolution of the number of hydrogen bonds per water molecule between the alumina surface and water with respect to time along with its distribution in presence of hydrophilic and hydrophobic alumina membranes at temperatures 25 °C and 45 °C. All the oxygens and hydrogens present on the alumina surface were taken into account in this regard. [86] A ~26-fold decrease in the number of hydrogen bonds is noticed in ALO_{hpb} emphasizing its hydrophobic character. Furthermore, the wider distribution in case of ALO_{hpl} signifies varying possibilities in the number of hydrogen bonds per water molecule.

X-ray diffractometer is used to determine the crystalline character of the membranes. The purchased and modified anodic alumina membranes are amorphous as evident from the absence of peaks in **Figure SI1(a)** and **SI1(b)** as well as from the lack of structural order in **Figure 4(b) and 4(c)**.

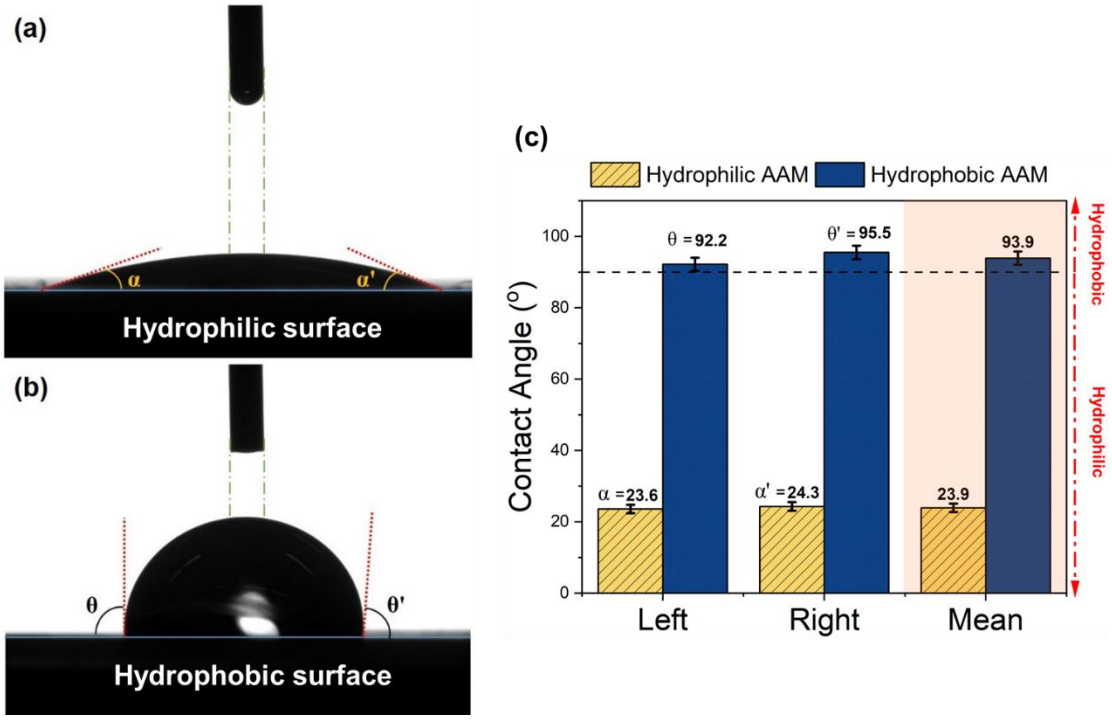

Figure 6 The water contact angle image of (a) hydrophilic and (b) hydrophobic anodic alumina membrane (AAM) as viewed using a contact angle measurer, (c) the left side, right side, and mean contact angle of the water droplet measured for the hydrophilic and hydrophobic membranes. The mean values of $\boldsymbol{\alpha}$, $\boldsymbol{\theta}$, $\boldsymbol{\alpha'}$, and $\boldsymbol{\theta'}$ are provided on top of the vertical bars.

3.2. *Crystallization of Magnesium Carbonate in Confined Nanochannels Under Different Physicochemical Conditions*

The mixtures of magnesium nitrate and sodium bicarbonate are loaded in 200 nm anodic alumina channels and the reaction was aged at room temperature for both hydrophilic and hydrophobic membranes. To understand the effect of temperature on the formation of different crystal phases, the hydrophilic and hydrophobic AAMs were loaded and immediately transferred into a vacuum oven to age at 45 °C for 15 minutes. This induction time is sufficient to influence the generation of different nuclei of varied phases and speciation in crystallization. After 15 minutes, the rest of the aging was

carried out at room temperature and pressure to prevent any liquid loss due to evaporation.

The formation of magnesium carbonate is determined through X-ray diffraction (XRD) after 6, 24, 48, 72, and 96 hours of loading magnesium nitrate and sodium bicarbonate solution into the AAMs. The XRD pattern for magnesium carbonate crystallized in hydrophilic nanochannels at 25 °C reveals the formation of anhydrous phase like $MgCO_3$, hydrated phases like $MgCO_3$. $2H_2O$, $MgCO_3$. $3H_2O$, $MgCO_3$. $5H_2O$, and hydrated hydroxyl-based phases such as $Mg_5(CO_3)_4(OH)_2$. $4H_2O$, $Mg_5(CO_3)_4(OH)_2$. $5H_2O$, $Mg_2(CO_3)(OH)_2$. $3H_2O$, $Mg_2(CO_3)(OH)_2$. $0.5H_2O$, and $Mg_7(CO_3)_5(OH)_4$. $24H_2O$ over 96 hours of loading as shown in **Figure 7(a)**. Similarly, the XRD pattern corresponding to magnesium carbonate crystallized in hydrophilic nanochannels at 45 °C revealed the formation of $MgCO_3$, $MgCO_3$. $2H_2O$, $MgCO_3$. $3H_2O$, $MgCO_3$. $5H_2O$, $Mg_5(CO_3)_4(OH)_2$. $4H_2O$, $Mg_5(CO_3)_4(OH)_2$. $5\text{-}6H_2O$ and $Mg_2(CO_3)(OH)_2$. $0.5H_2O$ over 96 hours of loading as shown in **Figure 7(c)**.

The XRD pattern for magnesium carbonate crystallized in hydrophobic nanochannels at 25 °C reveals the formation of $MgCO_3$. $2H_2O$, $MgCO_3$. $3H_2O$, $MgCO_3$. $5H_2O$, $Mg_5(CO_3)_4(OH)_2$. $4H_2O$, $Mg_5(CO_3)_4(OH)_2$. $5H_2O$, $Mg_5(CO_3)_4(OH)_2$. $5\text{-}6H_2O$ $Mg_2(CO_3)(OH)_2$. $3H_2O$, $Mg_2(CO_3)(OH)_2$. $0.5H_2O$, and $Mg_7(CO_3)_5(OH)_4$. $24H_2O$ over 96 hours of loading with no trace of anhydrous phase as shown in **Figure 7(b)**. The XRD data for magnesium carbonate crystallized in hydrophobic nanochannels at 45 °C revealed the formation of $MgCO_3$. $3H_2O$, $MgCO_3$. $5H_2O$, $Mg_5(CO_3)_4(OH)_2$. $4H_2O$, and $Mg_2(CO_3)(OH)_2$. $3H_2O$ over 96 hours of loading as shown in **Figure 7(d)**. The plane orientations of all the phases observed in hydrophilic and hydrophobic nanochannels

aged at 25 °C and 45 °C for over 96 hours are summarized in **Table 2**. Complete XRD diffraction pattern of all the magnesium carbonate phases is shown in **Figure SI2** for comparison.

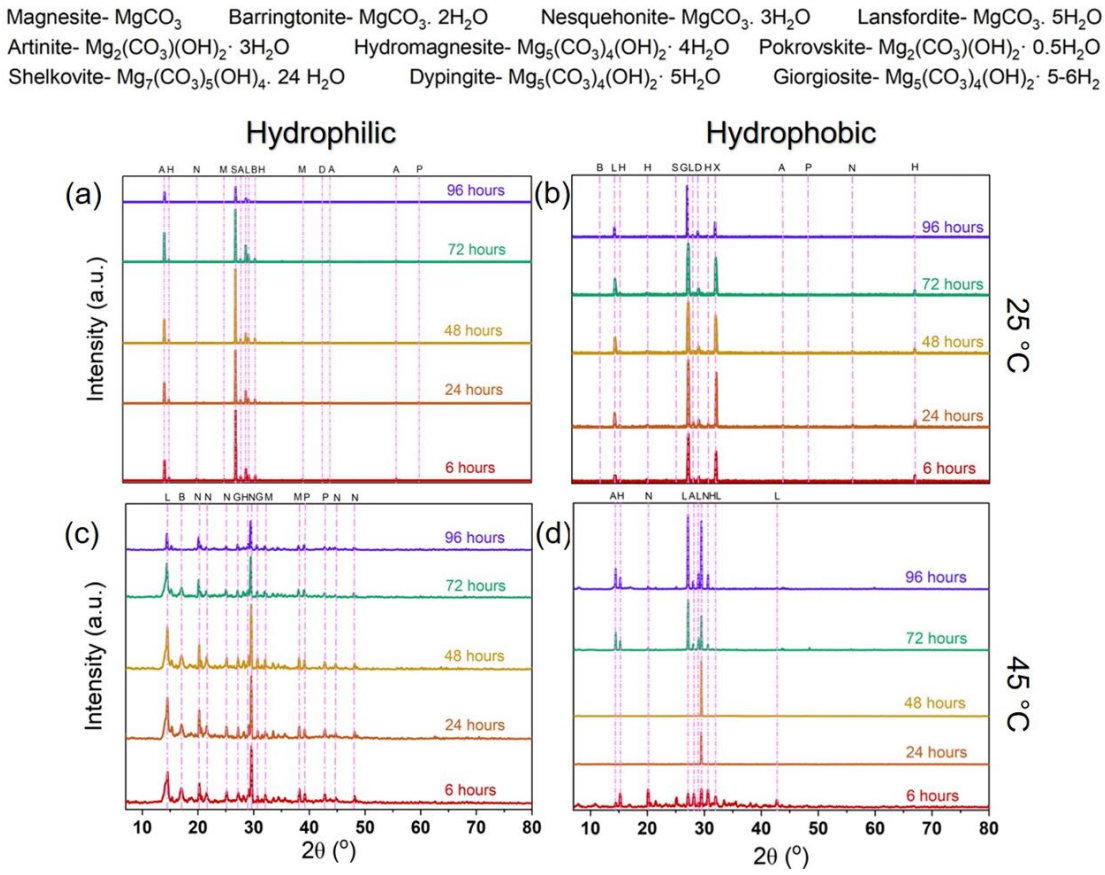

Figure 7 Identification of the crystal structure and phases of magnesium carbonate loaded in hydrophilic AAM at (a) 25 °C and (c) 45 °C, and in hydrophobic AAM at (b) 25 °C and (d) 45 °C using X-ray diffraction (XRD). The peaks are colored with respect to the time after loading.

Table 2 Plane orientation of all phases of magnesium carbonate observed in hydrophilic (ALOhpl) and hydrophobic (ALOhpb) nanochannels aged at 25 °C and 45 °C using X-ray diffraction (XRD). The chemical formulae for different phases can be obtained from Table 1.

Phase	**ALO_{hpl}, 25 ˚C**	**ALO_{hpl}, 45 ˚C**	**ALO_{hpb}, 25 ˚C**	**ALO_{hpb}, 45 ˚C**
Magnesite	(110)	(110)	-	-
Barringtonite	(001), ($1\bar{1}0$), (210)	($0\bar{1}1$), (210), (112), (220)	(100), (001)	-

Nesquehonite	(110), (211), (004), ($\bar{1}$05)	(002), ($\bar{2}$12)	($\bar{2}$02), (110), (021), (212)	(002), ($\bar{2}$02), (316)
Lansfordite	(100), (002), ($\bar{2}$11), ($\bar{1}$22), (214)	(002), (211), ($\bar{3}$04), (041)	(100), (002), (321), (423)	(211), (320), ($\bar{1}$22)
Artinite	(001), (401), (110), (202)	-	(001), (002), ($\bar{1}$11), (220)	(001), (401), ($\bar{2}$02)
Hydromagnesite	(321), (111), (620)	(300), (400)	(111), (020), (131), (006)	(111), (300), (112)
Dypingite	-	-	-	-
Pokrovskite	(200), (44$\bar{1}$), (320)	(21$\bar{1}$)	(020)	-
Shelkovite	(100), (14$\bar{1}$)	-	(040), (100)	-
Giorgiosite	-	-	-	-

Formation of anhydrous $MgCO_3$ is associated with high energy barrier that often requires dehydration of the metastable hydrated and hydrated hydroxyl-based phases. [87] In a 200 nm AAM, the core region of the nanopore is free from interactions due to the solid surface. However, minor concentration of $MgCO_3$ in case of hydrophilic AAM as opposed to absolute absence of $MgCO_3$ in hydrophobic AAM indicates the role of the solid surface in the generation of the anhydrous phase in the interface. It is well-known that water molecules form hydrogen bonded network of lower density and higher order in presence of hydrophobic surfaces that gives rise to clathrate-like structures of water near the solid surface. [88–92] Higher dehydration enthalpy of Mg^{2+} trapped in the water clathrates makes the formation of anhydrous $MgCO_3$ phases difficult, even at higher

temperatures like 45 °C. On the other hand, the corresponding energy barrier has overcome to a minute extent at 25 °C and to a higher extent at 45 °C in case of hydrophilic interfaces giving rise to ~ 1-13 weight % of $MgCO_3$ (**Table SI3**). This is evident from **Figure 8** where an increase in the number of intermolecular hydrogen bonds and spatial order is noticeable in the hydrophobic interface as opposed to the hydrophilic interface along with clathrate-like trapping of Mg^{2+} ions. The overall XRD pattern was quite different with respect to both temperature and surface wettability for the magnesium carbonate crystallized in bulk at 25 °C and 45 °C on hydrophilic and hydrophobic alumina surfaces as shown in **Figure SI5**. The phases of magnesium carbonate observed in bulk were $MgCO_3$. $3H_2O$, and $Mg_5(CO_3)_4(OH)_2$. $4H_2O$ in all physicochemical conditions as shown in **Figure SI6**. The plane orientation and timeline variation in weight percentage of both the phases are shown in **Table SI1** and **Table SI2** respectively.

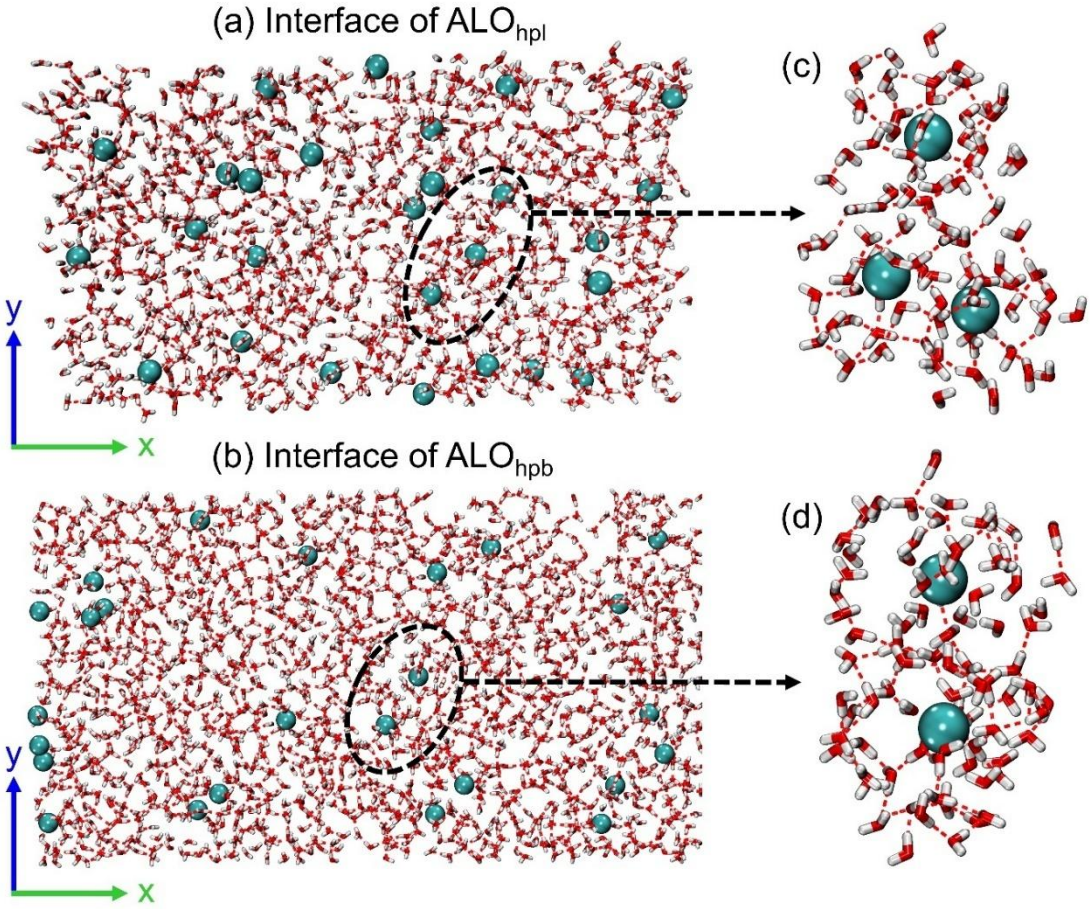

Figure 8 Hydrogen bonded interfacial water network in (a) hydrophilic (ALOhpl) and (b) hydrophobic (ALOhpb) AAM in the xy plane as obtained from the MD simulation studies. Hydrogen bonds are calculated using a distance cutoff of 3.5 Å and a D-H-A angle cutoff of 30°. (c) Amorphous structure of interfacial water around Mg^{2+} in case of ALO_{hpl} and (d) clathrate-like structure of interfacial water in case of ALO_{hpb}. Cyan vdW spheres represent Mg^{2+} ions whereas water molecules are shown in licorice with O and H in red and white respectively. Hydrogen bonds are shown as red dashed lines.

3.3. *Dynamic Trends in Magnesium Carbonate Phase Evolution in Response to Changing Physicochemical Conditions*

Understanding the overall trend of magnesium carbonate phases transforming over time is crucial in determining the most stable phase in certain physicochemical conditions aiding in construction, [93] plastics and coating, [94,95] and energy storage industries. [96,97] Based on the weight % of major phases obtained from XRD measurements as shown in

Figure 9(a), we can observe that in hydrophilic conditions at 25 °C initially $MgCO_3$. $3H_2O$, $MgCO_3$. $5H_2O$, $Mg_2(CO_3)(OH)_2$. $3H_2O$ and $Mg_5(CO_3)_4(OH)_2$. $4H_2O$ phases are observed after 6 hours of loading. As the reaction time proceeds from 6 to 96 hours of loading, $Mg_2(CO_3)(OH)_2$. $3H_2O$ phase increases till 72 hours and then disappears at 96 hours, $Mg_5(CO_3)_4(OH)_2$. $4H_2O$ phase is stable till 48 hours followed by a sudden variation that occurred till 96 hours, $MgCO_3$. $3H_2O$ phase is fairly stable till 72 hours and increases at 96 hours, whereas $MgCO_3$. $5H_2O$ phase shows inconsistent evolution with disappearance at 48 hours, reappearance at 72 hours, and an increase at 96 hours. Some of the minor phase formations as shown in **Figure 9(a')** are $Mg_2(CO_3)(OH)_2$. $0.5H_2O$ that appeared at 24 hours and gradually increased till 48 hours, disappeared at 72 hours, and reappeared at 96 hours. On the other hand, $MgCO_3$ appeared at 48 hours and 96 hours, $MgCO_3$. $2H_2O$ appeared at 48 hours with a brief increase at 72 hours and decline at 96 hours, $Mg_5(CO_3)_4(OH)_2$. $5H_2O$ appeared momentarily at 72 hours and $Mg_7(CO_3)_5(OH)_4$. $24H_2O$ appeared at 72 hours and gradually increased till 96 hours. In summary, based on the phase evolution trends, $MgCO_3$. $5H_2O$ and $Mg_5(CO_3)_4(OH)_2$. $4H_2O$ are the most predominant phases by the end of 96 hours after loading.

In hydrophilic conditions at 45 °C, $MgCO_3$. $5H_2O$, $Mg_2(CO_3)(OH)_2$. $0.5H_2O$, $MgCO_3$, and $MgCO_3$. $2H_2O$, phases are observed after 6 hours of loading as shown in **Figure 9(c)**. As the reaction proceeds till 96 hours, $MgCO_3$. $5H_2O$ disappeared and reappeared at 96 hours, $Mg_2(CO_3)(OH)_2$. $0.5H_2O$, and $MgCO_3$ gradually increased till 24 hours, disappeared, and reappeared at 72 hours as shown in **Figure 9(c')**. Interestingly, $MgCO_3$. $2H_2O$ was never observed over time. Some other phases which formed after 24 hours of reaction time are $Mg_5(CO_3)_4(OH)_2$. $4H_2O$ which steadily decreased till 96

hours, $MgCO_3$. $3H_2O$ momentarily decreased at 48 hours, being stable till 72 hours, and increased till 96 hours, and $Mg_5(CO_3)_4(OH)_2$. 5-$6H_2O$ forming at 48 hours and steadily decreased till 96 hours of loading. Overall, $MgCO_3$. $3H_2O$ and $MgCO_3$. $5H_2O$ are the most predominant phases by the end of 96 hours after loading based on phase trend.

In hydrophobic conditions at 25 °C, $Mg_5(CO_3)_4(OH)_2$. $4H_2O$, $MgCO_3$. $5H_2O$, $MgCO_3$. $2H_2O$, $Mg_7(CO_3)_5(OH)_4$. $24H_2O$, $Mg_5(CO_3)_4(OH)_2$. $5H_2O$, $Mg_5(CO_3)_4(OH)_2$. 5-$6H_2O$ phases are observed after 6 hours of loading as shown in **Figure 9(b)**. Based on the phase evolution trend, $Mg_5(CO_3)_4(OH)_2$. $4H_2O$ phase momentarily increased and gradually decreased till 72 hours and disappeared at 96 hours, $MgCO_3$. $5H_2O$ suddenly decreased at 24 hours and gradually increased over time, $MgCO_3$. $2H_2O$ disappeared and reappeared transiently at 48 hours and again disappeared as shown in **Figure 9(b')**. $Mg_7(CO_3)_5(OH)_4$. $24H_2O$ disappeared and reappeared at 48 hours gradually decreasing till 96 hours, $Mg_5(CO_3)_4(OH)_2$. 5-$6H_2O$ ranging between specific weight % limits till 96 hours, and $Mg_5(CO_3)_4(OH)_2$. $5H_2O$ was never observed over time. Other phases that evolved after 24 hours are $MgCO_3$. $3H_2O$ which gradually decreased over time, $Mg_2(CO_3)(OH)_2$. $0.5H_2O$ appeared only after 24 hours and was never observed again, and $Mg_2(CO_3)(OH)_2$. $3H_2O$ formed after 48 hours and gradually increased till 96 hours. The phase trends show $Mg_2(CO_3)(OH)_2$. $3H_2O$ and $Mg_5(CO_3)_4(OH)_2$. 5-$6H_2O$ are the most prevalent phases by the end of 96 hours after loading.

In hydrophobic conditions at 45 °C, $Mg_2(CO_3)(OH)_2$. $3H_2O$, $Mg_5(CO_3)_4(OH)_2$. $4H_2O$, $MgCO_3$. $3H_2O$, and $MgCO_3$. $5H_2O$ were observed after 6 hours of loading as shown in **Figure 9(d)**. Based on the phase evolving trends, $Mg_2(CO_3)(OH)_2$. $3H_2O$ disappeared, reappeared after 72 hours, and surged till 96 hours, $Mg_5(CO_3)_4(OH)_2$. $4H_2O$

disappeared, reappeared after 72 hours, and decreased at 96 hours, $MgCO_3$. $3H_2O$ instantly increased and stabilized till 48 hours and substantially dropped at 72 hours as shown in **Figure 9(d')**, $MgCO_3$. $5H_2O$ disappeared, reappeared after 72 hours, and surged till 96 hours after loading. In summary, based on the phase evolution trends, $MgCO_3$. $5H_2O$ and $Mg_5(CO_3)_4(OH)_2$. $4H_2O$ are the most predominant phases by the end of 96 hours after loading. Although this section gives an overview of the phase trends of magnesium carbonate in different physicochemical conditions, **Section 3.4** and **Section 3.5** explain the phase evolution of anhydrous, hydrated and hydrated hydroxyl-based phases in detail and **Section 3.7** explains the phase evolution mechanism undergoing in nanoconfinement providing further evidence into the trends observed.

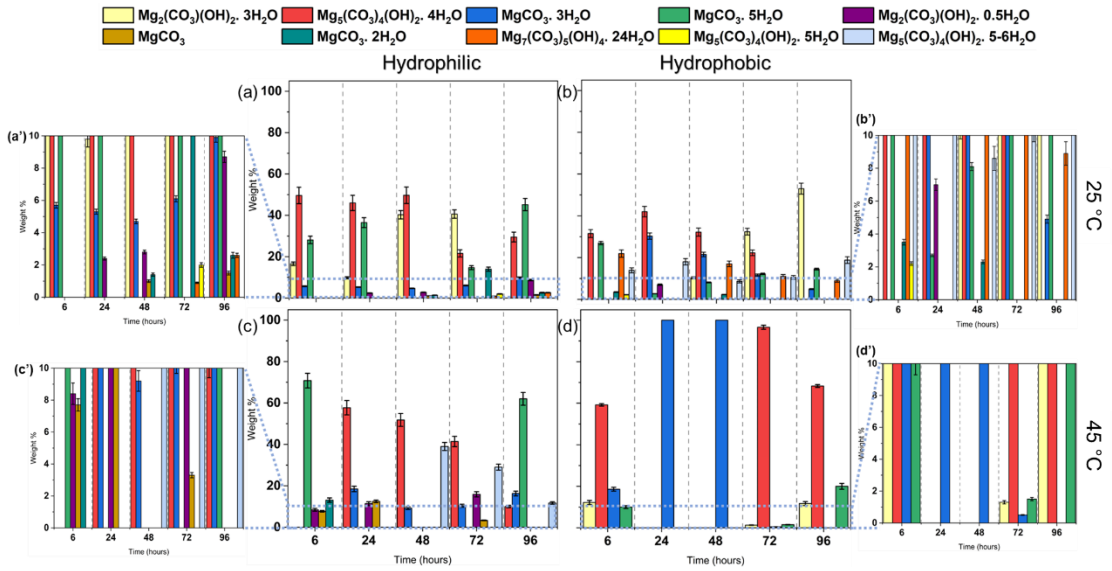

Figure 9 Identification of the phases of magnesium carbonate loaded in hydrophilic AAM at (a) 25 °C and (c) 45 °C, and in hydrophobic AAM at (b) 25 °C and (d) 45 °C using X-ray diffraction (XRD). Figures (a'), (b'), (c'), (d') correspond to weight % of magnesium carbonate phases from 0 to 10% showing the minor phase evolution in the respective experimental conditions. The bars are colored based on the chemical formula of the corresponding phase as given in the legend.

3.4. *Phase Polymorphism of Anhydrous and Hydrated Magnesium Carbonate in Various Physicochemical Conditions*

3.4.1. *Effect of Surface Wettability*

The different phases of magnesium carbonate crystallized in anodic alumina nanochannels were anhydrous phases like magnesite ($MgCO_3$), and hydrated phases like barringtonite ($MgCO_3$. $2H_2O$), nesquehonite ($MgCO_3$. $3H_2O$) and lansfordite ($MgCO_3$. $5H_2O$). In bulk solutions, crystallization of $MgCO_3$. $3H_2O$ was observed on hydrophilic and hydrophobic surface aged at 25 °C for over 96 hours as shown in **Figure SI6**. In comparison, the phase composition of magnesium carbonate aged at 25 °C in hydrophilic nanochannels after 6 hours of loading is $MgCO_3$. $3H_2O$ and $MgCO_3$. $5H_2O$ as shown in **Figure 10(a)**. At 24 hours of loading, the extent of $MgCO_3$. $5H_2O$ increases from 28.1% to 36.5% while $MgCO_3$. $3H_2O$ slightly decreased from 5.7% to 5.3%. At 48 hours of loading, the major change observed is in the disappearance of $MgCO_3$. $5H_2O$ and the formation of stable $MgCO_3$ and $MgCO_3$. $2H_2O$ with a decrease in the composition of $MgCO_3$. $3H_2O$ from 5.3% to 4.7%. At 72 hours, the stable $MgCO_3$ disappeared and $MgCO_3$. $5H_2O$ reappears while the weight composition of $MgCO_3$. $2H_2O$ and $MgCO_3$. $3H_2O$, increase from 1.4% to 14%, and 4.7% to 6.1% respectively. At 96 hours, the non-hydrated and hydrated phases appear with a weight composition of 1.5% for $MgCO_3$, 2.6% for $MgCO_3$. $2H_2O$, 9.9% for $MgCO_3$. $3H_2O$, and 45.2% for $MgCO_3$. $5H_2O$.

In hydrophobic nanochannels, magnesium carbonate was loaded and aged at 25 °C. Based on the XRD pattern, the phase behavior of non-hydrated and hydrated magnesium carbonate was quite opposite to what was observed in hydrophilic nanochannels as shown in **Figure 10(b)**. During the initial 6 hours after loading, the phases of $MgCO_3$.

$2H_2O$ and $MgCO_3$. $5H_2O$ were observed. At 24 hours, there was a decrease in weight percentage of $MgCO_3$. $5H_2O$ from 27% to 2.7% while the appearance of $MgCO_3$. $3H_2O$ and disappearance of $MgCO_3$. $2H_2O$ is seen. At 48 hours, there was a decrease in weight percentage of $MgCO_3$. $3H_2O$ (30.3% to 21.5%) and an increase of $MgCO_3$. $5H_2O$ (2.7% to 8.1%) was seen along with the reappearance of $MgCO_3$. $2H_2O$. At 72 hours, $MgCO_3$. $2H_2O$ again disappeared with a decrease in $MgCO_3$. $3H_2O$ and an increase in $MgCO_3$. $5H_2O$ which is consistent till 96 hours from 21.5% to 4.9% and 8.1% to 14.5% respectively. Such transient behavior of different magnesium carbonate phases, which are considered to be highly stable in bulk solutions, is supposedly due to the confinement effects reducing the metastability barrier and increasing the phase transition kinetics. [98,99]

3.4.2. *Effect of Surface Wettability Coupled with Temperature Variation*

The effect of temperature on phase formation of magnesium carbonate in bulk solution is negligible as $MgCO_3$. $3H_2O$ was observed in both hydrophilic and hydrophobic environments aged at 45 °C as shown in **Figure SI5**. Whereas, a similar behavior of anhydrous and hydrated phases of magnesium carbonate aged at 45 °C vs 25 °C in hydrophilic nanochannels was observed as shown in **Figure 10(c)**. Due to the influence of heat during the aging, stable $MgCO_3$ crystallizes within the first 6 hours of loading along with $MgCO_3$. $2H_2O$ and $MgCO_3$. $5H_2O$. At 24 hours of loading, the disappearance of $MgCO_3$. $2H_2O$ and $MgCO_3$. $5H_2O$ was observed and an appearance of $MgCO_3$. $3H_2O$ is seen along with an increase in anhydrous $MgCO_3$ from 7.7% to 12.5%. At 48 hours, all the phases disappeared except $MgCO_3$. $3H_2O$ with a decrease in weight percentage from 18.5% to 9.2%. At 72 hours, a reappearance of anhydrous $MgCO_3$ was seen along

with a slight increase in $MgCO_3$. $3H_2O$ from 9.2% to 10.4%. At 96 hours, the reappearance of $MgCO_3$. $5H_2O$ was observed with a weight percentage of 62% and an increase in $MgCO_3$. $3H_2O$ to 16.3%.

The influence of temperature on magnesium carbonate crystallization in hydrophobic nanochannels has resulted in further inconsistent phase evolution as shown in **Figure 10(d)** where $MgCO_3$. $3H_2O$ weight percentage increased from 18.6% at 6 hours to 100% at 24 and 48 hours. Meanwhile, $MgCO_3$. $5H_2O$ was observed within the initial 6 hours with a weight percentage of 10% while it is unseen for 24 and 48 hours after loading. At 72 hours, a complete dissociation of $MgCO_3$. $3H_2O$ is observed with a weight composition decreased from 100% to 0.5% and a reappearance of $MgCO_3$. $5H_2O$. At 96 hours, $MgCO_3$. $3H_2O$ was unseen but an increase in $MgCO_3$. $5H_2O$ was observed from 1.5% to 20%.

Based on the XRD patterns, it is noteworthy that in hydrophilic nanochannels, $MgCO_3$, $MgCO_3$. $2H_2O$ and $MgCO_3$. $5H_2O$ displayed volatile behavior irrespective of temperature. The only major difference observed was that by 96 hours the overall weight composition of hydrated and non-hydrated phases aged at 25 °C and 45 °C increased from 59.2% to 78.3%. Furthermore, we can interpret the behavior of non-hydrated and hydrated phases of magnesium carbonate as being fairly unstable in the hydrophobic environment irrespective of the aging temperature in comparison with hydrophilic environment. By 96 hours, the overall weight percentage of hydrated and non-hydrated phases crystallized at 25 °C and 45 °C is 19.4% and 20% respectively indicating a negligible effect of temperature in hydrophobic environment. With such behavior in phase transition, non-hydrated and hydrated phases were predominant and stable in

hydrophilic nanochannels in contrast with the hydrophobic nanochannels as recognized by weight % as shown in **Table SI3** and supported by the presence of higher number of surface–water hydrogen bonds in the hydrophilic environments as shown in **Figure 5(a)** exhibiting the proportionality to phase stability of hydrated phases of magnesium carbonate. [100,101]

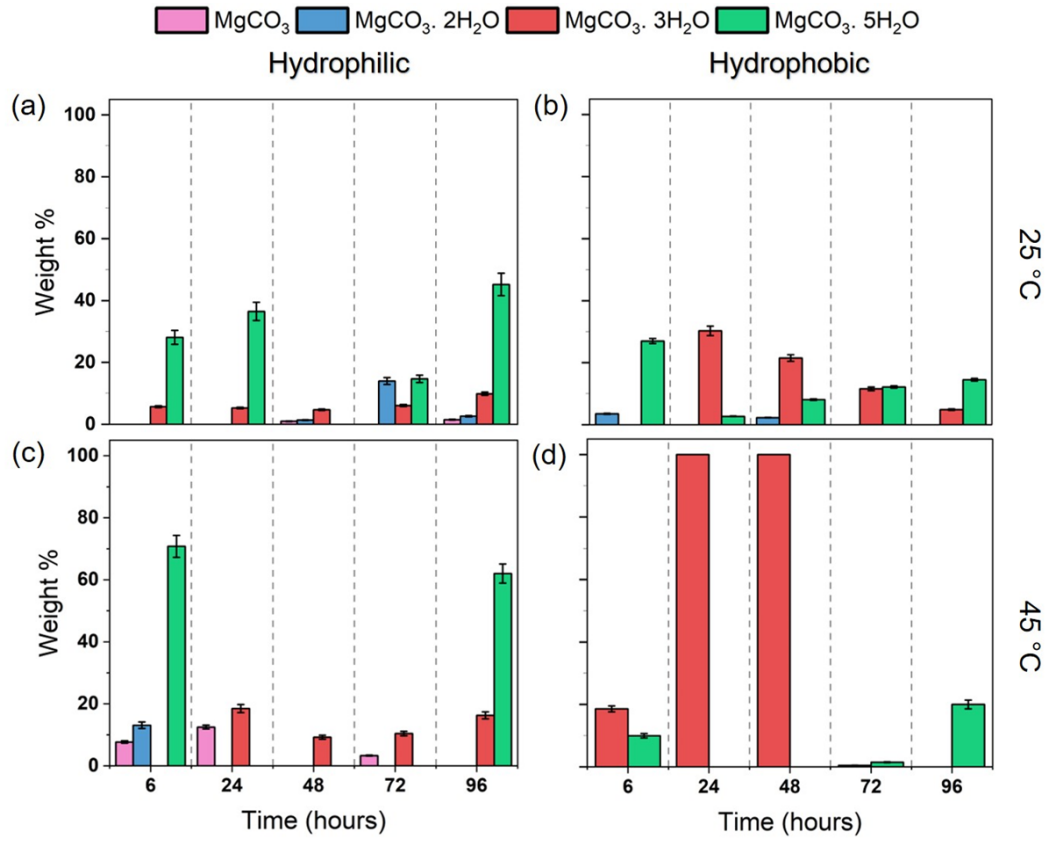

Figure 10 Identification of the weight composition of non-hydroxide-based phases of magnesium carbonate grown in hydrophilic AAM at (a) 25 °C and (c) 45 °C, and in hydrophobic AAM at (b) 25 °C and (d) 45 °C using X-ray diffraction (XRD). The bars are colored based on the chemical formula of the corresponding phase as given in the legend.

3.5. *Phase Polymorphism of Hydrated Hydroxyl-based Magnesium Carbonate in Various Physicochemical Conditions*

3.5.1. *Effect of Surface Wettability*

The hydrated hydroxyl-based phases of magnesium carbonate crystallized in anodic alumina nanochannels were artinite ($Mg_2(CO_3)(OH)_2.3H_2O$), hydromagnesite ($Mg_5(CO_3)_4(OH)_2.4H_2O$), dypingite ($Mg_5(CO_3)_4(OH)_2.5H_2O$), and unusual phases like pokrovskite ($Mg_2(CO_3)(OH)_2.\ 0.5H_2O$), shelkovite ($Mg_7(CO_3)_5(OH)_4.\ 24H_2O$) and giorgiosite ($Mg_5(CO_3)_4(OH)_2.\ 5\text{-}6H_2O$). In bulk solutions, crystallization of $Mg_5(CO_3)_4(OH)_2.\ 4H_2O$ was observed on hydrophilic and hydrophobic surfaces aged at 25 °C for over 96 hours as shown in **Figure SI6**. In contrast, based on the weight composition of magnesium carbonate loaded in hydrophilic nanochannels at 25 °C the hydrated hydroxyl-based phases observed after 6 hours in **Figure 11(a)** are $Mg_2(CO_3)(OH)_2.\ 3H_2O$ and $Mg_5(CO_3)_4(OH)_2.\ 4H_2O$. At 24 hours, the weight percentage of $Mg_2(CO_3)(OH)_2.\ 3H_2O$ decreases from 16.6% to 9.8% whereas the $Mg_2(CO_3)(OH)_2.\ 0.5H_2O$ phase appears. The phase of $Mg_5(CO_3)_4(OH)_2.\ 4H_2O$ was fairly stable till 48 hours with a minute change in weight percentage from 49.6% to 49.7% and $Mg_2(CO_3)(OH)_2.\ 0.5H_2O$ had a variation of 0.4% between 24 and 48 hours while the weight percentage of $Mg_2(CO_3)(OH)_2.\ 3H_2O$ increased from 9.8% to 40.3%. At 72 hours, there was a disappearance of $Mg_2(CO_3)(OH)_2.\ 0.5H_2O$ and the appearance of $Mg_7(CO_3)_5(OH)_4.\ 24H_2O$ and $Mg_5(CO_3)_4(OH)_2.\ 5H_2O$ was observed. Concurrently, $Mg_5(CO_3)_4(OH)_2.\ 4H_2O$ decreased in weight composition from 49.7% to 21.6% while $Mg_2(CO_3)(OH)_2.\ 3H_2O$ was stable with a net increase of 0.3%. At 96 hours, there was a disappearance of the phase $Mg_2(CO_3)(OH)_2.\ 3H_2O$ and the reappearance of $Mg_2(CO_3)(OH)_2.\ 0.5H_2O$ while a slight increase in weight composition was observed

for $Mg_5(CO_3)_4(OH)_2$. $4H_2O$ and $Mg_7(CO_3)_5(OH)_4$. $24H_2O$ from 21.6% to 29.5% and 0.9% to 2.6% respectively.

In hydrophobic nanochannels, magnesium carbonate was loaded and aged at 25 °C, and based on the XRD pattern, after 6 hours of loading the hydrated hydroxyl-based phases observed are $Mg_5(CO_3)_4(OH)_2$. $4H_2O$, $Mg_5(CO_3)_4(OH)_2$. $5H_2O$, $Mg_7(CO_3)_5(OH)_4$. $24H_2O$ and $Mg_5(CO_3)_4(OH)_2$. $5\text{-}6H_2O$. At 24 hours, there was a disappearance of phases like $Mg_5(CO_3)_4(OH)_2$. $5H_2O$ and $Mg_7(CO_3)_5(OH)_4$. $24H_2O$ and an appearance of $Mg_2(CO_3)(OH)_2$. $0.5H_2O$. Meanwhile, there was an increase in weight % of $Mg_5(CO_3)_4(OH)_2$. $4H_2O$ and $Mg_5(CO_3)_4(OH)_2$. $5\text{-}6H_2O$ from 31.5% to 42% and 13.9% to 18% respectively. At 48 hours, there was an absence of $Mg_2(CO_3)(OH)_2$. $0.5H_2O$ phase and a reappearance of $Mg_2(CO_3)(OH)_2$. $3H_2O$ and $Mg_7(CO_3)_5(OH)_4$. $24H_2O$ while a decrease in $Mg_5(CO_3)_4(OH)_2$. $4H_2O$ and $Mg_5(CO_3)_4(OH)_2$. $5\text{-}6H_2O$ was observed from 42% to 32.2% and 18% to 8.6% respectively. At 72 hours, there was a simultaneous increase in weight % of $Mg_2(CO_3)(OH)_2$. $3H_2O$ and $Mg_5(CO_3)_4(OH)_2$. $5\text{-}6H_2O$ from 10.3% to 32.4% and 8.6% to 10.5% respectively and a decrease in $Mg_5(CO_3)_4(OH)_2$. $4H_2O$ and $Mg_7(CO_3)_5(OH)_4$. $24H_2O$ from 32.2% to 22.3% and 17% to 11% respectively. At 96 hours, there was an increase in weight % of $Mg_2(CO_3)(OH)_2$. $3H_2O$ and $Mg_5(CO_3)_4(OH)_2$. $5\text{-}6H_2O$ from 32.4% to 53% and 10.5% to 18.8% respectively and a decrease in $Mg_7(CO_3)_5(OH)_4$. $24H_2O$ from 11% to 8.9% while a complete dissolution of $Mg_5(CO_3)_4(OH)_2$. $4H_2O$ was observed as shown in **Figure 11(b)**. This evolution of hydrated hydroxyl-based phases in hydrophilic and hydrophobic confinements is highly influenced by the arrangement of water molecules within nanoconfined space. [102]

3.5.2. *Effect of Surface Wettability Coupled with Temperature Variation*

In bulk solutions, crystallization of $Mg_5(CO_3)_4(OH)_2.\ 4H_2O$ is observed on hydrophilic and hydrophobic surfaces aged at 45 °C for over 96 hours as shown in **Figure SI6**. While, the phases of magnesium carbonate crystallized in hydrophilic nanochannels aged at 45 °C after 6 hours of loading is $Mg_2(CO_3)(OH)_2.\ 0.5H_2O$. At 24 hours, we observe the appearance of $Mg_5(CO_3)_4(OH)_2.\ 4H_2O$ and a slight increase in weight % of $Mg_2(CO_3)(OH)_2.\ 0.5H_2O$ from 8.4% to 11.4%. From 48 hours to 96 hours, we can notice a gradual decrease in weight % of $Mg_5(CO_3)_4(OH)_2.\ 4H_2O$ and $Mg_5(CO_3)_4(OH)_2.\ 5\text{-}6H_2O$ from 51.8% to 10% and 39% to 11.7% respectively. In between after 72 hours of loading the reappearance of $Mg_2(CO_3)(OH)_2.\ 0.5H_2O$ phase is observed as shown in **Figure 11(c)**.

The effect of temperature on hydrated hydroxyl-based phases crystallized in hydrophobic nanochannels is unusual as the behavior of phases is inconsistent as shown in **Figure 11(d)**. This volatile behavior can be attributed to critical temperature shifts necessary for phase transition, the formation of layer structure or due to local density fluctuations or fragmentations. [103,104] At 6 hours, the phases observed were $Mg_2(CO_3)(OH)_2.\ 3H_2O$ and $Mg_5(CO_3)_4(OH)_2.\ 4H_2O$. After 24 and 48 hours of loading, these phases dissipated and reappeared at 72 hours where $Mg_5(CO_3)_4(OH)_2.\ 4H_2O$ accounts for the majority of the total weight % of 96.6%. At 96 hours, $Mg_5(CO_3)_4(OH)_2.\ 4H_2O$ weight composition decreased to 68.3% whereas $Mg_2(CO_3)(OH)_2.\ 3H_2O$ increases to 11.7%.

Based on the phase behavior in hydrophilic nanochannels, we can infer the phase stability of $Mg_5(CO_3)_4(OH)_2.\ 4H_2O$ as fairly changeable irrespective of the influence of

temperature. Furthermore, due to the effect of temperature, the overall weight % of hydrated hydroxyl-based magnesium carbonate phases decreased from 40.8% at 25 °C to 21.7% at 45 °C. Whereas, the phase behavior in hydrophobic nanochannels is far more volatile in comparison with hydrophilic nanochannels. Overall, we can extrapolate based on the weight % as shown in **Table SI3**, that the hydrated hydroxyl-based magnesium carbonate phases are independent of temperature when nucleated in hydrophobic nanochannels contrary to hydrophilic nanochannels.

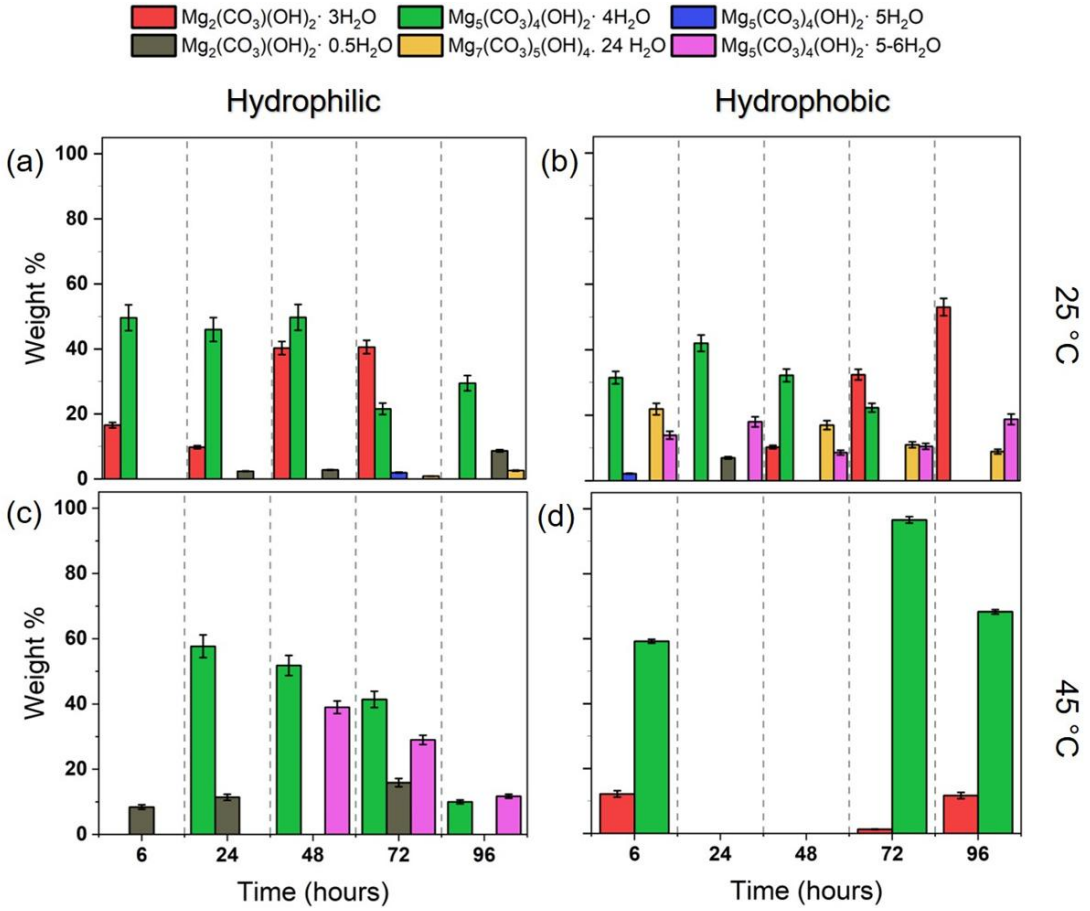

Figure 11 Identification of the weight composition of hydroxide-based phases of magnesium carbonate grown in hydrophilic AAM at (a) 25 °C and (c) 45 °C, and in hydrophobic AAM at (b) 25 °C and (d) 45 °C using X-ray diffraction (XRD). The bars are colored based on the chemical formula of the corresponding phase as given in the legend.

3.6. *Coordination Environment of Magnesium Elucidated from Classical Molecular Dynamics Simulations*

Pre-nucleated coordination of the Mg^{2+} ions direct the precipitated phase of the magnesium carbonates; therefore, **Figure 12** shows the radial distribution function (g(r)) of oxygen atoms from water, HCO_3^-, NO_3^- ions with respect to Mg^{2+} in the interfacial and bulk fluids at two temperatures, 25 °C and 45 °C. It is important to note that water exhibits differential behavior in contact with the solid surfaces, especially due to the electrostatic and vdW interactions from the metal oxide framework including partitioning of the water density in the interface and bulk region. Femtosecond acoustic pulse experiments by Sun et al. found that the local density of water can be up to five times higher than that of bulk water within 1 nm from the solid surface. [105] In the present study, to differentiate the interfacial water from the bulk phase, the mass density of water is plotted along the normal direction (i.e. z axis) of the alumina surface (**Figure SI7**). Bulk density of water (0.9950 g cm^{-3} at 25°C and 0.9902 g cm^{-3} at 45°C) [106,107] was reached approximately at a distance of 0.70-0.88 nm from the solid surface and therefore, a uniform width of 0.88 nm was used in all the systems as the interfacial water layer for probing the characteristics of Mg^{2+} in this region, while the rest of the simulation cell was considered as bulk. [52,108]

As observed from **Figure 12**, the spatial arrangement of water molecules in the first and second coordination shells of Mg^{2+} does not change appreciably with a change in surface wettability and temperature indicative of a strong and compact hydration shell of Mg^{2+}. [87] However, the arrangement of bicarbonate and nitrate ions exhibit significant changes with surface wettability, especially in the interfacial region. g(r) intensity reaches zero in all the cases after the first maximum followed by a second maximum

indicating a well-defined first coordination shell around Mg^{2+}. A distinct difference in the g(r) intensity is noticed in case of oxygens from the alumina membrane when the surface becomes hydrophobic. This clearly demonstrates a hindrance in the close proximity of Mg^{2+} with the alumina membrane when it is coated by a layer of hydrophobic fatty acids and water forms a clathrate-like network around Mg^{2+} ions (**Figure 8(d)**).

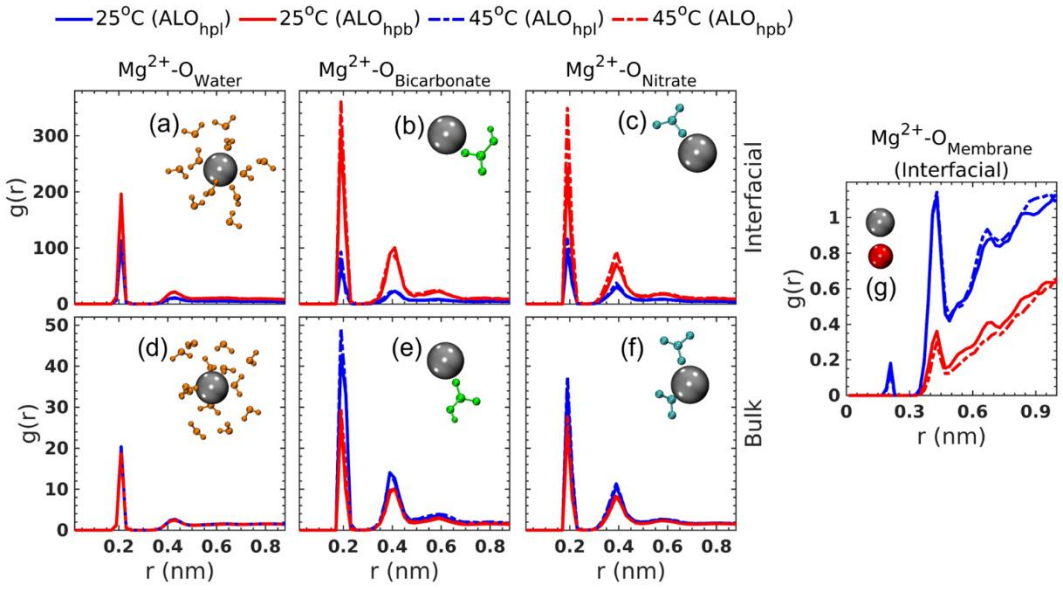

Figure 12 Representative Radial distribution function (g(r)) of oxygens from water, bicarbonate, and nitrate with respect to Mg2+ ions as a function of radial distance 'r' in the interfacial and bulk region at temperatures 25 °C and 45 °C. g(r) pertaining to the oxygens from alumina membrane ($O_{Membrane}$) is also provided. Calculations are done over the last 10 ns of the simulation trajectories. (a) to (g) correspond to the respective snapshots of the coordination environment of Mg^{2+} limited to its second coordination sphere. Grey and red vdW spheres represent Mg^{2+} and Oxygen respectively. Water, bicarbonate, and nitrate in the coordination shell are represented as orange, green, and cyan CPK respectively.

Figure 12 shows the coordination number (n(r)) of oxygens from water, HCO_3^-, NO_3^-, and the alumina surface with respect to Mg^{2+} ions obtained by integrating the corresponding g(r) profiles. As expected, the evolution of n(r) with radial distance hardly changes for water under different physiological conditions, whereas the coordination numbers diverge beyond the 2nd coordination shell for HCO_3^- ions and the

membrane oxygens. A list of the coordination numbers corresponding to the first and (first + second) coordination shells is provided in **Table 3**. It is widely known that in bulk aqueous medium, Mg^{2+} is typically surrounded by six water molecules ($[Mg(H_2O)_6]2^+$) in an octahedral arrangement. [109,110] However, in solvated bicarbonate and carbonate complexes, Tommaso et al. reported Mg^{2+} to be mainly five coordinated using *ab-initio* and Car-Parrinello MD studies. The most stable monomers of magnesium bicarbonate and magnesium carbonate were found to be $Mg[\eta^1\text{-}HCO_3](H_2O)_4^+$ and $Mg[\eta^1\text{-}CO_3](H_2O)_4$ respectively in bulk aqueous solution. [50] As evident from **Table 3**, the first coordination shell of Mg^{2+} is observed to contain ~ 4-5 oxygens from water and ~ 1 oxygen from the alumina surface, nitrate and bicarbonate ions at both the temperatures in hydrophilic and hydrophobic membranes. The results indicate that approximately one water molecule in the strong $[Mg(H_2O)_6]^{2+}$ complex can be substituted by the surrounding ions and/or membrane oxygens irrespective of the sampled temperatures and surface wettability. Nevertheless, major changes are evident in the second coordination shell of Mg^{2+}. Maximum coordination from the non-water species is noticed at 45 °C in presence of hydrophilic alumina interface indicating the experimental condition to favor precipitation of anhydrous and water-deficient phases of magnesium carbonates as discussed in **sections 3.3.** and **3.4.** An overall predominance of water coordination over non-water coordination toward pre-nucleated Mg^{2+} explains the frequent presence of hydrated phases in the experiments. An idea of the non-bonding interaction energies between the alumina membrane and water/ions can be obtained from **Table SI4**. At this point, it is important to note that not only the interfacial water, but the bulk water structure and dynamics are also impacted by the

presence of ions like Mg^{2+} and Na^{+}. Especially, Mg^{2+} ion, known as a 'water structure breaker' due to its high charge density, disrupts the bulk intermolecular hydrogen bonding network of water molecules as evident from **Figure 5(b)**. [111,112] Water that is usually observed to form ~ 3.6 hydrogen bonds per molecule in bulk, [112] is seen to form 0.34-0.36 hydrogen bonds per water molecule in an assembly of ions such as Mg^{2+}, Na^{+}, NO_3^-, and HCO_3^- due to severe competitive ion-dipole interactions. [113] This can further influence the phases of Mg-carbonates seen in the core region of a confinement.

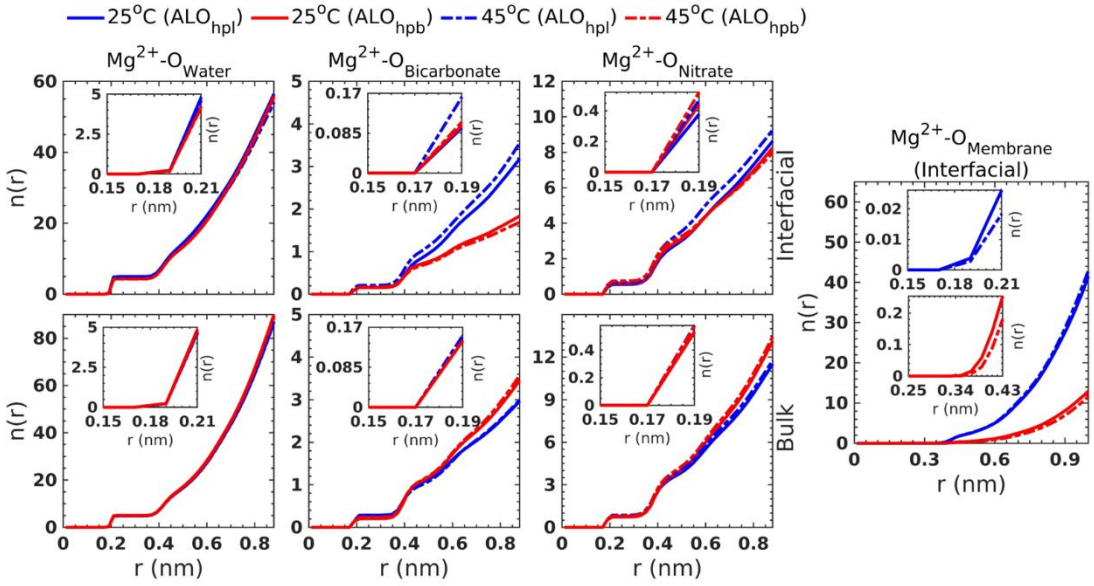

Figure 13 Cumulative Coordination number (n(r)) of oxygens from water, bicarbonate, and nitrate with respect to Mg2+ ions as a function of radial distance 'r' in the interfacial and bulk region at temperatures 25 °C and 45 °C obtained by integrating the g(r) profiles shown in Figure 11. n(r) pertaining to the oxygens from alumina membrane ($O_{Membrane}$) is also provided. The insets are provided to zoom in the first coordination sphere in each case.

Table 3 Coordination number (C.N.) of oxygen around Mg2+ in the interfacial and bulk region of the simulation cell at temperatures 25 oC and 45 oC in presence of hydrophilic (ALOhpl) and hydrophobic (ALOhpb) alumina membrane. The coordination numbers are segregated into coordination from water oxygen ($n(O_W)$) and coordination from oxygens in HCO_3^-, NO_3^-, and the alumina membrane ($n(O_{B+N+A})$). STDEV represents the standard deviation in the coordination number as obtained from triplicates of each simulation. Phase formula represents an approximate composition of the pre-nucleated Mg^{2+} with respect to coordination from water and non-water species (HCO_3^-, NO_3^- and alumina membrane). In the bulk phase, coordination from alumina membrane (A) is not applicable.

System	T (°C)	Phase	1st coordination shell		(1st + 2nd) coordination shell		Total C.N.	Phase formula
			$n(O_W)$ ± STDEV	$n(O_{B+N+A})$ ± STDEV	$n(O_W)$ ± STDEV	$n(O_{B+N+A})$ ± STDEV		
ALO_{hpl}	25	Interfacial	4.76 ± 0.12	0.95 ± 0.67	9.39 ± 0.25	5.38 ± 2.79	14.77	$Mg(O_W)_9(O_{B+N+A})_5$
		Bulk	4.76 ± 0.07	0.68 ± 0.04	10.76 ± 0.13	2.79 ± 0.17	13.55	$Mg(O_W)_{11}(O_{B+N+A})_3$
	45	Interfacial	4.64 ± 0.10	1.06 ± 0.74	9.16 ± 0.15	8.85 ± 4.16	18.01	$Mg(O_W)_9(O_{B+N+A})_9$
		Bulk	4.64 ± 0.01	0.73 ± 0.02	10.57 ± 0.05	3.01 ± 0.04	13.58	$Mg(O_W)_{11}(O_{B+N+A})_3$
ALO_{hpb}	25	Interfacial	4.31 ± 0.16	0.77 ± 0.11	8.96 ± 0.25	4.15 ± 0.22	13.11	$Mg(O_W)_9(O_{B+N+A})_4$
		Bulk	4.86 ± 0.02	0.67 ± 0.02	10.92 ± 0.04	2.98 ± 0.05	13.90	$Mg(O_W)_{11}(O_{B+N+A})_3$
	45	Interfacial	4.21 ± 0.16	0.78 ± 0.09	8.86 ± 0.29	4.21 ± 0.51	13.07	$Mg(O_W)_9(O_{B+N+A})_4$
		Bulk	4.72 ± 0.04	0.72 ± 0.02	10.63 ± 0.07	3.09 ± 0.10	13.72	$Mg(O_W)_{11}(O_{B+N+A})_3$

3.7. *Phase Transition Mechanism Observed in Confined Nanochannels*

The phase transition of magnesium carbonates involves a dynamic shift from a less stable to a more stable and ordered phase. [114] Based on the timeline variation in weight percentage of all phases as shown in **Figure 14**, we could observe the crystallization of $MgCO_3$. $5H_2O$ phase in all physicochemical conditions within 6 hours of loading. No other phase has showcased such a behavior and this is due to the bicarbonate anion, which was used in the precursor solution to cause a steric effect assisting in forming $MgCO_3$. $5H_2O$ and restricting $MgCO_3$. $3H_2O$ crystallization. [115] Based on this effect of bicarbonate anions, the seeding phase is $MgCO_3$. $5H_2O$ and the transition sets about

toward other phases. A transition of $MgCO_3$. $5H_2O$ into $Mg_2(CO_3)(OH)_2$. $3H_2O$ has been observed, supported by Tse et al., [116] who indicated that at high partial pressure of CO_2 (p_{CO2}) and p_{H2O}= 1 bar, $Mg_2(CO_3)(OH)_2$. $3H_2O$ has a phase boundary with $MgCO_3$. $5H_2O$. Moreover, as the magnesium carbonate phases are crystallized in nanoconfined spaces, the normal pressure within these spaces is of the order of 10^3 bar promoting this transition. [117] Furthermore, $Mg_2(CO_3)(OH)_2$. $3H_2O$ can also be formed from $Mg_5(CO_3)_4(OH)_2$. $4H_2O$ via the carbonation of MgO-hydromagnesite blends which was determined via thermodynamic calculations. [118] The transition of $Mg_2(CO_3)(OH)_2$. $3H_2O$ into $MgCO_3$. $3H_2O$ is viable due to the presence of phase boundary, which is also observed via XRD. [116] In addition, the phase of $Mg_2(CO_3)(OH)_2$. $3H_2O$ has the ability to get transformed into $Mg_2(CO_3)(OH)_2$. $0.5H_2O$ following the mechanism possible in bulk fluids and was also observed in confined nanochannels. [42] $Mg_2(CO_3)(OH)_2$. $0.5H_2O$ has a phase boundary with $MgCO_3$. $3H_2O$ and $Mg_5(CO_3)_4(OH)_2$. $4H_2O$. It is also noted that the behavior of $Mg_2(CO_3)(OH)_2$. $0.5H_2O$ is different as it is mostly found to form together with stable $MgCO_3$ displaying an interdependency as seen in the phase polymorphism based on XRD. [119] Lastly, during the transition between $MgCO_3$. $3H_2O$ into $Mg_5(CO_3)_4(OH)_2$. $4H_2O$, $Mg_5(CO_3)_4(OH)_2$. 5-$6H_2O$ acts as the metastable phase which was investigated experimentally and thermodynamically. [120,121]

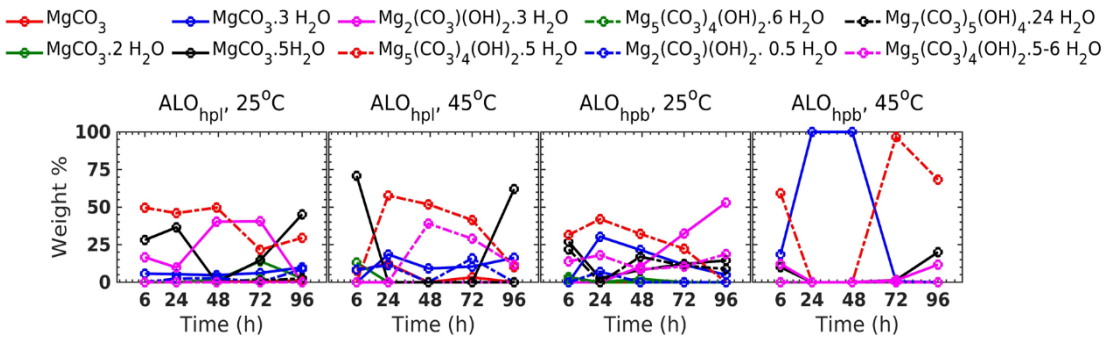

Figure 14 Variation in the weight percentage of different phases of magnesium carbonate with respect to time (in hours) in presence of hydrophilic (ALOhpl) and hydrophobic (ALOhpb) alumina membrane at temperatures of 25 °C and 45 °C.

3.8. *The Effect of Temperature and Surface Wettability on Grain Size*

To confirm the formation of magnesium carbonate in nanoconfinement, the grain size is calculated from the XRD pattern using the Scherrer equation shown below. [30]

$$D = \frac{K.\lambda}{B(2\theta).cos\theta} \qquad (1.1)$$

Where K is the Scherrer constant (K= 0.9), λ is the wavelength of the X-ray source (Cu Kα= 0.154 nm), 2θ is the Bragg angle, B(2θ) is the full width at half maximum (FWHM). All the angles are in radians. Within the hydrophilic membrane, the grain size varies between 96 nm to 103 nm representing stabilization and coarsening of the crystal structure between 6 hours and 96 hours when aged at 25 °C as shown in **Figure 15(a)**. The influence of temperature had an inverse effect on the grain size as shown in **Figure 15(c)** where initially the crystal dissolution and growth take place from 27.5 nm to 34.5 nm between 6 and 24 hours and stabilization of the crystal size is seen till 96 hours to grow till 36 nm. The behavior of crystal growth in hydrophobic nanochannels is quite dissimilar as shown in **Figure 15(b)** where initially the crystal size decreases between 6 hours and 48 hours from 63 nm to 37 nm which corresponds to the presence of excessive HCO^-_3 ions acting as a chain terminator and decaying the cluster size. [122] Once all the HCO^-_3 ions have been utilized, the crystal size grows to 95 nm by 96 hours via dissolution and reprecipitation. The crystal size in hydrophobic nanochannels is hardly affected by temperature as there is no shift in the grain size in comparison with the crystals precipitated at 25 °C. The only considerable change that occurred is in the

crystal size mechanism as shown in **Figure 15(d)** where initially crystal dissolution and growth took place till 24 hours and a stabilization of the crystal was observed till 96 hours.

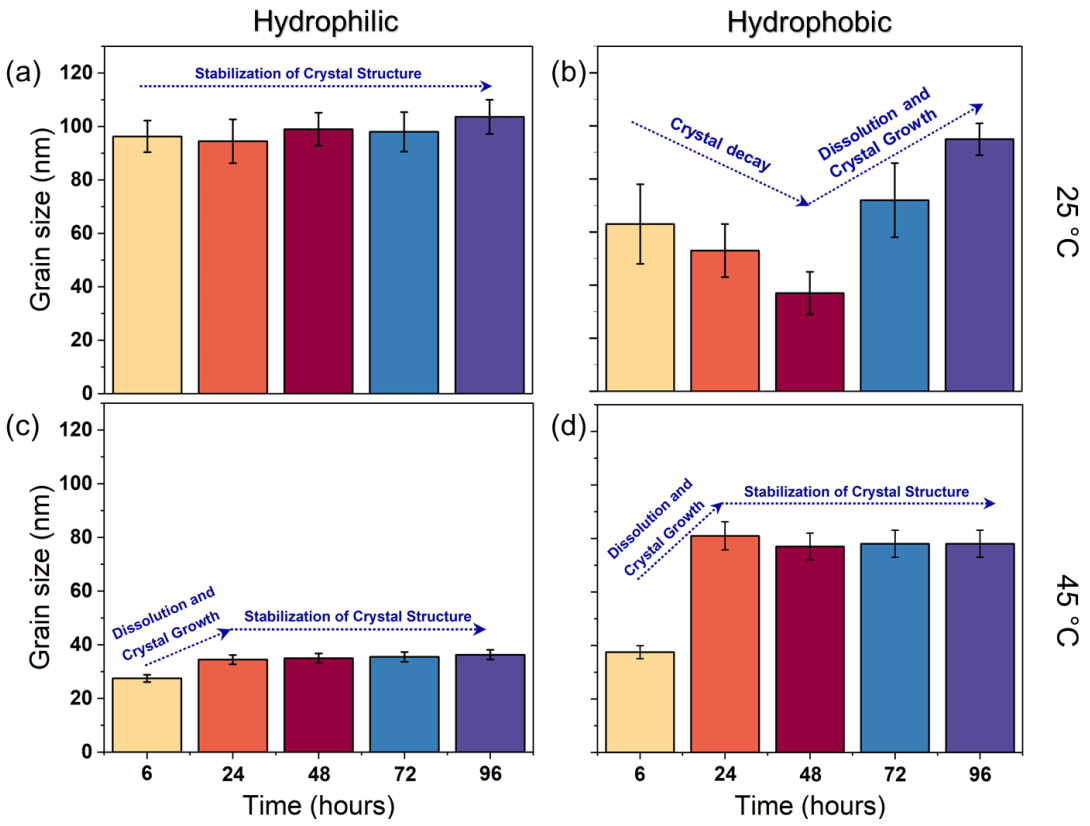

Figure 15 Variation of the grain size of crystallized magnesium carbonate with time in hydrophilic AAM at (a) 25 °C and (c) 45 °C, and hydrophobic AAM at (b) 25 °C and (d) 45 °C using Scherrer formula as given by equation 1.1. Different colors correspond to different time instants.

4. Conclusion

In this study, by loading magnesium nitrate and sodium bicarbonate mixture solutions in an anodic alumina membrane and allowing the Mg-carbonate nuclei to grow in nanoconfinement at 25 °C and 45 °C, we could observe distinctive phase compositions and crystal behaviors compared to those in bulk. These observations helped in recognizing the formation of various stable and metastable phases, and their transition

mechanism was investigated. The growth of magnesium carbonate in nanoconfinement along with the effect of modification in surface wettability was compared. Based on experimental observations, the anhydrous and hydrated phases of magnesium carbonate are predominant in hydrophilic environments whereas hydrated hydroxyl-based phases are predominant in hydrophobic environments. Due to the influence of temperature by the end of 96 hours after loading, non-hydroxide-based magnesium carbonate phases were predominantly identified in hydrophilic conditions and hydrated hydroxyl-based phases were predominant in hydrophobic conditions. Based on the phase formation, anhydrous $MgCO_3$ is formed only in hydrophilic conditions and $MgCO_3$. $5H_2O$ is the originating phase as it is the only phase which was observed after 6 hours of loading in all conditions by means of which other phases have evolved over time. The simulation results indicate the existence of a clathrate-like network of water around Mg^{2+} ions in hydrophobic interfaces that prevents the formation of anhydrous phase as opposed to the hydrophilic interface. On the other hand, a temperature of 45 $^{\circ}C$ is found to favor the formation of anhydrous Mg-carbonate phase in case of hydrophilic interfaces as a result of easier disruption of the hydration network of Mg^{2+} at this temperature. Nevertheless, a compact hydration shell around Mg^{2+} is seen to be ubiquitous in all the conditions directing the overall predominance of hydrated phases in experiments with effects of the bicarbonate ions being prominent beyond the second coordination shell. These findings highlight the critical role of investigating the mineralogy, chemistry, and nucleation pathway within highly reactive subsurface-abundant nanopores rich in magnesium-bearing minerals. Getting an insight into the mechanism of forming different magnesium carbonate phases in subsurface environments and their

interdependency aids in developing efficient technologies for carbon storage and management.

5. Supporting Information

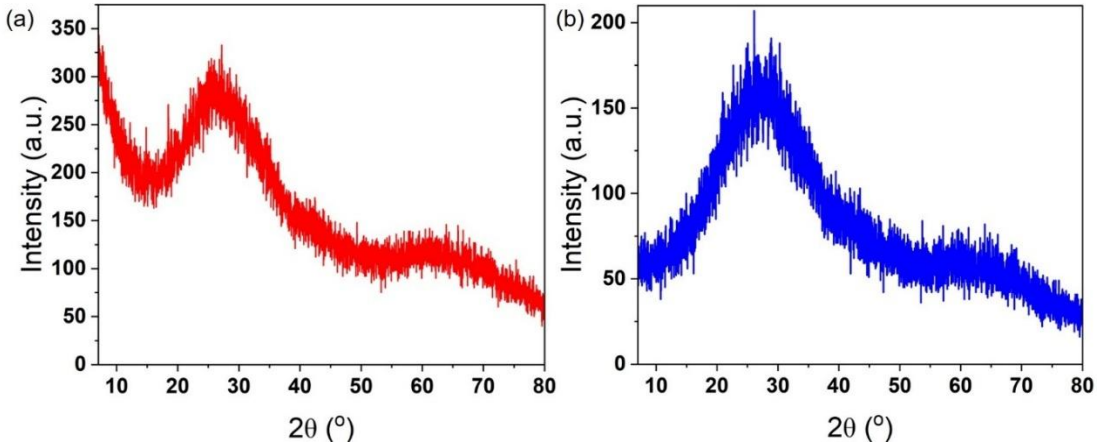

Figure SI 1 Identification of crystal peaks using X-ray diffractometer for (a) Hydrophilic and (b) Hydrophobic anodic alumina membrane.

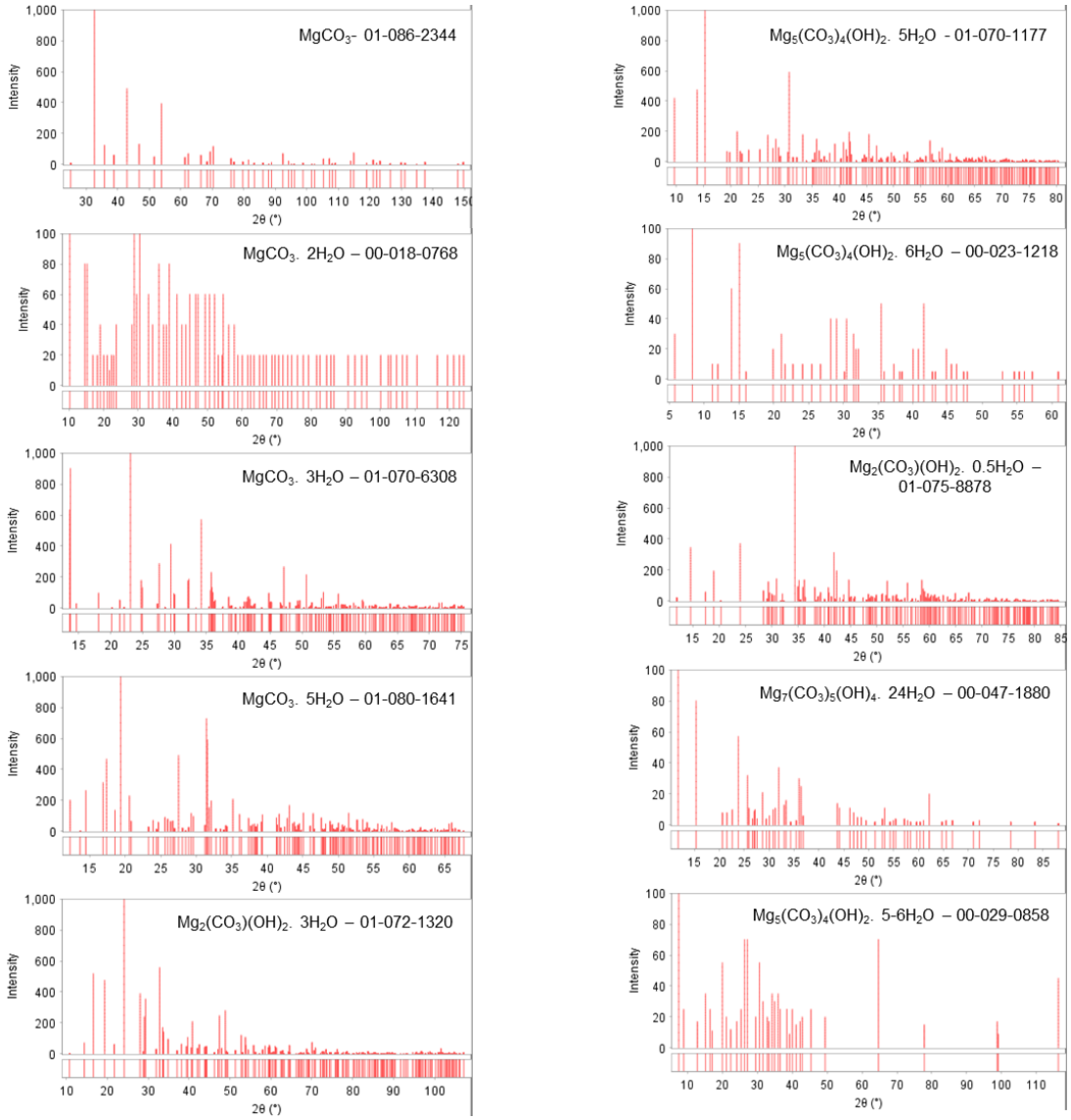

Figure SI 2 Diffraction pattern of various phases of magnesium carbonate obtained from the © 2024 Internation Centre for Diffraction Data

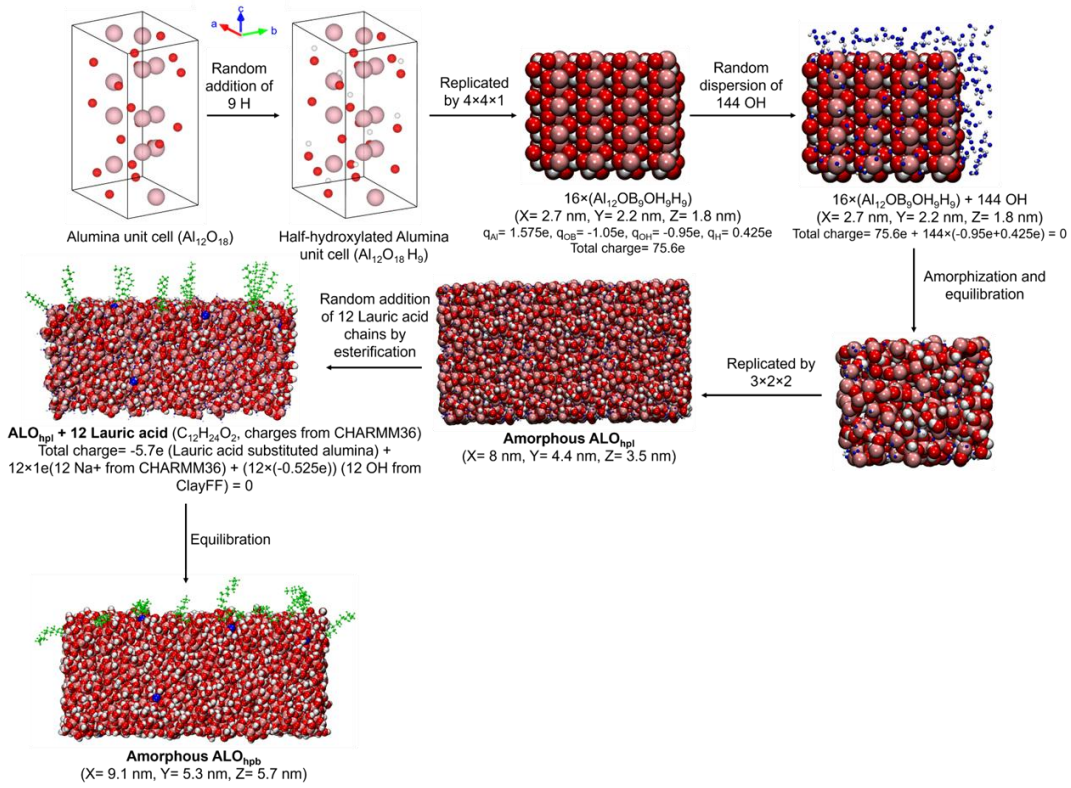

Figure SI 3 Flow chart for modelling amorphous hydrophilic (ALOhpl) and hydrophobic (ALOhpb) alumina membrane in-silico. Mauve, blue, red, and white vdW spheres represent Aluminum, Sodium, Oxygen, and Hydrogen respectively. Blue and white CPK spheres represent Oxygen and Hydrogen respectively whereas Lauric acid chains are drawn as green CPK chains. 'q' represents partial electronic charge as obtained from the respective force fields.

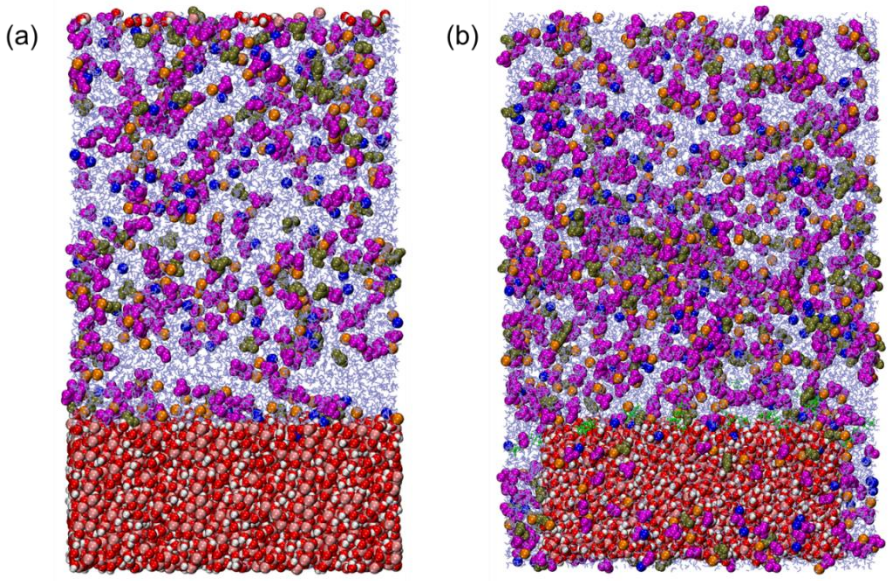

Figure SI 4 Snapshots of the simulation cell in presence of (a) ALOhpl and (b) ALOhpb. Orange, mauve, blue, red, and white vdW spheres correspond to Mg2+, Aluminum, Sodium, Oxygen, and Hydrogen respectively. Bicarbonate and nitrate ions are represented as tan and magenta vdW spheres respectively. Water is shown as blue lines and lauric acid fragments are represented as green CPK chains.

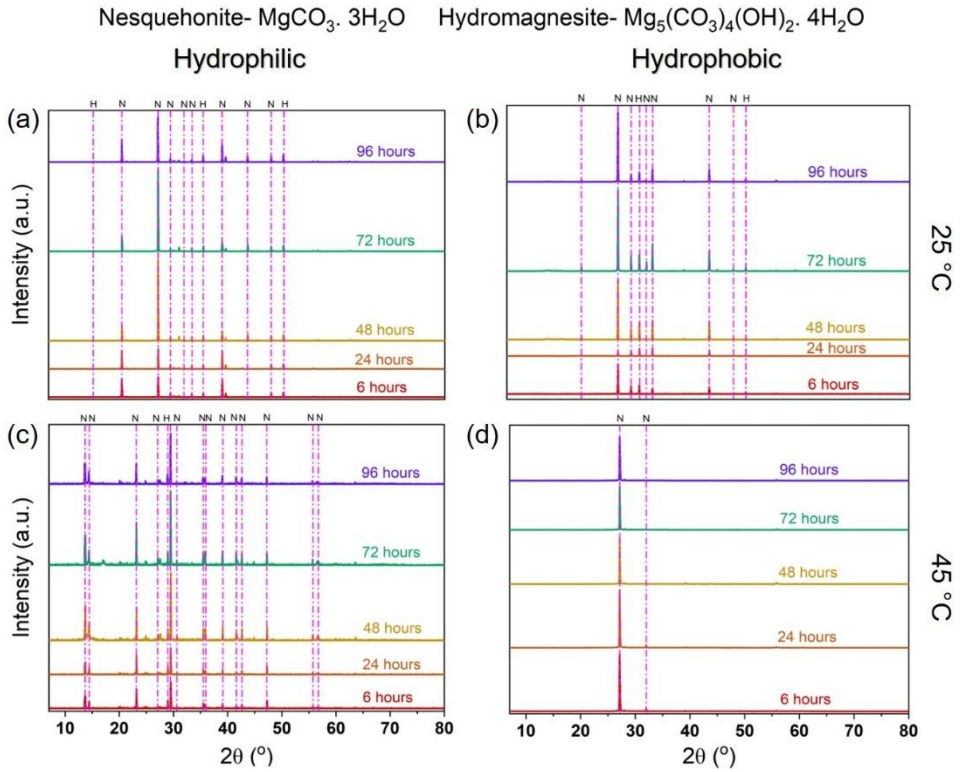

Figure SI 5 Identification of the crystal structure and phases of magnesium carbonate grown on hydrophilic bulk surface at (a) 25 °C and (c) 45 °C, and on hydrophobic bulk surface at (b) 25 °C and (d) 45 °C using X-ray diffraction (XRD).

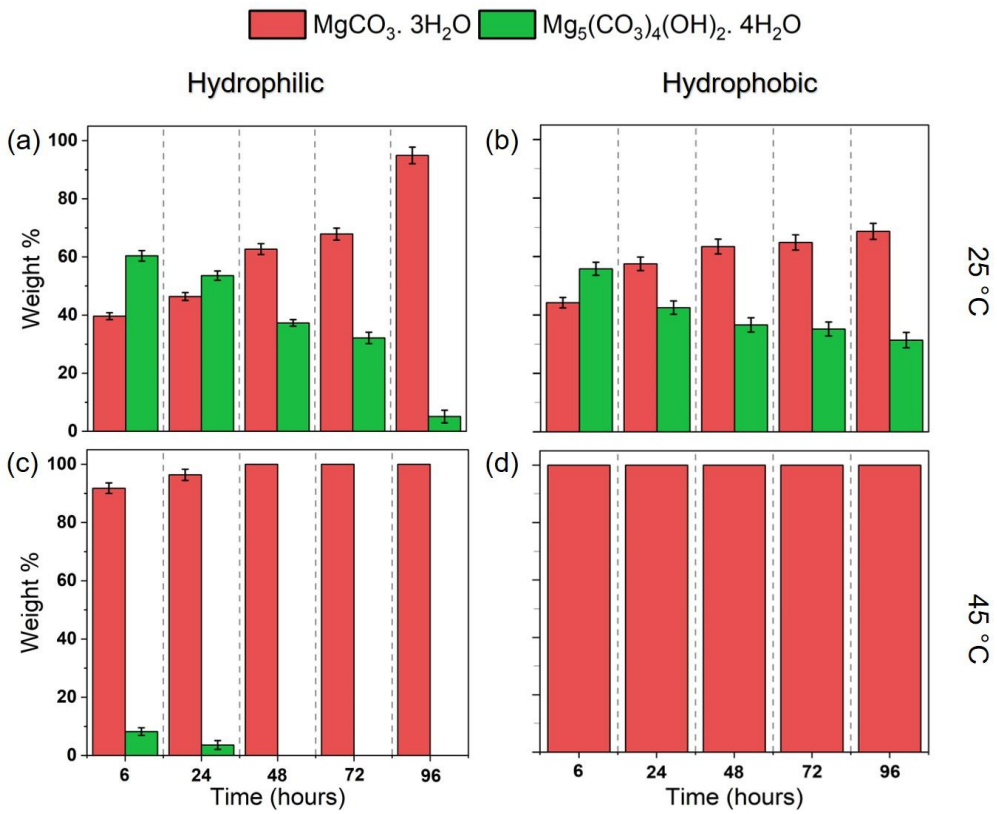

Figure SI 6 Identification of the weight composition of non-hydroxide and hydroxide-based phases of magnesium carbonate grown on hydrophilic bulk surface at (a) at 25 °C and (c) 45 °C, and on hydrophobic bulk surface at (b) 25 °C and (d) 45 °C using X-ray diffraction

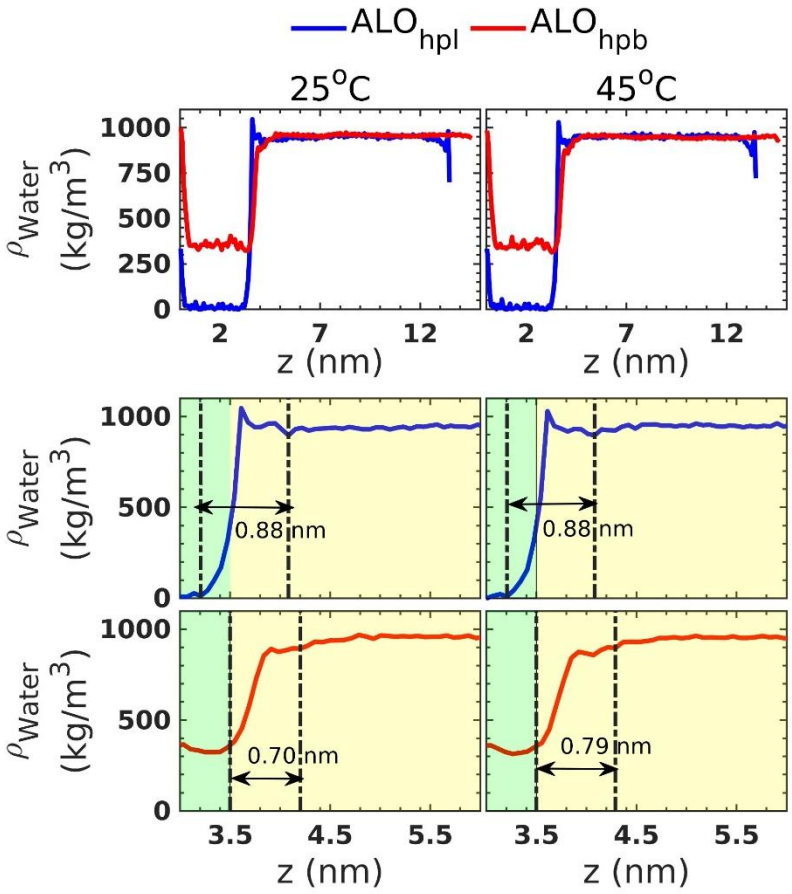

Figure SI 7 Density profile of water along the z axis of the simulation cell at temperatures 25 oC and 45 oC in presence of hydrophilic (ALOhpl) and hydrophobic (ALOhpb) alumina membrane. The middle and bottom panels are zoomed-in versions of the top panel to exhibit the width of the interfacial layers. The widths of the interfacial layers are mentioned on top of the arrows.

Table SI 1 Plane orientation of all phases of magnesium carbonate observed on bulk hydrophilic (ALOhpl) and bulk hydrophobic (ALOhpb) surface aged at 25 °C and 45 °C using X-ray diffraction (XRD).

Phase	**Bulk$_{hpl}$, 25 °C**	**Bulk$_{hpl}$, 45 °C**	**Bulk$_{hpb}$, 25 °C**	**Bulk$_{hpb}$, 45 °C**
Nesquehonite	($\bar{2}$02), ($\bar{3}$01), (222), (410)	(101), (200), (004), (120), (301), (400), (105)	(202), (211), (004), (020), ($\bar{2}$22)	($\bar{2}$02), (105), (413)
Hydromagnesite	(620), (442), (800), (913)	(402)	(310), (321), (442)	-

Table SI 2 Weight percentage of phases observed in bulk solutions crystallized at 25 °C and 45 °C on hydrophilic and hydrophobic surfaces.

System	**Temperature**	**Weight %**									
		Nesquehonite					**Hydromagnesite**				
		Time (hours)									
		6	**24**	**48**	**72**	**96**	**6**	**24**	**48**	**72**	**96**
Hydrophilic	25 °C	39.6 ±1.18	46.4 ±1.39	62.7 ±1.88	67.8 ±2.03	94.9 ±2.84	60.4 ±1.81	53.6 ±1.6	37.3 ±1.11	32.2 ±1.96	5.1± 2.15
	45 °C	91.8 ±1.83	96.4 ±1.92	100	100	100	8.2± 1.3	3.6± 1.53	-	-	-
Hydrophobic	25 °C	44.2 ±1.76	57.5 ±2.3	63.4 ±2.53	64.8 ±2.59	68.6 ±2.74	55.8 ±2.23	42.5 ±2.3	36.6 ±2.46	35.2 ±2.4	31.4 ±2.65
	45 °C	100	100	100	100	100	-	-	-	-	-

Phase	ALO_{hpl}, 25ºC					ALO_{hpl}, 45ºC					ALO_{hpb}, 25ºC					ALO_{hpb}, 45ºC				
	6h	24h	48h	72h	96h	6h	24h	48h	72h	96h	6h	24h	48h	72h	96h	6h	24h	48h	72h	96h
Magnesite	0	0	1±0.08	0	1.5±0.12	7.7±0.4	12.5±0.8	0	3.3±0.2	0	0	0	0	0	0	0	0	0	0	0
Barringtonite	0	0	1.4±0.09	14±1.04	2.6±0.2	13.1±1	0	0	0	0	3.5±0.2	0	2.3±0.1	0	0	0	0	0	0	0
Nesquehonite	5.7±0.17	5.3±0.16	4.7±0.14	6.1±0.2	9.9±0.3	0	18.5±1.3	9.2±0.7	10.4±0.7	16.3±1.2	0	30.3±1.5	21.5±1	11.6±0.6	4.9±0.3	18.6±1	100	100	0.5±0.04	0
Lansfordite	28.1±1.8	36.5±2.4	0	14.7±0.96	45.2±2.95	70.8±3.6	0	0	0	62±3.1	27±0.9	2.7±0.1	8.1±0.3	12.2±0.4	14.5±0.4	10±0.9	0	0	1.5±0.3	20±1.5
Artinite	16.6±0.8	9.8±0.5	40.3±2	40.6±2.1	0	0	0	0	0	0	0	0	10.3±0.5	32.4±1.6	53±2.7	12.2±1	0	0	1.3±0.1	11.7±1
Hydromagnesite	49.6±3.9	46±3.5	49.7±4	21.6±1.7	29.5±2.4	0	57.7±3.5	51.8±3.1	41.4±2.5	10±0.6	31.5±1.9	42±2.5	32.2±1.9	22.3±1.4	0	59.2±2.9	0	0	96.6±1.3	68.3±0.9
Dypingite	0	0	0	2±0.2	0	0	0	0	0	0	2.2±0.1	0	0	0	0	0	0	0	0	0
Pokrovskite	0	2.4±0.1	2.8±0.2	0	8.7±0.3	8.4±0.7	11.4±0.9	0	15.9±1.3	0	0	7±0.4	0	0	0	0	0	0	0	0
Shelkovite	0	0	0	0.9±0.05	2.6±0.15	0	0	0	0	0	21.9±1.8	0	17±1.4	11±0.9	8.9±0.7	0	0	0	0	0
Giorgiosite	0	0	0	0	0	0	0	39±2	29±1.5	11.7±0.6	13.9±1.2	18±1.5	8.6±0.7	10.5±0.9	18.8±1.6	0	0	0	0	0

Table SI 3 Weight percentages of the different phases of magnesium carbonate formed in the hydrophilic (ALO_{hpl}) and hydrophobic (ALO_{hpb}) nanochannel at 25 ºC and 45 ºC. The chemical formulae of different phases can be obtained from Table 1.

System	T (°C)	E_{av} (kJ mol^{-1}) (Mg^{2+}-Membrane)		E_{av} (kJ mol^{-1}) (Na^{+}-Membrane)		E_{av} (kJ mol^{-1}) (HCO_3^{-}-Membrane)		E_{av} (kJ mol^{-1}) (NO_3^{-}-Membrane)		E_{av} (kJ mol^{-1}) (Water-Membrane)	
		Elec. ± STDEV	vdW ± STDEV	Elec. ± STDEV	vdW ± STDEV	Elec. ± STDEV	vdW ± STDEV	Elec. ± STDEV	vdW ± STDEV	Elec. ± STDEV	vdW ± STDEV
ALO_{hpl}	25	-18.36 ± 0.02	-0.03 ± 1.40×10^{-3}	-51.01 ± 0.04	5.85 ± 4.50×10^{-3}	-114.83 ± 0.07	15.02 ± 0.01	-55.17 ± 0.04	3.41 ± 4.00×10^{-3}	-427.06 ± 0.01	81.57 ± 2.70×10^{-3}
	45	-18.46 ± 0.01	-0.17 ± 1.30×10^{-3}	-66.68 ± 0.02	8.01 ± 2.90×10^{-3}	-151.66 ± 0.03	20.61 ± 1.90×10^{-3}	-65.80 ± 0.06	4.65 ± 6.90×10^{-3}	-396.66 ± 0.02	76.32 ± 4.20×10^{-3}
ALO_{hpb}	25	-33.39 ± 0.02	-1.22 ± 4.23×10^{-4}	-67.58 ± 0.04	8.01 ± 4.50×10^{-3}	-176.66 ± 0.05	26.66 ± 0.01	-93.39 ± 0.02	-2.98 ± 4.70×10^{-3}	-810.89 ± 0.01	143.96 ± 1.40×10^{-3}
	45	-34.15 ± 0.02	-0.73 ± 1.80×10^{-3}	-76.61 ± 0.03	8.89 ± 4.10×10^{-3}	-240.47 ± 0.08	35.85 ± 0.01	-75.38 ± 0.01	-4.39 ± 2.90×10^{-3}	-780.85 ± 0.01	137.31 ± 3.60×10^{-3}

Table SI 4 Normalized average Electrostatic (Elec.) and vdW interaction energy (Eav) in kJ mol-1 between the alumina membrane (ALOhpl and ALOhpb) and different species (Mg2+, Na+, HCO3-, NO3-, and water) present in the simulation box at temperatures (T) 25 °C and 45 °C. Calculations are done over the last 10 ns of the simulation trajectory and averaged over three concordant simulations in each case. Normalization is done based on the total number of participating molecules in each combination. STDEV represents the standard deviation as obtained from triplicates of each simulation.

6. Acknowledgment

The authors acknowledge the use of shared facilities at Cornell Center for Materials Research (CCMR) supported through NSF MRFEC program (DMR- 1719875) and Cornell NanoScale Science and Technology Facility (CNF), a member of the National Nanotechnology Coordination Infrastructure (NNCI) supported by NSF (Grant NNCI-2025233). AM and RH are supported by NSF CAREER (Grant No- 2144373), YJ is supported by Military Project (Grant #). RH acknowledges the computation time provided by the Cornell G2-cluster. Few illustrations were created with BioRender.com.

7 References

1. Lu, S., Cui, W., Wang, R., Zhang, C. & Yan, P. Biomimetic mineralization and characterization of hierarchically structured hydrated magnesium carbonates: The effects of sodium alginate. *Journal of CO2 Utilization* **56**, (2022).

2. Gadikota, G. Carbon mineralization pathways for carbon capture, storage and utilization. *Communications Chemistry* vol. 4 Preprint at https://doi.org/10.1038/s42004-021-00461-x (2021).

3. Pan, S. Y., Chang, E. E., Kim, H., Chen, Y. H. & Chiang, P. C. Validating carbonation parameters of alkaline solid wastes via integrated thermal analyses: Principles and applications. *J Hazard Mater* **307**, (2016).

4. Wang, S. *et al.* Carbon mineralization under different saline-alkali stress conditions in paddy fields of northeast China. *Sustainability (Switzerland)* **12**, (2020).

5. Ibrahim, M. H., El-Naas, M. H., Benamor, A., Al-Sobhi, S. S. & Zhang, Z. Carbon mineralization by reaction with steel-making waste: A review. *Processes* vol. 7 Preprint at https://doi.org/10.3390/pr7020115 (2019).

6. Radha, A. V. & Navrotsky, A. Thermodynamics of carbonates. *Rev Mineral Geochem* **77**, (2013).

7. Gadikota, G. & Park, A. hyung A. Accelerated Carbonation of Ca- and Mg-Bearing Minerals and Industrial Wastes Using CO2. in *Carbon Dioxide Utilisation: Closing the Carbon Cycle: First Edition* (2015). doi:10.1016/B978-0-444-62746-9.00008-6.

8. Wang, T. *et al.* Particle carbonation kinetics models and activation methods under mild environment: The case of calcium silicate. *Chemical Engineering Journal* **423**, (2021).

9. Rakesh, S. *et al.* Carbon mineralization rates and kinetics of surface-applied and incorporated rice and maize residues in entisol and inceptisol soil types. *Sustainability (Switzerland)* **13**, (2021).

10. Carroll, S. A. & Knauss, K. G. Dependence of labradorite dissolution kinetics on CO2(aq), Al(aq), and temperature. *Chem Geol* **217**, (2005).

11. Wang, F., Dreisinger, D., Jarvis, M. & Hitchins, T. Kinetic evaluation of mineral carbonation of natural silicate samples. *Chemical Engineering Journal* **404**, (2021).

12. Miller, Q. R. S. *et al.* Anomalously low activation energy of nanoconfined MgCO3 precipitation. *Chemical Communications* **55**, (2019).

13. Wang, Y., Bryan, C., Xu, H. & Gao, H. Nanogeochemistry: Geochemical reactions and mass transfers in nanopores. *Geology* **31**, (2003).

14. Greathouse, J. A., Boyle, T. J. & Kemp, R. A. Computational Evaluation of Mg-Salen Compounds as Subsurface Fluid Tracers: Molecular Dynamics Simulations in Toluene-Water Mixtures and Clay Mineral Nanopores. *Energy and Fuels* **32**, (2018).

15. Santos, H. S. *et al.* Mechanisms of Mg carbonates precipitation and implications for CO2 capture and utilization/storage. *Inorganic Chemistry Frontiers* Preprint at https://doi.org/10.1039/d2qi02482a (2023).

16. Aluru, N. R. *et al.* Fluids and Electrolytes under Confinement in Single-Digit Nanopores. *Chemical Reviews* vol. 123 Preprint at https://doi.org/10.1021/acs.chemrev.2c00155 (2023).

17. Xu, X. *et al.* Water flow inside various geometric nano-confinement channels. *Physical Chemistry Chemical Physics* **22**, (2020).

18. Gubbins, K. E., Long, Y. & Śliwinska-Bartkowiak, M. Thermodynamics of confined nano-phases. *Journal of Chemical Thermodynamics* **74**, (2014).

19. Smeets, P. J. M. *et al.* A classical view on nonclassical nucleation. *Proc Natl Acad Sci U S A* **114**, (2017).

20. Ma, S. *et al.* In situ TEM investigation of nucleation and crystallization of hybrid bismuth nanodiamonds. *Nanoscale* (2023) doi:10.1039/d3nr01338c.

21. Zhang, Z. *et al.* Multistep nucleation visualized during solid-state crystallization. *Mater Horiz* **9**, (2022).

22. Tang, R., Jin, B., Jin, B. & Liu, Z. Recent experimental explorations of non-classical nucleation. *CrystEngComm* **22**, (2020).

23. Cölfen, H. Nonclassical nucleation and crystallization. *Crystals* vol. 10 Preprint at https://doi.org/10.3390/cryst10020061 (2020).

24. Lutsko, J. F. Novel Paradigms in Nonclassical Nucleation Theory. in *New Perspectives on Mineral Nucleation and Growth* (2017). doi:10.1007/978-3-319-45669-0_2.

25. Michalak, N. *et al.* Ostwald Ripening in an Oxide-on-Metal System. *Adv Mater Interfaces* **9**, (2022).

26. Yamada, R., Inubushi, H. & Ohno, M. Ostwald ripening under temperature gradient: A phase-field study. *J Appl Phys* **130**, (2021).

27. De Chalendar, J. A., Garing, C. & Benson, S. M. Pore-scale Considerations on Ostwald Ripening in Rocks. in *Energy Procedia* vol. 114 (2017).

28. Salzmann, B. B. V., Van Der Sluijs, M. M., Soligno, G. & Vanmaekelbergh, D. Oriented Attachment: From Natural Crystal Growth to a Materials Engineering Tool. *Acc Chem Res* **54**, (2021).

29. Pan, H. & Tang, R. Towards an understanding of crystallization by attachment. *Crystals (Basel)* **10**, (2020).

30. Asgar, H., Mohammed, S. & Gadikota, G. Confinement induces stable calcium carbonate formation in silica nanopores. *Nanoscale* **14**, (2022).

31. Zeng, M. *et al.* Confinement generates single-crystal aragonite rods at room temperature. *Proc Natl Acad Sci U S A* **115**, (2018).

32. Wang, Y., Zeng, M., Meldrum, F. C. & Christenson, H. K. Using confinement to study the crystallization pathway of calcium carbonate. *Cryst Growth Des* **17**, (2017).

33. Farhang, F. *et al.* Experimental study on the precipitation of magnesite from thermally activated serpentine for CO2 sequestration. *Chemical Engineering Journal* **303**, (2016).

34. Power, I. M., Kenward, P. A., Dipple, G. M. & Raudsepp, M. Room Temperature Magnesite Precipitation. *Cryst Growth Des* **17**, (2017).

35. Yan, X. X., Li, Y. F., Xue, D. F., Yan, C. L. & Wang, L. Bonding analysis on the crystallization of magnesium carbonate hydrates. *Rengong Jingti Xuebao/Journal of Synthetic Crystals* **36**, (2007).

36. Apriani, M., Hadi, W. & Masduqi, A. The kinetics of magnesium carbonate crystallization for traditional salt production wastewater recovery. in *Materials Science Forum* vol. 964 MSF (2019).

37. Chaka, A. M. Ab Initio Thermodynamics of Hydrated Calcium Carbonates and Calcium Analogues of Magnesium Carbonates: Implications for Carbonate Crystallization Pathways. *ACS Earth Space Chem* **2**, (2018).

38. Chen, Q., Hui, T., Sun, H., Peng, T. & Ding, W. Synthesis of magnesium carbonate hydrate from natural talc. *Open Chem* **18**, (2020).

39. Lou, Z., Chen, Q., Zhu, Y., Zhang, Y. & Gao, J. Growth of magnesium carbonate single crystal in supercritical carbon dioxide-molten sodium system. *Cryst Growth Des* **4**, (2004).

40. Xu, J. *et al.* Testing the cation-hydration effect on the crystallization of Ca-Mg-CO 3 systems. *Proc Natl Acad Sci U S A* **110**, (2013).

41. Guermech, S., Mocellin, J., Tran, L. H., Mercier, G. & Pasquier, L. C. A study of hydromagnesite and nesquehonite precipitation in indirect aqueous carbonation of thermally-activated serpentine in a batch mode. *J Cryst Growth* **584**, (2022).

42. Rheinheimer, V. *et al.* XPS study on the stability and transformation of hydrate and carbonate phases within MgO systems. *Materials* **10**, (2017).

43. Rieke, P. C. Application of Van Oss-Chaudhury-Good theory of wettability to interpretation of interfacial free energies of heterogeneous nucleation. *J Cryst Growth* **182**, (1997).

44. Papadopoulou, E., Zavadlav, J., Podgornik, R., Praprotnik, M. & Koumoutsakos, P. Tuning the Dielectric Response of Water in Nanoconfinement through Surface Wettability. *ACS Nano* **15**, (2021).

45. Sharma, M. M. & Freitas, A. M. Effect of surface hydrophobicity on the detachment of particles from surfaces. in *Particles on Surfaces: Detection, Adhesion and Removal, Volume 7* (2023). doi:10.1201/9780429070716-12.

46. Zhang, X., Zhang, X., Duan, R. & Liu, L. Effect of Hydrophilicity/Hydrophobicity of the Injector Wall on Atomization Performance. *International Journal of Aerospace Engineering* **2022**, (2022).

47. Tan, Y., Jin, H., Mao, S. S. & Shen, S. Surface hydrophobicity-hydrophilicity switching induced interface heat and water transfer enhancement for high-efficiency solar steam generation. *Carbon Neutrality* **2**, (2023).

48. Tao, J., Song, X., Bao, B., Zhao, S. & Liu, H. The role of surface wettability on water transport through membranes. *Chem Eng Sci* **219**, (2020).

49. Corsaro, C., Mallamace, D., Neri, G. & Fazio, E. Hydrophilicity and hydrophobicity: Key aspects for biomedical and technological purposes. *Physica A: Statistical Mechanics and its Applications* vol. 580 Preprint at https://doi.org/10.1016/j.physa.2021.126189 (2021).

50. Tommaso, D. Di & De Leeuw, N. H. Structure and dynamics of the hydrated magnesium ion and of the solvated magnesium carbonates: Insights from first principles simulations. *Physical Chemistry Chemical Physics* **12**, (2010).

51. Riahi, S., Roux, B. & Rowley, C. N. QM/MM molecular dynamics simulations of the hydration of Mg(II) and Zn(II) ions. *Can J Chem* **91**, (2013).

52. Argyris, D., Ho, T., Cole, D. R. & Striolo, A. Molecular dynamics studies of interfacial water at the alumina surface. *Journal of Physical Chemistry C* **115**, (2011).

53. Tavani, F. *et al.* Caught while Dissolving: Revealing the Interfacial Solvation of the Mg2+Ions on the MgO Surface. *ACS Appl Mater Interfaces* **14**, (2022).

54. Norek, M. & Krasiński, A. Controlling of water wettability by structural and chemical modification of porous anodic alumina (PAA): Towards super-hydrophobic surfaces. *Surf Coat Technol* **276**, (2015).

55. Argyris, D., Ashby, P. D. & Striolo, A. Structure and orientation of interfacial water determine atomic force microscopy results: Insights from molecular dynamics simulations. *ACS Nano* **5**, (2011).

56. Höllring, K., Baer, A., Vučemilović-Alagić, N., Smith, D. M. & Smith, A. S. Anisotropic molecular diffusion in confinement I: Transport of small particles in potential and density gradients. *J Colloid Interface Sci* **650**, (2023).

57. Garofalini, S. H. Molecular dynamics simulation of the frequency spectrum of amorphous silica. *J Chem Phys* **76**, (1982).

58. Rarivomanantsoa, M., Jund, P. & Jullien, R. Classical molecular dynamics simulations of amorphous silica surfaces. *Journal of Physics Condensed Matter* **13**, (2001).

59. Gutiérrez, G. & Johansson, B. Molecular dynamics study of structural properties of amorphous Al2O3. *Phys Rev B Condens Matter Mater Phys* **65**, (2002).

60. Nguyen, G. T., Nguyen, T. T., Nguyen, T. T. & Le, V. V. Molecular dynamics simulations of pressure-induced structural and mechanical property changes in amorphous Al2O3. *J Non Cryst Solids* **449**, (2016).

61. Adiga, S. P., Zapol, P. & Curtiss, L. A. Structure and morphology of hydroxylated amorphous alumina surfaces. *Journal of Physical Chemistry C* **111**, (2007).

62. Adiga, S. P., Zapol, P. & Curtiss, L. A. Atomistic simulations of amorphous alumina surfaces. *Phys Rev B* **74**, (2006).

63. Hass, K. C., Schneider, W. F., Curioni, A. & Andreoni, W. The chemistry of water on alumina surfaces: Reaction dynamics from first principles. *Science (1979)* **282**, (1998).

64. Tsirelson, V. G., Yu. Antipin, M., Gerr, R. G., Ozerov, R. P. & Struchkov, Y. T. Ruby structure peculiarities derived from X-ray diffraction data localization of chromium atoms and electron deformation density. *physica status solidi (a)* **87**, (1985).

65. Sah, A., Castricum, H. L., Bliek, A., Blank, D. H. A. & Ten Elshof, J. E. Hydrophobic modification of γ-alumina membranes with organochlorosilanes. *J Memb Sci* **243**, (2004).

66. Cygan, R. T., Liang, J. J. & Kalinichev, A. G. Molecular models of hydroxide, oxyhydroxide, and clay phases and the development of a general force field. *Journal of Physical Chemistry B* **108**, (2004).

67. Hass, K. C. & Schneider, W. F. First-principles molecular dynamics simulations of H2O on α-Al2O3 (0001). *Journal of Physical Chemistry B* **104**, (2000).

68. Choi, Y. *et al.* Anchoring catalytically active species on alumina via surface hydroxyl group for durable surface reaction. *Appl Catal B* **325**, (2023).

69. Ma, Y. *et al.* A thermodynamic model of the surface hydroxylation of γ-Al $_2$ O $_3$. *Physical Chemistry Chemical Physics* **26**, 19543–19553 (2024).

70. Dennington, R., Keith, T. A. & Millam, J. M. GaussView, Version 6.1.1. Preprint at (2016).

71. Chai, J., Liu, S. & Yang, X. Molecular dynamics simulation of wetting on modified amorphous silica surface. *Appl Surf Sci* **255**, (2009).

72. Wang, R. *et al.* Sodium Halide Adsorption and Water Structure at the α-Alumina(0001)/Water Interface. *Journal of Physical Chemistry C* **123**, (2019).

73. Berendsen, H. J. C., Grigera, J. R. & Straatsma, T. P. The missing term in effective pair potentials. *Journal of Physical Chemistry* **91**, (1987).

74. Mark, P. & Nilsson, L. Structure and dynamics of the TIP3P, SPC, and SPC/E water models at 298 K. *Journal of Physical Chemistry A* **105**, (2001).

75. Sambasivarao, S. V. & Acevedo, O. Development of OPLS-AA force field parameters for 68 unique ionic liquids. *J Chem Theory Comput* **5**, (2009).

76. Mosallanejad, S., Oluwoye, I., Altarawneh, M., Gore, J. & Dlugogorski, B. Z. Interfacial and bulk properties of concentrated solutions of ammonium nitrate. *Physical Chemistry Chemical Physics* **22**, (2020).

77. Beglov, D. & Roux, B. Finite representation of an infinite bulk system: Solvent boundary potential for computer simulations. *J Chem Phys* **100**, (1994).

78. Vanommeslaeghe, K. *et al.* CHARMM general force field: A force field for drug-like molecules compatible with the CHARMM all-atom additive biological force fields. *J Comput Chem* **31**, (2010).

79. Wacha, A. F. & Lemkul, J. A. charmm2gmx: An Automated Method to Port the CHARMM Additive Force Field to GROMACS. *J Chem Inf Model* **63**, (2023).

80. González, M. A. Force fields and molecular dynamics simulations. *École thématique de la Société Française de la Neutronique* **12**, (2011).

81. Abraham, M. J. *et al.* Gromacs: High performance molecular simulations through multi-level parallelism from laptops to supercomputers. *SoftwareX* **1–2**, (2015).

82. Bussi, G., Donadio, D. & Parrinello, M. Canonical sampling through velocity rescaling. *Journal of Chemical Physics* **126**, (2007).

83. Humphrey, W., Dalke, A. & Schulten, K. VMD: Visual molecular dynamics. *J Mol Graph* **14**, (1996).

84. Kim, H.-M., Choi, J.-W., Kwon, J.-S., Lee, C.-H. & Kim, B. Super-Hydrophobic Properties of Aluminum Surfaces Synthesized by a Two-Step Chemical Etching Process. *J Nanosci Nanotechnol* **19**, (2019).

85. Zhou, Y. *et al.* Facile synthesis of high surface area nanostructured ceria-zirconia-yttria-lanthana solid solutions with the assistance of lauric acid and dodecylamine. *Mater Res Bull* **99**, (2018).

86. Han, S., Kumar, P. & Stanley, H. E. Hydrogen-bond dynamics of water in a quasi-two-dimensional hydrophobic nanopore slit. *Phys Rev E Stat Nonlin Soft Matter Phys* **79**, (2009).

87. Ji, Y., Madhav, D. & Vandeginste, V. Kinetics of enhanced magnesium carbonate formation for CO2 storage via mineralization at 200 °C. *International Journal of Greenhouse Gas Control* **121**, (2022).

88. Tarasevich, Y. I. State and structure of water in vicinity of hydrophobic surfaces. *Colloid Journal* **73**, (2011).

89. Kim, J., Tian, Y. & Wu, J. Thermodynamic and Structural Evidence for Reduced Hydrogen Bonding among Water Molecules near Small Hydrophobic Solutes. *Journal of Physical Chemistry B* **119**, (2015).

90. Grdadolnik, J., Merzel, F. & Avbelj, F. Origin of hydrophobicity and enhanced water hydrogen bond strength near purely hydrophobic solutes. *Proc Natl Acad Sci U S A* **114**, (2017).

91. Galamba, N. Water tetrahedrons, hydrogen-bond dynamics, and the orientational mobility of water around hydrophobic solutes. *Journal of Physical Chemistry B* **118**, (2014).

92. Wawer, J. & Krakowiak, J. Structural changes of water caused by non-electrolytes: Volumetric and compressibility approach for urea-like analogues. *J Mol Liq* **259**, (2018).

93. Glasser, F. P. *et al.* Sequestering CO 2 by Mineralization into Useful Nesquehonite-Based Products. *Front Energy Res* **4**, (2016).

94. Cao, X. *et al.* A new environmentally-friendly route toin situform a high-corrosion-resistant nesquehonite film on pure magnesium. *RSC Adv* **10**, (2020).

95. Lu, S., Yan, P., Gao, Y., Zhang, C. & Lu, J. Insights into the structures, energies and electronic properties of nesquehonite surfaces by first-principles calculations. *Advanced Powder Technology* **31**, (2020).

96. Erlund, R. & Zevenhoven, R. Simulations on design and system performance of building heating boosted by thermal energy storage (TES) with magnesium hydro carbonates/silica gel. *Energies (Basel)* **13**, (2020).

97. Ortiz, C. Thermochemical energy storage based on carbonates: A brief overview. *Energies* vol. 14 Preprint at https://doi.org/10.3390/en14144336 (2021).

98. Jin, D., Wu, N., Zhong, J. & Coasne, B. Phase stability and nucleation kinetics of salts in confinement. *J Mol Liq* **394**, (2024).

99. Jin, D. & Coasne, B. Reduced phase stability and faster formation/dissociation kinetics in confined methane hydrate. *Proc Natl Acad Sci U S A* **118**, (2021).

100. Tsuchiya, J. & Thompson, E. C. The role of hydrogen bonds in hydrous minerals stable at lower mantle pressure conditions. *Progress in Earth and Planetary Science* vol. 9 Preprint at https://doi.org/10.1186/s40645-022-00521-3 (2022).

101. Yamamoto, G. ichiro, Kyono, A. & Okada, S. Temperature dependence of amorphous magnesium carbonate structure studied by PDF and XAFS analyses. *Sci Rep* **11**, (2021).

102. Soininen, A. J. *et al.* Dynamics of water confined in mesoporous magnesium carbonate. *Journal of Chemical Physics* **145**, (2016).

103. Bordin, J. R., Krott, L. B. & Barbosa, M. C. Surface phase transition in anomalous fluid in nanoconfinement. *Journal of Physical Chemistry C* **118**, (2014).

104. Keshavarzi, T., Sohrabi, R. & Mansoori, G. A. An analytic model for nano confined fluids phase-transition: Applications for confined fluids in nanotube and nanoslit. *J Comput Theor Nanosci* **3**, (2006).

105. Mante, P. A. *et al.* Probing hydrophilic interface of solid/liquid-water by nanoultrasonics. *Sci Rep* **4**, (2014).

106. O'Neil, M. J. (ed.). The Merck Index - An Encyclopedia of Chemicals, Drugs, and Biologicals. Cambridge. *UK: Royal Society of Chemistry* (2013).

107. Lemmon, E. W., McLinden, M. O. & Friend, and D. G. *'Thermophysical Properties of Fluid Systems' in NIST Chemistry Webbook; NIST Standard Reference Database No. 69*. *NIST Chemistry WebBook* (2017).

108. Argyris, D., Cole, D. R. & Striolo, A. Dynamic behavior of interfacial water at the silica surface. *Journal of Physical Chemistry C* **113**, (2009).

109. Allnér, O., Nilsson, L. & Villa, A. Magnesium ion-water coordination and exchange in biomolecular simulations. *J Chem Theory Comput* **8**, (2012).

110. Bock, C. W., Kaufman, A. & Glusker, J. P. Coordination of Water to Magnesium Cations. *Inorg Chem* **33**, (1994).

111. Bhattacharjee, A., Pribil, A. B., Randolf, B. R., Rode, B. M. & Hofer, T. S. Hydration of Mg2+ and its influence on the water hydrogen bonding network via ab initio QMCF MD. *Chem Phys Lett* **536**, (2012).

112. Marcus, Y. Effect of ions on the structure of water: Structure making and breaking. *Chemical Reviews* vol. 109 Preprint at https://doi.org/10.1021/cr8003828 (2009).

113. Atkins, P. *Concepts in Physical Chemistry*. (Royal Society of Chemistry, 2024). doi:10.1039/9781837674244.

114. Binder, K. Phase transitions in reduced geometry. *Annu Rev Phys Chem* **43**, (1992).

115. Song, X. *et al.* Synthesis of lansfordite under regulation of dicarbonate. *Huagong Xuebao/CIESC Journal* **66**, (2015).

116. Tse, J. S. *et al.* Location of Artinite (Mg2CO3(OH)2·3H2O) within the MgO-CO2-H2O system using ab initio thermodynamics. *Physical Chemistry Chemical Physics* **25**, (2023).

117. Long, Y. *et al.* High pressure effect in nanoporous carbon materials: Effects of pore geometry. *Colloids Surf A Physicochem Eng Asp* **437**, (2013).

118. Winnefeld, F., Epifania, E., Montagnaro, F. & Gartner, E. M. Further studies of the hydration of MgO-hydromagnesite blends. *Cem Concr Res* **126**, (2019).

119. Chaka, A. M. Ab Initio Thermodynamics and the Relationship between Octahedral Distortion, Lattice Structure, and Proton Substitution Defects in Malachite/Rosasite Group Endmember Pokrovskite Mg2CO3(OH)2. *Journal of Physical Chemistry A* **120**, (2016).

120. Giorgiosite Mineral data. https://webmineral.com/data/Giorgiosite.shtml.

121. Nguyen, H., Bernard, E., Winnefeld, F., Lothenbach, B. & Kinnunen, P. Synthesis and Thermodynamic Data of Acetate-Containing Giorgiosite – a Novel Hydrated Magnesium Carbonate. Preprint at https://doi.org/10.2139/ssrn.4952510 (2024).

122. Demichelis, R., Raiteri, P., Gale, J. D., Quigley, D. & Gebauer, D. Stable prenucleation mineral clusters are liquid-like ionic polymers. *Nat Commun* **2**, (2011).

CHAPTER 3
Unveiling the Role of Surface Chemistry of Alumina vs Silica Confinement in Magnesium Carbonate Polymorphism

1. Introduction

Understanding the behavior of carbon mineralization within nanoconfined environments is crucial for both geological sequestration and industrial applications. In particular, the typical mechanism of magnesium carbonate crystallization in bulk conditions is reported extensively [1–3] but the same crystallization mechanism in nanoconfined volumes is vastly different and unreported. The typical mineralization in ultramafic and mafic rocks involve the carbonate formation in the rock fractures and within the mineral matrix influencing the flow, reactivity and storage potential of CO_2 giving insights into its mineralization efficiency and technological deployment. [4,5]

During metal carbonate crystallization, a unique molecular mechanism involves the interaction of CO_2 or HCO_3^-, confined water films and solid surface chemistry, where delineating the mechanism is critical for preferential phase formation in respective conditions. Firstly, the interaction and reactivity of CO_2 differs significantly between bulk and nanoconfined systems due to thermodynamic and kinetic constraints. In bulk system, CO_2 is relatively inert requiring high temperature, pressure or the presence of additives to enhance the reactivity and mineral carbonation efficiency. [6,7] However, in nanoconfined systems, CO_2 is highly reactive in the presence of water interface enhancing the thermodynamics and kinetics due to altered dielectric constants, stronger solvation and enhanced proton transfer. [8,9] Secondly, the behavior of confined

water is vastly different from other fluids displaying enhanced diffusing in sub-nm pores, [10] variation in hydrogen bonding networks, [11,12] decrease in melting/freezing temperature, surface tension and density. [13] Lastly, the complex interplay of surface chemistry of confining nanopores in predicting and influencing the phase polymorph formation and transition is a crucial aspect. This phenomenon of modulating surface chemistry principles like adsorption, wetting, capillary action or surface charge polarity entirely regulates the shape and size of the final particle. Studying the surface chemistry of the nanopores unveil the characteristics of analyte transport facilitating preferential interactions in the solid-solid and solid-liquid interface. [14] Furthermore, the organization of ions and fluids in nanopores get influenced by surface phenomenon, facilitating distinct interfacial structure and dynamics. [15] Leveraging and associating the role of surface chemistry for carbon capture and mineral formation and experimentally interpreting the behavior and mechanism of nucleation in confined volumes has been of key interest and is predominantly crucial in the context of geological and engineered mineralization processes.

To elucidate the mechanism of magnesium carbonate crystallization in nanoconfined systems, it is crucial to take all these effects into consideration to determine the preferential phase formation under specific conditions. Prior literature has extensively studied the influence of various ions on the phase morphology during carbonate formation, where calcium carbonate (calcite) crystallization was inhibited by the presence of Mg^{2+} ions indicating a decrease in the crystal growth rate, [16] modifying the morphology and phase of calcium carbonate in the presence of seawater components like magnesium, potassium, sodium, sulfate and chloride ions and humic acid, [17]

observing the stack-like or rosette-like aggregates of (104) rhombohedra calcite in the presence of non-gelling and gelling biopolymers, [18] variation in the crystal morphology of calcium carbonate to form calcite, vaterite and aragonite in the presence of alumina, [19] alkaline or saline NaCl environment accelerating the dehydration of magnesium carbonate to form anhydrous magnesite. [20] To account for the effects of variation in surface properties on carbonate crystallization, it is observed that amorphous calcium carbonate is stabilized in hydrophobic conditions and stable calcite is precipitated in hydrophilic conditions when reacted in a packed bed system, [21] while calcium carbonate precipitated in the presence of dodecanoic acid results in rod-like and ellipse-like particles of calcite. [22]

Although prior literature provides key insights into the morphological changes of carbonate crystallization, these effects have been investigated in bulk fluids. It is primarily important to note the effects of surface chemistry, water dynamics and presence of various ions specifically on magnesium carbonate crystallization in confined volumes replicating natural CO_2 mineralization mechanisms. Elucidating the variation in surface material properties such as nanowall being alumina or silica, or being hydrophilic or hydrophobic, dictate the crystallization behavior and phase evolution of magnesium carbonate. For instance, alumina exhibits amphoteric behavior whereas silica contributes towards stronger or weaker interactions shifting the speciation, influencing the crystallization rate and morphology. [23,24] Further studies indicate that the presence of hydrophilic surface lowers the energy barrier for crystallization whereas the increase in intermolecular hydrogen bonding and ordering in hydrophobic surface increases, influencing magnesium carbonate crystallization. [25]

With the change in surface wettability, the inherent change in electrostatic charge of the nanowall is observed showcasing a slight negative potential in the presence of -OH groups while a higher negative potential in the presence of -COOH or -COR groups. [26–28] This combined effects of confinement and variation in surface chemistry leads to unique hydration kinetics and interaction among ions, ultimately affecting the final crystal formation mechanism and morphology of magnesium carbonate. [8,29]

Reaction kinetic measurements provide further insights into the role of surface chemistry on the stabilization and preferential phase formation deciphering reaction rates, mechanisms and surface mediated pathways. In nanoconfined systems, kinetics differ significantly from bulk systems due to spatial constraints, altered activation energies and enhanced collision frequencies. [30,31] To delve into understanding and delineating this response, mathematical interpretation of Johnson-Mehl-Avrami-Kolmogorov (JMAK) equation, also referred as Avrami equation, originally determined for phase formation, is used adapting to nanoconfined kinetics describing the nucleation and growth in isothermal conditions. [32] This equation is expressed as,

$$\theta = 1 - e^{-kt^n} \quad (1)$$

Where θ is the crystallinity, k is the reaction rate, n is the Avrami constant, and it is time. [33] By rearranging the equation (1) and applying logarithm on either side the equation changes to,

$$\ln(-\ln(1-\theta)) = lnk + nlnt \quad (2)$$

to identify the Avrami constant (n) and reaction rate (k). Values obtained from the Avrami constant (n) specifies the nucleation and growth rate where, n= 2.5, 2, 1.5 equate to 3-D, 2-D, and 1-D growth in sporadic nucleation system whereas n= 1.5, 1, 0.5 equate

to spherical, plate-like and needle growth in instantaneous nucleation system. [32] Prior studies reported that the Avrami constant decreases in nanoconfined conditions comparative to bulk systems indicating hindered nucleation. [34] The calculation of Avrami constant in a spherical domain showcase the decrease in value from 4 to 1 when transitioning from infinite to finite volume fraction indicating a slowing of transformation, [35] and similarly when poly(ethylene oxide) is confined in anodic alumina template the n<1 and in some case n=1-2 was seen, [36] while a study on block copolymer reports n value of 1.0 at high temperatures and 0.5 at lower ones transitioning from nucleation controlled to diffusion controlled. [37] Furthermore, one study explicitly states that confining tris(4-cumylphenol)-1,3,5-triazine in 50 nm pores decreases the Avrami exponent making the crystallization rate 30 times and 10 times slower at 80 ℃ and at temperature where crystallization is maximum in comparison to bulk solution. [34]

Taking all the surface chemistry, kinetics, and confinement effects into consideration, the current study focuses on delineating the magnesium carbonate crystallization in alumina and silica nanoconfinement having various pore sizes as shown in **Figure 16(a,b)**. Further, to test the evolution of different phases, the alumina and silica nanochannel membrane is functionalized to alter the surface wettability to hydrophobic. The introduction of magnesium carbonate into these nanochannels involved the use of 0.8M $Mg(NO_3)_2$. $6H_2O$ and 0.4M $NaHCO_3$ which are loaded using chemical vapor deposition technique (CVD) and aspiration and aged at 25 ℃ and 45 ℃. The crystal phase evolution is measured using X-ray diffraction (XRD) and the reaction kinetics of each evolved phase is determined using Avrami equation determining the dimension of growth and reaction rate. Lastly, to understand and probe

the behavior and motion of water in nanoconfined environment associated with magnesium carbonate, Quasi-elastic neutron scattering (QENS) measurements were performed determining the melting behavior, diffusion jump rate and mobility. This study outlines the variation in surface chemistry of nanochannels in determining the preferential formation of magnesium carbonate phases providing key applications in carbon capture and storage systems.

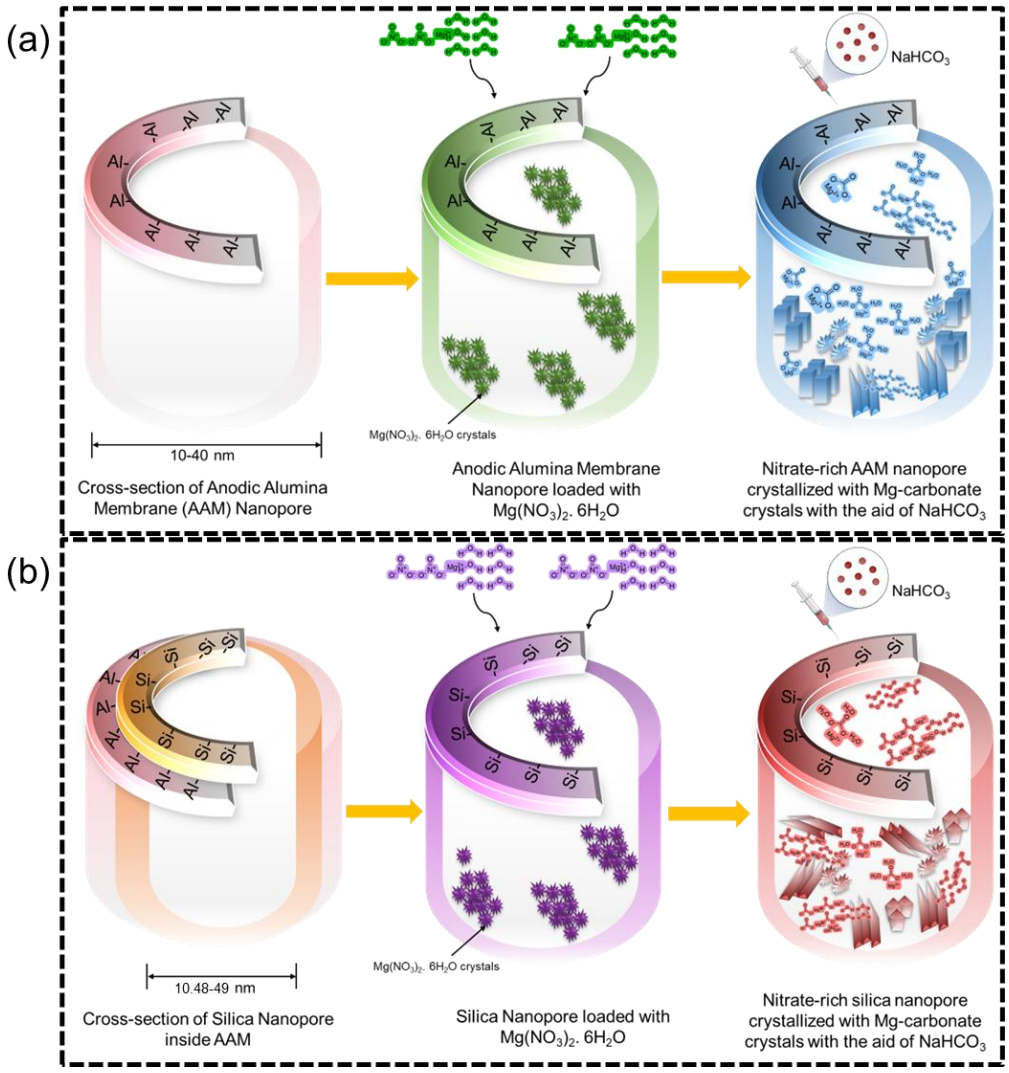

Figure 16 Schematic representation of the hierarchical crystallization of magnesium carbonate polymorphs inside (a) Anodic Alumina Membranes, and (b) Silica Nanopores

2. Experiments and Methodology

2.1 *Materials*

Anodic alumina membranes (AAM) acting as the alumina template having a pore size of 10 nm, and 40 nm were purchased from SPI® Supplies having diameter of 25 mm, a length of 50 μm. For synthesizing silica nanochannels (SNCs) inside a 200 nm AAM template with a diameter of 25 mm, purchased from Cytiva having trade name Whatman^{TM} Anodisc^{TM}, a precursor solution consisting of different molar compositions of PEG-PPG-PEG (P123) surfactant (Sigma Aldrich), anhydrous ethanol (C_2H_5OH) (Fischer Scientific, 96% v/v), hydrochloric acid (HCl) (Sigma Aldrich, 37% ACS reagent), and tetraethyl orthosilicate (TEOS) (Sigma Aldrich, 98% reagent grade) were utilized. For passing the precursor solution into the 200 nm AAM channels through aspiration, the membrane was placed on a 25 mm diameter, 50 mL capacity filter funnel which was purchased from Cytiva and used without any modification. To incorporate hydrophobicity, lauric acid ($C_{12}H_{24}O_2$) (Sigma Aldrich, FCC, FG, ≥ 98%), and anhydrous ethanol (C_2H_5OH) (Fischer Scientific, 96% v/v) were used.

For unfolding magnesium carbonate nucleation and crystallization, laboratory grade magnesium nitrate hexahydrate ($Mg(NO_3)_2$. $6H_2O$) (Sigma Aldrich, ACS Reagent 99%), and sodium bicarbonate ($NaHCO_3$) (Fischer Scientific, ACS Reagent 99%) powder were utilized. Deionized (DI) water (18.2 MΩ.cm) from the Milli-Q Q-POD® system was used in all experiments. All the chemical purchased from commercial vendors was utilized without any further modification.

2.2 *Synthesis of Silica Nanochannels inside AAM Membranes*

The synthesis of silica nanochannels follows a similar methodology where 1g of P123 was dissolved in a mixture of 19 mL ethanol, 84 µL of concentration HCl, and 2g of H_2O and stirred for 1 hour under reflux at 300 rpm. Once the surfactant gets dissolved completely, 2.28 mL of TEOS was added dropwise and the mixture was stirred at 400 rpm for 12 hours at 60 ℃ under reflux. For modifying the pore size of silica nanochannels, the composition of precursor solution was changed where 1g of P123 was dissolved in a mixture of 12.36 mL of ethanol, 84 µL of concentration HCl, and 2g of H_2O and stirred for 1 hour under reflux at 300 rpm. Then, 2.28 mL of TEOS was added dropwise and the mixture was stirred for 7 hours at 60 ℃ and 400 rpm under reflux. Once the solutions were prepared, they were passed through a 200 nm AAM placed on a filter funnel under aspiration. Each loading process consisted of 0.5 mL of the precursor solution permeating through the membrane and this step was repeated for 5 times to ensure all the pores are filled. To remove any excess silica precipitating on the surface, the membrane is washed with ethanol and aged for 24 hours. To remove the surfactant template from the nanochannels, the membranes were calcined at 550 °C for 4 hours at a ramp rate of 3 °C/min in a bench top muffle furnace (Thermo Scientific Thermolyne).

For distinguishing the different AAMs and SNCs, they will be denoted as X AAM and X SNC where X represents the pore size of anodic alumina membranes and silica nanochannels. The pore size for the AAMs is followed based on the information given by the manufacturer whereas the pore size distribution of silica nanochannels was identified from BET analysis. The BET analysis (Quantochrome AutoSorb iQ

Analyzer) requires at least 8 membranes which are outgassed at 130 ℃ for 24 hours and nonlocal density functional theory (NLDFT) model with N_2 adsorption at 77 K was considered for evaluation. The formation of different bonds during silica nanochannel synthesis is confirmed using FTIR (ThermoFisher Scientific) in the spectral range of 4000-400 cm^{-1}.

2.3 *Altering the Surface Wettability via Surface Functionalization and Measuring the Surface Charge of Anodic Alumina and Silica Nanochannels*

The surface alteration methodology was similar to the one reported where AAM membranes were rinsed with ethanol and water and dried at 85 °C for 30 minutes and then immersed in a solution of 20 g/L of lauric acid in ethanol and mixed at 120 rpm for 15 minutes at 50 °C. Later, the modified membranes were again rinsed with ethanol and dried at 85 °C for 30 minutes. For modifying the wettability of silica nanochannels, the rinsing and drying step were kept the same while the loading of lauric acid involved the chemical vapor deposition (CVD) technique. The membranes were immersed in a solution of 20 g/L of lauric acid in ethanol in a petri dish and the mixture was heated at 50 °C until all the solution evaporated. This procedure allows for the vapors of lauric acid to pass and attach to the walls of the silica nanochannels. The excess lauric acid precipitated on the surface of the membrane is rinsed using ethanol and dried at 85 °C for 30 minutes. The variation in surface wettability was measured using Ramé-Hart Contact Angle Goniometer 500 having a syringe volume of 250 μL, volume step of 10 μL, and droplet volume of 20 μL. The determination of surface charge for the

hydrophilic and hydrophobic membranes is performed using Malvern Nano ZS Zetasizer.

2.4 *Loading of Magnesium Nitrate and Sodium Bicarbonate Solutions in AAM and SNCs*

The as-purchased AAMs and the synthesized SNCs are inherently hydrophilic and for loading and allowing the nucleation of magnesium carbonate inside these channels, the membranes are immersed in 0.8M $Mg(NO_3)_2$. $6H_2O$ solution and heated at 80 °C until all the liquid has evaporated. This loading technique follows chemical vapor deposition (CVD) model allowing for nitrate ions to stick to the walls of the nanochannels. To remove any excess nitrate precipitation on the surface of the membrane, DI water is splashed dropwise and the membrane is dried at 85 °C for 30 minutes. Later, the magnesium-nitrate rich AAM and SNC nanochannel membranes are placed in an aspiration setup and 0.5 mL of 0.4M $NaHCO_3$ is passed through them. This step was repeat 3 times and the nitrate and bicarbonate loaded membranes are allowed to age at 25 °C. For deciphering the influence of temperature on the carbonate polymorph induction and evolution, the nitrate and bicarbonate loaded membrane is immediately transferred into a vacuum oven (Thermo Scientific Lindberg Blue M) and allowed for the reaction to proceed at 45 °C for 15 minutes and the rest of the aging is performed at 25 °C.

The loading of 0.8M $Mg(NO_3)_2$. $6H_2O$ and 0.4M $NaHCO_3$ is slightly different in hydrophobic membrane completely employing aspiration technique. For initiating

magnesium carbonate crystallization, 1 mL of $Mg(NO_3)_2$. $6H_2O$ and $NaHCO_3$ were passed through the AAM and SNC membranes sequentially and this process was repeat 3 times. Once the loading is completed, the nitrate and bicarbonate loaded membranes are allowed to age at 25 °C. Similar to the hydrophilic membranes, hydrophobic membranes are also transferred immediately into a vacuum oven after loading and allowed for the reaction to proceed at 45 °C for 15 minutes and the rest at 25 °C to interpret the temperature effects.

X-ray diffraction (XRD) measurement was performed using Bruker D8 Advance ECO Powder diffractometer having a Cu Kα radiation, operating voltage of 40 kV, and current of 25 mA, for evaluating the phase formation and transition over time from 6 hours to 96 hours after loading in both hydrophilic and hydrophobic AAM and SNC membranes. To further understand the polymorph transition in nanoconfinement, reaction kinetic studies were performed following the Avrami model which is considered for an isothermal and heterogenous crystallization system. To calculate the transformed fraction of crystallinity (θ), the peak area under the XRD curves are determined associating with each distinct phase. Once the peak areas are noted, all the values for each distinct phase are added together to get the aggregate number. These values are then plugged into the Avrami equation which is as follows,

$$1 - \theta = \frac{I_f - I_t}{I_f - I_o} = e^{-kt^n} \quad (3)$$

Where I_f is the levelling off peak area, I_t is the peak area at time t, I_o is the peak area at time zero which is 0 for a non-crystalline or amorphous sample. [33] This relation is used to determine Avrami exponent and the rate constant giving insights into interfacial growth and diffusion-controlled growth. [32]

2.5 *Quasi-Elastic Neutron Scattering (QENS) for Confined Water in Pure and Mg-Carbonate loaded Systems*

Quasi-Elastic Neutron Scattering (QENS) measurements were performed at a backscattering spectrometer (BASIS) [38] at the Spallation Neutron Source (SNS), Oak Ridge National Laboratory. These measurements focused on examining the dynamics of confined water within 10.48 nm silica nanochannel having both hydrophilic and hydrophobic character loaded with pure water and magnesium carbonate. For these measurements, the loaded membranes were arranged in a 1 mm thick, 5 cm tall, 3 cm wide flat plate aluminum sample holder, positioned perpendicular to the incident neutron beam. To reach the optimal sample thickness for neutron measurements, a stack of 15 pure water and carbonate-loaded membranes are stacked on top of each other. BASIS was operated with its chopper system set to 60 Hz, with the incident bandwidth centered at a wavelength $\lambda = 6.4$ Å. The detectors count rate was about 80 counts/sec at 1.7 MW of proton beam power to the neutron-producing target.

Initial QENS measurements were performed at 298 K on the hydrophilic SNC membranes containing pure water. These were followed by cooling the sample to 10 K to collect the resolution function and to conduct temperature-dependent elastic intensity scans ranging from 20 K to 320 K. This same sequence was applied for measuring the pure water in hydrophobic SNC system.

For magnesium carbonate loaded membranes, this sequential approach was modified due to concerns that repeated thermal cycling could potentially trigger chemical

reactions in the sample. To avoid this, two identical samples were prepared for each magnesium carbonate condition: one being solely used for temperature dependent elastic scans (20K to 320K) and the other for QENS measurements at 298 K followed by a resolution spectrum collection at 10 K. Lastly, to correct for background contributions from the aluminum sample holder, a control measurement was carried out at 298 K using an empty holder replicating experimental conditions.

3. Results and Discussions

3.1 *Surface Composition, Pore Size, Wettability, and Electrostatic Charge of Silica Nanochannels*

The architected silica nanochannels follow the sol-gel approach equating with the effects of water hydrolysis, alcohol condensation and the assembly of surfactants influencing the morphology and colloidal stability of the dispersion in the precursor solution. [39,40] These mechanisms were leveraged in the current study by changing the concentrations of the precursor solution and passing through the 200 nm AAM via aspiration to achieve different pore size silica nanochannels. Once the calcining step is completed to remove the surfactant, the surface composition of the SNCs is confirmed by analyzing under FTIR to examine the structure and the type of bonds. As reported in Mamidala, A (Chapter 4), the silica nanochannels consists of Si-O-Si antisymmetric stretching, Si-O stretching associated with Si-OH, Si-O-Si asymmetric stretching and O-H bending. For measuring the pore size of the silica nanochannels, BET analysis was performed where 8 membranes were contained inside a BET glass tube. Initially, the

membranes were outgassed at 130 ℃ for 24 hours to remove any residual moisture. Once the outgassing is completed, the BET analysis is performed in a liquid N_2 environment at 77 K performing adsorption and desorption studies. To measure the pore size, the nonlocal density functional theory (NLDFT) model for adsorption was considered. The BET data indicates that the silica nanochannel synthesized by using precursor solution consisting of 19 mL and 12.36 mL ethanol had a pore size of 10.48 nm and 49.09 nm.

3.2 *Wettability, and Electrostatic Charge of Anodic Alumina Membrane and Silica Nanochannels*

The alteration in surface wettability from hydrophilic to hydrophobic follows the similar procedure as reported in Mamidala, A (Chapter 4), where lauric acid in ethanol is functionalized to the walls of the anodic alumina and silica nanochannel surfaces. Once these nanochannels are functionalized, to test the extent of hydrophobicity, contact angle measurement was performed. For hydrophilic alumina and silica nanochannel loaded alumina membrane, the contact angle decreases as the pore size increases which can be attributed to reduction in air pockets, increase in liquid penetration or the presence of silanol groups, enhancing water adsorption. [41–43] In hydrophobic membranes, similar characteristic is observed where contact angle decreases as pore size increases and the key parameter influencing is solution adsorption and diffusion. [44,45] It is observed that smaller pores tend to adsorb and diffuse lauric acid faster than larger pores inclining towards increased contact angle. [44–46]

While the surface interaction between solid-liquid interface is determined, the electrostatic charge is determined using Zeta Sizer giving insights into the transport and reactivity of ions, and the thickness of water film in nanoconfinement. [47–49] The electrostatic charges indicate that the surface is more negative for hydrophobic AAM and SNC conditions than hydrophilic due to negative ester bond. [26,27,50] Furthermore, silica nanochannels display higher negative surface charge than alumina nanochannels which is inherently due to Si-O linkages. [51–55]

3.3 *Magnesium Carbonate Crystallization in Nanoconfined AAMs and SNCs*

Precipitation and crystallization of magnesium carbonate involves loading 0.8M $Mg(NO_3)_2$. $6H_2O$ and 0.4M $NaHCO_3$ passed through 10 nm and 40 nm AAM pores as shown in **Figure 17**. For hydrophilic membranes, initially the magnesium nitrate hexahydrate is passed through the channels using CVD method after which sodium bicarbonate solution is passed through the nitrate-rich pores via aspiration whereas for hydrophobic membranes, magnesium nitrate hexahydrate and sodium bicarbonate are passed through the nanochannels sequentially through aspiration to enable magnesium carbonate crystallization. From the XRD results we can deduce that in 10 nm hydrophilic AAMs, dominant growth of (012), and (104) plane of magnesite ($MgCO_3$); (202), (204), (113), (103), and (004) plane of nesquehonite ($MgCO_3$. $3H_2O$); (202), (113), (112), (100), and (222) plane of lansfordite ($MgCO_3$. $5H_2O$); and (100), (014), (211), and (020) plane of hydromagnesite ($Mg_5(CO_3)_4(OH)_2$. $4H_2O$) were observed while in 40 nm hydrophilic AAMs, dominant growth of (110), (211), and (212) plane

of nesquehonite; (002), and (122) plane of lansfordite; and (610), and (402) plane of hydromagnesite were observed at both 25 ℃ and 45 ℃. Similarly, the dominant planes of growth in 10 nm hydrophobic AAMs are (311), and (202) plane of nesquehonite; (201), and (211) plane of pokrovskite ($Mg_2(CO_3)(OH)_2$. $0.5H_2O$); (331), (320), and (023) plane of hydromagnesite; (202), (112), (121), and (211) plane of lansfordite; and (111) plane of artinite ($Mg_2(CO_3)(OH)_2$. $3H_2O$) while in 40 nm hydrophobic AAMs, dominant growth of (202), (004), and (013) plane of nesquehonite; (200), (412), (222), and (321) plane of hydromagnesite; and (111), and (220) plane of lansfordite were observed at both 25 ℃ and 45 ℃.

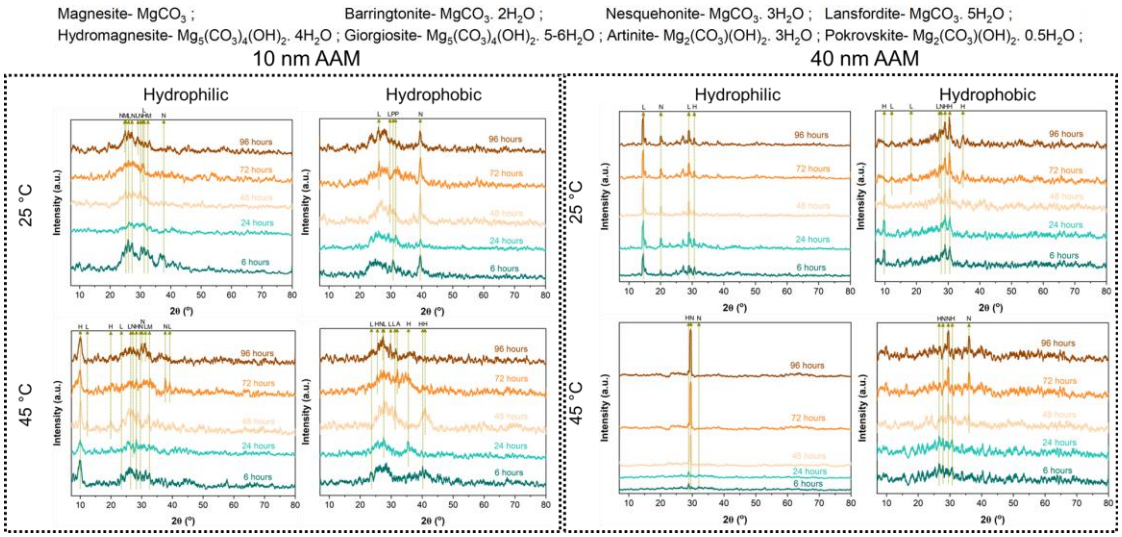

Figure 17 X-ray diffraction (XRD) measurements of magnesium carbonate evolution in anodic alumina membrane having pore size of 10 nm, and 40 nm, with varied reaction temperature and surface wettability from 6 hours to 96 hours after loading.

Precipitation and crystallization of magnesium carbonate involved slightly different polymorphs and plane orientations when confined in silica nanochannels as shown in **Figure 18**. In the 10.48 nm hydrophilic SNCs, from XRD the dominant growth of (004), (202), (211), and (210) plane of nesquehonite; (321), (313), (412), and (610)

plane of hydromagnesite; (301), and (201) plane of barringtonite ($MgCO_3$. $2H_2O$); and (021), and (032) plane of lansfordite were observed while dominant growth in 49 nm hydrophilic SNCs are (210), (213), (103) and (012) plane of nesquehonite; (412), (212), (222), (321), (600), and (430) plane of hydromagnesite; (201), and (301) plane of barringtonite; and (211) plane of lansfordite were observed at both 25 ℃ and 45 ℃. Similarly, in 10.48 nm hydrophobic SNCs, the dominant growth of (110), and (002) plane of nesquehonite; (200), (410), (412), (222), and (313) plane of hydromagnesite; (002), and (112) plane of lansfordite; and (201), (210), and (100) plane of barringtonite were observed while in 49 nm hydrophobic SNCs, the dominant growth of (012), (110), (004), and (113) plane of nesquehonite; (021), (521), (040), (002), (333), and (412) plane of hydromagnesite; (200), (120), and (113) plane of lansfordite; and (100), (001), and (101) plane of barringtonite were observed at both 25 ℃ and 45 ℃.

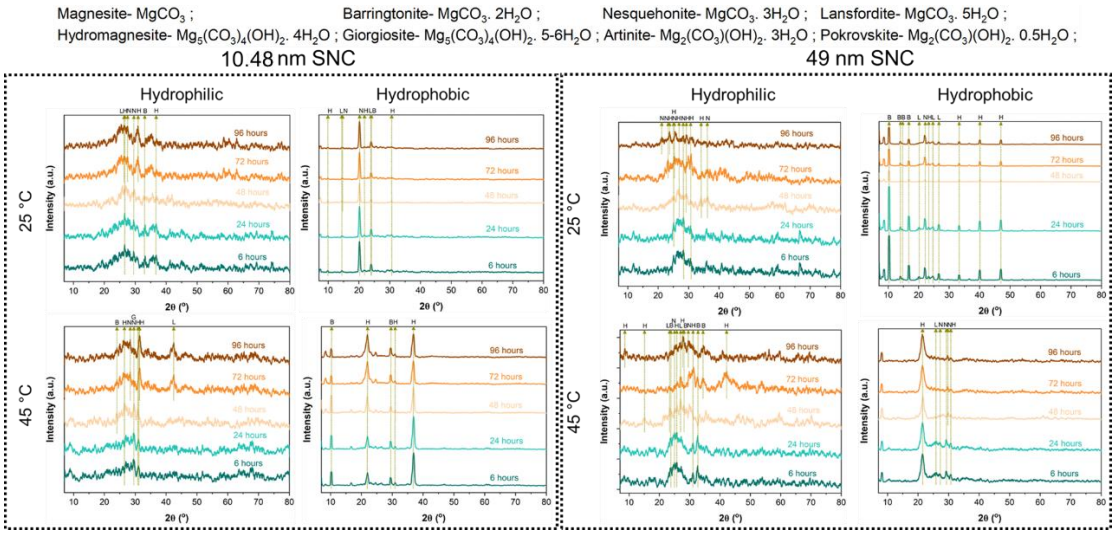

Figure 18 X-ray diffraction (XRD) measurements of magnesium carbonate evolution in silica nanochannels having pore size of 10.48 nm, and 49 nm, with varied reaction temperature and surface wettability from 6 hours to 96 hours after loading.

3.4 *Evolution and Phase Composition of the Respective Magnesium Carbonate Polymorphs Confined in Anodic Alumina and Silica Nanochannels*

The XRD peaks clearly indicate the formation of different planes and anisotropic growth in the respective nanoconfined environments, and the quantitative weight % has been calculated using the Rietveld method as shown in **Figure 19**. In the 10 nm hydrophilic AAMs, the initial observation is the formation of anhydrous $MgCO_3$, $MgCO_3$. $3H_2O$, $MgCO_3$. $5H_2O$, and $Mg_5(CO_3)_4(OH)_2$. $4H_2O$ in both 25 and 45 ℃. Crystallization at 25 ℃ indicate the predominant presence of hydrated magnesium carbonate phases ($MgCO_3$. $3H_2O$, and $MgCO_3$. $5H_2O$), while the stability of hydroxyl-containing complex phase ($Mg_5(CO_3)_4(OH)_2$. $4H_2O$) and anhydrous $MgCO_3$ is less associated with the requirement of higher energy barrier. [20] Furthermore, the predominance of $MgCO_3$. $5H_2O$ is significant attributing to the role of HCO_3^- ions assisting its formation due to steric effects and the transition moves towards other stable phases. [56] Crystallization at 45 ℃ promote the stability of anhydrous $MgCO_3$ and ($Mg_5(CO_3)_4(OH)_2$. $4H_2O$) and a consistent transition from $MgCO_3$. $5H_2O$ and $MgCO_3$. $3H_2O$. This experimental result clearly follows data reported in Mamidala, A, et al (Chapter 2), where maximum coordination from non-water species is seen in hydrophilic alumina at 45 ℃ favoring anhydrous $MgCO_3$ crystallization. Further, the stability of hydroxyl-containing complex and anhydrous phase is dependent on the temperature effects overcoming the energy barrier. The role of confinement also impacts the formation and stabilization of anhydrous phase, associated with the compression and merging of solvation layers enhancing dehydration, [57] which is observed in 10 nm AAM pores. In 40 nm hydrophilic AAMs, $MgCO_3$. $3H_2O$, $MgCO_3$. $5H_2O$, and $Mg_5(CO_3)_4(OH)_2$. $4H_2O$ is observed at 25

and 45 ℃. Both the systems clearly indicate following the bulk transition mechanism of evolving from less stable phase to more stable phase.

In relation to magnesium carbonate phase polymorphism in hydrophobic AAM conditions, the predominant hydrated magnesium carbonate phases are $MgCO_3.\ 3H_2O$, $MgCO_3.\ 5H_2O$, $Mg_5(CO_3)_4(OH)_2.\ 4H_2O$, $Mg_2(CO_3)(OH)_2.\ 3H_2O$, and $Mg_2(CO_3)(OH)_2.\ 0.5H_2O$. In the hydrophobic AAM conditions, there is an absence of anhydrous phase due to the formation of clatharate-like structure of water trapping the Mg^{2+} ions, making it very difficult for phase dehydration. [58–62, Mamidala,A (Chapter 2)] In 10 nm hydrophobic AAMs aged at 25 ℃, we observe the phase formation of $MgCO_3.\ 3H_2O$, and $Mg_2(CO_3)(OH)_2.\ 0.5H_2O$ and as the reaction time increases the transition of $Mg_2(CO_3)(OH)_2.\ 0.5H_2O$ to $MgCO_3.\ 5H_2O$ is noted. Further, the crystallization and reprecipitation of $MgCO_3.\ 5H_2O$ is observed which could be attributed to the steric effect of HCO_3^- ions in the preferential formation. [56] Same membranes when aged at 45 ℃ display the formation of $MgCO_3.\ 3H_2O$, $MgCO_3.\ 5H_2O$, $Mg_5(CO_3)_4(OH)_2.\ 4H_2O$, and $Mg_2(CO_3)(OH)_2.\ 3H_2O$. Initially we observed the formation of $MgCO_3.\ 5H_2O$, and $Mg_5(CO_3)_4(OH)_2.\ 4H_2O$ and as the reaction ages, the increase in $Mg_5(CO_3)_4(OH)_2.\ 4H_2O$ is seen. Later, a non-linear phase transition is seen with the formation of $Mg_2(CO_3)(OH)_2.\ 3H_2O$ and the complete disappearance of $Mg_5(CO_3)_4(OH)_2.\ 4H_2O$. This non-linear phase evolution and the preferential formation of $MgCO_3.\ 3H_2O$ and $MgCO_3.\ 5H_2O$ could be attributed to the intermolecular hydrogen bonding and spatial orientation necessitation higher energy to overcome the barrier. [Mamidala,A (Chapter 2)] In 40 nm hydrophobic AAMs, the phase evolution and transition of $MgCO_3.\ 3H_2O$, $MgCO_3.\ 5H_2O$, and $Mg_5(CO_3)_4(OH)_2.\ 4H_2O$ is observed at 25 ℃ and 45 ℃. This linear and

stable transition could be attributed to the increased pore size effects offering more bulk-like behavior while lessening the nanowall surface effects.

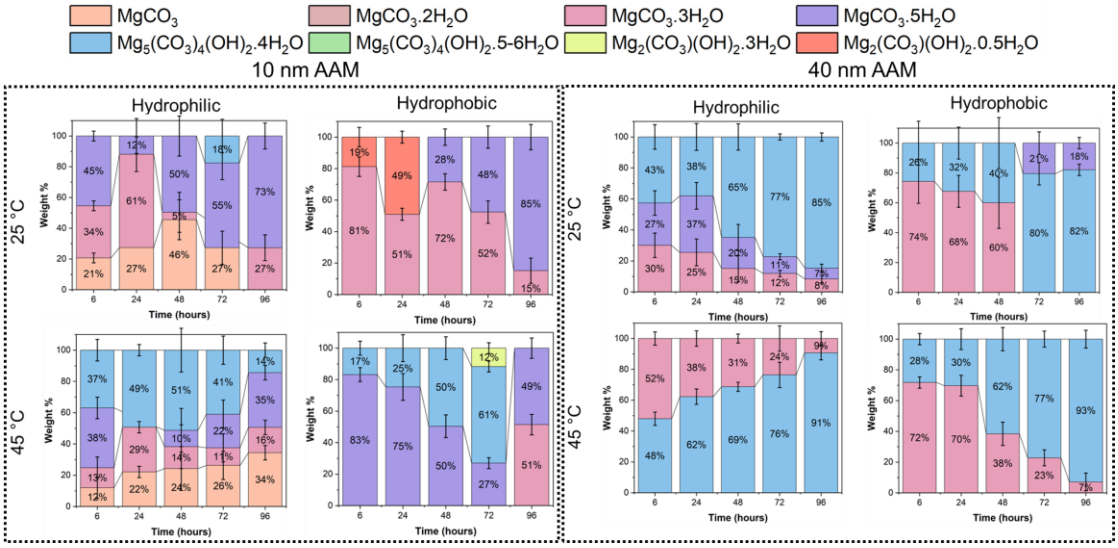

Figure 19 Phase polymorphism of magnesium carbonate in anodic alumina membrane of varied pore size, reaction temperature and surface wettability from 6 hours to 96 hours after loading.

The influence of silica nanochannels amplifies the preferential formation of respective polymorphs in various physicochemical conditions which were observed through XRD as shown in **Figure 20**. In 10.48 nm hydrophilic SNCs, the predominant phases formed initially at 25 ℃ are $MgCO_3.2H_2O$, $MgCO_3.3H_2O$, and $Mg_5(CO_3)_4(OH)_2.4H_2O$ and as the reaction aging increases, we observed a non-monotonic evolution of $MgCO_3.2H_2O$, $MgCO_3.3H_2O$, $MgCO_3.5H_2O$, and $Mg_5(CO_3)_4(OH)_2.4H_2O$. The phase of $MgCO_3.2H_2O$ might transition into $MgCO_3.3H_2O$ representing the opposite of the bulk phase transition attributing to the increased stability and preferential formation of $MgCO_3.3H_2O$ in the presence of silica which lowers the energy barrier for its nucleation [63], or $MgCO_3.2H_2O$ might transition into $Mg_5(CO_3)_4(OH)_2.4H_2O$ following bulk transition. [64] As the ageing time advances, the appearance of $MgCO_3.5H_2O$ is seen attributing to the steric effect of HCO_3^- ions.

Temperature effects played a crucial role when the membrane was aged at 45 ℃ advancing the evolution of $MgCO_3$. $3H_2O$, $Mg_5(CO_3)_4(OH)_2$. $4H_2O$ and unstable $Mg_5(CO_3)_4(OH)_2$. $5\text{-}6H_2O$. As the ageing time moves to 48 hours, the transition of $Mg_5(CO_3)_4(OH)_2$. $5\text{-}6H_2O$ into $Mg_5(CO_3)_4(OH)_2$. $4H_2O$ is observed while $MgCO_3$. $3H_2O$ into $MgCO_3$. $2H_2O$. [65,66] This transition follows bulk-like behavior but these phases again recrystallize back into $MgCO_3$. $3H_2O$ and $MgCO_3$. $5H_2O$ attributing to either the limited reactant supply lowering the super saturation and preferring the formation of low energy required phases or the role of water in facilitating the nucleation process. [67] In 49 nm hydrophilic SNCs, a clear transition of $MgCO_3$. $3H_2O$ into $Mg_5(CO_3)_4(OH)_2$. $4H_2O$ is observed at 25 ℃ whereas the reaction at 45 ℃ displayed an initial transition of $MgCO_3$. $3H_2O$ and $MgCO_3$. $2H_2O$ into $Mg_5(CO_3)_4(OH)_2$. $4H_2O$. At an intermediate reaction time point of 48 hours after loading, $MgCO_3$. $5H_2O$ emerges and dissolves finally transition into $MgCO_3$. $2H_2O$ and $Mg_5(CO_3)_4(OH)_2$. $4H_2O$. In this system, a non-linear evolution of $MgCO_3$. $3H_2O$ is observed which might be due to the presence of silica nanochannels.

Magnesium carbonate polymorphism with respect to hydrophobic silica nanochannels clearly indicate a bulk-like transition in various physicochemical conditions. In 10.48 nm hydrophobic SNCs, we observe the initial formation of $MgCO_3$. $3H_2O$, $MgCO_3$. $5H_2O$, and $Mg_5(CO_3)_4(OH)_2$. $4H_2O$ at 25 ℃. The transition of $MgCO_3$. $5H_2O \rightarrow MgCO_3$. $3H_2O \rightarrow Mg_5(CO_3)_4(OH)_2$. $4H_2O$ is noted till 48 hours and after this time interval, the transition pathway is altered with the transition of $MgCO_3$. $3H_2O \rightarrow MgCO_3$. $2H_2O \rightarrow Mg_5(CO_3)_4(OH)_2$. $4H_2O$. When the aging temperature is increased to 45 ℃, the transition becomes much more linear from $MgCO_3$. $2H_2O$ into

$Mg_5(CO_3)_4(OH)_2.4H_2O$ indicating that the increase in reaction temperature aided in overcoming the energy barrier and stabilizing. In 49 nm hydrophobic SNCs, the transition pathway of $MgCO_3.5H_2O$ → $MgCO_3.3H_2O$ → $MgCO_3.2H_2O$ → $Mg_5(CO_3)_4(OH)_2.4H_2O$ is observed at 25 °C whereas the transition of $MgCO_3.5H_2O$ → $MgCO_3.3H_2O$ → $Mg_5(CO_3)_4(OH)_2.4H_2O$ is noted at 45 °C. Overall, we can perceive that in hydrophobic silica nanochannels, $Mg_5(CO_3)_4(OH)_2.4H_2O$ is preferred irrespective of pore size or reaction ageing temperature.

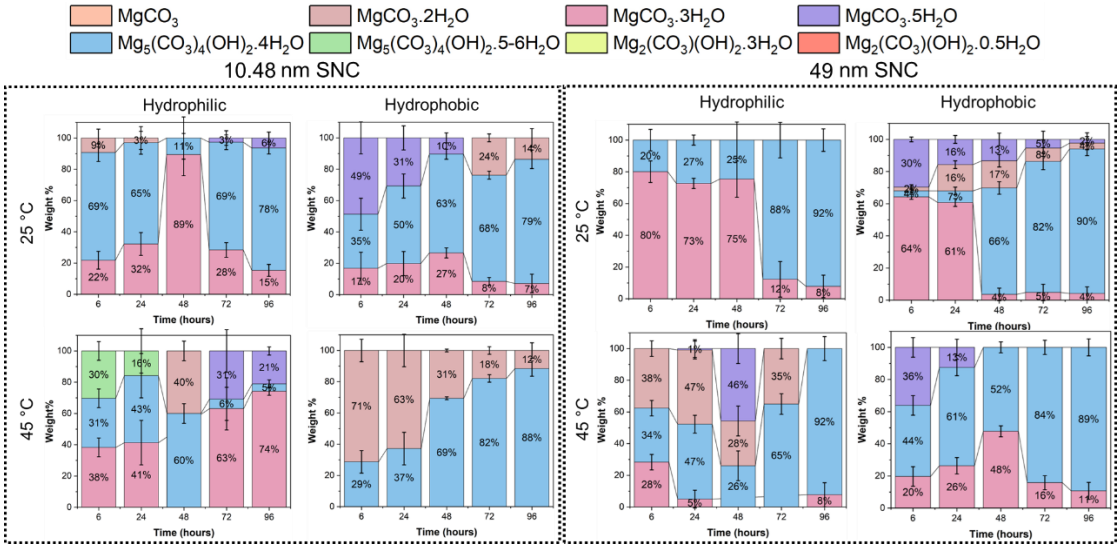

Figure 20 Phase polymorphism of magnesium carbonate in silica nanochannels of varied pore size, reaction temperature and surface wettability from 6 hours to 96 hours after loading.

3.5 *Crystal Growth and Nucleation Rate of Magnesium Carbonate Phases Identified from Reaction Kinetics In Nanoconfined Systems*

Reaction kinetics measured from Avrami equation provides insights into the nucleation and growth of materials, wherein the current analysis focus on understanding the nucleation and dimensionality of crystal growth through determining Avrami constant

(n), and rate constant (k) in nanoconfined volumes. In determining n and k, the area under the curve from XRD data was determined for the respective phases and these values are plugged-in the Avrami equation. The kinetic data from 10 nm hydrophilic and hydrophobic AAMs at 25 and 45 ℃ presented in **Table 4** as shown in **Figure 21(a)** reveal the Avrami constant (n) and rate constant (k) as,

Table 4 Determining the Avrami and rate constant for various Mg-carbonate polymorphs loaded in 10 nm AAMs

Confined System Conditions	**Phases**	**Avrami Constant (n)**	**Rate Constant (k)**
10 nm Hydrophilic AAM-25 ℃	$MgCO_3$	0.52859 ± 0.33555	0.0089
	$MgCO_3.3H_2O$	0.34981 ± 0.18175	0.027895218
	$MgCO_3.5H_2O$	0.53526 ± 0.48811	0.006921588
10 nm Hydrophilic AAM- 45 ℃	$MgCO_3$	0.71883 ± 0.2997	0.00453
	$MgCO_3.3H_2O$	0.21975 ± 0.07048	0.2333
	$MgCO_3.5H_2O$	0.15849 ± 0.01004	0.7742
	$Mg_5(CO_3)_4(OH)_2.4H_2O$	0.11146 ± 0.03023	0.3459
10 nm Hydrophobic AAM- 25 ℃	$MgCO_3.3H_2O$	0.77047 ± 0.98948	0.00167559
	$MgCO_3.5H_2O$	1.40994 ± 0	$6.35671*10^{-6}$

10 nm Hydrophobic AAM- 45 ℃	$MgCO_3$. $5H_2O$ $Mg_5(CO_3)_4(OH)_2$. $4H_2O$	1.32579 ± 0.4894 0.31178 ± 0.03012	$3.03413*10^{-5}$ 0.02208

From the given kinetic data we can deduce that in hydrophilic conditions at 25 ℃, $MgCO_3$, $MgCO_3$. $3H_2O$ and $MgCO_3$. $5H_2O$ display very slow nucleation with diffusion-controlled growth while confirming 1-D or needle-like growth. [32] In hydrophilic condition at 45 ℃, $MgCO_3$ indicate slightly higher n hinting at improved nucleation with respect to 25 ℃ condition whereas $MgCO_3$. $3H_2O$, $MgCO_3$. $5H_2O$, and $Mg_5(CO_3)_4(OH)_2$. $4H_2O$ display very low n values suggesting very slow nucleation or kinetic trapping. The reaction constant k for $MgCO_3$. $3H_2O$, $MgCO_3$. $5H_2O$, and $Mg_5(CO_3)_4(OH)_2$. $4H_2O$ indicate a different behavior where the growth kinetics rapidly increase at 45 ℃ vs 25 ℃ conditions. In hydrophobic conditions at 25 ℃, $MgCO_3$. $3H_2O$ indicate a slightly better nucleation vs hydrophilic conditions suggesting 1-D growth whereas $MgCO_3$. $5H_2O$ indicate high n value corresponding with 2-D or spherical growth. [32] In hydrophobic conditions at 45 ℃, $MgCO_3$. $5H_2O$ display fast higher dimensional growth whereas $Mg_5(CO_3)_4(OH)_2$. $4H_2O$ indicate slow. The kinetics of $MgCO_3$. $3H_2O$, $MgCO_3$. $5H_2O$, and $Mg_5(CO_3)_4(OH)_2$. $4H_2O$ indicate very slow growth in hydrophobic conditions. In conclusion, $MgCO_3$ showed dimensional growth in hydrophilic conditions as temperature increased whereas $MgCO_3$. $3H_2O$, and $MgCO_3$. $5H_2O$ showed very slow kinetics in hydrophobic conditions at 25 and 45 ℃.

The reaction kinetics of magnesium carbonate phases nucleated and crystallized in 40 nm AAM as shown in **Figure 21(b)** is vastly different as shown in the **Table 5**,

Table 5 Determining the Avrami and rate constant for various Mg-carbonate polymorphs loaded in 40 nm AAMs

Confined System Conditions	**Phases**	**Avrami Constant (n)**	**Rate Constant (k)**
40 nm Hydrophilic AAM-25 ℃	$MgCO_3.\ 3H_2O$ $MgCO_3.\ 5H_2O$ $Mg_5(CO_3)_4(OH)_2.\ 4H_2O$	0.76236 ± 0.20475 0.56165 ± 0.16199 0.19134 ± 0.01787	0.003145 0.022239173 0.236475659
40 nm Hydrophilic AAM- 45 ℃	$MgCO_3.\ 3H_2O$ $Mg_5(CO_3)_4(OH)_2.\ 4H_2O$	1.58537 ± 0.55691 0.16356 ± 0.07178	$2.31442*10^{-6}$ 0.182116261
40 nm Hydrophobic AAM- 25 ℃	$MgCO_3.\ 3H_2O$ $Mg_5(CO_3)_4(OH)_2.\ 4H_2O$	0.05423 ± 0 0.22686 ± 0.07706	0.331376529 0.131988564
40 nm Hydrophobic AAM- 45 ℃	$MgCO_3.\ 3H_2O$ $Mg_5(CO_3)_4(OH)_2.\ 4H_2O$	0.35441 ± 0.256 0.61646 ± 0.04029	0.121837145 0.021276119

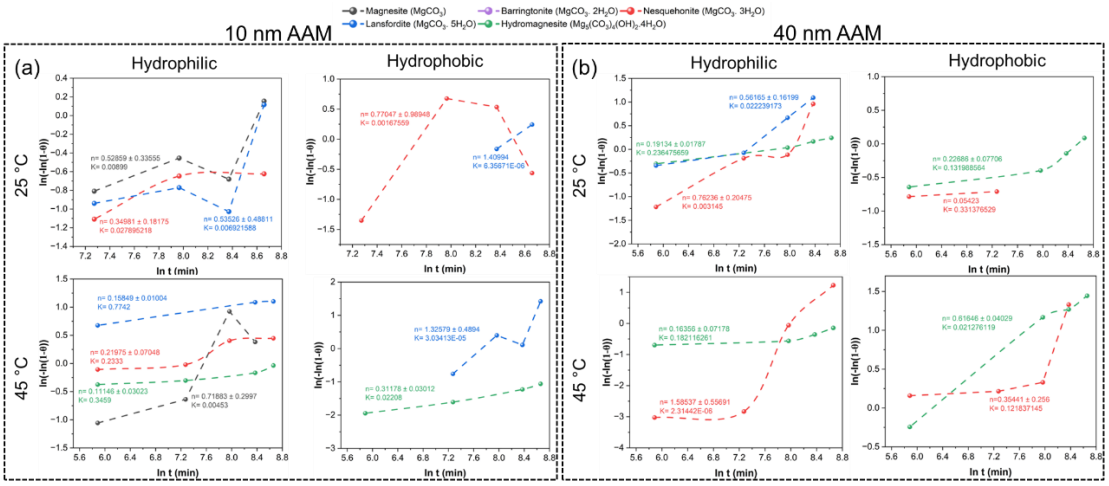

Figure 21 Determining the dimensional growth and nucleation rate of magnesium carbonate phases using Avrami equation in (a) 10 nm alumina membrane, (b) 40 nm alumina membrane at varied reaction temperature and surface wettability

The kinetic data indicates that in hydrophilic condition at 25 ℃, $MgCO_3$. $3H_2O$ display a 1-D growth, while $MgCO_3$. $5H_2O$ indicate average growth, and $Mg_5(CO_3)_4(OH)_2$. $4H_2O$ indicate very slow growth. In hydrophilic condition at 45 ℃, $MgCO_3$. $3H_2O$ display 2-D growth which could be caused due to influence of temperature, while $Mg_5(CO_3)_4(OH)_2$. $4H_2O$ showcase very slow growth. With regards to kinetics, $MgCO_3$. $3H_2O$, $MgCO_3$. $5H_2O$, and $Mg_5(CO_3)_4(OH)_2$. $4H_2O$ indicate very slow kinetics with increasing reaction temperature. In hydrophobic condition at 25 ℃, $MgCO_3$. $3H_2O$ display slow kinetics while $Mg_5(CO_3)_4(OH)_2$. $4H_2O$ display a much slower kinetics. In hydrophobic conditions at 45 ℃, $MgCO_3$. $3H_2O$ and $Mg_5(CO_3)_4(OH)_2$. $4H_2O$ display further reduced kinetics while the same polymorphs displays higher dimensional 1-D growth attributing to temperature effects. The overall insights from 40 nm AAM pores vs 10 nm AAM pores is that the nucleation, and crystallization becomes slower in hydrophilic conditions while growth of the crystal either becomes more uniform or multidimensional. In hydrophobic conditions, the nucleation, crystallization, and

growth become faster as the pore size increases from 10 nm to 40 nm attributing to translocation in large nanopores. [68]

Subsequently, the reaction kinetics of magnesium carbonate polymorphs in silica nanochannels indicate a wide range of nucleation and dimensional growth with respect to respective physicochemical conditions. This nucleation and growth is presented in **Table 6** and as shown in **Figure 22(a)** as,

Table 6 Determining the Avrami and rate constant for various Mg-carbonate polymorphs loaded in 10.48 nm SNCs

Confined System Conditions	**Phases**	**Avrami Constant (n)**	**Rate Constant (k)**
10.48 nm Hydrophilic SNC-25 ℃	$MgCO_3.\ 3H_2O$ $Mg_5(CO_3)_4(OH)_2.\ 4H_2O$	0.29603 ± 0.19573 0.34089 ± 0.14732	0.079218137 0.065219942
10.48 nm Hydrophilic SNC- 45 ℃	$MgCO_3.\ 3H_2O$ $Mg_5(CO_3)_4(OH)_2.\ 4H_2O$	0.89003 ± 0.58034 0.68919 ± 0.29039	0.001093119 0.006996257
10.48 nm Hydrophobic SNC- 25 ℃	$MgCO_3.\ 3H_2O$ $MgCO_3.\ 5H_2O$ $Mg_5(CO_3)_4(OH)_2.\ 4H_2O$	0.38137 ± 0.12905 0.28617 ± 0 0.09112 ± 0.2861	0.085894971 0.175537954 0.705541278

10.48 nm Hydrophobic SNC- 45 ℃	$MgCO_3$. $2H_2O$ $Mg_5(CO_3)_4(OH)_2$. $4H_2O$	0.11925 ± 0.04247 0.49528 ± 0.19234	0.15131977 0.02911971

The kinetic data indicating the nucleation and growth determine that in hydrophilic condition at 25 ℃, the growth and crystallization rate is very slow for both $MgCO_3$. $3H_2O$, and $Mg_5(CO_3)_4(OH)_2$. $4H_2O$ attributing to strong confinement restricting the water and ion diffusion [69] whereas in hydrophilic condition at 45 ℃, $MgCO_3$. $3H_2O$, and $Mg_5(CO_3)_4(OH)_2$. $4H_2O$ indicate further decelerated nucleation and but higher growth influenced by higher temperature. In hydrophobic condition at 25 ℃, $MgCO_3$. $3H_2O$, and $MgCO_3$. $5H_2O$ show similar slow kinetics and growth whereas $Mg_5(CO_3)_4(OH)_2$. $4H_2O$ display faster kinetics. In hydrophobic condition at 45 ℃, $MgCO_3$. $2H_2O$ indicate slow kinetics with limited nucleation while $Mg_5(CO_3)_4(OH)_2$. $4H_2O$ indicate an enhanced growth but extremely slow kinetics which is attributed to temperature effects.

The reaction kinetics of magnesium carbonate phases in 49 nm silica nanochannels is noted in **Table 7** and as shown in **Figure 22(b)** as,

Table 7 Determining the Avrami and rate constant for various Mg-carbonate polymorphs loaded in 49 nm SNCs

Confined System Conditions	**Phases**	**Avrami Constant (n)**	**Rate Constant (k)**

49 nm Hydrophilic SNC-25 ℃	$MgCO_3$. $3H_2O$ $Mg_5(CO_3)_4(OH)_2$. $4H_2O$	0.32478 ± 0.32533 0.08123 ± 0.06315	0.030156946 0.7293
49 nm Hydrophilic SNC- 45 ℃	$MgCO_3$. $2H_2O$ $MgCO_3$. $3H_2O$ $Mg_5(CO_3)_4(OH)_2$. $4H_2O$	0.06244 ± 0.0259 0.32802 ± 0.10666 0.4049 ± 0.39203	0.608438159 0.028772938 0.017016871
49 nm Hydrophobic SNC- 25 ℃	$MgCO_3$. $2H_2O$ $MgCO_3$. $3H_2O$ $MgCO_3$. $5H_2O$ $Mg_5(CO_3)_4(OH)_2$. $4H_2O$	0.13851 ± 0.05256 0.21862 ± 0.05055 0.35962 ± 0.07603 0.29488 ± 0.05531	0.79136973 0.400196341 0.14506984 0.218718448
49 nm Hydrophobic SNC- 45 ℃	$MgCO_3$. $3H_2O$ $Mg_5(CO_3)_4(OH)_2$. $4H_2O$	0.17029 ± 0.04935 0.38054 ± 0.22676	0.322458769 0.174446007

The overall inference from the kinetic data is that in the hydrophilic condition at 25 ℃, $MgCO_3$. $3H_2O$ indicate very slow nucleation and low dimensional growth and $Mg_5(CO_3)_4(OH)_2$. $4H_2O$ indicate faster kinetics while in hydrophilic condition at 45 ℃, $MgCO_3$. $2H_2O$ indicate moderately fast kinetics, and $MgCO_3$. $3H_2O$, and $Mg_5(CO_3)_4(OH)_2$. $4H_2O$ indicate extremely slow kinetics but higher growth in comparison with 25 ℃ condition attributing to temperature effects. In hydrophobic condition at 25 ℃, $MgCO_3$. $2H_2O$ indicates low growth but fast nucleation, while

$MgCO_3$. $3H_2O$, $MgCO_3$. $5H_2O$ and $Mg_5(CO_3)_4(OH)_2$. $4H_2O$ displayed moderate growth and kinetics whereas in hydrophobic condition at 45 °C, $MgCO_3$. $3H_2O$, and $Mg_5(CO_3)_4(OH)_2$. $4H_2O$ although shows higher dimensional growth vs 25 °C condition, both polymorphs displays slower nucleation even with the assistance of temperature. Overall, the insights between the kinetic data from 10.48 nm vs 49 nm silica nanochannel in hydrophilic and hydrophobic conditions is that the Avrami constant is lower in all conditions for 49 nm pores vs 10.48 nm pores indicating that the dimensional growth is very slow and diffusion-limiting while the reaction rate is independent of pore size for each respective polymorph.

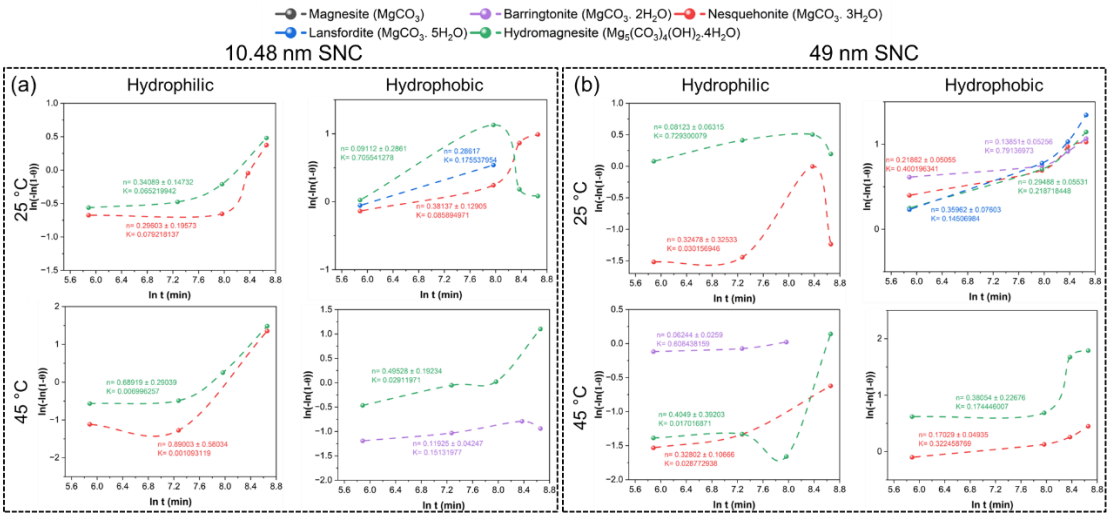

Figure 22 Determining the dimensional growth and nucleation rate of magnesium carbonate phases using Avrami equation in (a) 10.48 nm silica nanochannels, (b) 49 nm silica nanochannels at varied reaction temperature and surface wettability

3.6 *QENS Studies for Discerning the Water Characteristics in Silica Nanoconfined System*

The QENS studies were performed on the 10.48 nm hydrophilic and hydrophobic silica nanochannel membranes loaded with pure water and magnesium carbonate as shown in **Figure 23**. Before performing the measurements, temperature-dependent energy-resolved "elastic" intensity scan diagnostic measurements were performed from 20 K to 320 K on all samples to determine the melting temperature. For pure water samples, the "elastic" intensity scans and QENS measurements were carried out on the same samples, whereas separate samples with magnesium carbonate were used for "elastic" intensity scans and QENS measurements. From the diagnostic measurements of hydrophilic membrane loaded with pure water, we observe that the transition in the intensity associated with melting is at ca. 273 K, indicating bulk-like behavior. This characteristic was corroborated when Vycor-109 and Vycor-145 having pore size of 10.9 nm and 14.5 nm were filled with water (D_2O), and the melting scans from DSC indicated a transition temperature of ~273 K. [70] In parallel, water confined in silica matrices having pore size >2.7 nm exhibit freezing-melting transitions and phase formations similar to bulk. [71] Similarly, when the measurements were performed for hydrophilic silica membrane loaded with magnesium carbonate, the melting transition is seen at 264 K indicating a faster transition from solid to liquid which might be attributed to the alteration in the water hydrogen bonding network influenced by silica-water interactions or due to the role of magnesium ions. [13] Correspondingly, diagnostics was performed for pure water loaded hydrophobic SNC membrane, where we observe no clear melting transition till at least 320 K. This phenomena of lack of a clear melting

transition could be associated with the dynamics of water being slow, thus requiring very high activation energy, suggestive of the extreme sluggish behavior, or due to de-wetting of the nanopore with minimized interaction between water molecules and nanowall surface. [72–74] It should be noted that suppression of the melting transition was also observed in a systematic study of hydrated hydrophilic silica once the pore diameter was reduced to below 2 nm, [75] showcasing the influence of the confinement size on the state of the water even when the interaction of the water molecules with the wall remains unchanged.

The temperature-dependent diagnostics for magnesium carbonate loaded SNC displayed higher intensity than pure water system but similarly attributing to the absence of any clear melting transition for the hydrophobic host and a prominent melting transition for the hydrophilic host. In the latter case, the presence of magnesium carbonated led to a depression of the transition temperature compared to pure water in the same hydrophilic SNC.

Based on the transition temperature from diagnostics data, the QENS measurements were performed at 298 K to mimic experimental conditions. From the measurements, HWHM(Q) of the QENS signal as a function of Q was determined from fitting the QENS data as follows:

$$I(Q,E) = \left[x(Q)\delta(E) + \left(1 - x(Q)\right)\frac{1}{\pi}\frac{HWHM(Q)}{HWHM(Q)^2+E^2}\right] \otimes R(Q,E) + Background(Q,E)$$

Here a weighted superposition of the elastic scattering, defined by the delta function, and the QENS signal Lorentz function is numerically convolved with the resolution function, R(Q,E), and a linear fitted background term, Background(Q,E), is added. This fitting directly gives one important parameter, x(Q), representing the fraction of the

elastic scattering signal in the measured spectra. For hydrated samples, x(Q) approximates the fraction of "immobilized" water molecules. Other relevant parameters, e.g., the characteristic residence time between diffusion jumps of water molecules, can be determined from fitting the Q-dependence of the HWHM(Q) with jump diffusion model.

Based on the HWHM(Q) data, we can observe that the presence of magnesium carbonate strongly affects the water dynamics in the hydrophilic system but barely in the hydrophobic system. For pure water in hydrophilic system, the time between diffusion jump is (1.4 ± 0.6) ps, being almost as fast as in bulk water. In the hydrophilic system, when magnesium carbonate is loaded, the time between diffusion jumps becomes (32.0 ± 22.1) ps, indicating much slower water dynamics. This observation is supported by literature, where QENS studies performed for water confined in the pores of Upsalite showed extremely slow relaxation times even above melting point of water, while other measurements focused on residence time of translational diffusion of water in a 1M $MgCl_2$ in SBA-15 and determined that the water dynamics significantly slows down to (5.7 ± 0.3) ps. [76,77] These findings clearly corroborate with the observation of slower dynamics during magnesium carbonate crystallization in nanoconfinement. The time between diffusion jump for H_2O in hydrophobic SNC also indicates slower dynamics of (11.8 ± 2.2) ps in comparison with H_2O in hydrophilic system, which might be due to the sluggish behavior of water requiring higher activation energy. [72] The water dynamics in the hydrophobic system associated with $MgCO_3$ is only slightly higher, (13.9 ± 1.4) ps, which might be due to the alteration of Mg^{2+} ions on the coordination networks for molecular motion or due to concentration-dependent dynamics. [78,79]

Besides, it is important to note that not all molecules in the confined systems are mobile on the ps-ns time scale of the QENS measurements, as confirmed by the fraction of mobile water molecules, determined as the parameter (1-x(Q)) in the equation above. While most of the H_2O molecules in hydrophilic SNC are mobile, only a very small fraction of H_2O molecules associated with hydrophilic $MgCO_3$ is mobile, with most of them being bound or reacted water. Similarly, H_2O in hydrophobic SNC represents a reduced mobile fraction depicting bound or stationary water, whereas the presence of $MgCO_3$ in hydrophobic SNC slightly increases the mobile water fraction, which is ascribed to the changes in the hydrogen bonding network. [80,81]

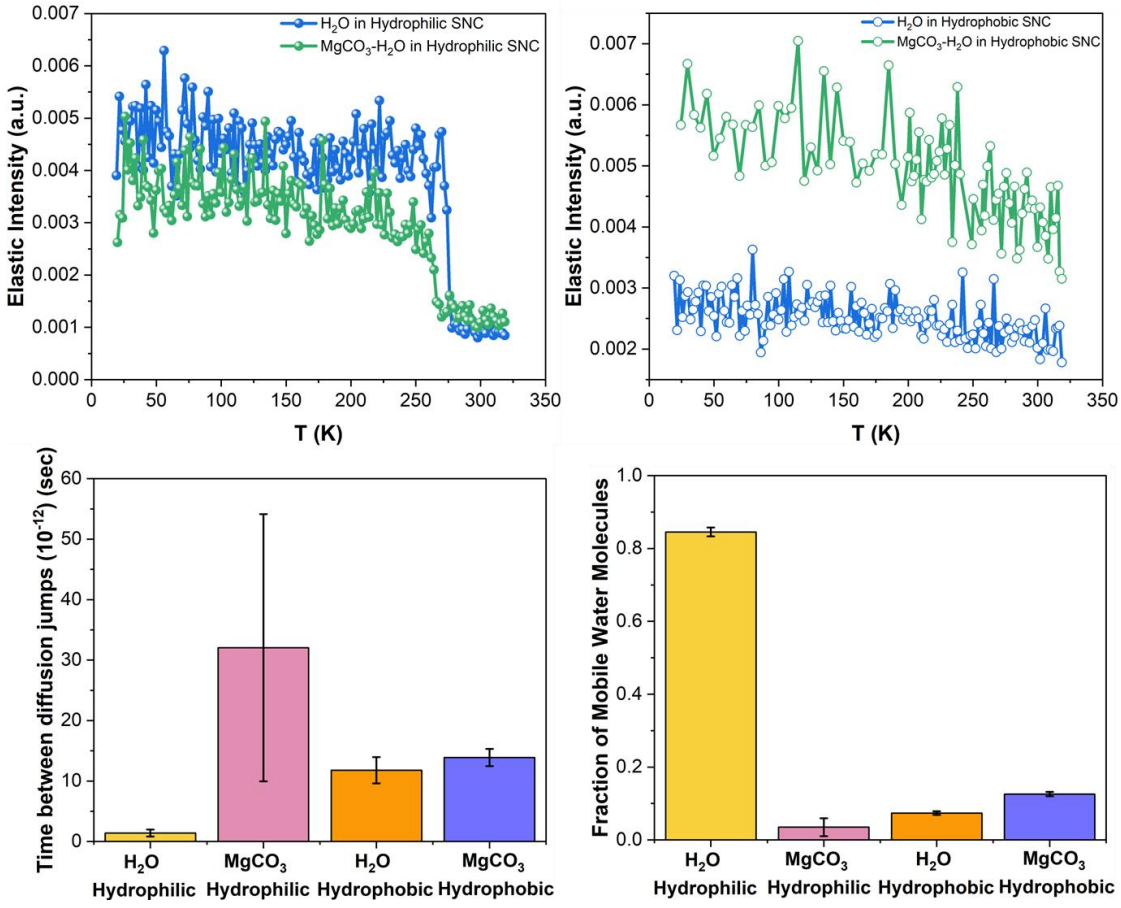

Figure 23 Determining the temperature-dependent elastic scans of (a) hydrophilic 10.48 nm SNCs filled with pure H_2O and $MgCO_3$, (b) hydrophobic 10.48 nm SNCs filled with pure H_2O and $MgCO_3$, (c)

identifies the residence time of water molecules between successive jumps, and (d) identifies the fraction of mobile water molecules in each respective nanoconfined system.

4. Conclusion

Precise understanding of the mechanism of carbon mineralization in subsurface environments require the investigation of the influence of solid interface, surface chemistry involved, inherent behavior of confined water and the role of various ions, giving insights into the nucleation, growth and stability of carbonate phases. Deciphering this mechanism with respect to $MgCO_3$ mimics the carbonation process in Mg-rich mafic and ultra-mafic rocks aiding in development of carbon storage technologies. This study present a detailed investigation of the behavior of magnesium carbonate and its phase evolution in nanoconfined volumes by interchanging the solid interface from alumina to silica, altering the reaction temperature and surface wettability from hydrophilic to hydrophobic. The crystallization in the nanochannels was initiated by passing 0.8M $Mg(NO_3)_2$. $6H_2O$ and 0.4M $NaHCO_3$ using chemical vapor deposition and aspiration technique and the phase changes were investigated using X-ray diffraction measurements. The phase evolution from XRD indicate that phases of $MgCO_3$ (magnesite) is observed only in 10 nm alumina membrane whereas $MgCO_3$. $3H_2O$ (nesquehonite), $MgCO_3$. $5H_2O$ (lansfordite) and $Mg_5(CO_3)_4(OH)_2$. $4H_2O$ (hydromagnesite) are the most stable phases in anodic alumina membrane and silica nanochannels irrespective of reaction temperature and surface wettability. Reaction kinetic studies further underscore the role of surface chemistry over mere confinement giving insights into the dimensional growth and nucleation rate of different phases of

magnesium carbonate. The dynamics of water in confined volumes associated with $MgCO_3$ is determined from QENS studies exhibiting a slower diffusion jump rate and less mobile water ions. By systematically decoupling the surface effects on magnesium carbonate phase evolution, we are able to find new insights having implications ranging from carbon sequestration to biomineralization to material synthesis.

5. Acknowledgment

The authors acknowledge the use of shared facilities at Cornell Center for Materials Research (CCMR) supported through NSF MRFEC program (DMR- 1719875) and Cornell NanoScale Science and Technology Facility (CNF), a member of the National Nanotechnology Coordination Infrastructure (NNCI) supported by NSF (Grant NNCI-2025233). The authors would also like to acknowledge Oak Ridge National Laboratory (ORNL) for accepting the proposal and providing the facilities for beamline. AM and RH are supported by NSF CAREER (Grant No- 2144373).

6. References

1. Sayles, F. L. & Fyfe, W. S. The crystallization of magnesite from aqueous solution. *Geochim Cosmochim Acta* **37**, (1973).

2. Han, B., Qu, H., Niemi, H., Sha, Z. & Louhi-Kultanen, M. Mechanistic study of magnesium carbonate semibatch reactive crystallization with magnesium hydroxide and CO2. *Ind Eng Chem Res* **53**, (2014).

3. Yamamoto, G. ichiro, Kyono, A. & Okada, S. Structural variations of amorphous magnesium carbonate during nucleation, crystallization, and decomposition of nesquehonite MgCO3·3H2O. *Phys Chem Miner* **50**, (2023).

4. Scheller, E. L. *et al.* Formation of Magnesium Carbonates on Earth and Implications for Mars. *Journal of Geophysical Research: Planets* vol. 126 Preprint at https://doi.org/10.1029/2021JE006828 (2021).

5. Nisbet, H. *et al.* Carbon Mineralization in Fractured Mafic and Ultramafic Rocks: A Review. *Reviews of Geophysics* **62**, (2024).

6. Sanna, A., Uibu, M., Caramanna, G., Kuusik, R. & Maroto-Valer, M. M. A review of mineral carbonation technologies to sequester CO2. *Chemical Society Reviews* vol. 43 Preprint at https://doi.org/10.1039/c4cs00035h (2014).

7. Wang, F. & Dreisinger, D. Status of CO2 mineralization and its utilization prospects. *Minerals and Mineral Materials* **1**, (2022).

8. Stolte, N., Hou, R. & Pan, D. Nanoconfinement facilitates reactions of carbon dioxide in supercritical water. *Nat Commun* **13**, (2022).

9. Dasgupta, N., Ho, T. A., Rempe, S. B. & Wang, Y. Hydrophobic Nanoconfinement Enhances CO2 Conversion to H2CO3. *Journal of Physical Chemistry Letters* **14**, (2023).

10. Leoni, F., Calero, C. & Franzese, G. Nanoconfined Fluids: Uniqueness of Water Compared to Other Liquids. *ACS Nano* **15**, (2021).

11. Oh, M. I., Gupta, M., Oh, C. I. & Weaver, D. F. Understanding the effect of nanoconfinement on the structure of water hydrogen bond networks. *Physical Chemistry Chemical Physics* **21**, (2019).

12. Ravindra, P., Advincula, X. R., Schran, C., Michaelides, A. & Kapil, V. Quasi-one-dimensional hydrogen bonding in nanoconfined ice. *Nat Commun* **15**, 7301 (2024).

13. Knight, A. W., Kalugin, N. G., Coker, E. & Ilgen, A. G. Water properties under nano-scale confinement. *Sci Rep* **9**, (2019).

14. Hagan, J. T. *et al.* Chemically tailoring nanopores for single-molecule sensing and glycomics. *Anal Bioanal Chem* **412**, (2020).

15. Gadikota, G. & Mamidala, A. Carbon mineralization in confinement. *AGU Fall Meeting Abstracts* **2023**, GC31G-1109 (2023).

16. Reddy, M. M. & Wang, K. K. Crystallization of calcium carbonate in the presence of metal ions: I. Inhibition by magnesium ion at pH 8.8 and 25°C. *J Cryst Growth* **50**, (1980).

17. Falini, G., Fermani, S., Tosi, G. & Dinelli, E. Calcium carbonate morphology and structure in the presence of seawater ions and humic acids. *Cryst Growth Des* **9**, (2009).

18. Butler, M. F., Glaser, N., Weaver, A. C., Kirkland, M. & Heppenstall-Butler, M. Calcium carbonate crystallization in the presence of biopolymers. *Cryst Growth Des* **6**, (2006).

19. S, R. QUANTITATIVE ANALYSIS OF AMORPHOUS CALCIUM CARBONATE PRECIPITATE WITH THE PRESENCE OF ALUMINA IN THE FLOW WATER. in *3rd International Seminar on Education Technology 2017* (2017).

20. Ji, Y., Madhav, D. & Vandeginste, V. Kinetics of enhanced magnesium carbonate formation for CO2 storage via mineralization at 200 °C. *International Journal of Greenhouse Gas Control* **121**, (2022).

21. Tzachristas, A., Kanellopoulou, D. G., Koutsoukos, P. G., Paraskeva, C. & Sygouni, V. The effect of surface wettability on calcium carbonate precipitation in packed beds. *Surfaces and Interfaces* **34**, (2022).

22. Wang, C., Piao, C., Zhai, X., Hickman, F. N. & Li, J. Synthesis and characterization of hydrophobic calcium carbonate particles via a dodecanoic acid inducing process. *Powder Technol* **198**, (2010).

23. Trybula, M. E., Zydek, A., Korzhavyi, P. A. & Wojewoda-Budka, J. Structure and Behavior of Oxide-Coated Aluminum in Contact with Acidic and Alkaline Aqueous Solutions─A Reactive Molecular Dynamics Simulation Study. *Journal of Physical Chemistry C* **127**, (2023).

24. Eiblmeier, J. *et al.* Crystallization of mixed alkaline-earth carbonates in silica solutions at high pH. *Cryst Growth Des* **14**, (2014).

25. Al-Gailani, A. *et al.* Role of temperature, roughness and pressure in crystallization fouling from potable water on aluminium surface. *Thermal Science and Engineering Progress* **23**, (2021).

26. Deng, H. *et al.* Two competitive nucleation mechanisms of calcium carbonate biomineralization in response to surface functionality in low calcium ion concentration solution. *Regen Biomater* **2**, (2015).

27. Zhang, Y. *et al.* Physical adsorption of OH^- causes anomalous charging at oxide–water interfaces. *Chemical Communications* **60**, 9113–9116 (2024).

28. Zhang, Z. A new method for estimating zeta potential of carboxylic acids' functionalised particles. *Mol Phys* **122**, (2024).

29. Pokrovsky, O. S. & Schott, J. Processes at the magnesium-bearing carbonates/solution interface. II. Kinetics and mechanism of magnesite dissolution. *Geochim Cosmochim Acta* **63**, (1999).

30. Wordsworth, J. *et al.* The Influence of Nanoconfinement on Electrocatalysis. *Angewandte Chemie - International Edition* vol. 61 Preprint at https://doi.org/10.1002/anie.202200755 (2022).

31. Prieto, M. J. *et al.* Insights into Reaction Kinetics in Confined Space: Real Time Observation of Water Formation under a Silica Cover. *J Am Chem Soc* **143**, (2021).

32. Shirzad, K. & Viney, C. A critical review on applications of the Avrami equation beyond materials science. *Journal of the Royal Society Interface* vol. 20 Preprint at https://doi.org/10.1098/rsif.2023.0242 (2023).

33. Jouppila, K. & Roos, Y. H. Glass Transitions and Crystallization in Milk Powders. *J Dairy Sci* **77**, (1994).

34. Koh, Y. P. & Simon, S. L. Crystallization and vitrification of a cyanurate trimer in nanopores. *Journal of Physical Chemistry B* **116**, (2012).

35. Alekseechkin, N. V. On the kinetics of phase transformation of small particles in Kolmogorov's model. *Condens Matter Phys* **11**, (2008).

36. Su, C. *et al.* Crystallization Kinetics of Poly(ethylene oxide) under Confinement in Nanoporous Alumina Studied by in Situ X-ray Scattering and Simulation. *Langmuir* **35**, (2019).

37. Xu, J. T., Ryan, A. J., Mai, S. M., Yuan, J. J. & Cheng, S. Y. Diffusion control of homogeneous crystallization in nanoconfined domains of block copolymers. *J Macromol Sci Phys* **43 B**, (2004).

38. Osti, N. C., Jalarvo, N. & Mamontov, E. Backscattering silicon spectrometer (BASIS): sixteen years in advanced materials characterization. *Mater Horiz* **11**, 4535–4572 (2024).

39. Alexeev, V. L. *et al.* Dispersions of silica particles in surfactant phases. *Langmuir* **12**, (1996).

40. Jiang, X., Tang, X., Tang, L., Zhang, B. & Mao, H. Synthesis and formation mechanism of amorphous silica particles via sol–gel process with tetraethylorthosilicate. *Ceram Int* **45**, (2019).

41. Chunbo, R., Guqiao, D., Weichang, L., Yan, D. & Wentao, H. Wetting on nanoporous alumina surface: Transition between Wenzel and Cassie states controlled by surface structure. *Langmuir* **24**, (2008).

42. Guo, C., Wang, X. W. & Yuan, Z. H. Pore diameter-dependence wettability of porous anodized aluminum oxide membranes. *Journal of Porous Materials* **20**, (2013).

43. Iler, R. K. The chemistry of silica: solubility, polymerization, colloid and surface properties, and biochemistry. *Lavoisierfr* (1979) doi:10.1002/ange.19800920433.

44. O. David, R. *et al.* The role of contact angle and pore width on pore condensation and freezing. *Atmos Chem Phys* **20**, (2020).

45. Zhu, M. & Mao, Y. Large-pore-size membranes tuned by chemically vapor deposited nanocoatings for rapid and controlled desalination. *RSC Adv* **10**, (2020).

46. Krainer, S. & Hirn, U. Contact angle measurement on porous substrates: Effect of liquid absorption and drop size. *Colloids Surf A Physicochem Eng Asp* **619**, (2021).

47. Liu, S., Luo, J., Xie, G. & Guo, D. Effect of surface charge on water film nanoconfined between hydrophilic solid surfaces. in *Journal of Applied Physics* vol. 105 (2009).

48. Dutta, N., Mitra, S. & Nirmalkar, N. Understanding the Role of Surface Charge on Nanobubble Capillary Bridging during Particle-Particle Interaction. *Langmuir* **40**, (2024).

49. Greathouse, J. A. *et al.* Effects of nanoconfinement and surface charge on iron adsorption on mesoporous silica. *Environ Sci Nano* **8**, (2021).

50. Lutze, J. *et al.* α-((4-cyanobenzoyl)oxy)-ω-methyl poly(ethylene glycol): A new stabilizer for silver nanoparticles. *Beilstein Journal of Nanotechnology* **8**, (2017).

51. Romero, V. & Benavente, J. Electrochemical Characterization of Nanoporous Alumina-Based Membranes with Different Structure and Geometrical Parameters by Membrane Potential Analysis. *Micro* **2**, (2022).

52. Vajandar, S. K. *et al.* SiO2-coated porous anodic alumina membranes for high flow rate electroosmotic pumping. *Nanotechnology* **18**, (2007).

53. Kang, H., Long, D. J. & Haynes, C. L. Preparation of Colloidally Stable Positively Charged Hollow Silica Nanoparticles: Effect of Minimizing Hydrolysis on ζ Potentials. *Langmuir* **35**, (2019).

54. Prakash, S. *et al.* Electrokinetic transport in silica nanochannels with asymmetric surface charge. *Microfluid Nanofluidics* **19**, (2015).

55. Pedimonte, B. J. *et al.* Morphological zeta-potential variation of nanoporous anodic alumina layers and cell adherence. *Acta Biomater* **10**, (2014).

56. Song, X. *et al.* Synthesis of lansfordite under regulation of dicarbonate. *Huagong Xuebao/CIESC Journal* **66**, (2015).

57. Brekke-Svaland, G. & Bresme, F. Interactions between Hydrated Calcium Carbonate Surfaces at Nanoconfinement Conditions. *Journal of Physical Chemistry C* **122**, (2018).

58. Tarasevich, Y. I. State and structure of water in vicinity of hydrophobic surfaces. *Colloid Journal* **73**, (2011).

59. Kim, J., Tian, Y. & Wu, J. Thermodynamic and Structural Evidence for Reduced Hydrogen Bonding among Water Molecules near Small Hydrophobic Solutes. *Journal of Physical Chemistry B* **119**, (2015).

60. Grdadolnik, J., Merzel, F. & Avbelj, F. Origin of hydrophobicity and enhanced water hydrogen bond strength near purely hydrophobic solutes. *Proc Natl Acad Sci U S A* **114**, (2017).

61. Galamba, N. Water tetrahedrons, hydrogen-bond dynamics, and the orientational mobility of water around hydrophobic solutes. *Journal of Physical Chemistry B* **118**, (2014).

62. Wawer, J. & Krakowiak, J. Structural changes of water caused by non-electrolytes: Volumetric and compressibility approach for urea-like analogues. *J Mol Liq* **259**, (2018).

63. Pokharel, R., Popa, I. C., de Kok, Y. & King, H. E. Enhanced Nesquehonite Formation and Stability in the Presence of Dissolved Silica. *Environ Sci Technol* **58**, (2024).

64. Hopkinson, L., Rutt, K. & Cressey, G. The transformation of nesquehonite to hydromagnesite in the system CaO-MgO-H2O-CO2: An experimental spectroscopic study. *Journal of Geology* **116**, (2008).

65. Giorgiosite Mineral data. https://webmineral.com/data/Giorgiosite.shtml.

66. Nguyen, H., Bernard, E., Winnefeld, F., Lothenbach, B. & Kinnunen, P. Synthesis and Thermodynamic Data of Acetate-Containing Giorgiosite – a Novel Hydrated Magnesium Carbonate. Preprint at https://doi.org/10.2139/ssrn.4952510 (2024).

67. Xu, J. *et al.* Testing the cation-hydration effect on the crystallization of Ca-Mg-CO 3 systems. *Proc Natl Acad Sci U S A* **110**, (2013).

68. Wang, R., Zhang, Y., Ma, Q. D. Y. & Wu, L. Recent advances of small molecule detection in nanopore sensing. *Talanta* **277**, 126323 (2024).

69. Ma, J. *et al.* Drastically Reduced Ion Mobility in a Nanopore Due to Enhanced Pairing and Collisions between Dehydrated Ions. *J Am Chem Soc* **141**, (2019).

70. Xia, Y. *et al.* Layer-by-Layer Freezing of Nanoconfined Water. *Sci Rep* **10**, (2020).

71. Mamontov, E. *et al.* Dynamics of water in LiCl and CaCl2 aqueous solutions confined in silica matrices: A backscattering neutron spectroscopy study. *Chem Phys* **352**, (2008).

72. Kumar, P. & Han, S. Dynamics of two-dimensional monolayer water confined in hydrophobic and charged environments. *J Chem Phys* **137**, (2012).

73. Baek, S., Kwon, S. R. & Bohn, P. W. Potential-induced wetting and dewetting in hydrophobic nanochannels for mass transport control. *Current Opinion in Electrochemistry* vol. 34 Preprint at https://doi.org/10.1016/j.coelec.2022.100980 (2022).

74. Lynch, C. I., Klesse, G., Rao, S., Tucker, S. J. & Sansom, M. S. P. Water Nanoconfined in a Hydrophobic Pore: Molecular Dynamics Simulations of Transmembrane Protein 175 and the Influence of Water Models. *ACS Nano* **15**, (2021).

75. Liu, L. *et al.* Quasielastic and inelastic neutron scattering investigation of fragile-to-strong crossover in deeply supercooled water confined in nanoporous silica matrices. *Journal of Physics: Condensed Matter* **18**, S2261–S2284 (2006).

76. Soininen, A. J. *et al.* Dynamics of water confined in mesoporous magnesium carbonate. *Journal of Chemical Physics* **145**, (2016).

77. Baum, M., Rébiscoul, D., Juranyi, F. & Rieutord, F. Structural and Dynamical Properties of Water Confined in Highly Ordered Mesoporous Silica in the Presence of Electrolytes. *Journal of Physical Chemistry C* **122**, (2018).

78. Gao, Y. *et al.* A Nanoconfined Water–Ion Coordination Network for Flexible Energy-Dissipation Devices. *Advanced Materials* **35**, (2023).

79. Hung, S. T., Roget, S. A. & Fayer, M. D. Effects of Nanoconfinement on Dynamics in Concentrated Aqueous Magnesium Chloride Solutions. *J Phys Chem B* **128**, 5513–5527 (2024).

80. Li, H. *et al.* Role of Exchange Cations and Layer Charge on the Dynamics of Confined Water. *Journal of Physical Chemistry A* **128**, (2024).

81. Ockwig, N. W. *et al.* Nanoconfined water in magnesium-rich 2:1 Phyllosilicates. *J Am Chem Soc* **131**, (2009).

CHAPTER 4

Calcium Carbonate Polymorphism in Nano-confinement: An Investigation of Alumina and Siliceous Hosts in Various Physicochemical Conditions

1. Introduction

Nanopores are pervasive in the environment mediating the flow of water and ions, and have become a subject of profound interest as they play a crucial role in a multitude of engineered and natural processes from biosensing, environmental monitoring, catalytic kinetics to rock weathering. [1–3] These nanopores significantly influence the characteristics of fluids by varying the fluid transport dynamics enabling fast transport, preferential structure and bond formations, and anomalous dielectric parameters enhancing the selectivity in various applications. [4] This intrinsic nature of nanopores can be extrapolated and capitalized for the applications of carbon capture and storage (CCS) strategies aiding in understanding the interactions of water-CO_2 systems, the adsorption and diffusion mechanisms, and the phase evolution of carbonic acid into stable carbonates. [5] Nanopores in the subsurface environments play a vital role in increasing the CO_2 storage density with decreasing pore sizes due to strong surface-fluid interactions, gas solubility, and transport promoting effective carbon storage technologies. [6]

First and foremost, the surface composition and chemistry of nanopores in the subsurface environment vary extensively and it is imperative to understand the behavior of these minerals on the transport kinetics of water and ions. The subsurface environment is rich in elements like Ca, Mg, Al, Fe, and K and the role of each element on the diffusion of ions depends on electrostatic interactions influencing the transport

dynamics. [7,8] This alteration of cation composition affects the cation-π interactions between the ions and the surface wall influencing the ion density and the water flux near the nanopores. Such behavior was observed in alkali metals where the presence of Na^+ ion slowed down the water transport rate due to strong binding in comparison with Li^+, K^+, and Cs^+ ions. [9,10] Secondly, the surface charge effects become an important factor as they can either enhance or inhibit the transport of water and ions creating ion enrichment or depletion zones while the surface charge distribution influences the ionic conductance, enabling the tunable change in ionic transport. [11] This interplay of surface charge was studied in 50 nm long nanopores where positive charge currents reduced depletion layers while negatively charged surfaces created depletion layers at the exit of the nanopore. [12]

Delineating the behavior of water in the interfacial and bulk regions in a confined volume system is also pivotal as it enhances the geological storage capacity of CO_2 into stable carbonate minerals whose effects are beyond the surface composition, charge, and chemistry. Nanoconfined water behaves differently from other simple or anomalous fluids under similar confinement along with unusual density, surface properties, and temperature profiles. [13,14] In confinement, water displays significantly low refractive index and strengthened hydrogen bonding at the interface while having different quantum states in comparison with bulk, making the weakly interactive molecule model inapplicable. [15,16] In a hydrophilic nanopore, the behavior of water depends on pore size, surface structure, and temperature and can display liquid-like to solid-like characteristics with viscosity ranging from bulk-like to orders of magnitude higher. [17] Classical MD simulations demonstrate that water in heterogenous hydrophilic structures

undergo structural rearrangement, breaking, and formation of hydrogen bonds and asymmetrical orientation in single and multi-dimensional confinement. [18] Water in the core of the hydrophilic nanopore has significantly different interfacial tension and viscous flow properties [19] resulting in the molecules being denser and orientally distorted resembling glassy behavior. [20] Within the hydrophobic nanopore, the formation of ion clusters is observed due to the high interaction density between the coordination system leading to reduced particle dynamics. [21] Hydrophobic nanopores lead to enhanced diffusion of water [22] and affect the hydrogen bond dynamics mimicking bulk water. [23] Reduction of the energy barrier and the conversion of reaction from endothermic to exothermic is observed [24] along with stronger solvation and enhanced proton transfer properties. [25]

Outlining the mechanism of carbon mineralization by taking surface composition, chemistry, and the interfacial and bulk water properties into account and utilizing one of the major subsurface elements, Calcium, in discrete confined nanopores provides complete long-term workings and transformation of greenhouse gases in these environments. The underlying mechanism of precipitating calcium carbonate using synthetic materials to natural rock systems has been studied extensively in bulk and confined volume systems. Prior studies investigating in bulk solutions focused on the preferential rhombohedral calcite formation having no agglomeration using supercritical CO_2 and no other additives, while the preferential formation of vaterite from C&D waste using sodium glycinate additive was studied giving insights into the mechanisms involved for various selective polymorph evolution using different

reagents and experimental conditions. [26,27] The conventional bulk transition mechanism for calcium carbonate phases is given below, [28–31]

$$\text{ACC} \rightarrow \text{Vaterite } (CaCO_3) \rightarrow \text{Aragonite } (CaCO_3) \rightarrow \text{Calcite } (CaCO_3)$$

$$\text{Ikaite } (CaCO_3.\ 6H_2O) \rightarrow \text{ACC} \rightarrow \text{Vaterite} \rightarrow \text{Calcite}$$

$$\text{ACC} \rightarrow \text{Monohydrocalcite } (CaCO_3.\ H_2O) \rightarrow \text{Aragonite} \rightarrow \text{Calcite}$$

$$\text{ACC.}\ H_2O \rightarrow \text{ACC} \rightarrow \text{Calcite}$$

Although these studies provide insights into calcium carbonate crystallization, they are atypical of the mechanisms observed in confined volume systems, which facilitate short-lived phases to become more stable, inducing favorable and unique phase transition behavior. These effects are complemented in studies where amorphous calcium carbonate (ACC) gets transitioned in aragonite in 1.5-5 μm fungal hyphae tubular cell pores at 134 °C and 2.5 bar pressures. [32] Single crystal vaterite is also seen getting stabilized in 200 nm track-etched membranes purchased from Millipore whereas 1:1 calcite/vaterite were crystallized in the same membranes purchased from Sterlitech, [33] and the crystallization of calcite in 50 nm track-etched membranes in the presence of poly(acrylic acid) was observed. [34] All these studies indicate that the calcium carbonate phase formation and stabilization in confined volumes is highly dependent on the surface environment, and even a small change in the morphology of the templates can change the polymorph evolution. Along this line, an MD simulation-based study by Yu et al. investigated the formation mechanism of $CaCO_3$ in confined calcium silicate hydrate (C-S-H) nanopores with different Ca/Si ratios and found that a Ca/Si ratio of 1.5 is more favorable for the formation and growth of the $CaCO_3$ clusters in the nanopores. It was also seen that apart from directly clustering with CO_3^{2-} ions in

solution, Ca^{2+} ions present in the solid template act as adsorption sites attracting more $CaCO_3$ aggregates with the help of ionic and hydrogen bonding. [35] A recent simulation study by Li et al. found the Ca^{2+} ions favoring bidentate coordination with CO_3^{2-} ions in the interfacial region of a 2 nm graphene nanoslit beneficial for forming aragonite. [36] However, critical elucidation of the energetic basis for the formation of different phases of Ca-carbonates in nanoconfinement is sparse in the literature. Among one of those few reports, the application of metadynamics bias on Ca-carbonate nanoparticles in water indicated that calcite-like structure is thermodynamically favorable for a nanoparticle of size ~ 2 nm in bulk at a temperature and pressure of 310 K and 1 atm respectively. Besides, this model by Quigley et al. was unable to locate aragonite-like particles in the system and vaterite was found to be unstable. [37]

Studying the peculiar behavior of nanoconfined water with mineral carbonation gives insights into the reactivity and the efficiency as it affects the chemical speciation making CO_2 more reactive. [38] Previous studies investigated that water films of nanometer thickness when considered as a facilitating medium for nucleation, dissolution, and precipitation, are supposed to slowdown the kinetics of carbonate precipitation. However, these 2-D quasi-confined water films not only facilitate carbonate growth rapidly but also display phases that are not generally observed in bulk. [39] Confined water changes the phase orientation of carbonates due to entropic and repulsive effects [40] and screening of electrostatic charges is reduced drastically between ions due to confinement resulting in a strong interaction between divalent cation and carbonate anion. Furthermore, to interpret the characteristics of water in the interfacial region of the confined systems, the functionalized group predominant on the surface of the

confined volume plays a crucial role. The presence of -OH, -COOH, -NH groups in the interfacial region of the nanowall restricts the mobility of water by stabilizing the water molecules and slowing down the hydrogen bond dynamics. [41,42] This attribute also becomes relevant to carbonate phase crystallization where the presence of -COOH group makes the surface more negative in comparison with -OH groups forming stable calcite through strong electrostatic interactions. [43]

By weighing all these effects into consideration, the current study focuses on comparing the phase evolution of calcium carbonate in two different porous membranes and varying the surface wettability by altering the presence of functional groups while allowing for the reaction to proceed at 25 °C and 45 °C with changing pore sizes. In specific, the surface of the porous membranes selected as the confining template are anodic alumina membranes (AAM) and silica nanochannels (SNC). The functional groups that are present in the interfacial regions of the AAMs and SNCs are -OH groups for maintaining the hydrophilic environment and -COR groups for maintaining the hydrophobic environment. A mixture of 0.1M calcium nitrate tetrahydrate ($Ca(NO_3)_2.4H_2O$) and 0.1M sodium bicarbonate ($NaHCO_3$) were utilized to precipitate calcium carbonate in nanoconfined volumes and the phase evolution was investigated over time at different conditions. **Figure 24(a,b)** displays the schematic of different phases of calcium carbonate structures loaded in AAM and SNC membranes. Furthermore, to delineate the water melting behavior, the diffusion jumps rate and mobility of water in the presence of various ions, quasi-elastic neutron scattering (QENS) measurements were performed. To complement the experimental results with the information on the structural characteristics of interfacial Ca^{2+} ions in their pre-nucleated state, classical

MD simulations are done in the presence of an amorphous silica/alumina framework. Realistic hydrophilic and hydrophobic silica and alumina membranes are modeled and simulated under varying temperature conditions, serving as an indispensable addition to the *in-silico* studies in this field. This study interprets the structural behavior of calcium ions in pre-nucleated conditions and the mechanism behind the formation of the calcium carbonate phases in nanoconfinement while altering the wettability, pore size, and reaction temperature, which is pivotal in deducing the reaction mechanism, thermodynamics, and kinetics of mineral carbonation for safe storage of CO_2 in subsurface environments.

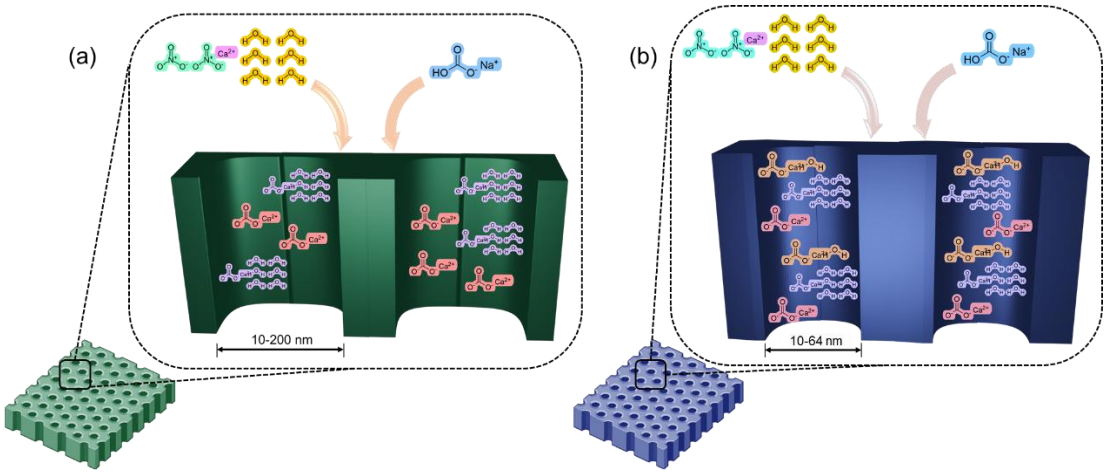

Figure 24 Schematic of calcium carbonate loaded in (a) Anodic Alumina Membrane (AAM), (b) Silica Nanochannels (SNCs)

2. Experiments and Methodology

2.1. *Materials*

Anodic alumina membranes (AAM) having a diameter of 25 mm, a length of 50 μm, and a pore size of 10 nm, and 40 nm were purchased from SPI® Supplies, and a Whatman™ Anodisc™ having length of 60 μm with pore size of 200 nm was purchased from Cytiva. To synthesize silica nanochannels (SNCs), a precursor solution consisting of different molar compositions of PEG-PPG-PEG (P123) surfactant (Sigma Aldrich), anhydrous ethanol (C_2H_5OH) (Fischer Scientific, 96% v/v), hydrochloric acid (HCl) (Sigma Aldrich, 37% ACS reagent), and tetraethyl orthosilicate (TEOS) (Sigma Aldrich, 98% reagent grade) were utilized. To incorporate hydrophobicity, lauric acid ($C_{12}H_{24}O_2$) (Sigma Aldrich, FCC, FG, ≥ 98%), and anhydrous ethanol (C_2H_5OH) (Fischer Scientific, 96% v/v) were used.

Laboratory grade calcium nitrate tetrahydrate ($Ca(NO_3)_2$. $4H_2O$) (Sigma Aldrich, BioXtra, ≥ 99%) and sodium bicarbonate ($NaHCO_3$) (Fischer Scientific, ACS reagent 99%) are used for precipitating calcium carbonate. All chemicals were purchased from commercial vendors and used as received without any further purification. Deionized (DI) water (18.2 MΩ.cm) from the Milli-Q Q-POD® system was used in all experiments. The aspiration setup with a 25 mm filter funnel and a capacity of 50 mL was purchased from Cytiva and used without any modification.

2.2. *Synthesis of Silica Nanochannels*

For the synthesis of silica nanochannels of varying pore size different compositions of silica precursor solutions were prepared and the solutions were passed through AAM.

During the synthesis of SNCs, 1g of Pluronic P123 was dissolved in a mixture containing 19 mL of ethanol and 84 μL of concentrated HCl and was stirred at 300 rpm under reflux for 1 hour at room temperature. For incorporating the silica component, 2.13 g of tetraethyl orthosilicate (TEOS) was added dropwise and the mixture was stirred at 400 rpm for 12 hours at 60 °C under reflux. A slightly different precursor solution composition was prepared for obtaining different pore size SNCs where 1g of P123 was dissolved in 12.36 mL and 18.54 mL of ethanol, 2g of DI water, and 84 μL of concentrated HCl and the mixture was stirred at 300 rpm under reflux for 1 hour at room temperature. Then, 2.13 g of TEOS was added to the solution dropwise and the mixture was stirred at 400 rpm for 7 hours at 60 °C under reflux. Once these respective precursor solutions were prepared, a 200 nm AAM was placed on the filter in an aspiration setup and 0.5 mL of the solution was passed through the membrane for loading silica nanochannels and this step was carried out 5 times with the same volume. Once the loading is completed, to prevent any excess silica from precipitating on the surface, the membrane was washed with ethanol. The reaction within the membrane was allowed to proceed for 24 hours after which the surfactant template was removed to finally obtain silica nanochannels in anodic alumina membrane as shown in **Figure 25**. To remove the surfactant, the loaded membranes were placed in a benchtop muffle furnace (Thermo Scientific Thermolyne) where the samples were calcined at 550 °C for 4 hours at a ramp rate of 3 °C/min. Hereon, the silica nanochannels loaded in anodic alumina membrane will be denoted as X nm SNC's where X represents the pore size of the silica nanochannels. The pore size distribution was measured through N_2 adsorption NLDFT analysis (Quantochrome AutoSorb iQ Analyzer) at 77 K after outgassing the

sample at 130 °C for 24 hours. To determine the morphology of the silica nanochannels, scanning electron microscope (Zeiss Gemini 500) was used with an accelerating voltage of 3 keV for imaging and for determining the structure and type of bonds, Fourier transform infrared spectroscopy (ThermoFisher Scientific) was used for each measurement in the spectral range of 4000-400 cm^{-1}.

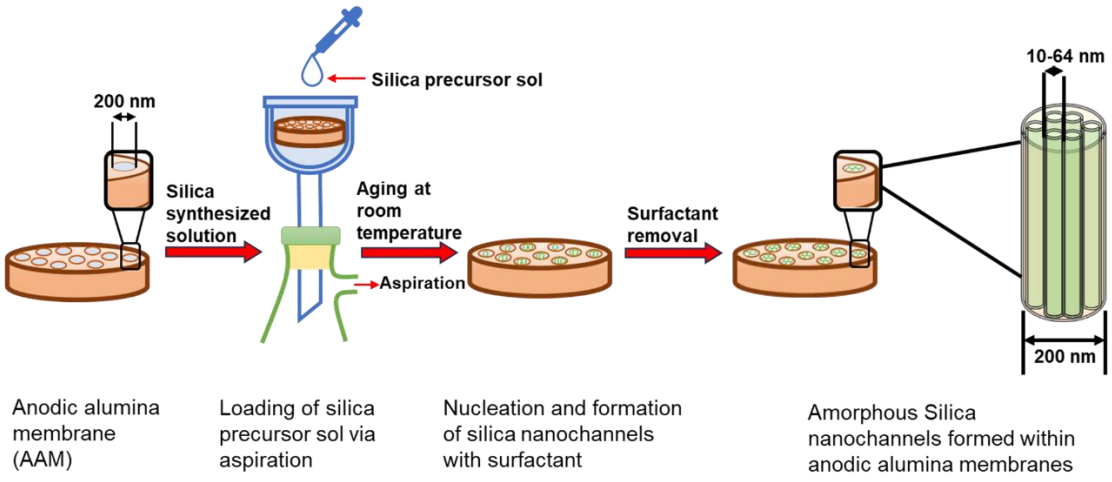

Figure 25 Schematic of the approach in architecting silica nanochannels in AAM

2.3. *Surface Functionalization of Anodic Alumina Membranes and Silica Nanochannels for Altering Surface Wettability*

The approach of surface functionalization of anodic alumina membrane is similar to the one reported in Mamidala, A (Chapter-2), where the membranes were initially rinsed with ethanol and water and dried at 85 °C for 30 minutes and then immersed in a solution of 20 g/L of lauric acid in ethanol and mixed at 50 °C for 15 minutes at 120 rpm. Subsequently, the wettability modified membranes were again rinsed with ethanol and water and dried at 85 °C for 30 minutes.

While varying the surface wettability of silica nanochannels, the initial and final rinsing, and lauric acid in ethanol concentration were kept the same but the approach of functionalization was slightly altered due to the brittle nature of the silica nanochannels containing membrane restricting the stirring process. To functionalize the surface of the silica nanochannels, the SNC membranes were placed in a petri dish consisting of a mixture of lauric acid in ethanol and the mixture was heated at 50 °C until all the solution got evaporated. This approach of surface functionalization follows chemical vapor deposition (CVD) technique where the vapors of lauric acid gets attached to the walls of the nanochannels. After complete evaporation, the SNC membranes are rinsed with ethanol to remove any excess lauric acid being precipitated on the surface of the membrane and dried at 85 °C for 30 minutes (refer to **Figure 26** indicating the surface restructuring of chemical bond breaking and formation during surface wettability alteration).

For measuring the alteration in surface wettability, a contact angle measurement was performed. Ramé-Hart Contact Angle Goniometer 500 having a syringe volume of 250 µL, volume step of 10 µL, and droplet volume of 20 µL was used to measure the contact angle of the AAM and SNC membranes.

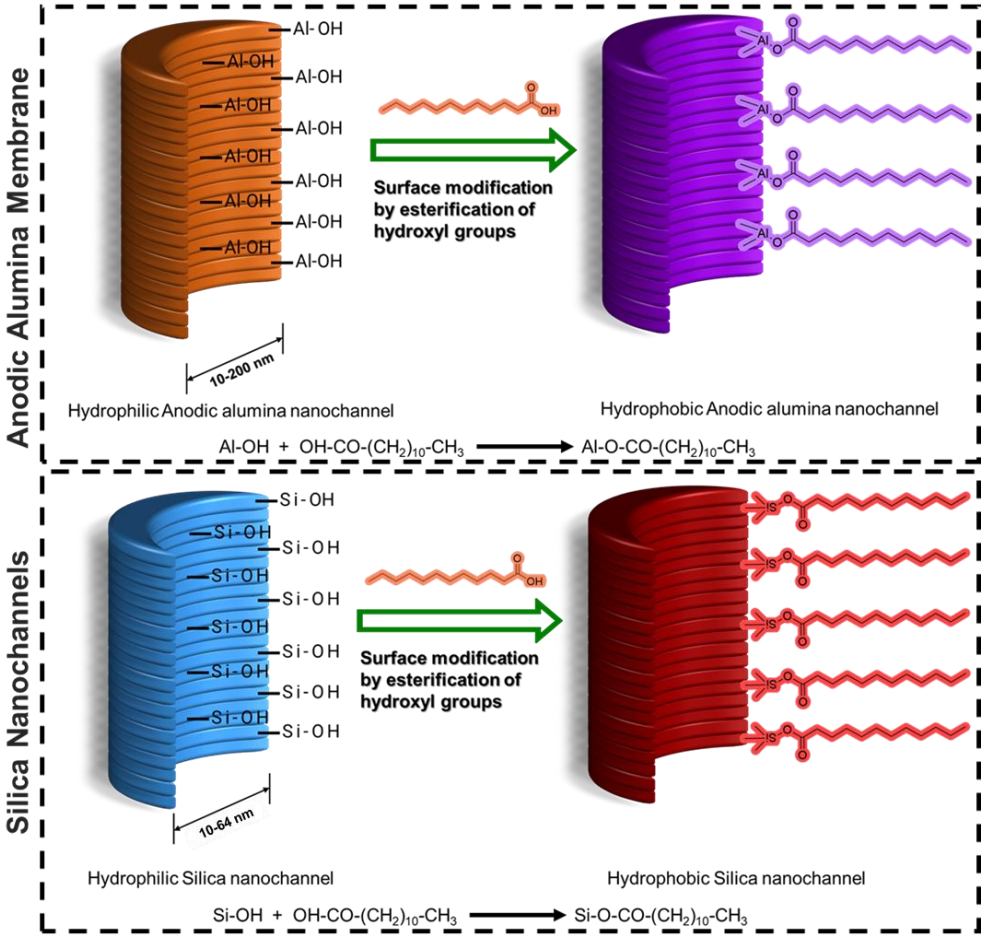

Figure 26 Schematic representation of the approach in varying the surface wettability of AAM and silica nanochannels

2.4. *Methodology for Determining the Zeta Potential for Anodic Alumina Membrane and Silica Nanochannels*

To determine the surface charge that forms between the surface of the nanochannels and the liquid medium, a zeta potential measurement was performed. Malvern Nano ZS Zetasizer was utilized to measure the zeta potential. Due to the nature of the samples, the as-purchased anodic alumina membrane and as-synthesized silica nanochannels in AAM were initially broken into a ~4x3 mm sample and then taped and placed on a

sample holder. This sample holder is then placed in a surface zeta potential cell and is tightened with a screw. The sample is then surface aligned using a height adjusting tool and then the zeta potential cell consisting of sample holder is then dipped in a quartz cuvette consisting of 1 mL tracer solution (polystyrene solution).

Before measurement, a fine alignment of the surface related to the laser is performed by adjusting the sample height and measuring the counts in the count rate meter. This fine adjustment is crucial such that the signal is high but the surface is still closer to the laser. Each sample had 15 sub-runs per measurement and 3 different measurements at 3 different locations. The wait time between measurements for the sample to re-equilibrate is 60 seconds.

2.5. *Loading of Ca-Carbonate in Hydrophilic Membranes*

The as-purchased AAMs as shown in **Figure SI9** and synthesized SNCs having diverse pore sizes are inherently hydrophilic and were used to precipitate calcium carbonate in nanoconfinement. A mixture of 0.1 M $Ca(NO_3)_2$. $4H_2O$ and 0.1 M $NaHCO_3$ were prepared and initially, the AAMs and SNCs were placed in a petri dish and 30 mL of 0.1 M $Ca(NO_3)_2$. $4H_2O$ solution was added into it and the solution was heated at 50 °C until all the solution evaporated following the CVD technique. Once the solution evaporates, the AAM and SNC membranes are washed with water to remove any excess nitrate-salt being precipitated and prevent the carbonate growth on the surface of the membrane. After water wash, the membranes are dried at 85 °C for 30 minutes. Then, the calcium nitrate-rich AAM and SNCs were placed in an aspiration setup and 0.5 mL of 0.1M $NaHCO_3$ solution was passed through the nanochannels as shown in **Figure**

SI10. This loading process was repeated 3 times and the reaction within the loaded membranes was allowed to proceed at room temperature conditions. While studying the influence of temperature on carbonate growth, immediately after loading bicarbonate solution the AAM and SNC membranes are immediately transferred into a vacuum oven (Thermo Scientific Lindberg Blue M) and heated at 45 °C for 15 minutes and rest of the reaction was allowed at 25 °C. As mentioned in Mamidala, A (under review), this induction time of 15 minutes was adequate to influence the final calcium carbonate growth during precipitation and crystallization.

2.6. *Loading of Ca- Carbonate in Hydrophobic Membranes*

The loading of Ca-nitrate and Na-bicarbonate solutions in surface-altered hydrophobic AAM and SNCs was slightly different employing the aspiration technique as shown in **Figure SI11**. To investigate the evolution of calcium carbonate polymorphs, 0.6 mL of 0.1M $Ca(NO_3)_2$. $4H_2O$ and 0.1 M $NaHCO_3$ solutions were passed through the membranes sequentially and this process was repeated 3 times. Once the solutions were passed, the membranes were stored at room temperature conditions allowing for the reaction to proceed. Similar to the hydrophilic loading method, to evaluate the effect of temperature on carbonate phase polymorphism, the loaded AAM and SNC membranes were transferred immediately into a vacuum oven and heated at 45 °C for 15 minutes and rest of the reaction was allowed at 25 °C.

For analyzing the calcium carbonate phase formation and transition over time, X-ray diffraction (XRD) measurement was performed using Bruker D8 Advance ECO Powder diffractometer having a Cu Kα radiation, operating voltage of 40 kV, and current of 25

mA. The XRD pattern was obtained in the range of 2θ= 7° to 80° after 6 hours till 96 hours of loading for both hydrophilic and hydrophobic AAM and SNC membranes.

2.7. *Quasi-Elastic Neutron Scattering (QENS) for Water Confined in Pure and Mg-Carbonate loaded Systems*

Quasi-Elastic Neutron Scattering (QENS) measurements were performed at a backscattering spectrometer (BASIS) [44] at the Spallation Neutron Source (SNS), Oak Ridge National Laboratory. QENS studies were performed on the hydrophilic and hydrophobic 10.48 nm SNC membrane loaded with pure water and magnesium carbonate for identifying the behavior and motion of confined water. For these measurements, a 1 mm thick, 5 cm tall, 3 cm wide flat plate aluminum sample holder, positioned perpendicular to the incident neutron beam, was used, in which the loaded membranes were arranged. To achieve the minimum thickness desired for neutron scattering measurements, 15 pure water and carbonate-loaded membranes are stacked on top of each other. For measurements, the spectrometer's chopper system was operated at 60 Hz, with the incident bandwidth centered at a wavelength λ= 6.4 Å. The detectors count rate was about 80 counts/sec at 1.7 MW of proton beam power to the neutron-producing target.

Initially, for pure water in hydrophilic SNC system, QENS measurements were performed at 298 K, followed by cooling to 10 K for collecting the resolution spectrum. Subsequently, a diagnostic measurement of the temperature-dependent energy-resolved "elastic" intensity scan was performed from 20 K to 320 K. This same methodology was also used for measuring the pure water in hydrophobic SNC system. On the other

hand, this methodology could not be used for samples with magnesium carbonate. Instead, each sample with magnesium carbonate was prepared in duplicate and measured separately, one for a diagnostic temperature-dependent energy-resolved "elastic" intensity scan from 20 K to 320 K, another for a QENS measurement at 298 K and subsequent resolution spectrum measurement at 10 K. This approach was necessitated by a concern that, unlike for the pure water samples, thermal cycling of the samples with magnesium carbonate during the diagnostic measurement might have caused a chemical reaction/alteration of the samples before the commencement of QENS measurements.

Finally, to subtract the background signal originated from the aluminum sample holder, a measurement with an empty sample holder was performed at 298 K.

2.8. *Simulation Methodology*

2.8.1. *Methodology for Modeling Amorphous Alumina and Silica Membranes*

To resemble the cylindrical AAM and SNC nanopores of diameter ≥ 10 nm used in experiments, water-exposed amorphous alumina and silica membranes were modeled *in-silico* (**Figure SI12**). To build an amorphous silica membrane starting from crystalline silica, the β-cristobalite structure of SiO_2 was obtained from the Crystallography Open Database (COD ID: 1010944) with unit cell parameters as a = b = c = 7.12 ± 0.01 Å and α = β = γ = 90°. [45] The unit cell was then replicated in space by 8×6×6 to obtain a larger membrane of crystalline silica with lengths along x, y, and z dimensions as approximately 5.7, 4.3, and 4.3 nm respectively. The methodology

developed by Iglesia et al. was adopted to generate an amorphous membrane from this crystalline silica slab. [46] First, the membrane structure was relaxed using the steepest descent minimization algorithm for 50,000 steps and then melted at 6000 K during the first 3000 NVT MD steps. This was followed by a 7 ps NVE run. A more realistic appearance of the modeled silica membrane was obtained by adding hydroxyl functionalities and H atoms to the valency unsaturated Si and O atoms respectively on the amorphous silica membrane, replicating the intrinsic hydroxyl groups observed on SBA-15 surfaces. [47,48] This addition was confined within 5 Å from the top of the silica surface. [49] The resultant hydrophilic silica membrane is henceforth termed as SIL_{hpl}. The steps followed to model this membrane are shown in **Figure SI13**.

The amorphous alumina membrane was modeled similarly. The unit cell structure of Corundum (Al_2O_3) was obtained from Crystallography Open Database (COD ID: 1000017) with unit cell parameters as a = b = 4.7606 ± 0.0005 Å, c = 12.994 ± 0.001 Å, and $\alpha = \beta = 90^o$, $\gamma = 120^o$. [50] The unit cell was replicated in space by 12×11×4 to generate a larger crystalline alumina membrane with lengths of ~ 5.7, 4.5, and 5.2 nm, respectively, along the x, y, and z directions. The resultant crystalline membrane was first subjected to steepest descent energy minimization for 50,000 steps followed by a 20 ps of equilibration at a temperature of 298 K in the NVT ensemble using a timestep of 0.1 fs. Thereafter, the system temperature was raised to and held at 5000 K for 200 ps using a timestep of 1 fs. [51,52] This helped the crystalline alumina to lose the structural order and gain an amorphous morphology. The system was then cooled down to 300 K from 5000 K in steps with 3000 K, 2000 K, 1000 K, 700 K, and 400 K as intermediate temperatures. To obtain a more realistic feature resembling commercial AAM

membranes' structural characteristics, hydroxyl functionalities, and H atoms were added to the valency unsaturated Al and O atoms on the amorphous alumina membrane. [47,48] Like silica, this addition was confined within 5 Å from the top of the alumina surface. [49] The resultant hydrophilic alumina membrane is called as ALO_{hpl}. A detailed workflow of modeling the amorphous alumina membrane is provided in **Figure SI14**.

To model hydrophobic amorphous silica/alumina membranes, lauric acid (LAU) molecules equivalent to a concentration of 20 g L^{-1} were attached to the exposed hydroxyl groups on the amorphous hydrophilic membrane surfaces by creating ester linkage between -OH (membrane) and -COOH (LAU). This leads to the addition of 15 LAU on SIL_{hpl} and 16 LAU on ALO_{hpl}. The resultant hydrophobic membranes are henceforth called SIL_{hpb} and ALO_{hpb} respectively. The crystal structure of LAU is obtained from the Cambridge Crystallography Database (CCDC number: 197251) [53] and manually grafted on the membrane surface using Gaussview. [54] To obtain the thermodynamically stable configurations of the hydrocarbon chains, SIL_{hpb} and ALO_{hpb} are first energy-minimized for 50,000 steps using steepest descent method followed by NVT equilibration for 5 ns using a timestep of 1 fs at 298 K. Throughout the dynamics, position restraint potential [55,56] was applied on silica/alumina atoms and the ester oxygens to retain the shape of the solid membrane and the spatial locations of the LAU grafts. The resultant equilibrated geometries of SIL_{hpb} and ALO_{hpb} can be seen in **Figure SI15**.

2.8.2. *Methodology for Modeling and Simulating Aqueous Solutions in Contact with Solid Membranes*

To model the aqueous solutions in contact with SIL_{hpl}, SIL_{hpb}, ALO_{hpl}, and ALO_{hpb}, a 10 nm water slab was placed on the top surface (functionalized surface in case of hydrophobic membranes) of the membranes along the z direction (**Figure SI12**). The resultant simulation cells are subjected to steepest descent energy minimization for 50,000 steps followed by NVT equilibration for 5 ns and NPT equilibration for 20 ns at a temperature of 298 K/318 K and pressure of 1 bar. This ensured the right density of water at the simulated temperature and pressure. A timestep of 1 fs was used throughout and position restraint potential [55,56] was intact on the silica/alumina membrane and the LAU grafts. The resultant aqueous solutions were used to add ions like Na^+, Ca^{2+}, HCO_3^-, and NO_3^- according to the concentration of $NaHCO_3$ and $Ca(NO_3)_2$ used in experiments i.e. 0.1 M and 0.1 M respectively. The number of ions added in each system can be found in **Table SI5** and the resultant simulation cells can be visualized in **Figure SI12**. The ionized systems were now equilibrated in the NVT ensemble for 10 ns and 50 ns in the NPT ensemble using a timestep of 1 fs. Starting structures were sampled from the last 5 ns of the NVT equilibration to run simulation triplicates with different random number seeds. All simulations were run at two temperatures, 25 ℃ (298 K) and 45 ℃ (318 K) at a pressure of 1 bar.

2.8.3. *Force Field and Simulation Parameters*

The non-bonding potential in silica/alumina membrane is described using ClayFF potential. [57] The bonding and non-bonding potential in LAU, Na^+, and HCO_3^- ions are defined using CHARMM CGENFF, [58,59] and those in Mg^{2+} and NO_3^- ions are defined using OPLS-AA. [60,61] The SPC/E model is used for water. [62] Holonomic constraints were applied on all bonds containing H using the LINCS algorithm. [63] Newton's equations of motion were solved using leap-frog integrator and the Verlet cut-off scheme was used for calculating the non-bonding interactions. [64,65] A cut-off distance of 12 Å was used for short-range electrostatics and van der Waals (vdW) interactions along with long-range dispersion correction for energy and pressure. Particle Mesh Ewald (PME) method with cubic interpolation was used for evaluating long-range electrostatics. [66] A grid spacing of 0.16 nm was used for PME. Temperature coupling in the system was achieved by velocity rescaling with a stochastic term using a time constant of 0.1 ps and reference temperature same as the target temperature i.e. either 298 K or 318 K. C-rescale barostat [67] was used for isotropic pressure coupling with a time constant of 2 ps and reference pressure of 1 bar. Periodic boundary conditions were applied in all directions of the simulation cells. GROMACS 2024 was used as the simulation software. [55,56] VMD was used for visualization of the trajectories, [68] and VMD and MATLAB R2023b were used for analysis.

3. Results and Discussions

3.1. *Characterization of Silica Nanochannels*

The synthesis of mesoporous silica nanochannels using a sol-gel approach is characterized by high surface area, and variable pore sizes and lengths, which increases their functional capability for encapsulation in biosensing and environmental applications. The sol-gel process is influenced by the hydrolysis, water/alcohol condensation reactions, and the self-assembly of silica precursors affecting the overall morphology of the mesoporous silica. [69] In this study, the silica precursor solution of varied concentrations is prepared and the solution is passed through the AAMs via CVD technique and aspiration. To confirm whether the SNCs were formed inside the AAM pores, the loaded membranes were directly imaged using a scanning electron microscope as shown in **Figure 27(a)(i)**. Based on this, we can conclude that the synthesis approach of SNCs and the excess removal of deposited silica on the surface of the AAM using ethanol was successful as the SNCs were formed inside the AAMs. For determining the morphology of the synthesized SNCs inside AAMs, the loaded membranes are dissolved in 10% H_3PO_4 solution for 24 hours and the SNCs are recovered through centrifugation. The recovered samples are then dried at 80 °C for 24 hours and then imaged under a microscope as shown in **Figure 27(a)(ii)**. A conclusion drawn over here is that the SNCs mostly have a uniform orientation and have a cylindrical channel morphology. The absence of any discrete particles confirms the formation of silica nanochannels. Once the morphology of the SNCs has been investigated, the subsequent step is to determine the pore size of the silica nanochannels synthesized using different precursor solution compositions. To determine the pore size,

8 membranes of the same composition were transferred into a BET glass tube and the samples were outgassed at 130 ℃ for 24 hours. After outgassing, the samples were analyzed from NLDFT adsorption model using liquid N_2 at 77 K. The pore size of silica nanochannels synthesized using 19 mL, 12.36 mL, and 18.54 mL ethanol are 10.48 nm, 49.098 nm, and 63.23 nm as shown in **Figure 27(b)**.

An FTIR measurement was carried out to examine the structure, type of bonds, and morphological assessment of silica nanochannels. [70,71] Although the SNCs were synthesized in AAM pores, the FTIR beam was unable to penetrate the nanopores and provide information about the SNCs. To overcome this drawback, the SNCs, which were etched in 10% H_3PO_4 solution, were utilized. Due to the dissolution of the AAM, the absorbance peaks generated from the SNCs of various pore sizes were evident as shown in **Figure 27(c)**. The SNCs of different pore sizes demonstrated major peaks around 870-880 cm^{-1} associated with Si-O-Si antisymmetric stretching, 960-970 cm^{-1} associated with Si-O stretching in the Si-O-H group, 1076-1090 cm^{-1} associated with the asymmetric vibrations of Si-O-Si, and 1620-1634 cm^{-1} associated with the scissor bending vibrations of O-H or the distortion of adsorbed water on the surface of Si-O-Si structure. [72–78] Furthermore, we can observe that as the pore size increases, FTIR peaks display a small red shift toward lower wavelengths attributing to an increase in the distance of the Si-O bond network. [79,80] This suggests that an open structure is formed, allowing the vibrations to occur more freely. [80] Based on the observed FTIR peaks, the structure of the nanochannels can be outlined by having a siloxane bond in the interior, while hydroxide bonded silica on the surface as shown in **Figure 27(d)**. Additionally, we observed a reduction in the intensity of the Si-O-Si peak around 1076-1090 cm^{-1},

typically found in the FTIR peaks of SNCs. This could be due to the role of the 10% H_3PO_4 solution, which was used to etch the SNCs before FTIR measurement.

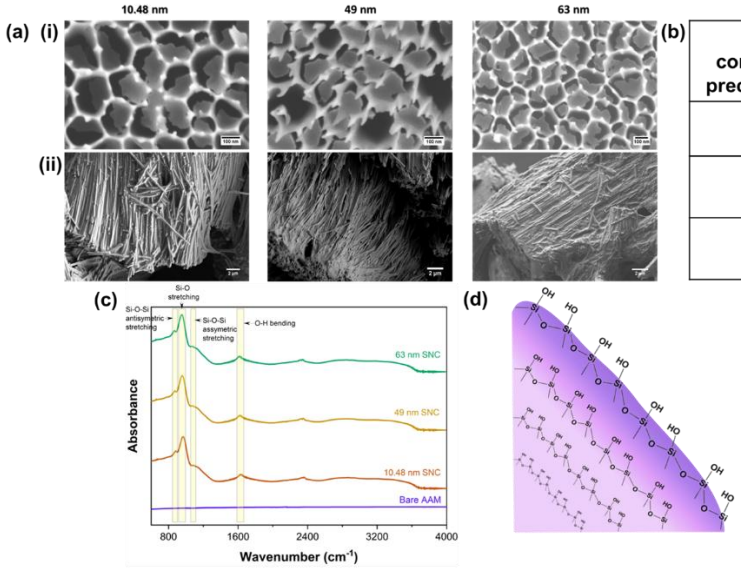

Ethanol concentration in precursor solution	Pore size determined by NLDFT method
19 mL	10.48 nm
12.36 mL	49.098 nm
18.54 mL	63.23 nm

Figure 27 (a) Architected silica nanochannels synthesized in anodic alumina membrane (i) before etching, and (ii) after etching using 10 wt% H_3PO_4 as viewed using a scanning electron microscope, (b) Pore size of silica nanochannels obtained from BET analysis (c) FTIR measurement to identify the bonding of silica nanochannels and (d) the representative bond formation based on FTIR determining the structure of silica nanochannels

3.2. *Surface Wettability of AAM and SNC Membranes*

The interfacial liquid-solid interactions and insights into materials' surface free energy can be deduced via contact angle measurements subsequently determining the ease of liquid spreading on the material. [81–83] These measurements determine the surface adsorption and adhesion with respect to hydrophilic or hydrophobic wettability. [84–86] In the current study, the contact angle measurement was performed using the sessile drop approach (**Figure 28**) where the water droplet was placed on the surface of the as-purchased, synthesized and the lauric acid functionalized AAM and SNC-loaded membranes. [87,88] The contact angles of 10 nm, 40 nm, and 200 nm hydrophilic and

hydrophobic AAMs are 43.1°, 24.6°, 23.9° and 118.2°, 113.6°, 93.9° respectively. Similarly, the contact angles of 10.48 nm, 49 nm, and 63 nm hydrophilic and hydrophobic SNC-loaded AAM membranes are 14.5°, 7°, 6.9°, and 97°, 96.4°, 92.3° respectively.

Based on these observations, we can extrapolate that the contact angle begins to recede as the pore size increases for both hydrophilic and hydrophobic membranes. This is associated with the phenomena of an increase in the opening size as the pore size increases, allowing for the liquid to pass through easily and hence reducing the contact angle. [89] Other factors like surface roughness, pore depth, and pore width will affect the AAM and SNC contact angle. [90,91] According to the results, we can conclude that the contact angle being highest in small pores is due to trapped air pockets in the pores restricting the liquid from penetrating and as the pore size increases, the trapped air is being released. [92] Furthermore, water penetration is high for larger pores displaying a reduction in contact angle. [93,94]

Silica nanochannels in this study are loaded inside anodic alumina membranes acting as a bi-material system where the contact angle is based on surface roughness and is highly dependent on material properties. [95,96] Based on reported literature by Sekiguchi et al. [97] the fabricated silica nanoparticles on an anodic aluminum oxide template displayed a reduction in contact angle in comparison with a pure anodic aluminum oxide template attributing to the role of silanol groups. [98] According to the investigation in the current study for silica nanochannels, the contact angle could then be affected by water uptake and pore sizes. Prior literature investigated that water adsorption into the silica nanopores increases as the pore size increases transitioning from a sparse monolayer to

bilayer formation. [99] This behavior is also specified where liquid penetration increases with increasing porosity or pore size. [90] These studies correspond to the results observed in contact angle measurement where there is a decrease in contact angle as the pore size increases for SNCs due to better water penetration.

For incorporating hydrophobicity these AAM and SNC nanochannels were immersed in a solution of lauric acid in ethanol. Based on the results, we observe the hydrophobicity of the membranes as the contact angle is >90°. Furthermore, we observe that as the pore size increases the contact angle begins to decrease for both AAM and SNC-loaded AAM membranes. This corresponds to the behavior of lauric acid where a larger pore size generally leads to a smaller contact angle while using lauric acid. [100] Furthermore, this effect also corresponds with solution adsorption and gas diffusion. [101–103] Smaller pores tend to adsorb and diffuse more lauric acid resulting in a higher contact angle whereas as the pores become larger, an increase in the immersion time is required to fill the pores with lauric acid molecules enhancing contact angle. [90,101,103] As the immersion time is kept constant irrespective of pore size, the dropping of contact angle for both AAM and SNC membranes is observed.

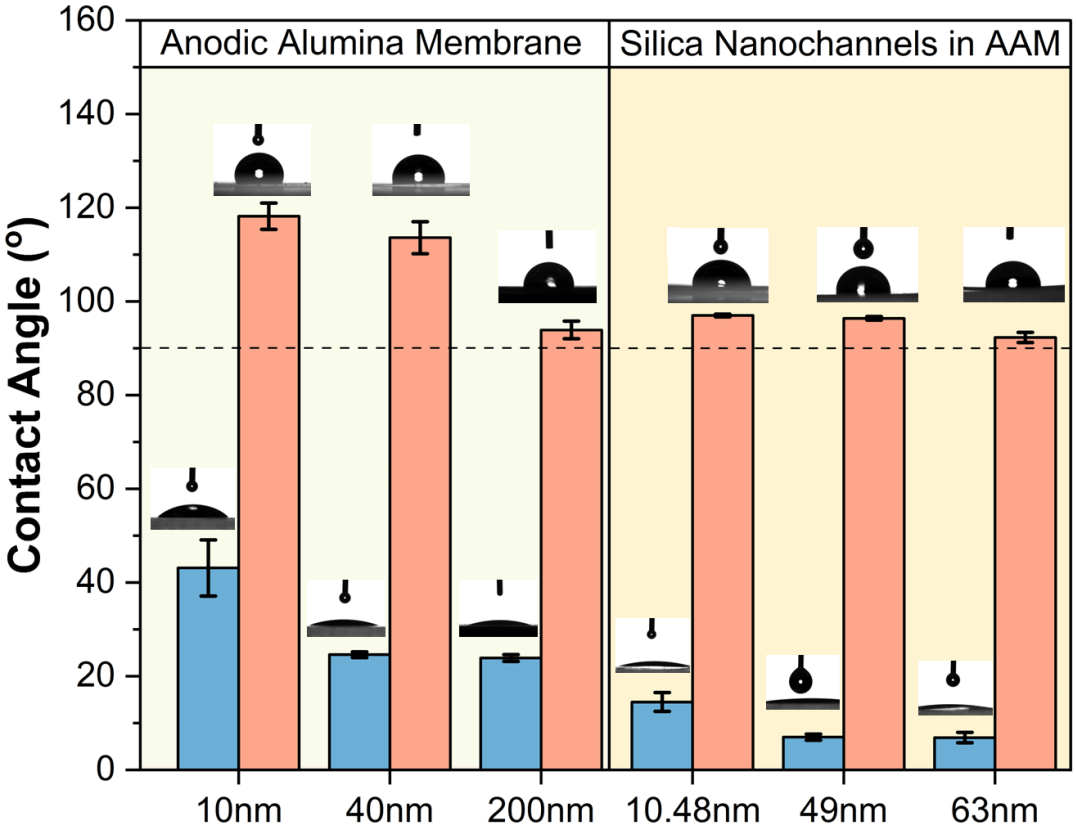

Figure 28 Determination of contact angle of hydrophilic and hydrophobic AAM and SNC surfaces of varying pore sizes

To further compare the hydrophobicity of the AAM and SNC membranes, **Figure 29** represents the variation of the number of membrane surface–interfacial water hydrogen bonds per water molecule ($N_{av,HB}$/water) with simulation time for SIL_{hpl}, SIL_{hpb}, ALO_{hpl}, and ALO_{hpb} at two temperatures, 25 ℃, and 45 ℃. As water in contact with the metal oxide surfaces is known to exhibit differential structural and dynamical properties, the water layer is divided into interfacial and bulk regions using MD simulation (**Figure SI16**). [104,105] Using the mass density of water along the normal direction (z-axis) of the membrane, the overall width of the interfacial water layer is found to vary from ~ 0.6 nm to 1.4 nm. For silica membranes, $N_{av,HB}$/water decreases by one order of magnitude when the surface is hydrophobic, however, for alumina membranes, the decrease is less

prominent. It is noteworthy that temperature exhibits a less significant effect on the hydrogen bonding propensity of the interfacial water with the solid surfaces which is also in agreement with the thermodynamically stable interfacial water layer in contact with the silica/alumina surface (**Table SI6**). Independent of the membrane hydrophobicity, the intramolecular hydrogen bonding network in bulk water is disrupted due to the presence of ions (**Figure SI17**) like Na^+, Ca^{2+}, HCO_3^-, and NO_3^-. From an average number of intramolecular hydrogen bonding as 4 in neat bulk water, this reduces to ~ 1.2 in the bulk region of the simulation cells in SIL_{hpl}, SIL_{hpb}, ALO_{hpl}, and $ALO_{hpb.}$ Modification of the water dipole-dipole interaction by the ion-dipole interaction between water and ions causes this significant change. [106]

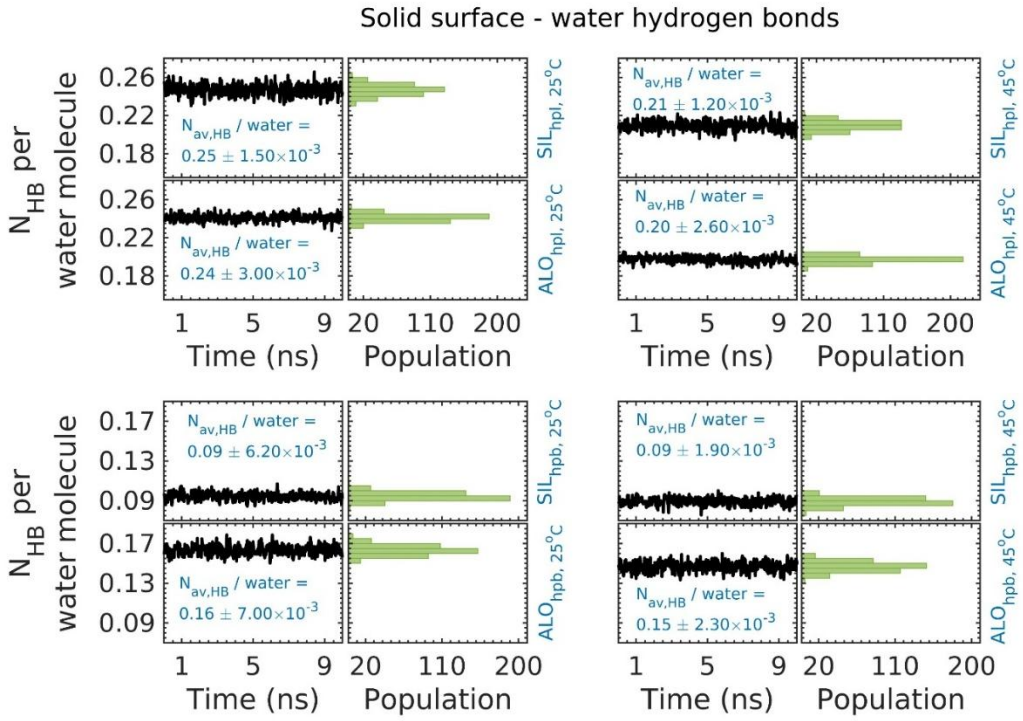

Figure 29 Variation of the number of hydrogen bonds (NHB) per water molecule between the membrane surface and interfacial water with time at temperatures 25 ℃ and 45 ℃. Last 10 ns of the simulation trajectories are used for calculation. A donor-acceptor distance cutoff of 3.5 Å and a donor-hydrogen-acceptor angle cutoff of 30° are used for calculating the hydrogen bonds. 'SIL' and 'ALO' represent silica

and alumina membrane respectively while 'hpl' and 'hpb' represent hydrophilic and hydrophobic membrane respectively. Beside each timeline plot, a distribution of the corresponding N_{HB} per water molecule is provided. The numbers within each subplot indicate the average N_{HB} per water molecule along with its standard deviation as obtained from simulation triplicates.

3.3. *Determining the Surface Charge of AAM and SNC-loaded AAM membranes*

The surface charge of nanochannels plays a crucial role in understanding the adsorption, interaction, transport, and reactivity of ions in the interfacial layers of the nanochannels and their ripple effect for the ions in the bulk regions. [107,108] Additionally, the surface charge in nanoconfined systems further affects the electrostatic interactions forming a double layer, and electrokinetic properties that reflect the behavior of liquid at the solid-liquid interface. [109–111] Moreover, the behavior of nanoconfined water film is notable as there is a more ordered hydrogen bonding network between the solid nano surfaces as the surface charge density increases promoting a dense water film. [112] Taking all the effects into account, the surface charge was investigated for AAM and SNC-loaded AAM membranes through zeta potential measurement for hydrophilic and hydrophobic surfaces with varying pore sizes. The average zeta potential for 10 nm, 40 nm, and 200 nm hydrophilic AAMs are -13.84 mV, -0.47 mV, and 3.67 mV whereas for hydrophobic AAMs are -16.66 mV, -14.1 mV, and -12.54 mV respectively. Similarly, the zeta potential for 10.48 nm, 49 nm, and 63 nm SNC-loaded AAM membranes are -9.35 mV, -2.36 mV, and -1.88 mV whereas for hydrophobic SNCs are -38.26 mV, -32 mV, and -5.07 mV respectively. All the zeta potential measurements concerning surface displacements are shown in **Figure 30(a)** and the average zeta potential for pore size and surface functionalization are shown in **Figure 30(b)**. The chief observation from the average zeta potential measurement data is that the hydroxide-predominant

hydrophilic surfaces have less negative potential than ester-predominant hydrophobic surfaces. Prior literature corroborates that zeta potential tends to become more negative in the presence of ester or carboxylic groups attributing to greater electron delocalization or charge group dissociation whereas for hydroxide groups the physical adsorption of the OH^- ions does not contribute significantly to negative potentials. [43,113–115] In addition, a decrease in the absolute value of zeta potential is observed as the pore size increases for both hydrophilic and hydrophobic surfaces and the absolute zeta potential of SNCs are higher than AAMs. The effect of increasing pore size is associated with the reduction in the fixed charge density, the surface area, and ion selectivity reducing the zeta potential values whereas the absolute value of SNCs is higher than AAMs due to the presence of the silanol group (Si-OH) on the surface of the nanochannels which can lose its proton and ionize readily contributing to higher negative charge. [116–120] The zeta potential of AAMs is less negative due to the built-in positive charge immediately after anodizing and the gradual formation of oxide layer over time results in slow creeping towards a negative charge. [120–122] These findings describe the variation in surface potential by changing the nano surface chemistry, the functionalized molecule, and pore sizes, which can substantially impact the ions in the interfacial region.

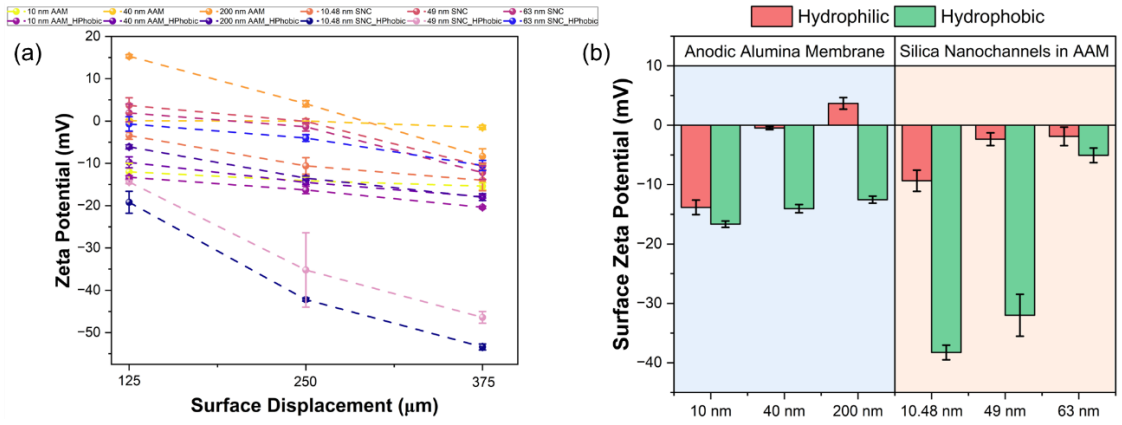

Figure 30 Determination of the zeta potential for AAM and SNC's of varying pore sizes and surface wettability with respect to surface displacement, (b) Indicates the average zeta potential for the respective AAM and SNC's of varying pore sizes and surface wettability

3.4. *Behavior of Calcium Ions Prior to Calcium Carbonate Crystallization*

The chemistry of the ions in the pre-nucleated condition can be understood from the classical MD simulations. Coordination characteristics of the Ca^{2+} ions are a major contributor in deciding the phases of calcium carbonate post-reaction. **Figure 31** represents the radial distribution function (g(r)) of the Ca^{2+} ions with respect to oxygens from water, NO_3^-, HCO_3^- ions, and the metal oxide membrane at different physicochemical conditions. Whether the interface or the bulk region, water molecules and the anions (NO_3^- and HCO_3^-) are seen to form the first coordination layer at ~ 0.23 nm around Ca^{2+} ions at 25 °C and 45 °C in both hydrophilic and hydrophobic conditions. Overall, the local density of the oxygen atoms around Ca^{2+} ions is observed to follow the order HCO_3^- > NO_3^- > water > membrane. The maximum local density of bicarbonate ions in the first coordination shell of Ca^{2+} is observed in the hydrophobic silica interface at 25 °C whereas it is the minimum for the hydrophobic alumina interface at the same temperature. Similarly, the nitrate ions exhibit a maximum local density in the case of interfacial ALO_{hpb} at 25 °C and a minimum in the bulk region of the same system at 45 °C. Water oxygens acquire their maximum local density around Ca^{2+} ions in the interfacial hydrophobic alumina at 25 °C and a minimum in the bulk region of the system SIL_{hpl} at 45 °C. However, the membrane oxygens exhibit a moderately higher density in the hydrophobic silica interfaces at 45 °C compared to other physicochemical conditions in either silica/alumina. Overall, local density analysis from the

representative g(r) profiles of pre-nucleated Ca^{2+} ions gives an idea that the probability of forming anhydrous phases of calcium carbonate like calcite, aragonite, and vaterite is higher than the hydrated phases and this is most favorable in the presence of a hydrophobic silica interface at room temperature.

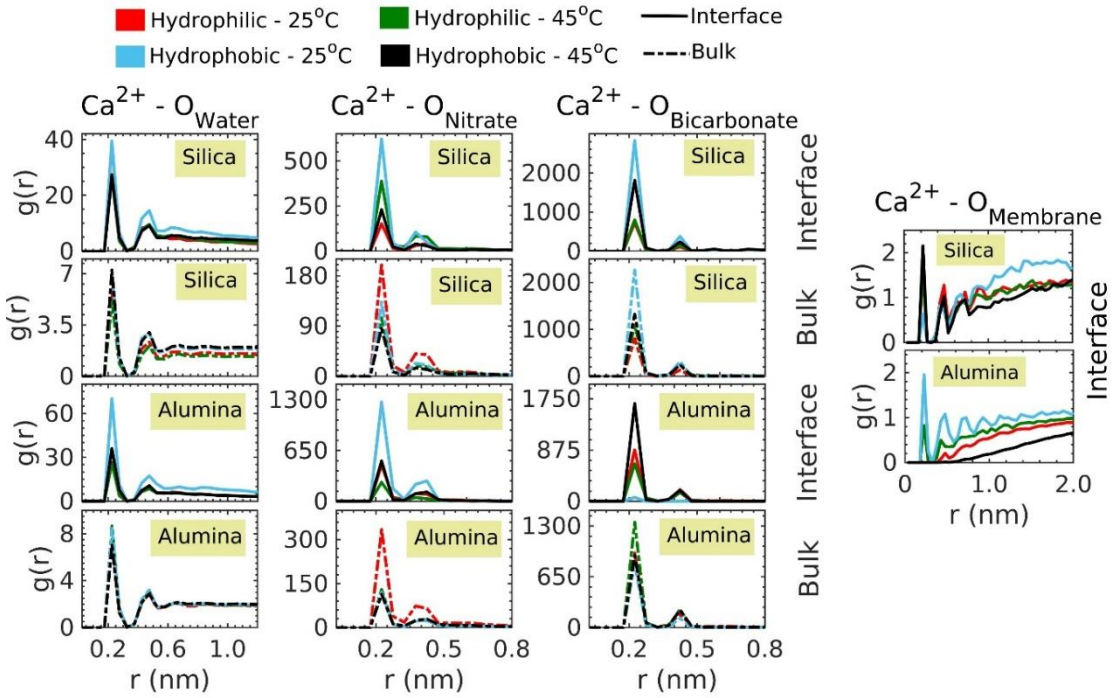

Figure 31 Representative radial distribution function (g(r)) of calcium ions with respect to oxygens from water molecules (O_{Water}), nitrate ($O_{Nitrate}$), and bicarbonate ($O_{Bicarbonate}$) ions as well as membrane oxygens ($O_{Membrane}$) as a function of distance (r) in the interfacial and bulk regions at temperatures of 25 °C and 45 °C in hydrophilic and hydrophobic silica and alumina membranes. The interfacial width is obtained from density profiles as shown in Figure SI8 whereas the rest of the simulation cell is considered as bulk.

However, obtaining the exact coordination number of pre-nucleated Ca^{2+} ions pertaining to several anhydrous and hydrated phases is a crucial task, and averaging over multiple starting configurations is necessary. Therefore, **Figure 32** and **Figure SI18** represent the variation of the coordination number (n(r)) of Ca^{2+} with respect to water, nitrate, bicarbonate ions, and membrane oxygens as a function of radial distance.

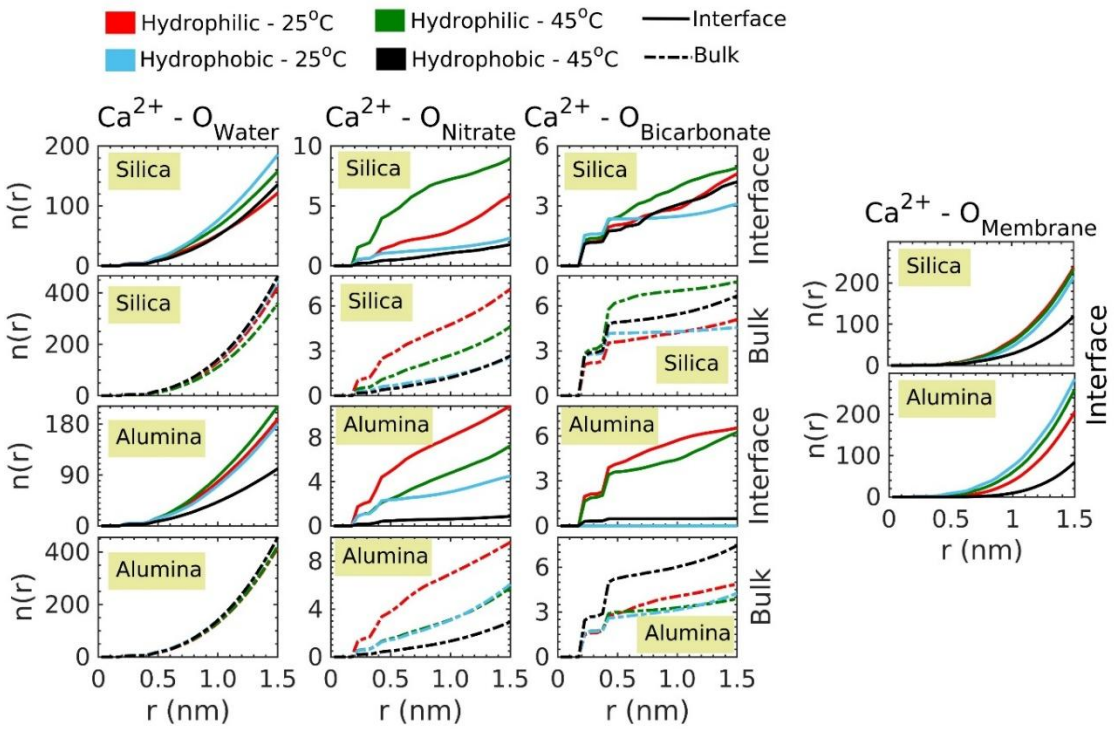

Figure 32 Representative variation of the coordination number (n(r)) of calcium ions with respect to oxygens from water molecules (O_{Water}), nitrate ($O_{Nitrate}$), and bicarbonate ($O_{Bicarbonate}$) ions as well as membrane oxygens ($O_{Membrane}$) as a function of distance (r) in the interfacial and bulk regions at temperatures of 25 °C and 45 °C in hydrophilic and hydrophobic silica and alumina membranes. The interfacial width is obtained from density profiles as shown in Figure SI16 whereas the rest of the simulation cell is considered as bulk

Table 8 and **Table 9** list the corresponding coordination numbers respectively from the first and (first + second) coordination shells of Ca^{2+} ions in the interface considering the simulation triplicates. On average, it is observed that the first hydration shell around interfacial Ca^{2+} ions is composed of ~ 2 to 4 water molecules in line with previous literature, [123] and the maximum anhydrous coordination is seen in the case of hydrophilic alumina interface at 25 °C. The scenario changes moderately as the second coordination shell is taken into consideration. The maximum values of anhydrous coordination are present in the hydrophilic silica and alumina interfaces at 45 °C as well as in the hydrophilic alumina interface at 25 °C. It is important to note that although the

coordination contribution of water and non-water oxygens in the first coordination shell of interfacial Ca^{2+} ion is comparable, the second coordination shell is always dominated by oxygens from water. Therefore, it is intelligible that the phases of calcium carbonate post-nucleation are mostly guided by the changes in the first coordination shell of Ca^{2+}. In a nutshell, pre-nucleated Ca^{2+} ions have a primary coordination number (C.N.) of 6 (3 from water and 3 from non-water oxygens) in SIL_{hpl} at 25 °C and 45 °C and SIL_{hpb} at 25 °C, a primary C.N. of 5 (2 from water and 3 from non-water oxygens) in SIL_{hpb} at 45 °C, C.N. of 7 (3 from water and 4 from non-water oxygens) in ALO_{hpl} at 25 °C and 45 °C, C.N. of 6 (4 from water and 2 from non-water) in ALO_{hpb} at 25 °C, and C.N. of 2 (1 from water and 1 from non-water) in ALO_{hpb} at 45 °C. On the other hand, as crystalline phases are associated with specific interatomic distances in the unit cell, **Figure 33** represents the distribution of the average distance between Ca^{2+} ion and oxygen atoms from water, bicarbonate, and nitrate ions in the silica/alumina interfaces. The average distance between Ca^{2+} and oxygens from different sources (water, bicarbonate, and nitrate ions) is seen to vary from 2.24 to 2.37 Å essentially leaning toward calcite phases post-nucleation (**Table SI7**). [124] To extract the exact phases after the reaction, XRD patterns of the crystals are analyzed as explained in **section 3.5 and 3.6**.

Table 8 Coordination number of oxygen atoms from water (O_{Water}), nitrate ions ($O_{Nitrate}$), bicarbonate ions ($O_{Bicarbonate}$), and silica/alumina membrane ($O_{Membrane}$) in the first coordination shell of Ca2+ ions in the interfacial region of hydrophilic and hydrophobic silica and alumina membranes at temperatures 25°C and 45°C. The standard deviations in each case are obtained from simulation triplicates. The empirical formulae are written in terms of coordination from water (O_W) and coordination from non-water species (O_{N+B+M}).

Membrane	Surface characteristic	T (°C)	Coordination number					
			Ca^{2+} - O_{Water}	Ca^{2+} - $O_{Nitrate}$	Ca^{2+} - $O_{Bicarbonate}$	Ca^{2+} - $O_{Membrane}$	Total anhydrous coordination	Empirical formula
Silica	Hydrophilic	25	3.27 ± 0.45	0.53 ± 0.40	1.20 ± 0.33	0.82 ± 0.28	2.55	$Ca(O_W)_3(O_{N+B+M})_3$
		45	2.79 ± 0.20	1.08 ± 0.43	1.57 ± 0.27	0.82 ± 0.20	3.47	$Ca(O_W)_3(O_{N+B+M})_3$
	Hydrophobic	25	3.03 ± 0.28	0.88 ± 0.29	1.77 ± 0.23	0.20 ± 0.05	2.85	$Ca(O_W)_3(O_{N+B+M})_3$
		45	1.73 ± 1.49	0.44 ± 0.34	2.00 ± 1.27	0.73 ± 0.20	3.17	$Ca(O_W)_2(O_{N+B+M})_3$
Alumina	Hydrophilic	25	3.08 ± 0.39	1.40 ± 0.34	1.88 ± 0.11	0.53 ± 0.31	3.81	$Ca(O_W)_3(O_{N+B+M})_4$
		45	2.59 ± 0.64	1.46 ± 0.58	1.72 ± 0.48	0.60 ± 0.22	3.78	$Ca(O_W)_3(O_{N+B+M})_4$
	Hydrophobic	25	3.78 ± 0.27	0.63 ± 0.46	0.40 ± 0.64	0.99 ± 0.41	2.02	$Ca(O_W)_4(O_{N+B+M})_2$
		45	1.36 ± 0.76	0.18 ± 0.06	0.51 ± 0.18	0.50 ± 0.00	1.19	$Ca(O_W)_1(O_{N+B+M})_1$

Table 9 Coordination number of oxygen atoms from water (O_{Water}), nitrate ions ($O_{Nitrate}$), bicarbonate ions ($O_{Bicarbonate}$), and silica/alumina membrane ($O_{Membrane}$) in the first and second coordination shells of Ca2+ ions in the interfacial region of hydrophilic and hydrophobic silica and alumina membranes at temperatures 25°C and 45°C. The standard deviations in each case are obtained from simulation triplicates. The empirical formulae are written in terms of coordination from water (O_W) and coordination from non-water species (O_{N+B+M}).

Membrane	Surface characteristic	T (°C)	Coordination number					
			Ca^{2+} - O_{Water}	Ca^{2+} - $O_{Nitrate}$	Ca^{2+} - $O_{Bicarbonate}$	Ca^{2+} - $O_{Membrane}$	Total anhydrous coordination	Empirical formula
Silica	Hydrophilic	25	10.74 ± 1.32	1.41 ± 1.08	2.04 ± 0.73	4.70 ± 0.60	8.13	$Ca\ (O_W)_{11}(O_{N+B+M})_8$
		45	11.00 ± 0.64	2.74 ± 1.17	2.99 ± 0.63	4.22 ± 0.94	9.95	$Ca\ (O_W)_{11}(O_{N+B+M})_{10}$
	Hydrophobic	25	12.07 ± 0.55	2.03 ± 1.02	3.23 ± 0.77	1.61 ± 0.30	6.87	$Ca\ (O_W)_{12}(O_{N+B+M})_7$
		45	7.30 ± 6.75	0.66 ± 0.79	2.47 ± 2.86	3.49 ± 1.01	6.62	$Ca\ (O_W)_7(O_{N+B+M})_7$
Alumina	Hydrophilic	25	12.10 ± 1.44	3.35 ± 1.26	3.69 ± 0.31	2.76 ± 0.23	9.8	$Ca\ (O_W)_{12}(O_{N+B+M})_{10}$
		45	10.67 ± 1.58	3.83 ± 2.11	3.48 ± 0.98	2.63 ± 1.06	9.94	$Ca\ (O_W)_{11}(O_{N+B+M})_{10}$
	Hydrophobic	25	12.69 ± 1.10	1.47 ± 1.06	0.62 ± 1.02	6.63 ± 1.24	8.72	$Ca\ (O_W)_{13}(O_{N+B+M})_9$
		45	4.96 ± 2.35	0.47 ± 0.25	0.87 ± 0.46	4.42 ± 0.00	5.76	$Ca\ (O_W)_6(O_{N+B+M})_6$

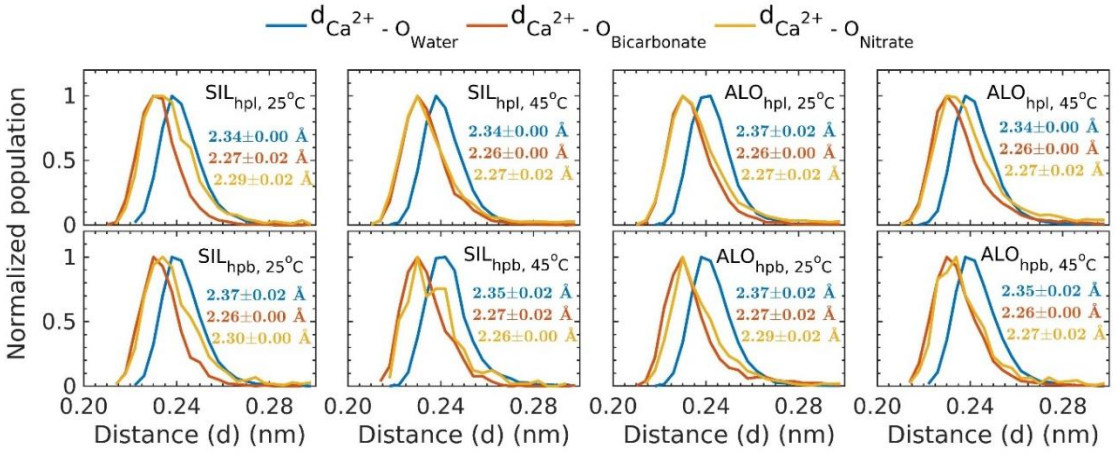

Figure 33 Representative variation of the distance between Ca^{2+} ions and oxygens from water (O_{Water}), bicarbonate ($O_{Bicarbonate}$), and nitrate ($O_{Nitrate}$) ions in the interfacial regions of the respective simulation cells containing hydrophilic and hydrophobic silica and alumina membranes at temperatures 25 °C and 45 °C. The interfacial width is obtained from density profiles as shown in Figure SI8 whereas the rest of

the simulation cell is considered as bulk. The calculations are confined within the first coordination shell of Ca^{2+} ions as obtained from Figure 8 and the last 10 ns of the respective trajectories is used in this regard. The numbers inside each subplot represent the average distance between Ca^{2+} and O_{Water} (blue), Ca^{2+} and $O_{Bicarbonate}$ (brown), and Ca^{2+} and $O_{Nitrate}$ (yellow) along with the corresponding standard deviations evaluated from simulation triplicates.

On the other hand, the width of the bulk region of the simulation cell is obtained by subtracting the interfacial width (**Figure SI16**) from the total length of the cell along the normal direction of the membranes. In the bulk phase, the total coordination number of Ca^{2+} ions (**Table SI8**) stays nearly invariant for the hydrophilic systems compared to the interface, however, increases significantly for the hydrophobic systems with higher contribution from water oxygens as the augmenting distance from the hydrophobic metal oxide surface helps closer proximity of water with respect to Ca^{2+}. **Figure 34** shows a few representative structures of Ca^{2+} ions surrounded by water, NO_3^-, HCO_3^- ions, and silica/alumina membrane oxygens.

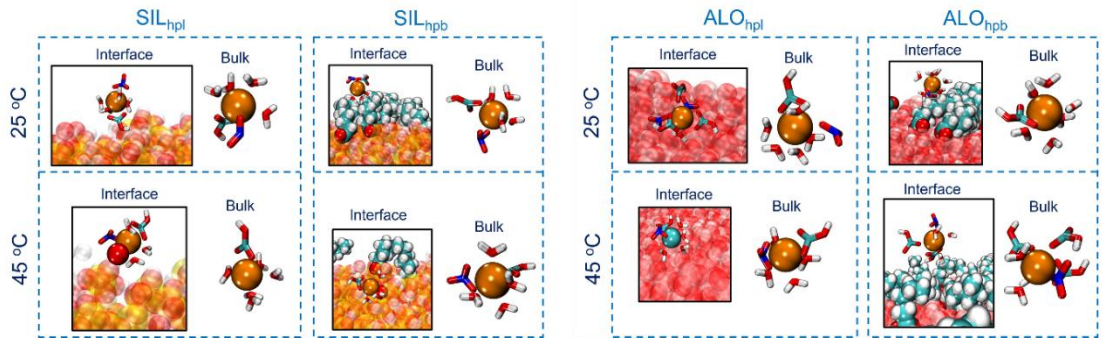

Figure 34 Simulation snapshots representing the interfacial and bulk Ca^{2+} ions surrounded by water, NO3-, HCO3- ions, and hydrophilic/hydrophobic silica/alumina membrane in the first coordination shell at temperatures 25 °C and 45 °C. Ca^{2+} ions are represented as yellow ochre vdW spheres whereas water, nitrate, and bicarbonate ions are represented as ball and stick models. O, N, C, and H in water, and the anions are shown in red, blue, cyan, and white respectively. The silica and alumina membranes are shown as transparent (opaque if within the primary coordination shell of Ca^{2+}) vdW spheres with Si, Al, O, and H in yellow, mauve, red, and white respectively. The lauric acid (LAU) chains are represented as vdW chains with C, O, and H in cyan, red, and white respectively.

3.5. *Calcium Carbonate Crystallization and Phase Evolution in Nano-Confined AAMs Under Various Physicochemical Conditions*

A mixture of 0.1 M calcium nitrate tetrahydrate and 0.1 M sodium bicarbonate is passed through the hydrophilic and hydrophobic AAMs having 10, 40, and 200 nm pore sizes. Once the mixture is passed through the nanochannels, the reaction is allowed to proceed at 25 °C and 45 °C. For the identification of different calcium carbonate phases formed in different pore sizes and physicochemical conditions, X-ray diffraction (XRD) measurements were performed after 6, 24, 48, 72, and 96 hours of loading as shown in **Figure 35**. By discerning the XRD peaks, the major phases formed are calcite, vaterite, aragonite, and the hydrated phase of ikaite in various environments. The XRD pattern exhibits the dominant growth of the (104), (006), (110), (116) plane of calcite, (110), (112), (100) plane of vaterite, and (011) plane of aragonite in 10, 40, and 200 nm hydrophilic AAMs aged at 25 °C and 45 °C. In hydrophobic AAMs, the dominant growth is observed at (104), (012), (110) plane of calcite, (104), (112), (002), (100), (102) plane of vaterite, (111) plane of aragonite, and (002), (202) plane of ikaite aged at 25 °C and 45 °C. Prior literature indicates that the XRD patterns that attribute to high crystallinity are the (104), (110), (113), and (116) planes for the rhombohedral structure of calcite, (100), (101), (110) planes for hexagonal vaterite, (110), (111), (112) plane for orthorhombic aragonite, and (001) plane for monoclinic ikaite, which are evident in the current study. [123,125–127] Through observation, we can also deduce that as the pore size of the AAMs increases, the XRD peaks in hydrophilic and hydrophobic conditions tend to shift from broad to sharp peaks, attributing to lattice deformation and microstructural parameters. [128–130]

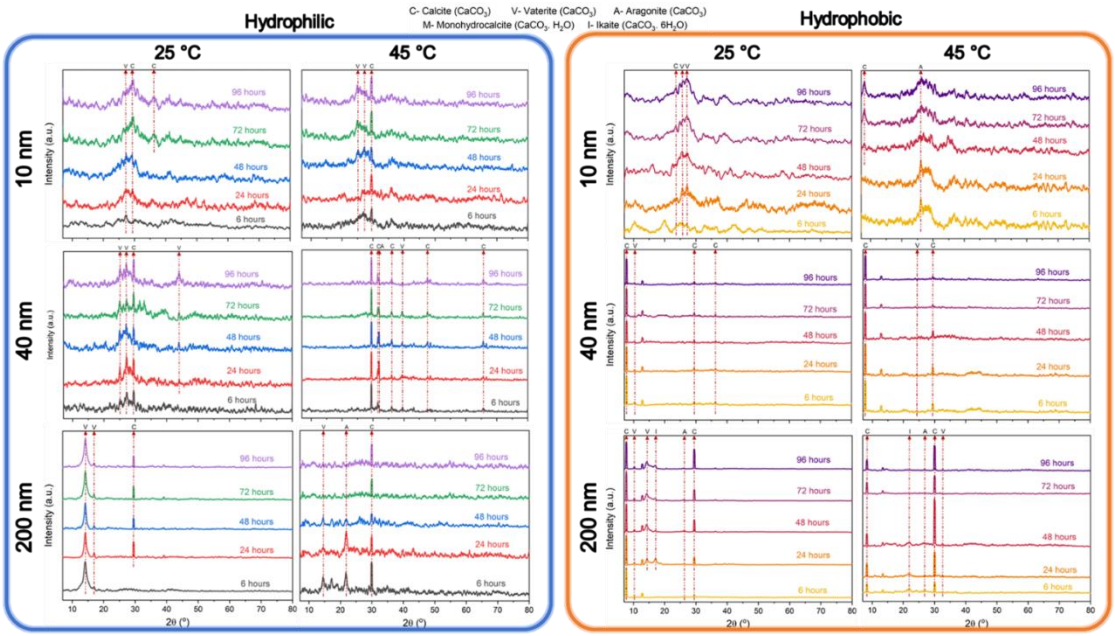

Figure 35 X-ray diffraction (XRD) measurement of calcium carbonate evolved in anodic alumina membrane of varied pore size, reaction temperature, and surface wettability after 6 hours to 96 hours of loading. The color difference is only a representation of the measurements at different time intervals.

The quantitative weight % of crystallized calcium carbonate phases are measured through XRD for hydrophilic and hydrophobic membranes of varying pore sizes and reaction temperatures as shown in **Figure 36**. In hydrophilic AAM, the phase transition in confinement entirely follows the bulk phase transition mechanism where amorphous calcium carbonate (ACC) transitions into metastable vaterite then aragonite, and finally into water-insoluble and stable calcite. [29] In 10 nm AAMs, the polymorph transition of vaterite into calcite is observed at both 25 and 45 °C. In 40 nm AAMs, the transition of vaterite into calcite is observed at 25 °C whereas at 45 °C, metastable vaterite and aragonite transition into stable calcite is seen. In 200 nm AAMs, the phase transition follows vaterite to calcite mechanism at 25 °C and vaterite to aragonite to calcite mechanism at 45 °C. In all the pore sizes, the weight % of calcite is higher by the end

of 96 hours after loading attributed to the water dehydration or the onset of calcite being faster at 45 °C.

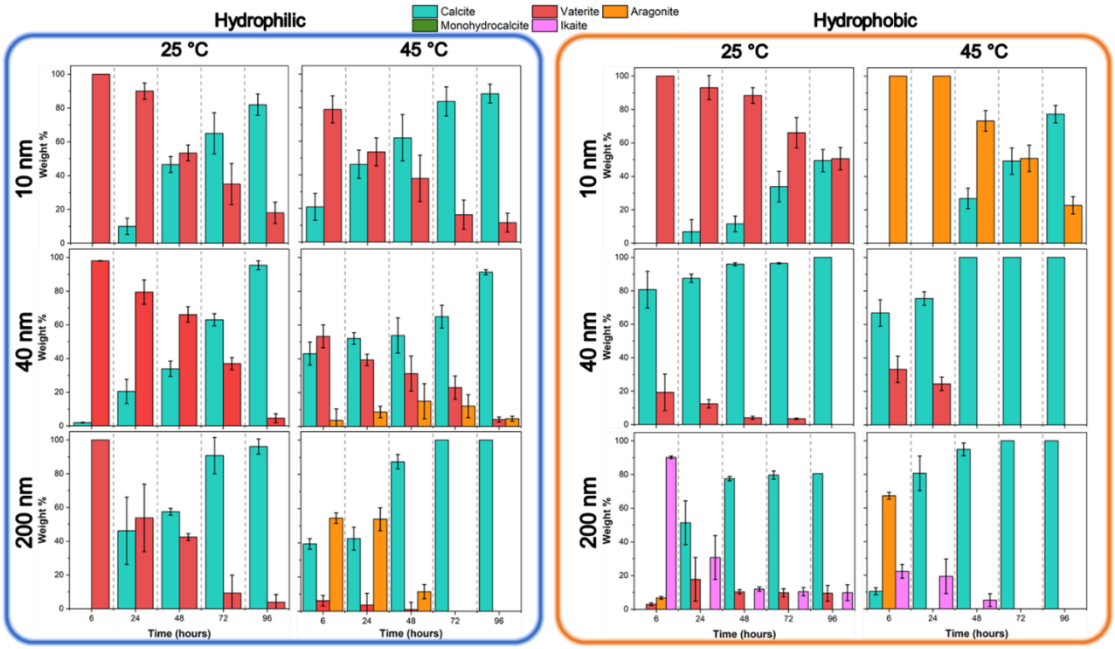

Figure 36 Phase polymorph evolution of calcium carbonate in anodic alumina membranes of varied pore size, reaction temperature, and surface wettability after 6 hours to 96 hours of loading. The color difference is only a representation of the different $CaCO_3$ phases.

In hydrophobic AAMs, due to the surface charge being more negative than the hydrophilic counterparts as analyzed through zeta potential measurement, the stability of stable calcium carbonate phases is higher due to electrostatic interaction. In 10 nm hydrophobic AAMs, vaterite to calcite transition is observed at 25 °C whereas aragonite to calcite transition is observed at 45 °C indicating the impact of temperature-dependent nucleation mechanism. [131] In 40 nm hydrophobic AAMs, vaterite to calcite mechanism is observed at 25 °C and 45 °C with a faster onset of stable phase at higher temperature. In 200 nm hydrophobic AAMs, we observe the precipitation of ikaite at 25 °C and as the reaction is allowed to proceed, the transition into vaterite and then into calcite is observed. After 48 hours of loading, the entire system gets stabilized with a slight

change in weight % of calcium carbonate phases. This study validates that the unstable phases become much more stabilized due to the influence of nanoconfinement. As the reaction temperature increases, the phenomenon of dehydration of the hydrated phase of calcium carbonate results in the dissipation of ikaite and the simultaneous transition of aragonite into calcite. This study corroborates the mechanism of confined growth of the hydrated phase and its transition into metastable and stable calcium carbonate in large pore sizes. [132,133] Concurrently, as the pore size decreases the solvation layers begin to merge and the layers of water are pushed out of the nanopore thus facilitating dehydration. [134,135]

The mechanism of calcium carbonate phase formation and transition in nanoconfinement will be confirmed if the grain size is smaller than the pore size of the nanochannel. To evaluate this phenomenon, the XRD pattern is considered and the Debye Scherrer equation is used which is shown below in **equation (1)**,

$$D = \frac{K.\lambda}{B(2\theta).cos\theta} \quad (1)$$

Where, the value of K=0.9 (Scherrer constant), λ is the wavelength of the X-ray source (Cu Kα= 0.154 nm), 2θ is the Bragg angle, B(2θ) is the full width at half maximum (FWHM), and D is the crystallite size. The crystallite size denotes the size of the single crystal of a particular phase but in this study, we investigate the grain size by considering all the crystallite sizes from multiple polymorphs and measuring the average size as shown in **Figure 37**. [136] Overall the mechanism of grain size evolution follows three steps in this system- crystal growth, stabilization, and dissolution. Within these steps, crystal growth and stabilization are associated with the nature of molecular interactions

and the nucleation mechanism following the classical mechanism of Ostwald Ripening or non-classical theories. The crystal dissolution mechanism is a diffusion or kinetically controlled mechanism that can be influenced by surface tension, viscous dissipation, and ion concentration, leading to varied dissolution dynamics. [137–139] Furthermore, these crystal growth, stabilization, and dissolution mechanisms are influenced by the 2-D transport of fluids in confined volumes which creates a concentration gradient between the interfacial and the bulk layers, leading to unique crystal or grain behaviors. [140] In the 10 nm hydrophilic AAMs, the grain size increases from 5.65 nm to 7.5 nm over 96 hours of loading at 25 °C while the grain size increases from 8.7 nm to 9 nm over 96 hours at 45 °C. In both systems, the crystal mechanism follows dissolution, crystal growth, and stabilization. In 40 nm hydrophilic AAMs, the grain size increases from 12.7 nm to 15.2 nm demonstrating a crystal growth mechanism at 25 °C whereas the grain size reduces at 45 °C from 17.3 nm to 15.9 nm demonstrating crystal growth and dissolution mechanism. In 200 nm hydrophilic AAMs, the grain size increases from 9.3 nm to 18.2 nm at 25 °C whereas the grain size increases from 15.7 nm to 24.5 nm at 45 °C where both systems exhibit crystal growth and stabilization mechanism.

In hydrophobic AAMs, the use of surface modifiers in carbonation reactions promotes narrow pore size distribution and constant particle morphology and, in this study, the influence of lauric acid as a surface wettability modifier is critical in influencing the grain size and the growth mechanism. [141] In 10 nm hydrophobic AAMs, the grain size increases from 7.4 nm to 8.95 nm demonstrating crystal growth, dissolution, and stabilization mechanism at 25 °C whereas, at 45 °C, the grain size increases from 3.3 nm to 6.4 nm demonstrating stabilization and growth mechanism. In 40 nm hydrophobic

AAMs, the grain size increases from 17.7 nm to 23.5 nm exhibiting dissolution and growth mechanism at 25 °C whereas at 45 °C, the grain size increases from 18.3 nm to 24.8 nm exhibiting crystal growth and stabilization mechanism. In 200 nm hydrophobic AAMs, the grain size decreases from 21 nm to 17 nm exhibiting dissolution and stabilization mechanism at 25 °C while the grain size increases from 14 nm to 21.4 nm exhibiting crystal growth mechanism at 45 °C.

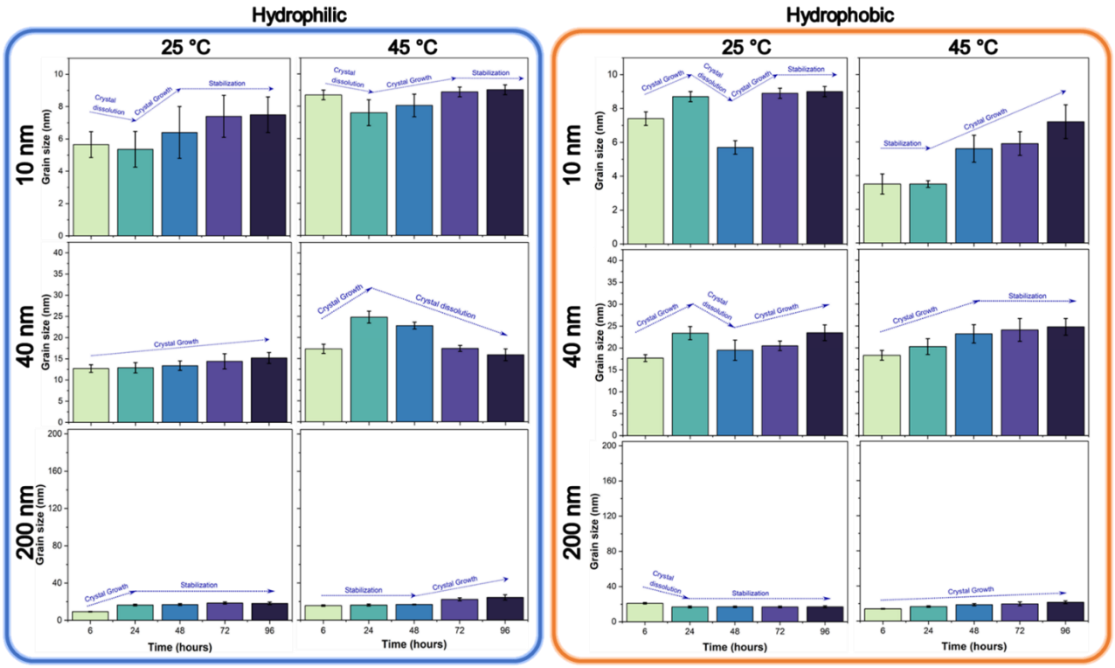

Figure 37 Grain size evolution of calcium carbonate in anodic alumina membranes of varied pore size, reaction temperature, and surface wettability after 6 hours to 96 hours of loading calculated using the Scherrer equation. The color difference is only a representation of the different time intervals.

3.6. *Calcium Carbonate Crystallization and Phase Evolution in Nano-Confined SNCs Under Various Physicochemical Conditions*

The crystallization of calcium carbonate in SNCs is distinct from the one observed in AAMs. This dissimilar behavior is due to the role of silica nano-walls enhancing the stabilization of the prenucleation clusters, the kinetics of phase transition from

amorphous to crystalline, and crystal size dynamics. [142,143] Furthermore, the silica nano-walls showcase more negative surface charge as indicated in this study which alters the interfacial fluid structure affecting the distribution and bonding network of the counter ions affecting the final crystal structure. [144] To investigate this change in crystal structure, XRD measurements were performed after loading 0.1 M $Ca(NO_3)_2$. $4H_2O$ and 0.1 M $NaHCO_3$ into these SNCs and aged at different conditions. Based on XRD data, the predominant phases observed over 96 hours of loading are calcite, vaterite, aragonite, and hydrated phases like monohydrocalcite and ikaite as shown in **Figure 38**. In hydrophilic SNCs, the major phases and peaks observed are associated with calcite and vaterite which could be owing to reduced hydration around calcium ions. [123] The XRD pattern from calcium carbonate crystallized in SNCs showcases (104), (113) planes of calcite, and (004), (110), (112), (114), (300), (118) planes of vaterite in hydrophilic conditions aged at 25 °C and 45 °C. In hydrophobic conditions aged at 25 °C and 45 °C, we perceive the formation of (104), (110), (012) planes of calcite, (100), (101), (112), (204) planes of vaterite, (111) plane of aragonite, (100), (111), (201) planes of monohydrocalcite, and (200) plane of ikaite.

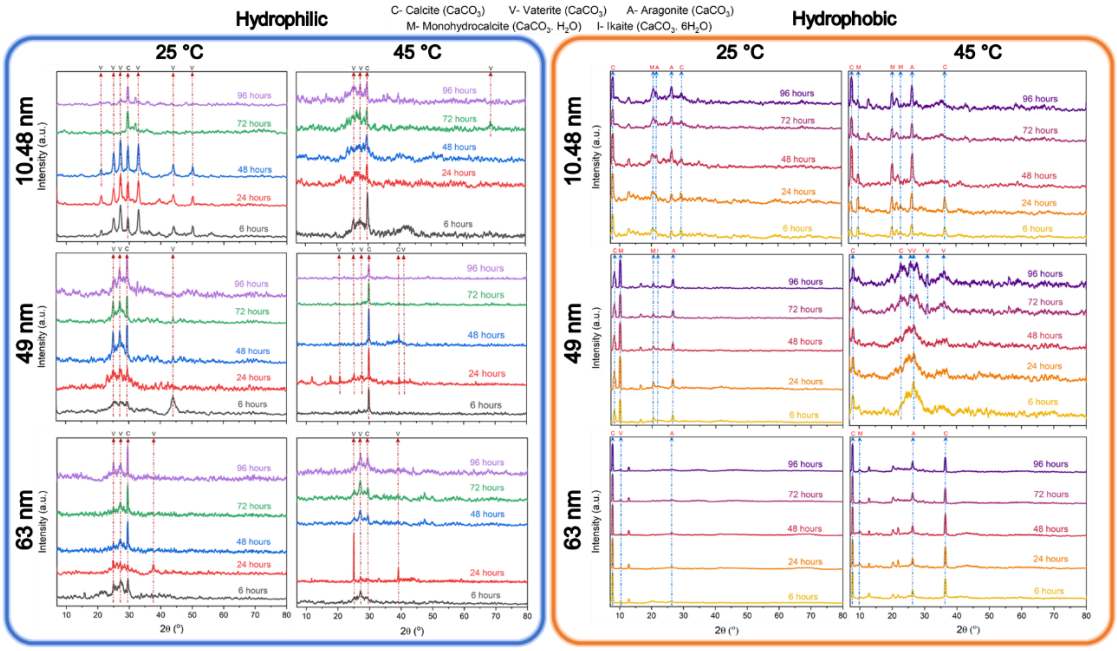

Figure 38 X-ray diffraction (XRD) measurement of calcium carbonate evolved in silica nanochannels of varied pore size, reaction temperature, and surface wettability after 6 hours to 96 hours of loading. The color difference is only a representation of the measurement at different time interval.

The weight % composition of various phases of calcium carbonate was quantitatively calculated using XRD data and the phase evolution over time was identified as shown in **Figure 39**. In hydrophilic SNCs of varied pore sizes aged at 25 °C and 45 °C, the prevalent phases observed are calcite and vaterite. Within these conditions, the primary observation is the initial precipitation of vaterite getting transitioned into stable water-insoluble calcite. The key observation at 25 °C condition is that at 10.48 nm pore size, the final weight % of calcite after 96 hours of loading is the highest while the weight % of calcite in 49 nm and 63 nm pore sizes is fairly less. This observation could be attributed to the low dielectric constant for the interfacial water at small confinements, and the suppression of vibrational energies affecting the overall dynamics and at the same time enhancing dehydration in comparison with large nanopores which are less restricted, allowing for the water-mediated interfacial surface to behave like bulk.

[134,145,146] The key observation when the reaction was aged at 45 °C condition is that calcite is the paramount phase in 10.48 nm and 49 nm conditions whereas at 63 nm pore size, the transition behaves like bulk conditions. The role of heat becomes important in this study as heat intensifies molecular diffusion and water depletion, lowering the energy barrier and accelerating the nucleation events initially, but leads to crystal or phase instability as the liquid depletes. [147,148] Additionally, in certain aging conditions, we observe a dynamic evolution of calcite to vaterite transition which is attributed to the inherent mechanism of calcite growth showcasing rough or smooth intermittent growth patterns, where the former being favorable due to the distribution and unique transport of ions in confined volumes. [143,149]

In hydrophobic SNCs, we discern the crystallization of non-hydrated and hydrated phases of calcium carbonate in all conditions. In these conditions, the transition from hydrated phases to anhydrous phases is observed which follows bulk transition. [30,31] When the membranes are aged at 25 °C, monohydrocalcite and ikaite are initially formed in 10.48 nm and 49 nm SNCs and over time these hydrated phases reduce in weight % and the transition into aragonite and calcite is observed. In 63 nm SNCs, there is no formation of hydrated phases, and a transition of vaterite to aragonite to calcite is observed. This preferential phase formation and stability of hydrated phases in small hydrophobic nanopores is associated with the diffusion, slower translational motion, and hydrogen bond dynamics of water in the interfacial region. [150,151] For the hydrophobic SNC membranes aged at 45 °C, we observe the transition of monohydrocalcite into aragonite and calcite in 10.48 nm and 63 nm pore sizes, whereas, in 49 nm pore size, the transition of vaterite into calcite is observed. This inconsistent

characteristic could be attributed to enhanced dynamic penetration of interfacial water in hydrophobic confined volumes leading to enhanced mobility and variation in the overall hydration behavior. [152,153] Besides, the change in interfacial water properties like surface tension, contact angle, and the presence of other ions become more pronounced at elevated temperatures supporting this inconsistent characteristic. [154]

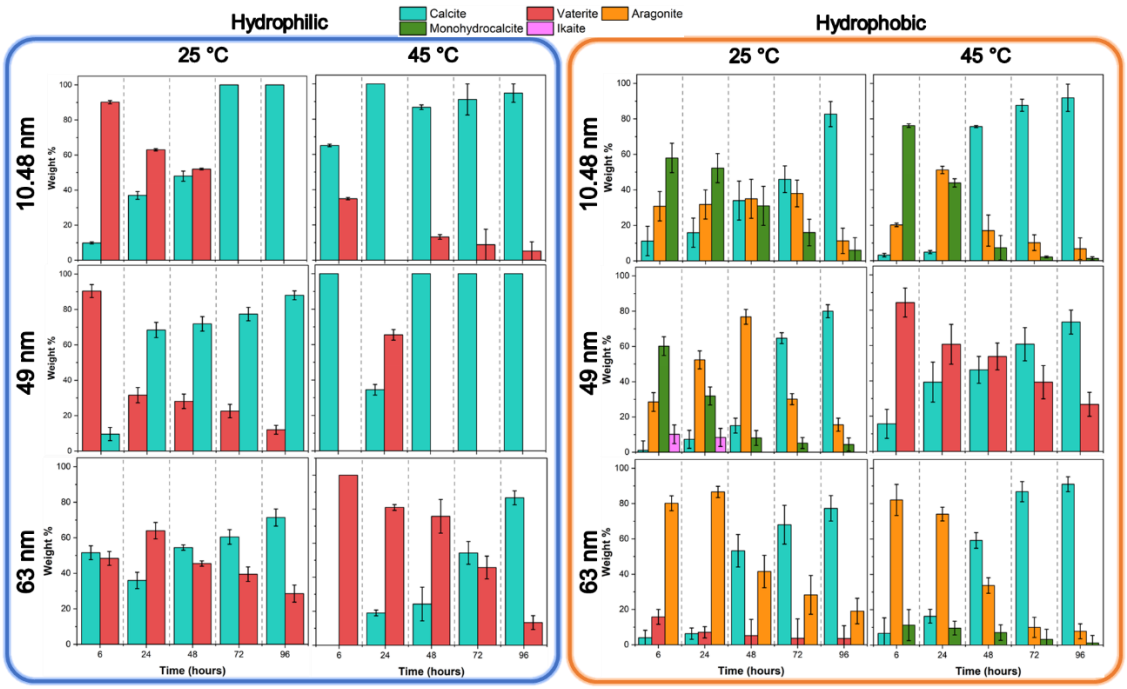

Figure 39 Phase polymorph evolution of calcium carbonate in silica nanochannels of varied pore size, reaction temperature, and surface wettability after 6 hours to 96 hours of loading. The color difference is only a representation of the different $CaCO_3$ phases.

The investigation of the grain size growth and mechanism in silica nanochannels at different conditions is performed using the Scherrer equation and XRD data as shown in **Figure 40**. The calculation methodology is similar as shown in equation (1) for determining the grain size of calcium carbonate in AAMs. In 10.48 nm hydrophilic SNCs aged at 25 °C, the grain size does not vary much with 8.63 nm at 6 hours after loading to 8.97 nm at 96 hours after loading. Based on this observation, we can

determine that the grain size is said to be stabilized over 96 hours. In 10.48 nm hydrophilic SNCs aged at 45 °C, the grain size initially nucleates till 8.4 nm at 6 hours and is then stable till 24 hours followed by a dissolution mechanism to 6 nm at 48 hours and then a growth and stabilization mechanism is observed till the grain reaches 8.4 nm size at 96 hours. This mechanism of stabilization, dissociation, and growth in this system is associated with the influence of heat affecting the crystal instability due to the depletion of liquid in confined volumes. [147,148] In 49 nm hydrophilic SNCs, the grain size drastically increases from 3.52 nm to 15.2 nm between 6 hours to 24 hours after loading followed by a constant decrease till 8.3 nm till 96 hours at 25 °C whereas the grain size increases from 23.2 nm to 26 nm from 6 hours to 24 hours and the crystal is stable till 72 hours with a small change in size to 25 nm and by 96 hours the crystal dissociates to 19.4 nm when aged at 45 °C. In 63 nm hydrophilic SNCs, the grain size crystallized at 25 °C increased vastly from 5.4 nm to 17 nm between 6 hours to 24 hours after loading and a gradual size dissociation till 12 nm by 96 hours while the grain size crystallized at 45 °C has enormously increased from 1.73 nm to 40.2 nm till 24 hours and a drastic reduction in crystal size to 1.8 nm is observed till 96 hours after loading. Within the system of 49 nm at 25 °C, and 63 nm at 25 and 45 °C, the rapid increase and sudden decrease in the grain size in a short period is associated with crystal agglomeration where the agglomerates are formed due to crystal self-bridging mechanism or due to particle collisions affected by supersaturation levels and the dissociation is attributed to energy losses or fracturing in the grain boundary. [155–157]

The grain size mechanism is observed to vary as the presence of hydrophobic moieties alters the dynamics of crystal growth and enhances the stability of the crystal due to the

smooth mobility of water and reduced intermolecular interactions. [158,159] In 10.48 nm hydrophobic SNCs, we initially observe a grain size stabilization of 7.89 nm to 8 nm between 6 hours and 24 hours after loading and then a growth mechanism is observed till 8.91 nm at 96 hours after loading when aged at 25 °C. Similarly, when the grain is aged at 45 °C in 10.48 nm hydrophobic SNCs, the grain size grows from 8.06 nm to 8.46 nm till 24 hours and a stabilization till 8.8 nm is observed till 96 hours. In 49 nm hydrophobic SNCs, the grain size gradually increases from 8.9 nm to 18.3 nm over 96 hours after loading at 25 °C likewise the grain size increases from 7.9 nm to 13.3 nm over 96 hours at 45 °C. In 63 nm hydrophobic SNCs, the grain size is said to be stabilized with size ranging from 17.7 nm to 17.9 nm over 96 hours of loading in 25 °C whereas the grain size increases from 14.3 nm to 24.9 nm over 96 hours of loading in 45 °C conditions. All these observations support that the influence of SNCs and the incorporation of hydrophobic characteristics has enhanced the stability of the calcium carbonate grains irrespective of temperatures.

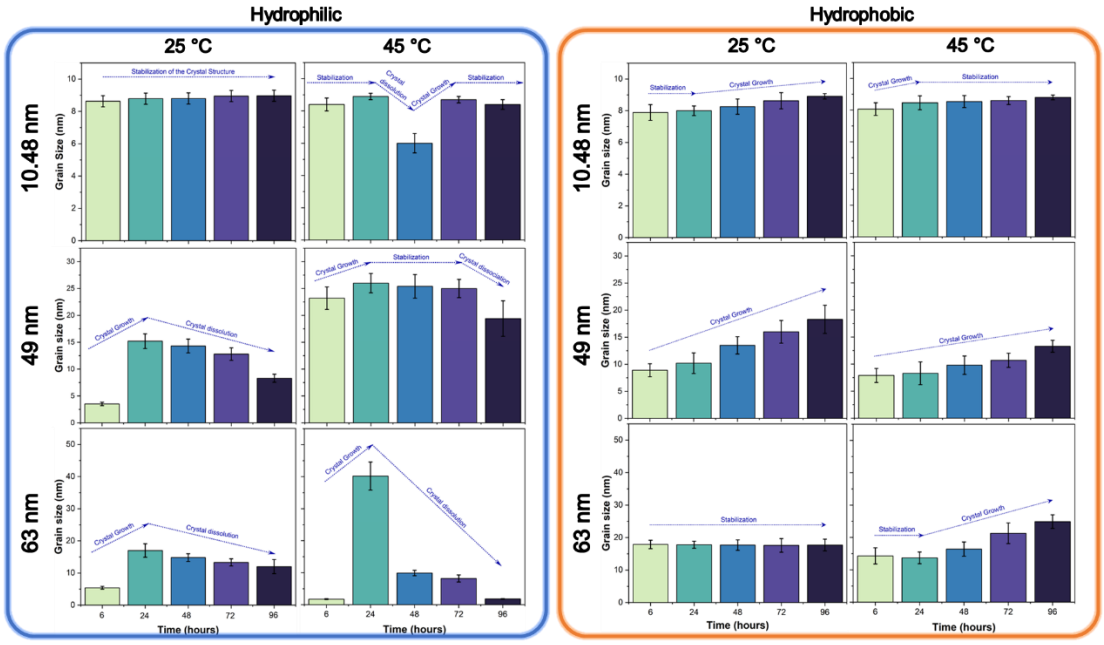

Figure 40 Grain size evolution of calcium carbonate in silica nanochannels of varied pore size, reaction temperature, and surface wettability after 6 hours to 96 hours of loading calculated using the Scherrer equation. The color difference is only a representation of the different time intervals.

3.7. *Quasi-Elastic Neutron Scattering Studies of Water Confined in Pure and Calcium Carbonate loaded Silica Nanochannels Systems*

The dynamics of water in nanoconfinement, as probed by QENS measurements, provides key insights into the transport and evolution of water and ions. To investigate this behavior, the current study focuses on understanding the water dynamics in pure and calcium carbonate associated systems loaded in silica nanochannels. The pore size of silica nanochannels considered for QENS measurements is 10.48 nm, replicating experimental conditions. Before investigating the dynamics of water, temperature-dependent energy-resolved "elastic" neutron scattering intensity diagnostic scans were conducted from 20 K to 320 K to determine the melting behavior of associated water and the temperature range of any probable chemical reactions, as shown in panel **(a)** and **(b)** of **Figure 41**. From the diagnostics data, pure water loaded in hydrophilic SNCs displayed a melting transition (manifested by a sharp decrease in the "elastic" intensity) at 273 K, indicating water transforming from solid to liquid state, exhibiting bulk-like characteristics, whereas water associated with calcium carbonate loaded in hydrophilic SNCs displayed a melting transition at 270 K. This observation suggests that the meting behavior of water confined in hydrophilic SNCs does not change much, even in the presence of calcium carbonate. On the other hand, the diagnostics data for pure water and calcium carbonate loaded in hydrophobic SNCs indicate that there is no associated melting transition, which might be attributed to slower water dynamics and the need for

higher activation energy, [160] which arises due to the cage-like network of water in presence of a hydrophobic interface. [161–165]

The diagnostics data stipulate that the major transition occurs at ~273 K, and the QENS measurements were performed at 298 K to match experimental conditions. From the measurements, half width at half-maximum, HWHM(Q), of the QENS signal was determined from fitting the QENS data as a function of Q:

$$I(Q,E) = \left[x(Q)\delta(E) + \left(1 - x(Q)\right)\frac{1}{\pi}\frac{HWHM(Q)}{HWHM(Q)^2+E^2}\right] \otimes R(Q,E) + Background(Q,E)$$

Here a superposition of the elastic signal, defined by the delta function, and the QENS Lorentz function is numerically convolved with the measured resolution function, R(Q,E), and then a linear fitted background term, Background(Q,E), is added. This fitting procedure directly produces one important parameter, x(Q), representing the fraction of the elastic scattering signal in the measured spectra. For aqueous samples, x(Q) approximates the fraction of "immobilized" water molecules. Other relevant parameters, e.g., the characteristic residence time between diffusion jumps of water molecules, can be determined from fitting the Q-dependence of the HWHM(Q) with jump diffusion model.

The measured water dynamics is strongly influenced by the presence of calcium carbonate in hydrophilic system as opposed to hydrophobic system, as shown in panel **(c)** of **Figure 41**. The residence time between diffusion jump is (1.4 ± 0.6) ps for pure water in hydrophilic SNCs, demonstrating bulk-water characteristics. The time for diffusion jumps slows down drastically to (20.6 ± 5.3) ps in the presence of calcium carbonate in hydrophilic SNCs, attributing to the inherent characteristic of Ca^{2+} ions

being kosmotropic (structure making) and thus inducing stronger structured ordering and slowing the diffusion of water molecules. [166,167] Furthermore, the presence of calcium ions modifies the water properties in silica nanoconfinement, with pore size >6.6 nm showing pronounced kosmotropic properties for modifying hydrogen bonding and water dynamics. [168] This is also evident from the ~5-13 times reduction in the number of water-water H-bonds in the hydrophilic and hydrophobic silica interface compared to that in the bulk as more Ca^{2+} ions are concentrated in the interface. The diffusion jump time of (11.8 ± 2.2) ps, and (11.2 ± 2.2) ps for pure water and water associated with calcium carbonate in hydrophobic SNCs, respectively, indicate no change, inferring similar water dynamics. This emerges from the fact that water forms a more ordered H-bonded network in close proximity of a hydrophobic interface irrespective of a foreign metal ion. [161–165] It is imperative to note that not all water molecules in the samples are mobile on the ps-ns time scale of QENS measurement. From the fraction of mobile water molecules calculated as (1-x(Q)) in the equation above, as shown in panel **(d)** of **Figure 41**, we can observe that a high fraction of water molecules are mobile in the pure water system in hydrophilic SNC, whereas the mobile water fraction decreases significantly in the presence of calcium carbonate. This lower mobile water fraction could be associated with the kosmotropic properties inducing more ordering in water and enhanced interaction between the ions and the water molecules. [168,169] The mobile water fraction for pure and calcium carbonate associated water in hydrophobic SNCs is nearly identical, indicating similar amounts of bound and unbound water. It is important to note while comparing the hydrophobic and hydrophilic systems, the water in modeled hydrophobic membranes is found to approach the bulk

density at a larger distance (**Figure SI16**) from the membrane surface compared to that of the hydrophilic membranes due to the surface characteristics which gives rise to a thinner water core in the hydrophobic confinements (**Figure 29, SI17**). This also leads to a smaller number of water molecules in hydrophobic silica in the first coordination shell of Ca^{2+} compared to hydrophilic silica (**Table 8).** Although water forms an amorphous network around metal ions in a hydrophilic interface, the clathrate water network in a hydrophobic interface gives rise to a depression in the fraction of mobile water molecules in agreement with the QENS measurements.

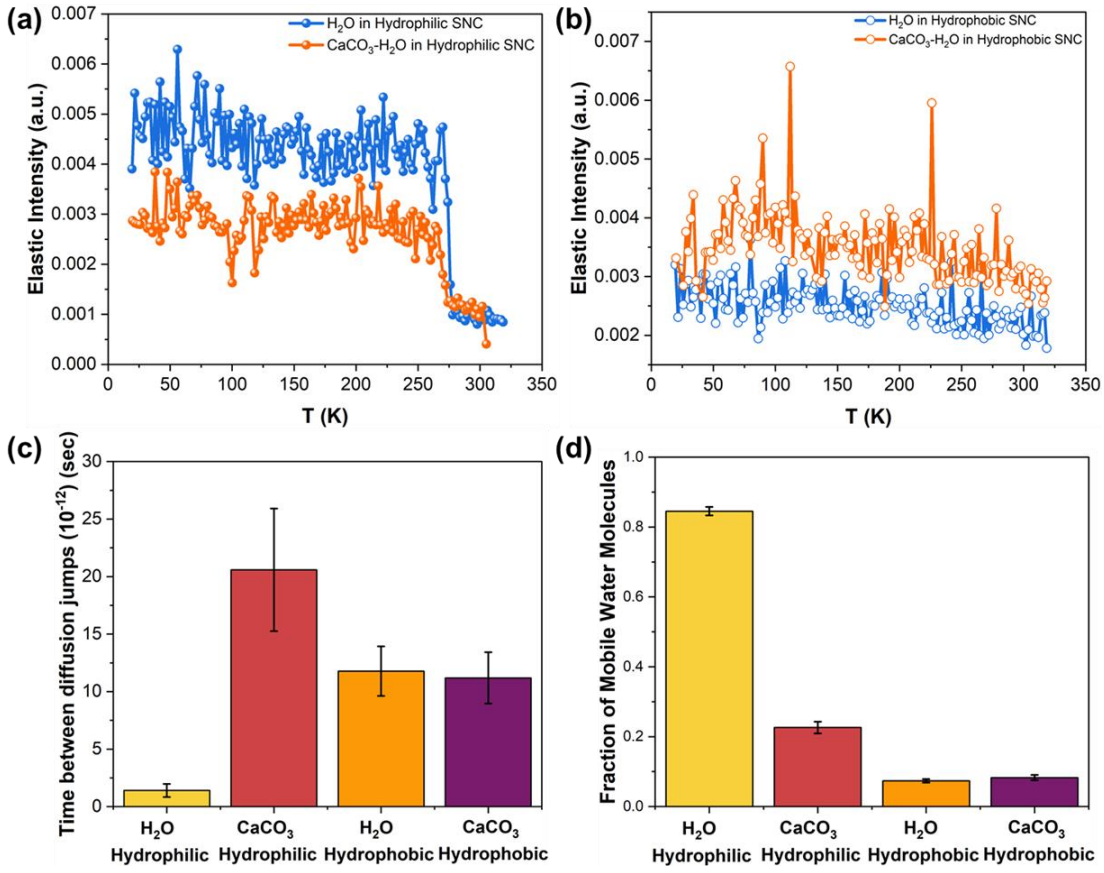

Figure 41 The temperature-dependent energy-resolved "elastic" neutron scattering intensity scans of (a) hydrophilic SNCs filled with pure H_2O and $CaCO_3$, (b) hydrophobic SNCs filled with pure H_2O and $CaCO_3$, (c) the residence time of water molecules between successive diffusion jumps, and (d) the fraction of mobile water molecules in each respective nanoconfined system.

4. Conclusion

The context of carbon mineralization in nanopores provides a complete view of the fundamental mechanism governing the nucleation, growth, and stability of mineral phases while deducing the role and behavior of water on carbonate evolution which is vastly different from their bulk counterparts. Interpreting this mechanism is pivotal in studying the natural carbonation process in mafic and ultramafic rocks and developing technologies associated with carbon capture. In this study using XRD analysis coupled with classical MD simulation, we explored and analyzed the behavior of calcium carbonate polymorph evolution within nanoconfined environments by systematically varying the pore size, reaction temperature, and surface wettability of the purchased anodic alumina membranes and synthesized silica nanochannels. The variation in surface wettability for both hydrophilic and hydrophobic AAMs and SNCs was observed using a contact angle measurement where they moved towards a reduction in contact angle as the pore size increased as well as through hydrogen bonding between the membrane and interfacial water molecules which decreased as the membrane surface turned hydrophobic. To measure the surface charge in these systems, a zeta potential measurement was performed where, as the pore size increased the surface charge moved from greater to lesser negative values. These findings elucidate the nature of different environments on the preferential nucleation, evolution, and stability of calcium carbonate polymorphs. Pre-nucleated coordination of Ca^{2+} obtained from MD simulation indicated a preference for the anhydrous phases over the hydrated ones and exhibited an almost equal probability of forming calcite, vaterite, and aragonite. For experimentally interpreting the growth of calcium carbonate, 0.1M $Ca(NO_3)_2$ and 0.1M

$NaHCO_3$ are loaded into the nanopores and allowed for the reaction to proceed at 25 °C and 45 °C. The key conclusion from these findings is that the calcium carbonate polymorph transition predominantly follows the bulk mechanism in AAMs but in some cases, preferential formation of specific phases is observed. Calcium carbonate crystallized in SNCs slightly deviates from bulk mechanisms, including the anomalous transition from stable calcite to metastable vaterite. In both AAMs and SNCs, we observe the crystallization of hydrated forms of calcium carbonate and their transition into anhydrous forms over time irrespective of reaction temperature. The crystal size evolution was determined for calcium carbonate in confined volumes indicating a modified and unique crystal growth mechanism and kinetics. The behavior and dynamics of water in hydrophilic and hydrophobic nanoconfined environments associated with pure water and calcium carbonate were performed using quasi-elastic neutron scattering giving insights into the temperature dependent melting and mobile/immobile water molecule fraction. These results not only determine the fundamental mechanism of mineralization in confined volumes but also offer applications in designing and synthesizing novel materials with tailored properties. Future research focusing on the effects of different nanochannels, surface functionalities, and solution compositions is crucial in unraveling the complexities and anomalous characteristics involved in nanoconfined volumes, harnessing its potential for technological applications.

5. Supporting Information

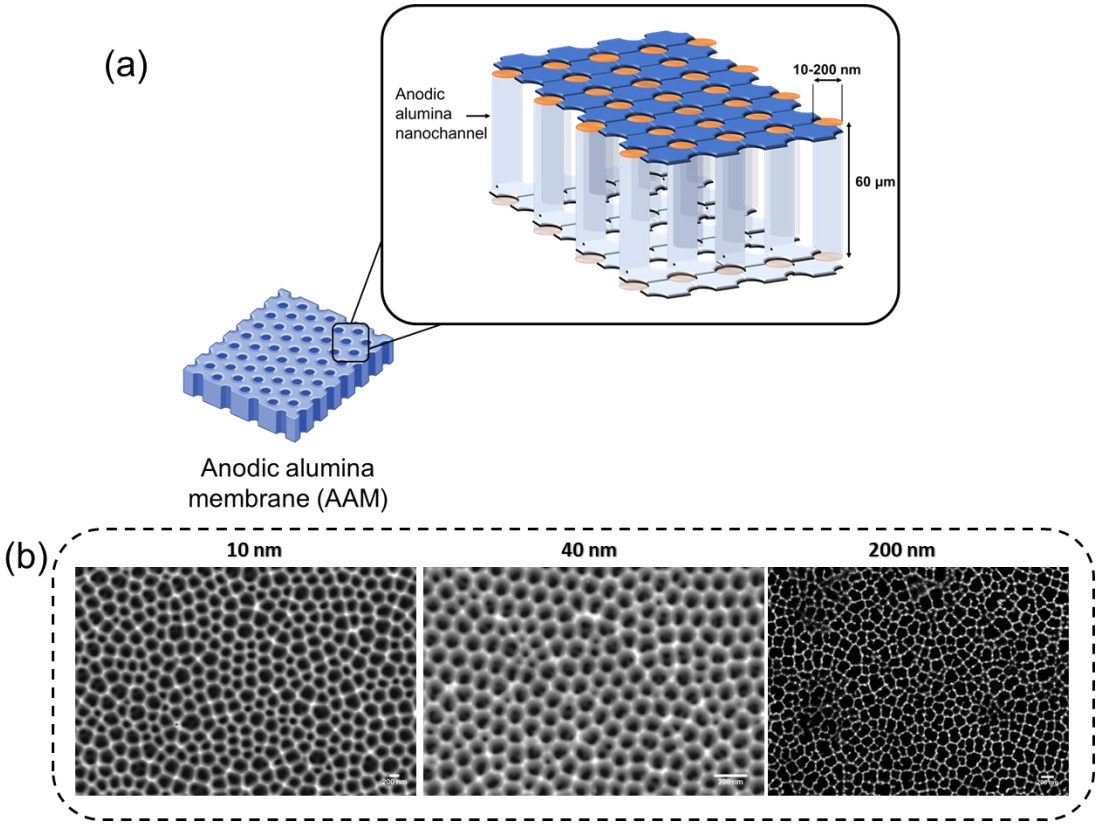

Figure SI 8 Schematic representation of (a) the anodic alumina membrane (AAM) and (b) the respective images of AAM of varying pore sizes

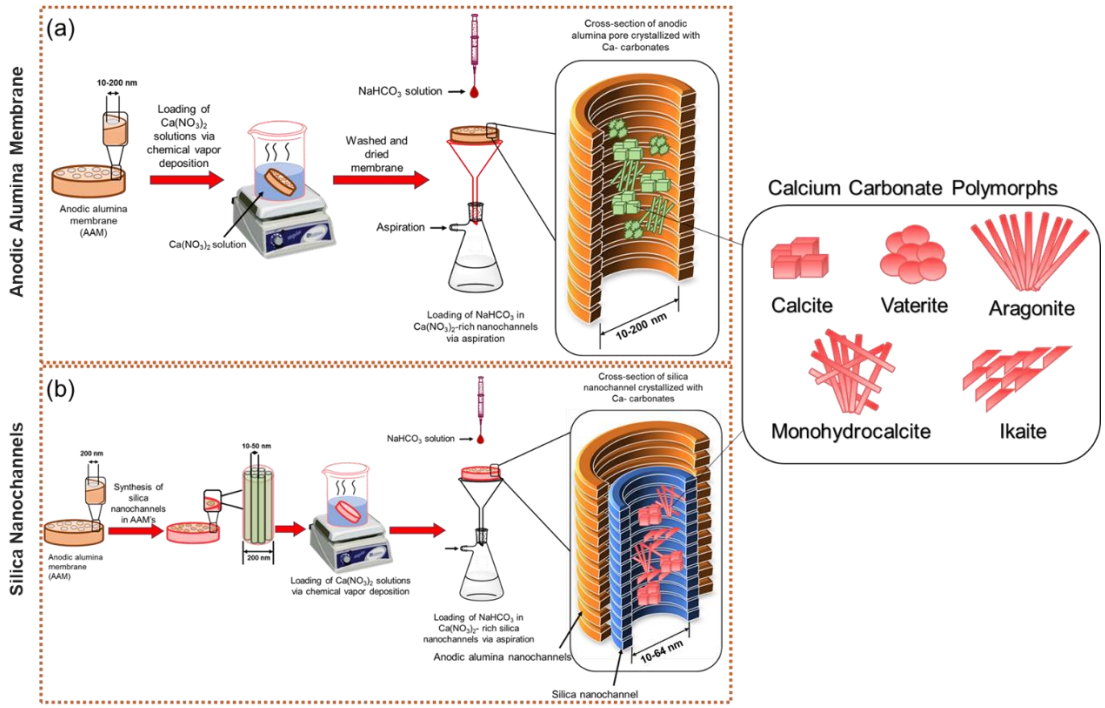

Figure SI 9 Loading methodology of $Ca(NO_3)_2.4H_2O$ and $NaHCO_3$ to precipitate Ca-carbonate polymorphs in hydrophilic (a) anodic alumina membranes, and (b) Silica Nanochannels

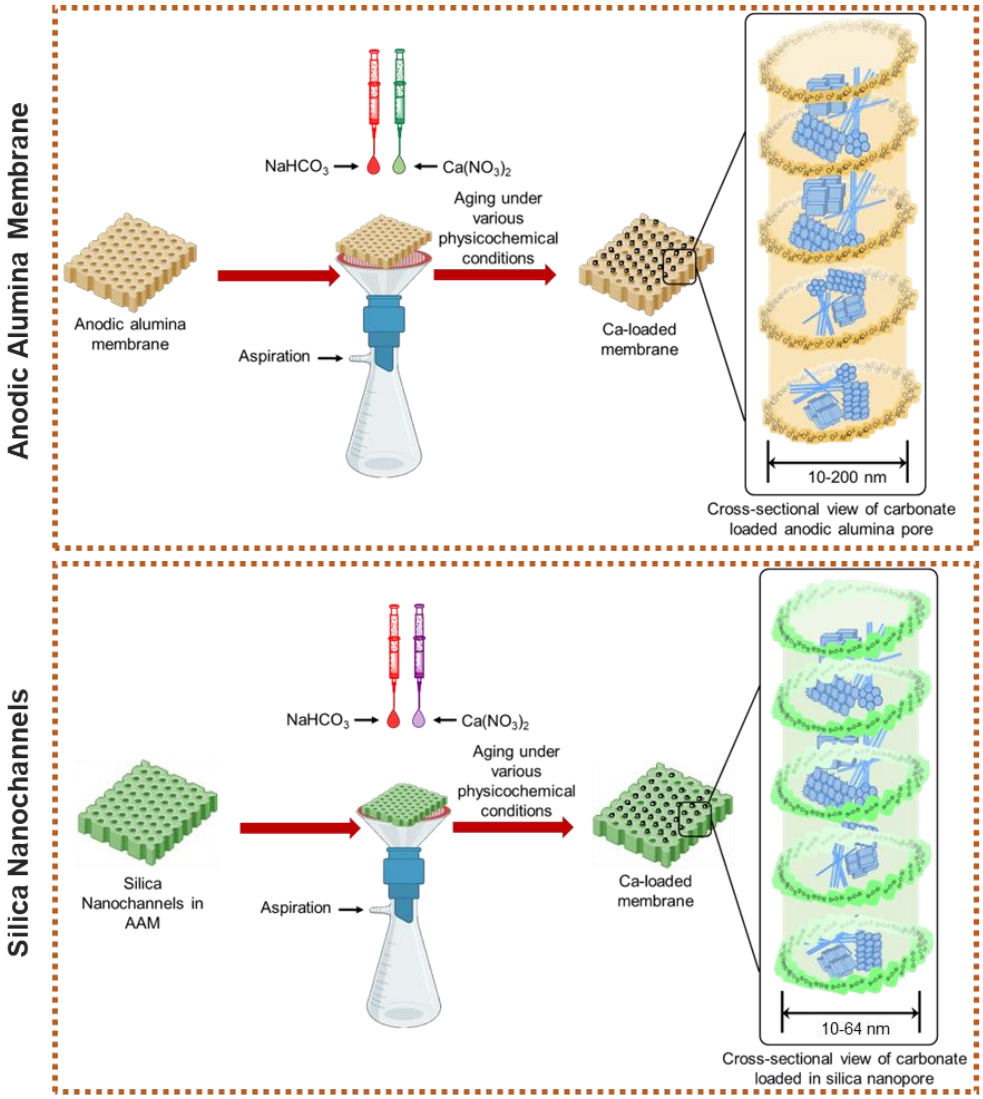

Figure SI 10 Loading methodology of $Ca(NO_3)_2$. $4H_2O$ and $NaHCO_3$ to precipitate Ca-carbonate polymorphs in hydrophobic (a) anodic alumina membranes, and (b) Silica Nanochannels

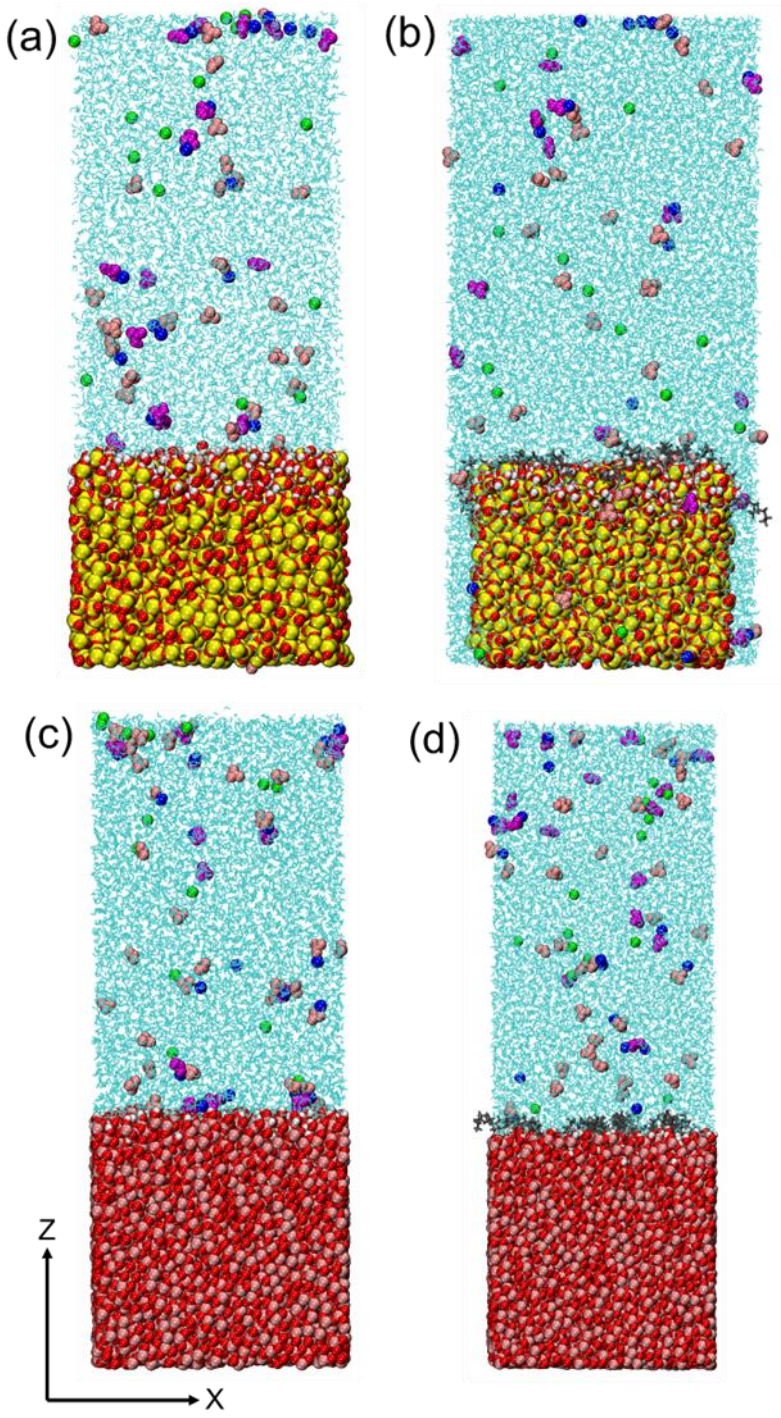

Figure SI 11 Structures of the simulation cells modeled in this study in the presence of membranes (a) hydrophilic silica (SILhpl), (b) hydrophobic silica (SILhpb), (c) hydrophilic alumina (ALOhpl), and (d) hydrophobic alumina (ALOhpb). Water is represented as blue lines whereas Na^{+}, Ca^{2+}, HCO_3^{-}, and NO_3^{-} ions in the solution are shown in green, navy blue, magenta, and pink respectively. The silica and alumina membranes are at the bottom of the aqueous phase. In silica, Si, O, and H atoms are represented as yellow, red, and white vdW spheres, and In alumina, Al, O, and H atoms are shown in mauve, red, and white vdW spheres respectively. Lauric acid chains in (b) and (d) are represented as gray licorice chains.

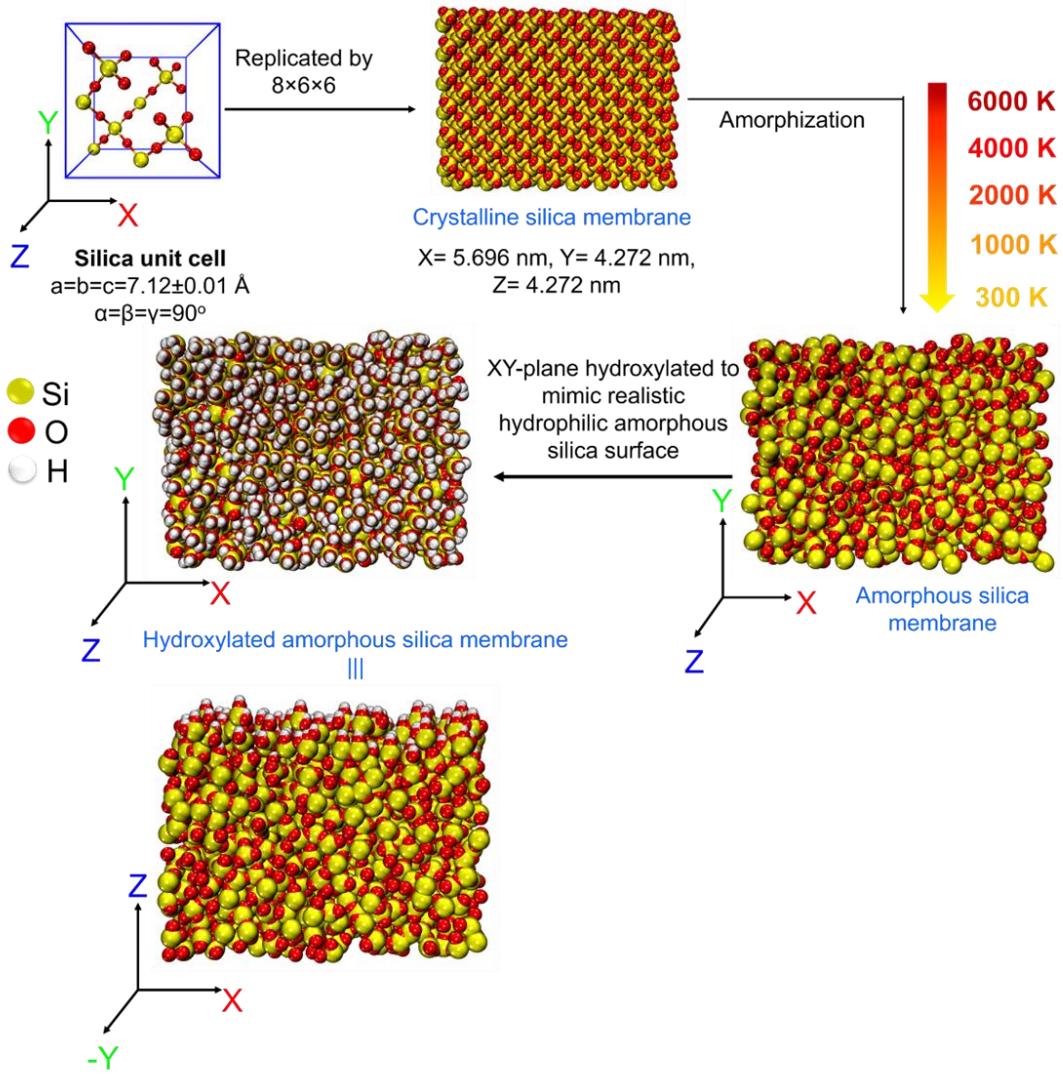

Figure SI 12 Methodology flowchart for in-silico modeling of amorphous hydrophilic silica membrane from crystalline silica.

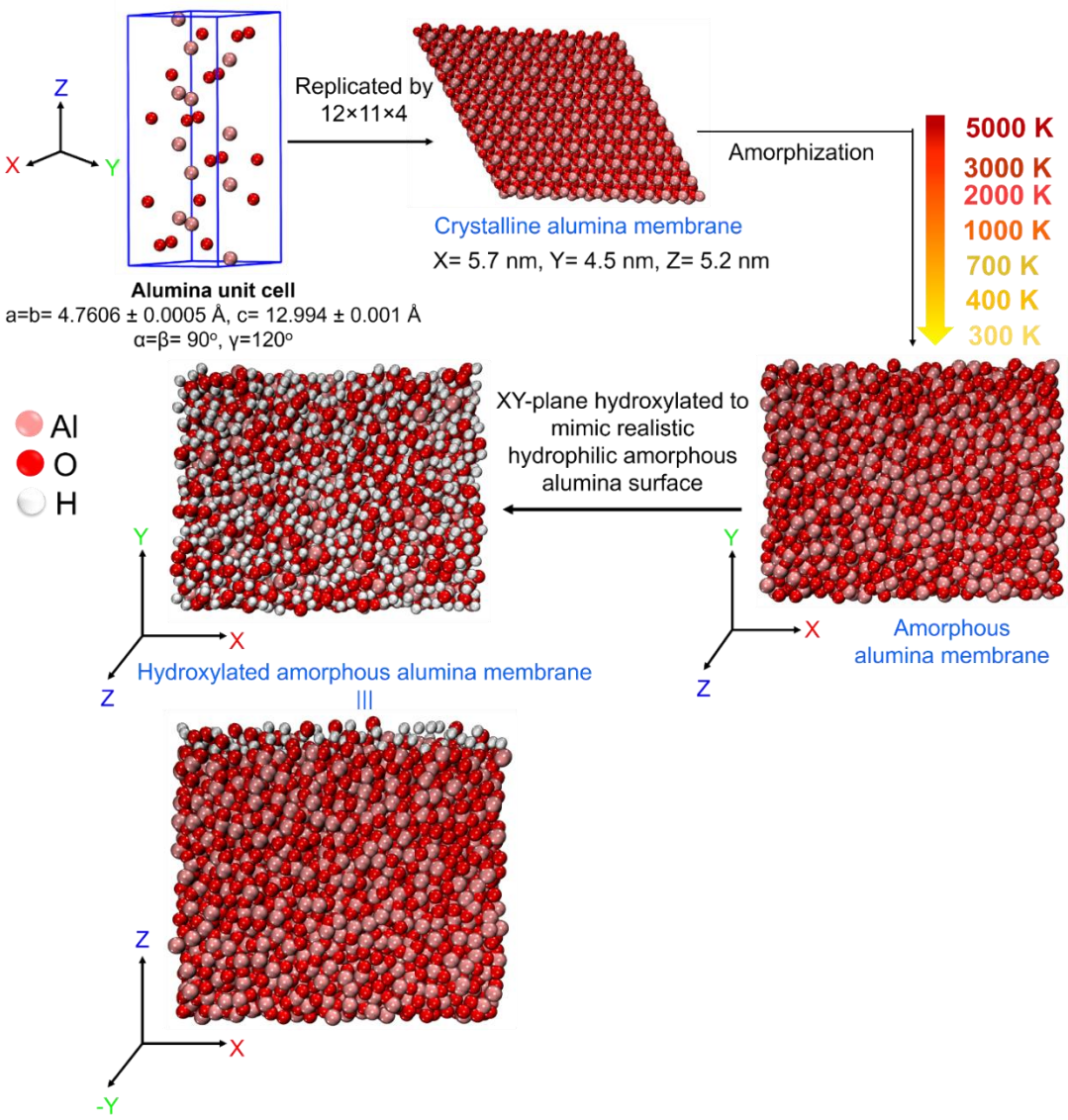

Figure SI 13 Methodology flowchart for in-silico modeling of amorphous hydrophilic alumina membrane from crystalline alumina.

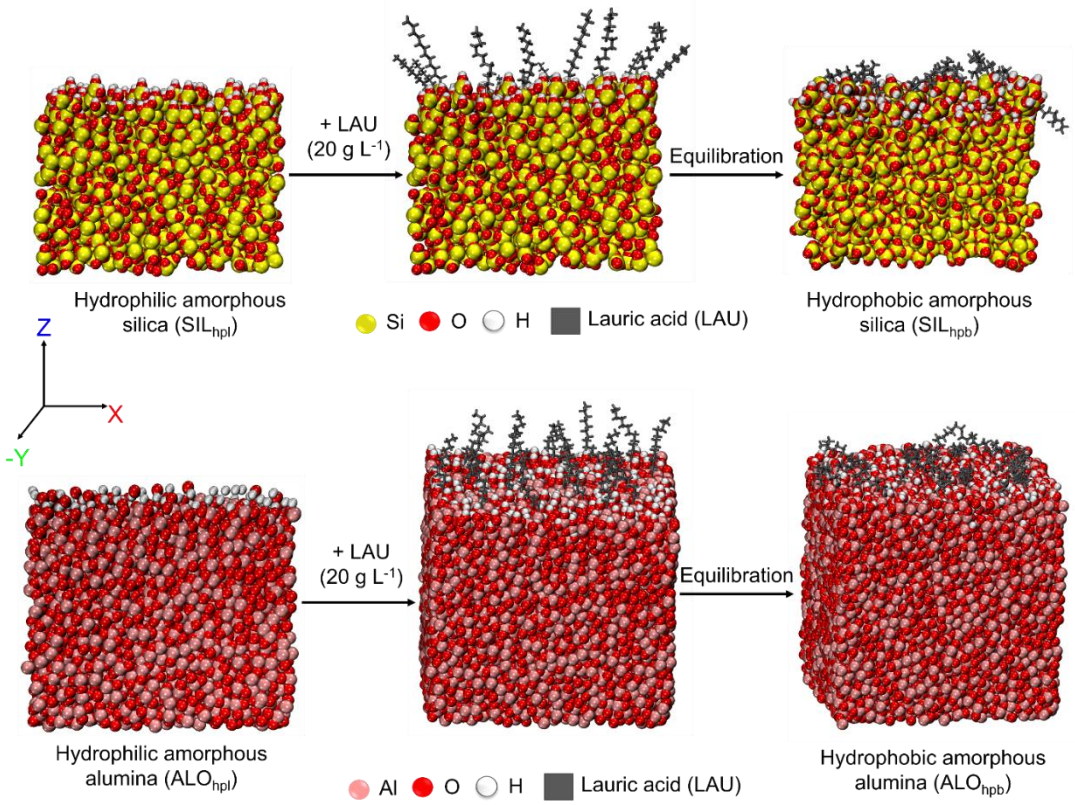

Figure SI 14 Methodology flowchart for in-silico modeling of hydrophobic alumina and silica membranes from hydrophilic counterparts by grafting lauric acid (LAU).

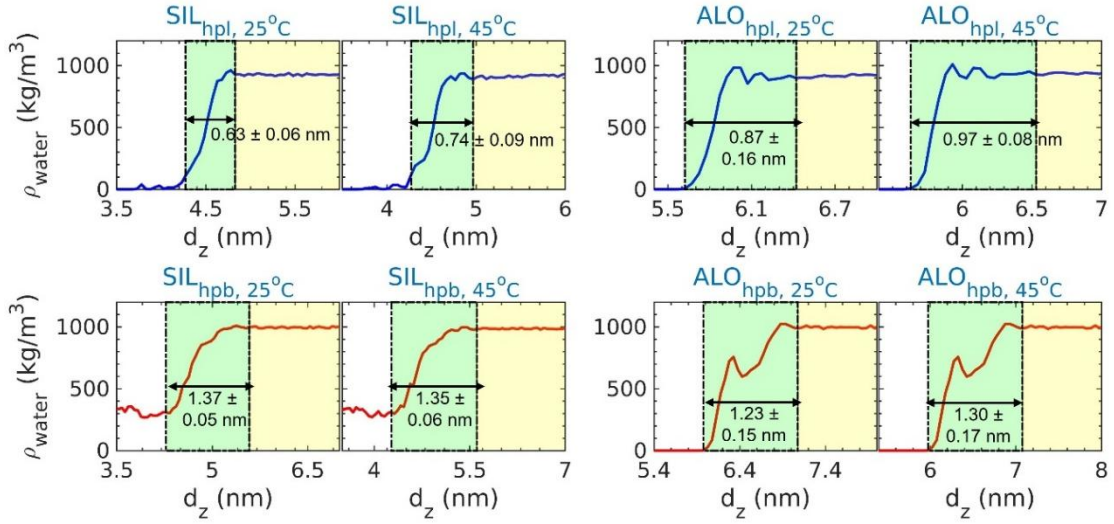

Figure SI 15 Representative mass density of water along the longest axis (Z) of the simulation cell normal to the interfacial surface in presence of hydrophilic and hydrophobic silica and alumina membranes at temperatures of 25 °C and 45 °C. The interfacial region in each case is shaded in green whereas the bulk phase is shaded in yellow. Width of the interface is mentioned in each case along with the standard deviation evaluated using simulation triplicates.

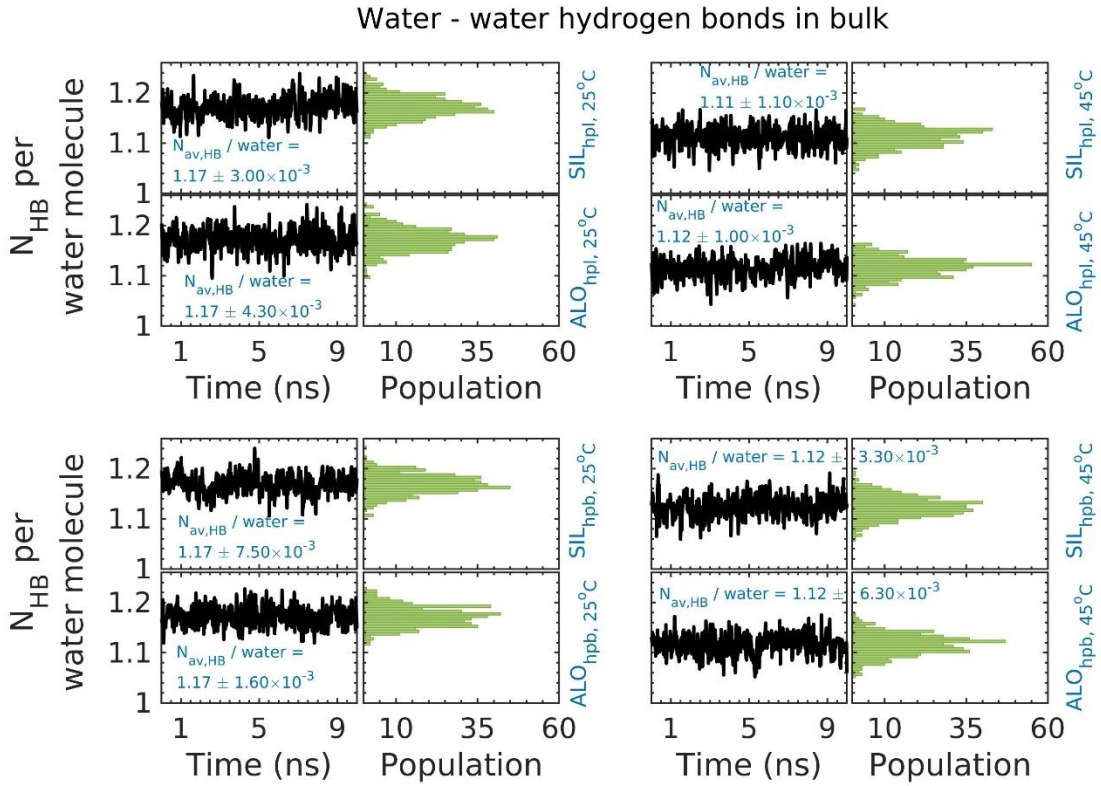

Figure SI 16 Variation of the number of hydrogen bonds (NHB) per water molecule between the bulk water molecules themselves with time at temperatures 25 ℃ and 45 ℃. Last 10 ns of the simulation trajectories are used for calculation. A donor-acceptor distance cutoff of 3.5 Å and a donor-hydrogen-acceptor angle cutoff of 30° are used for calculating the hydrogen bonds. 'SIL' and 'ALO' represent silica and alumina membrane respectively while 'hpl' and 'hpb' represent hydrophilic and hydrophobic membrane respectively. Beside each timeline plot, a distribution of the corresponding N_{HB} per water molecule is provided. The numbers within each subplot indicate the average N_{HB} per water molecule along with its standard deviation as obtained from simulation triplicates.

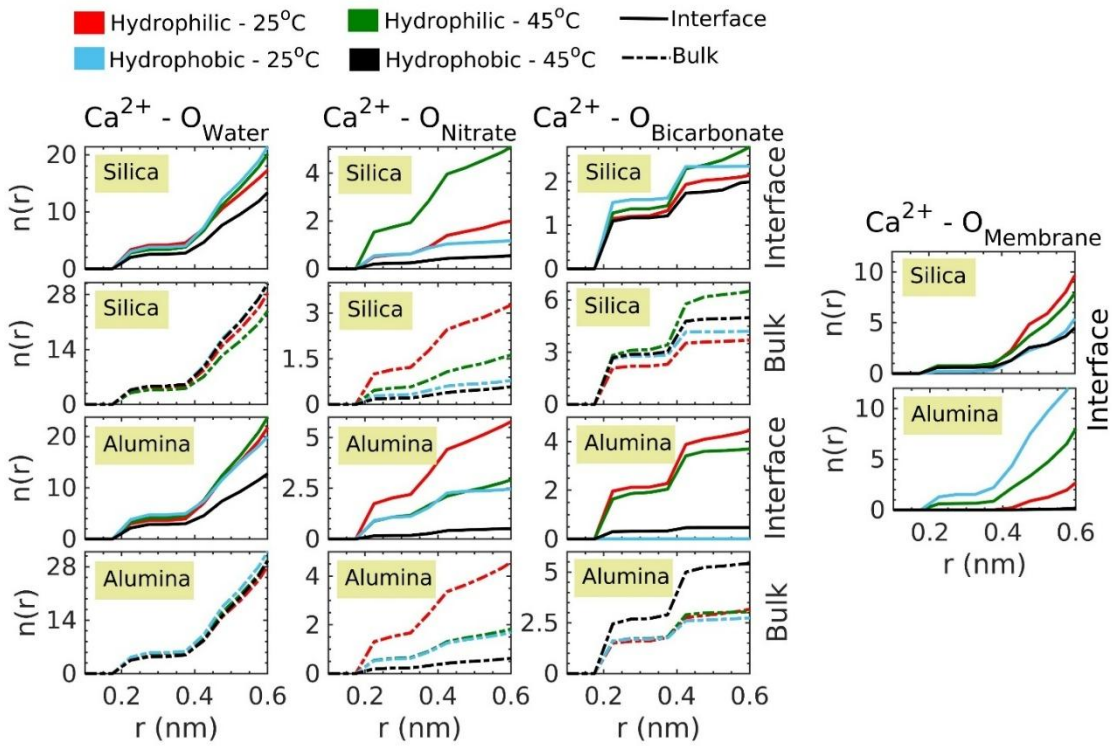

Figure SI 17 Representative variation of the coordination number (n(r)) of calcium ions with respect to oxygens from water molecules (O_{Water}), nitrate ($O_{Nitrate}$), and bicarbonate ($O_{Bicarbonate}$) ions as well as membrane oxygens ($O_{Membrane}$) as a function of distance (r) in the interfacial and bulk regions focusing within the respective second coordination shells (maximum 0.6 nm) at temperatures of 25 ℃ and 45 ℃ in hydrophilic and hydrophobic silica and alumina membranes. The interfacial width is obtained from density profiles as shown in Figure SI16 whereas the rest of the simulation cell is considered as bulk.

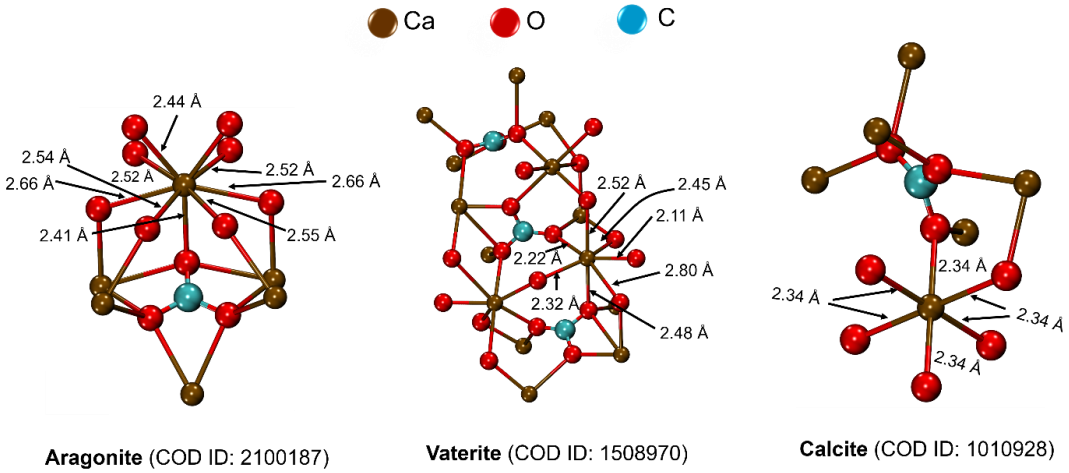

Figure SI 18 Distance between Ca and O atoms in the unit cell of Aragonite, Vaterite, and Calcite as collected from Crystallography Open Database. The brown, red, and cyan colors represent Ca, O, and C respectively.

Table SI 5 Number of Na^{+}, Ca^{2+}, NO^{3-}, and HCO^{3-} ions added to the aqueous phase in contact with hydrophilic and hydrophobic silica and alumina membranes at 25 ℃ and 45 ℃.

Membrane	Surface characteristic	Temperature (°C)	No. of Na^{+} ions	No. of Ca^{2+} ions	No. of NO_3^- ions	No. of HCO_3^- ions
Silica	Hydrophilic	25	15	15	30	15
		45	15	15	30	15
	Hydrophobic	25	16	16	32	16
		45	16	16	32	16
Alumina	Hydrophilic	25	17	17	34	17
		45	17	17	34	17
	Hydrophobic	25	17	17	34	17
		45	17	17	34	17

Table SI 6 Absolute values of average Electrostatic (Elec.) and vdW interaction energy (Eav) in kJ mol-1 between the silica/alumina membrane (SILhpl, SILhpb, ALOhpl and ALOhpb) and different species (Ca^{2+}, Na^{+}, HCO^{3-}, NO^{3-}, and water) present in the simulation box at temperatures (T) 25 °C and 45 °C. Calculations are done over the last 10 ns of the simulation trajectory and averaged over three concordant simulations in each case. STDEV represents the standard deviation as obtained from triplicates of each simulation. High STDEV in most of the cases indicates high structural variance between the simulation triplicates.

System	T (°C)	E_{av} (kJ mol^{-1}) (Ca^{2+}-Membrane)		E_{av} (kJ mol^{-1}) (Na^{+}-Membrane)		E_{av} (kJ mol^{-1}) (HCO_3^--Membrane)		E_{av} (kJ mol^{-1}) (NO_3^--Membrane)		E_{av} (kJ mol^{-1}) (Water-Membrane)	
		Elec. ± STDEV	vdW ± STDEV	Elec. ± STDEV	vdW ± STDEV	Elec. ± STDEV	vdW ± STDEV	Elec. ± STDEV	vdW ± STDEV	Elec. ± STDEV	vdW ± STDEV
SIL_{hpl}	25	-2.38×10^3 ± 335.46	170.02 ± 13.67	-1.90×10^3 ± 411.55	142.99 ± 26.59	-197.23 ± 622.04	28.79 ± 80.44	-608.17 ± 30.45	-38.29 ± 17.90	-4.20×10^4 ± 721.38	8.07×10^3 ± 200.46
	45	-2.91×10^3 ± 1.15×10^3	220.22 ± 89.28	-1.91×10^3 ± 253.65	136.15 ± 18.45	-63.18 ± 220.00	13.31 ± 48.51	-511.62 ± 322.52	-42.61 ± 40.19	-4.32×10^4 ± 643.39	8.28×10^3 ± 88.18
SIL_{hpb}	25	-3.23×10^3 ± 699.56	221.52 ± 75.83	-786.16 ± 288.08	56.74 ± 24.89	-801.26 ± 668.47	87.74 ± 106.03	-660.45 ± 197.21	-9.68 ± 18.68	-1.08×10^5 ± 880.67	2.04×10^4 ± 139.79
	45	-3.31×10^3 ± 970.88	243.39 ± 89.74	-1.81×10^3 ± 194.59	116.37 ± 17.94	-1.02×10^3 ± 218.35	142.17 ± 65.77	-1.11×10^3 ± 268.94	108.10 ± 34.28	-1.07×10^5 ± 1.42×10^3	2.03×10^4 ± 291.40
ALO_{hpl}	25	-904.51 ± 867.25	49.68 ± 62.85	-2.61×10^3 ± 683.91	213.16 ± 56.11	-667.97 ± 429.40	50.91 ± 41.91	-272.84 ± 136.26	-26.59 ± 21.20	-4.74×10^4 ± 385.77	8.94×10^3 ± 98.29
	45	-1.91×10^3 ± 943.82	129.71 ± 63.73	-2.67×10^3 ± 295.93	227.62 ± 26.71	-1.09×10^3 ± 882.76	147.65 ± 109.14	-239.71 ± 177.39	-31.01 ± 17.01	-4.40×10^4 ± 195.81	7.98×10^3 ± 57.46
ALO_{hpb}	25	-1.24×10^3 ± 1.17×10^3	89.64 ± 89.29	-1.37×10^3 ± 362.74	118.69 ± 29.60	-1.16×10^3 ± 327.42	181.43 ± 44.42	-97.02 ± 59.24	-17.82 ± 0.96	-3.70×10^4 ± 356.52	7.21×10^3 ± 42.60
	45	-241.07 ± 412.43	13.90 ± 24.40	-870.04 ± 257.07	68.15 ± 21.56	-110.76 ± 188.65	11.59 ± 22.52	-118.41 ± 104.48	-7.44 ± 13.47	-3.69×10^4 ± 566.74	7.00×10^3 ± 95.46

Table SI 7 Distance between Ca^{2+} ions and oxygens from different sources collected from previous literature reports for different phases of calcium carbonate. The values are compared with the global Ca-O distances obtained in this work.

Polymorph	Lattice plane / crystal information	Distance (Å)	Reference
Calcite	$\{10\bar{1}4\}$	$d_{Ca\text{-}Owater}$ = 2.4	de Leeuw, N.H. and Parker, S.C., 1998. Surface structure and morphology of calcium carbonate polymorphs calcite, aragonite, and vaterite: an atomistic approach. *The Journal of Physical Chemistry B*, *102*(16), pp.2914-2922.
	$\{11\bar{2}0\}$	$d_{Ca\text{-}Owater}$ = 2.28 – 2.46	
Aragonite	{011}	$d_{Ca\text{-}Owater}$ = 2.43 – 2.49	
	{110}	$d_{Ca\text{-}Owater}$ = 2.53	
Hydrous and anhydrous Ca-carbonate phases	-	$d_{Ca\text{-}O}$ = 2.45±0.01	Singer, J.W., Yazaydin, A.O., Kirkpatrick, R.J. and Bowers, G.M., 2012. Structure and transformation of amorphous calcium carbonate: A solid-state 43Ca NMR and computational molecular dynamics investigation. *Chemistry of Materials*, *24*(10), pp.1828-1836.
Calcite (**Figure SI11**)	Unit cell	$d_{Ca\text{-}O}$ = 2.34±0.00	Elliott, N., 1937. A Redetermination of the Carbon—Oxygen Distance in Calcite and the Nitrogen—Oxygen Distance in Sodium Nitrate. *Journal of the American Chemical Society*, *59*(7), pp.1380-1382.
Aragonite (**Figure SI11**)	Unit cell	$d_{Ca\text{-}O}$ = 2.53±0.09	Pokroy, B., Fitch, A.N., Lee, P.L., Quintana, J.P., Caspi, E.A.N. and Zolotoyabko, E., 2006. Anisotropic lattice distortions in the mollusk-made aragonite: A widespread phenomenon. *Journal of Structural Biology*, *153*(2), pp.145-150.
Vaterite (**Figure SI11**)	Unit cell	$d_{Ca\text{-}O}$ = 2.41±0.23	Mugnaioli, E., Andrusenko, I., Schüler, T., Loges, N., Dinnebier, R.E., Panthöfer, M., Tremel, W. and Kolb, U., 2012. Ab initio structure determination of vaterite by automated electron

			diffraction. *Angewandte Chemie International Edition*, *51*(28), pp.7041-7045.
Pre-nucleated Ca^{2+}	-	d_{Ca-O} = 2.26 – 2.34 ($SIL_{hpl,25C}$)	This work
		d_{Ca-O} = 2.25 – 2.33 ($SIL_{hpl,45C}$)	
		d_{Ca-O} = 2.24 – 2.36 ($ALO_{hpl,25C}$)	
		d_{Ca-O} = 2.25 – 2.33 ($ALO_{hpl,45C}$)	
		d_{Ca-O} = 2.25 – 2.37 ($SIL_{hpb,25C}$)	
		d_{Ca-O} = 2.24 – 2.34 ($SIL_{hpb,45C}$)	
		d_{Ca-O} = 2.26 – 2.36 ($ALO_{hpb,25C}$)	
		d_{Ca-O} = 2.24 – 2.34 ($ALO_{hpb,45C}$)	

6. Acknowledgment

The authors acknowledge the use of shared facilities at Cornell Center for Materials Research (CCMR) supported through NSF MRFEC program (DMR- 1719875) and Cornell NanoScale Science and Technology Facility (CNF), a member of the National Nanotechnology Coordination Infrastructure (NNCI) supported by NSF (Grant NNCI-2025233). A portion of this research used resources at the Spallation Neutron Source, a DOE Office of Science User Facility operated by the Oak Ridge National Laboratory. The beam time was allocated to BASIS (BL-2) on proposal number IPTS-34626. AM and RH are supported by NSF CAREER (Grant No- 2144373). RH acknowledges the

computation time provided by the Cornell G2-cluster. Few illustrations were created with BioRender.com.

7. References

1. Wang, S., Zhao, Z., Haque, F. & Guo, P. Engineering of protein nanopores for sequencing, chemical or protein sensing and disease diagnosis. *Current Opinion in Biotechnology* vol. 51 Preprint at https://doi.org/10.1016/j.copbio.2017.11.006 (2018).

2. Lybrand, R. A. *et al.* A coupled microscopy approach to assess the nano-landscape of weathering. *Sci Rep* **9**, (2019).

3. Kärger, J., Ruthven, D. M. & Valiullin, R. Diffusion in nanopores: inspecting the grounds. *Adsorption* **27**, (2021).

4. Aluru, N. R. *et al.* Fluids and Electrolytes under Confinement in Single-Digit Nanopores. *Chemical Reviews* vol. 123 Preprint at https://doi.org/10.1021/acs.chemrev.2c00155 (2023).

5. Niu, J. & Zhang, K. Molecular-scale insights into nanoconfined water-CO2 interactions in geological carbon storage. *Chem Eng Sci* **299**, 120457 (2024).

6. Miao, F. *et al.* CO2 storage in organic nanopores with varying widths: Molecular simulation and simplified local density model. *Science of the Total Environment* **907**, (2024).

7. Massoud, A., Abdou, F. S. & Yousif, M. Evaluation of mineral compositions of surface and subsurface rock samples by neutron activation analysis. *Int J Environ Anal Chem* **103**, (2023).

8. Apel, P., Bondarenko, M., Yamauchi, Y. & Yaroshchuk, A. Osmotic Pressure and Diffusion of Ions in Charged Nanopores. *Langmuir* **37**, (2021).

9. Shen, Y. *et al.* Controlling Water Flow through a Synthetic Nanopore with Permeable Cations. *ACS Cent Sci* **7**, (2021).

10. Ronghe, A. & Ayappa, K. G. Graphene Nanopores Enhance Water Evaporation from Salt Solutions: Exploring the Effects of Ions and Concentration. *Langmuir* **39**, (2023).

11. Paul, A. & Aluru, N. R. Mechanically activated and deactivated ion transport across nanopores with heterogeneous surface charge distributions. *J Appl Phys* **136**, (2024).

12. Ma, L. *et al.* Ion transport through short nanopores modulated by charged exterior surfaces. *Journal of Chemical Physics* **160**, (2024).

13. Köhler, M. H. & Bordin, J. R. Surface, Density, and Temperature Effects on the Water Diffusion and Structure Inside Narrow Nanotubes. *Journal of Physical Chemistry C* **122**, (2018).

14. Leoni, F., Calero, C. & Franzese, G. Nanoconfined Fluids: Uniqueness of Water Compared to Other Liquids. *ACS Nano* **15**, (2021).

15. Reiter, G. F. *et al.* Anomalous ground state of the electrons in nanoconfined water. *Phys Rev Lett* **111**, (2013).

16. Le, T. H. H., Morita, A. & Tanaka, T. Refractive index of nanoconfined water reveals its anomalous physical properties. *Nanoscale Horiz* **5**, (2020).

17. Coridan, R. H., Schmidt, N. W., Lai, G. H., Abbamonte, P. & Wong, G. C. L. Dynamics of confined water reconstructed from inelastic x-ray scattering measurements of bulk response functions. *Phys Rev E Stat Nonlin Soft Matter Phys* **85**, (2012).

18. Fang, F. *et al.* Molecular-Level Insights into Unique Behavior of Water Molecules Confined in the Heterojunction between One- and Two-Dimensional Nanochannels. *Langmuir* **38**, (2022).

19. De Almeida, J. M. & Miranda, C. R. Confinement and hydrophilicity effects on geologically relevant fluids in silica nanopores. *Phys Rev Fluids* **5**, (2020).

20. Alabarse, F. G. *et al.* Different Water Networks Confined in Unidirectional Hydrophilic Nanopores and Transitions with Temperature. *Journal of Physical Chemistry C* **125**, (2021).

21. Gao, Y. *et al.* A Nanoconfined Water–Ion Coordination Network for Flexible Energy-Dissipation Devices. *Advanced Materials* **35**, (2023).

22. Zaragoza, A. *et al.* Molecular dynamics study of nanoconfined TIP4P/2005 water: How confinement and temperature affect diffusion and viscosity. *Physical Chemistry Chemical Physics* **21**, (2019).

23. Han, S., Kumar, P. & Stanley, H. E. Hydrogen-bond dynamics of water in a quasi-two-dimensional hydrophobic nanopore slit. *Phys Rev E Stat Nonlin Soft Matter Phys* **79**, (2009).

24. Dasgupta, N., Ho, T. A., Rempe, S. B. & Wang, Y. Hydrophobic Nanoconfinement Enhances CO2 Conversion to H2CO3. *Journal of Physical Chemistry Letters* **14**, (2023).

25. Breynaert, E. *et al.* Water as a tuneable solvent: A perspective. *Chemical Society Reviews* vol. 49 Preprint at https://doi.org/10.1039/c9cs00545e (2020).

26. Domingo, C., Loste, E., Gómez-Morales, J., García-Carmona, J. & Fraile, J. Calcite precipitation by a high-pressure CO2 carbonation route. *Journal of Supercritical Fluids* **36**, (2006).

27. Prabhu, S. D. *et al.* Valorization of Construction and Demolition Wastes via Organic Acid Mediated Calcium Recovery and CO_2 Mineralization with Regenerable Sodium Glycinate Solvent: A Pathway toward Circularity in the Construction Industry. *Ind Eng Chem Res* **63**, 19359–19374 (2024).

28. Gong, Y. U. T. *et al.* Phase transitions in biogenic amorphous calcium carbonate. *Proc Natl Acad Sci U S A* **109**, (2012).

29. Freeman, C. L. & Harding, J. H. The transformation of amorphous calcium carbonate to calcite and classical nucleation theory. *J Cryst Growth* **603**, (2023).

30. Vickers, M. L. *et al.* The ikaite to calcite transformation: Implications for palaeoclimate studies. *Geochim Cosmochim Acta* **334**, (2022).

31. Fukushi, K., Munemoto, T., Sakai, M. & Yagi, S. Monohydrocalcite: A promising remediation material for hazardous anions. *Science and Technology of Advanced Materials* vol. 12 Preprint at https://doi.org/10.1088/1468-6996/12/6/064702 (2011).

32. Livne, A. *et al.* A fungal mycelium templates the growth of aragonite needles. *J Mater Chem B* **7**, (2019).

33. Schenk, A. S., Albarracin, E. J., Kim, Y. Y., Ihli, J. & Meldrum, F. C. Confinement stabilises single crystal vaterite rods. *Chemical Communications* **50**, (2014).

34. Kim, Y. Y. *et al.* Capillarity creates single-crystal calcite nanowires from amorphous calcium carbonate. *Angewandte Chemie - International Edition* **50**, (2011).

35. Yu, J. *et al.* Simulation of calcium carbonate nucleation processes in confined C-S-H nanopores with different calcium-silicon ratios. *Constr Build Mater* **438**, 137157 (2024).

36. Li, J.-Y., Ma, R.-T., Zheng, S.-Q., Xia, T. & Yi, H.-B. Microscopic insights into the effects of interfacial dynamics and nanoconfinement on characteristics of calcium carbonate clusters within two-dimensional nanochannels. *Physical Chemistry Chemical Physics* **27**, 3263–3277 (2025).

37. Quigley, D., Freeman, C. L., Harding, J. H. & Rodger, P. M. Sampling the structure of calcium carbonate nanoparticles with metadynamics. *Journal of Chemical Physics* **134**, (2011).

38. Stolte, N., Hou, R. & Pan, D. Nanoconfinement facilitates reactions of carbon dioxide in supercritical water. *Nat Commun* **13**, (2022).

39. Abdolhosseini Qomi, M. J. *et al.* Molecular-scale mechanisms of CO2 mineralization in nanoscale interfacial water films. *Nature Reviews Chemistry* Preprint at https://doi.org/10.1038/s41570-022-00418-1 (2022).

40. Dziadkowiec, J., Zareeipolgardani, B., Dysthe, D. K. & Røyne, A. Nucleation in confinement generates long-range repulsion between rough calcite surfaces. *Sci Rep* **9**, (2019).

41. Rosenfeld, D. E. & Schmuttenmaer, C. A. Dynamics of the water hydrogen bond network at ionic, nonionic, and hydrophobic interfaces in nanopores and reverse micelles. *Journal of Physical Chemistry B* **115**, (2011).

42. Hou, D., Li, Z., Zhao, T. & Zhang, P. Water transport in the nano-pore of the calcium silicate phase: Reactivity, structure and dynamics. *Physical Chemistry Chemical Physics* **17**, (2015).

43. Deng, H. *et al.* Two competitive nucleation mechanisms of calcium carbonate biomineralization in response to surface functionality in low calcium ion concentration solution. *Regen Biomater* **2**, (2015).

44. Osti, N. C., Jalarvo, N. & Mamontov, E. Backscattering silicon spectrometer (BASIS): sixteen years in advanced materials characterization. *Mater Horiz* **11**, 4535–4572 (2024).

45. Wyckoff, R. W. G. Crystal structure of high temperature cristobalite. *Am J Sci* **s5-9**, (1925).

46. Stallons, J. M. & Iglesia, E. Simulations of the structure and properties of amorphous silica surfaces. *Chem Eng Sci* **56**, (2001).

47. Pirez, C., Morin, J. C., Manayil, J. C., Lee, A. F. & Wilson, K. Sol-gel synthesis of SBA-15: Impact of HCl on surface chemistry. *Microporous and Mesoporous Materials* **271**, (2018).

48. Yang, L. M., Wang, Y. J., Luo, G. S. & Dai, Y. Y. Functionalization of SBA-15 mesoporous silica with thiol or sulfonic acid groups under the crystallization conditions. *Microporous and Mesoporous Materials* **84**, (2005).

49. Geske, J. & Vogel, M. Creating realistic silica nanopores for molecular dynamics simulations. *Mol Simul* **43**, (2017).

50. Tsirelson, V. G., Yu. Antipin, M., Gerr, R. G., Ozerov, R. P. & Struchkov, Y. T. Ruby structure peculiarities derived from X-ray diffraction data localization of chromium atoms and electron deformation density. *physica status solidi (a)* **87**, (1985).

51. Gutiérrez, G. & Johansson, B. Molecular dynamics study of structural properties of amorphous <math display="inline"> <mrow> <msub> <mrow> <mi mathvariant="normal">Al</mi> </mrow> <mrow> <mn>2</mn> </mrow> </msub> </mrow> <mrow> <msub> <mrow> <mi mathvariant="normal">O</mi> </mrow> <mrow> <mn>3</mn> </mrow> </msub> </mrow> </math>. *Phys Rev B* **65**, 104202 (2002).

52. Nguyen, G. T., Nguyen, T. T., Nguyen, T. T. & Le, V. V. Molecular dynamics simulations of pressure-induced structural and mechanical property changes in amorphous Al2O3. *J Non Cryst Solids* **449**, (2016).

53. Bond, A. D. On the crystal structures and melting point alternation of the n-alkyl carboxylic acids. *New Journal of Chemistry* **28**, (2004).

54. Dennington, R. D. I. I., Keith, T. A., & Millam, J. M. GaussView, version 6.0. 16. *Semichem Inc Shawnee Mission KS.* **450**, (2024).

55. H. Bekker *et al.* Gromacs: a parallel computer for molecular dynamics simulations – ScienceOpen. *Physics Computing* **92**, (1993).

56. Abraham, M. J. *et al.* Gromacs: High performance molecular simulations through multi-level parallelism from laptops to supercomputers. *SoftwareX* **1–2**, (2015).

57. Cygan, R. T., Liang, J. J. & Kalinichev, A. G. Molecular models of hydroxide, oxyhydroxide, and clay phases and the development of a general force field. *Journal of Physical Chemistry B* **108**, (2004).

58. Vanommeslaeghe, K. *et al.* CHARMM general force field: A force field for drug-like molecules compatible with the CHARMM all-atom additive biological force fields. *J Comput Chem* **31**, (2010).

59. Wacha, A. F. & Lemkul, J. A. charmm2gmx: An Automated Method to Port the CHARMM Additive Force Field to GROMACS. *J Chem Inf Model* **63**, (2023).

60. Kaminski, G. A., Friesner, R. A., Tirado-Rives, J. & Jorgensen, W. L. Evaluation and reparametrization of the OPLS-AA force field for proteins via comparison with accurate quantum chemical calculations on peptides. *Journal of Physical Chemistry B* **105**, (2001).

61. Mosallanejad, S., Oluwoye, I., Altarawneh, M., Gore, J. & Dlugogorski, B. Z. Interfacial and bulk properties of concentrated solutions of ammonium nitrate. *Physical Chemistry Chemical Physics* **22**, (2020).

62. Mark, P. & Nilsson, L. Structure and dynamics of the TIP3P, SPC, and SPC/E water models at 298 K. *Journal of Physical Chemistry A* **105**, (2001).

63. Hess, B., Bekker, H., Berendsen, H. J. C. & Fraaije, J. G. E. M. LINCS: A Linear Constraint Solver for molecular simulations. *J Comput Chem* **18**, (1997).

64. Van Gunsteren, W. F. & Berendsen, H. J. C. A Leap-Frog Algorithm for Stochastic Dynamics. *Mol Simul* **1**, (1988).

65. GrubmüLler, H., Heller, H., Windemuth, A. & Schulten, K. Generalized verlet algorithm for efficient molecular dynamics simulations with long-range interactions. *Mol Simul* **6**, (1991).

66. Essmann, U. *et al.* A smooth particle mesh Ewald method. *J Chem Phys* **103**, (1995).

67. Bernetti, M. & Bussi, G. Pressure control using stochastic cell rescaling. *Journal of Chemical Physics* **153**, (2020).

68. Humphrey, W., Dalke, A. & Schulten, K. VMD: Visual molecular dynamics. *J Mol Graph* **14**, (1996).

69. Jiang, X., Tang, X., Tang, L., Zhang, B. & Mao, H. Synthesis and formation mechanism of amorphous silica particles via sol–gel process with tetraethylorthosilicate. *Ceram Int* **45**, (2019).

70. Zhang, X., Bhuvana, S. & Loo, L. S. Characterization of layered silicate dispersion in polymer nanocomposites using Fourier transform infrared spectroscopy. *J Appl Polym Sci* **125**, (2012).

71. Osswald, J. & Fehr, K. T. FTIR spectroscopic study on liquid silica solutions and nanoscale particle size determination. *J Mater Sci* **41**, (2006).

72. Ellerbrock, R., Stein, M. & Schaller, J. Comparing amorphous silica, short-range-ordered silicates and silicic acid species by FTIR. *Sci Rep* **12**, (2022).

73. Petrisor, G. *et al.* Mesoporous Silica Materials Loaded with Gallic Acid with Antimicrobial Potential. *Nanomaterials* **12**, (2022).

74. Hasan, I., Binsharfan, I. I., Khan, R. A. & Alsalme, A. L-ascorbic acid-g-polyaniline mesoporous silica nanocomposite for efficient removal of crystal violet: A batch and fixed bed breakthrough studies. *Nanomaterials* **10**, (2020).

75. Zhang, X. *et al.* Controllable synthesis of raspberry-like PS-SiO2 nanocomposite particles: Via Pickering emulsion polymerization. *RSC Adv* **8**, (2018).

76. Thahir, R., Wahab, A. W., Nafie, N. L. & Raya, I. Synthesis of mesoporous silica sba-15 through surfactant set-up and hydrothermal process. *Rasayan Journal of Chemistry* **12**, (2019).

77. BM, V. & M, V. Photocatalytic Degradation of Toxic Methyl Red Dye Using Silica Nanoparticles Synthesized from Rice Husk Ash. *J Environ Anal Toxicol* **05**, (2015).

78. Sutha, S. *et al.* Structural studies of nano silica employing on-line ultrasonic studies. *Phase Transitions* **85**, (2012).

79. Wang, Y., Muramatsu, A. & Sugimoto, T. FTIR analysis of well-defined α-Fe2O3 particles. *Colloids Surf A Physicochem Eng Asp* **134**, (1998).

80. Rizzi, F. *et al.* High surface area mesoporous silica nanoparticles with tunable size in the sub-micrometer regime: Insights on the size and porosity control mechanisms. *Molecules* **26**, (2021).

81. Xu, Y. *et al.* Revisiting the Surface Energy Parameters of Standard Test Liquids with a Corrected Contact Angle Method over Rough Surfaces. *Langmuir* **38**, (2022).

82. Zhang, Z. *et al.* Binary Liquid Mixture Contact-Angle Measurements for Precise Estimation of Surface Free Energy. *Langmuir* **35**, (2019).

83. Singh, M. K. & Singh, A. Contact angle and surface wettability measurement. in *Characterization of Polymers and Fibres* (2022). doi:10.1016/b978-0-12-823986-5.00013-0.

84. Giridhar, G., Manepalli, R. K. N. R. & Apparao, G. Contact Angle Measurement Techniques for Nanomaterials. in *Thermal and Rheological Measurement Techniques for Nanomaterials Characterization* vol. 3 (2017).

85. Domínguez, N. *et al.* Contact angle measurement by means of a confocal device. in *Modeling Aspects in Optical Metrology VI* vol. 10330 (2017).

86. Liber-Kneć, A. & Łagan, S. Surface testing of dental biomaterials—determination of contact angle and surface free energy. *Materials* **14**, (2021).

87. Ponomar, M. *et al.* Sessile Drop Method: Critical Analysis and Optimization for Measuring the Contact Angle of an Ion-Exchange Membrane Surface. *Membranes (Basel)* **12**, (2022).

88. Dalton, L. E. *et al.* Contact Angle Measurements Using Sessile Drop and Micro-CT Data from Six Sandstones. *Transp Porous Media* **133**, (2020).

89. Chunbo, R., Guqiao, D., Weichang, L., Yan, D. & Wentao, H. Wetting on nanoporous alumina surface: Transition between Wenzel and Cassie states controlled by surface structure. *Langmuir* **24**, (2008).

90. Krainer, S. & Hirn, U. Contact angle measurement on porous substrates: Effect of liquid absorption and drop size. *Colloids Surf A Physicochem Eng Asp* **619**, (2021).

91. Li, C., Zhang, J., Han, J. & Yao, B. A numerical solution to the effects of surface roughness on water–coal contact angle. *Sci Rep* **11**, (2021).

92. Guo, C., Wang, X. W. & Yuan, Z. H. Pore diameter-dependence wettability of porous anodized aluminum oxide membranes. *Journal of Porous Materials* **20**, (2013).

93. Fillion, R. M., Riahi, A. R. & Edrisy, A. A review of icing prevention in photovoltaic devices by surface engineering. *Renewable and Sustainable Energy Reviews* vol. 32 Preprint at https://doi.org/10.1016/j.rser.2014.01.015 (2014).

94. Spencer, S. J., Deacon, C. G. & Andrews, G. T. Contact Angle Studies on Porous Silicon: Evidence for Heterogeneous Wetting and Implications of Oxidation. *Silicon* **15**, (2023).

95. Gao, L. & McCarthy, T. J. How Wenzel and Cassie were wrong. *Langmuir* **23**, (2007).

96. Wang, M., Zheng, H., Lin, X. & Huang, W. Wenzel model based investigation of heterogeneous nucleation on a coarse substrate. in *IOP Conference Series: Materials Science and Engineering* vol. 27 (2011).

97. Sekiguchi, K., Nakanishi, T., Segawa, H. & Yasumori, A. Fabrication of Silica Nanoparticle Monolayer Arrays Using an Anodic Aluminum Oxide Template. *ACS Omega* **4**, (2019).

98. Iler, R. K. The chemistry of silica: solubility, polymerization, colloid and surface properties, and biochemistry. *Lavoisierfr* (1979) doi:10.1002/ange.19800920433.

99. Rother, G. *et al.* Water Uptake by Silica Nanopores: Impacts of Surface Hydrophilicity and Pore Size. *Journal of Physical Chemistry C* **124**, (2020).

100. Buijnsters, J. G., Zhong, R., Tsyntsaru, N. & Celis, J. P. Surface wettability of macroporous anodized aluminum oxide. *ACS Appl Mater Interfaces* **5**, (2013).

101. O. David, R. *et al.* The role of contact angle and pore width on pore condensation and freezing. *Atmos Chem Phys* **20**, (2020).

102. Strangfeld, C. Quantification of the Knudsen Effect on the Effective Gas Diffusion Coefficient in Partially Saturated Pore Distributions. *Adv Eng Mater* **23**, (2021).

103. Zhu, M. & Mao, Y. Large-pore-size membranes tuned by chemically vapor deposited nanocoatings for rapid and controlled desalination. *RSC Adv* **10**, (2020).

104. Argyris, D., Ho, T., Cole, D. R. & Striolo, A. Molecular dynamics studies of interfacial water at the alumina surface. *Journal of Physical Chemistry C* **115**, (2011).

105. Argyris, D., Cole, D. R. & Striolo, A. Dynamic behavior of interfacial water at the silica surface. *Journal of Physical Chemistry C* **113**, (2009).

106. Hribar, B., Southall, N. T., Vlachy, V. & Dill, K. A. How ions affect the structure of water. *J Am Chem Soc* **124**, (2002).

107. Dutta, N., Mitra, S. & Nirmalkar, N. Understanding the Role of Surface Charge on Nanobubble Capillary Bridging during Particle-Particle Interaction. *Langmuir* **40**, (2024).

108. Greathouse, J. A. *et al.* Effects of nanoconfinement and surface charge on iron adsorption on mesoporous silica. *Environ Sci Nano* **8**, (2021).

109. Langford, A., Bruchsaler, M. & Gupta, M. Suspension properties and characterization of aluminum-adjuvanted vaccines. in *Practical Aspects of Vaccine Development* (2021). doi:10.1016/B978-0-12-814357-5.00008-8.

110. Mark Fleharty. Surface Charge Regulation Effects on Fluidic Nanoscale Systems. (2015).

111. Niu, Y., Yu, W., Yang, S. & Wan, Q. Understanding the relationship between pore size, surface charge density, and Cu2+ adsorption in mesoporous silica. *Sci Rep* **14**, 13521 (2024).

112. Liu, S., Luo, J., Xie, G. & Guo, D. Effect of surface charge on water film nanoconfined between hydrophilic solid surfaces. in *Journal of Applied Physics* vol. 105 (2009).

113. Lutze, J. *et al.* α-((4-cyanobenzoyl)oxy)-ω-methyl poly(ethylene glycol): A new stabilizer for silver nanoparticles. *Beilstein Journal of Nanotechnology* **8**, (2017).

114. Zhang, Y. *et al.* Physical adsorption of OH^- causes anomalous charging at oxide–water interfaces. *Chemical Communications* **60**, 9113–9116 (2024).

115. Zhang, Z. A new method for estimating zeta potential of carboxylic acids' functionalised particles. *Mol Phys* **122**, (2024).

116. Romero, V. & Benavente, J. Electrochemical Characterization of Nanoporous Alumina-Based Membranes with Different Structure and Geometrical Parameters by Membrane Potential Analysis. *Micro* **2**, (2022).

117. Vajandar, S. K. *et al.* SiO2-coated porous anodic alumina membranes for high flow rate electroosmotic pumping. *Nanotechnology* **18**, (2007).

118. Kang, H., Long, D. J. & Haynes, C. L. Preparation of Colloidally Stable Positively Charged Hollow Silica Nanoparticles: Effect of Minimizing Hydrolysis on ζ Potentials. *Langmuir* **35**, (2019).

119. Prakash, S. *et al.* Electrokinetic transport in silica nanochannels with asymmetric surface charge. *Microfluid Nanofluidics* **19**, (2015).

120. Pedimonte, B. J. *et al.* Morphological zeta-potential variation of nanoporous anodic alumina layers and cell adherence. *Acta Biomater* **10**, (2014).

121. Vi, L. D., Dudich, V. V., Rabatuev, G. G., Lazarouk, A. S. & Korotkevich, A. V. The Changes of Surface Potential and Built-in Charge in Alumina Films after the Anodization Process. in *International Journal of Nanoscience* vol. 18 (2019).

122. Kovaleva, E. G. *et al.* Electrostatic properties of inner nanopore surfaces of anodic aluminum oxide membranes upon high temperature annealing revealed by EPR of pH-sensitive spin probes and labels. *J Memb Sci* **604**, (2020).

123. Asgar, H., Mohammed, S. & Gadikota, G. Confinement induces stable calcium carbonate formation in silica nanopores. *Nanoscale* **14**, (2022).

124. Hakim, S. S. *et al.* Interactions of the calcite {10.4} surface with organic compounds: Structure and behaviour at mineral-organic interfaces. *Sci Rep* **7**, (2017).

125. Sulimai, N. H. *et al.* XRD Line Profile Analysis for Calcite Produced by Precipitation Method at Different Pre-Cursor Concentration. Preprint at https://doi.org/10.21203/rs.3.rs-3272744/v1 (2023).

126. Hayakawa, S., Hajima, Y., Qiao, S., Namatame, H. & Hirokawa, T. Characterization of calcium carbonate polymorphs with Ca K edge X-ray absorption fine structure spectroscopy. in *Analytical Sciences* vol. 24 (2008).

127. Ikaite: Mineral Information, Data, and Localities. *https://www.mindat.org/min-2007.html*.

128. Holder, C. F. & Schaak, R. E. Tutorial on Powder X-ray Diffraction for Characterizing Nanoscale Materials. *ACS Nano* vol. 13 Preprint at https://doi.org/10.1021/acsnano.9b05157 (2019).

129. Bouras, M., Boumaiza, A., Ji, V. & Rouag, N. XRD peak broadening characterization of deformed microstructures and heterogeneous behavior of carbon steel. *Theoretical and Applied Fracture Mechanics* **61**, (2012).

130. Himabindu, B., Latha Devi, N. S. M. P. & Rajini Kanth, B. Microstructural parameters from X-ray peak profile analysis by Williamson-Hall models; A review. in *Materials Today: Proceedings* vol. 47 (2021).

131. Cherkas, O. *et al.* On the kinetics of phase transformations of dried porous vaterite particles immersed in deionized and tap water. *Advanced Powder Technology* **29**, (2018).

132. Strohm, S. B., Berghofer, S. A., Kaiser, C. & Jordan, G. On the Ephemeral Occurrence of Ikaite in Aqueous Solutions between 0 and 20 °C. *ACS Earth Space Chem* **8**, 1725–1736 (2024).

133. Simon, P. *et al.* Nested Formation of Calcium Carbonate Polymorphs in a Bacterial Surface Membrane with a Graded Nanoconfinement: An Evolutionary Strategy to Ensure Bacterial Survival. *ACS Biomater Sci Eng* **8**, (2022).

134. Brekke-Svaland, G. & Bresme, F. Interactions between Hydrated Calcium Carbonate Surfaces at Nanoconfinement Conditions. *Journal of Physical Chemistry C* **122**, (2018).

135. Katsman, A., Polishchuk, I. & Pokroy, B. On the mechanism of calcium carbonate polymorph selection via confinement. *Faraday Discuss* **235**, (2022).

136. Hassanzadeh-Tabrizi, S. A. Precise calculation of crystallite size of nanomaterials: A review. *Journal of Alloys and Compounds* vol. 968 Preprint at https://doi.org/10.1016/j.jallcom.2023.171914 (2023).

137. Gagliardi, L. & Pierre-Louis, O. Thin film modeling of crystal dissolution and growth in confinement. *Phys Rev E* **97**, (2018).

138. Vavouraki, A. I., Putnis, C. V., Putnis, A. & Koutsoukos, P. G. Crystal growth and dissolution of calcite in the presence of fluoride ions: An atomic force microscopy study. *Cryst Growth Des* **10**, (2010).

139. Høgberget, J., Røyne, A., Dysthe, D. K. & Jettestuen, E. Microscopic modeling of confined crystal growth and dissolution. *Phys Rev E* **94**, (2016).

140. Kohler, F., Pierre-Louis, O. & Dysthe, D. K. Crystal growth in confinement. *Nat Commun* **13**, (2022).

141. Hydrophobic calcium carbonate and preparation method thereof. (2019).

142. Kellermeier, M. *et al.* Colloidal stabilization of calcium carbonate prenucleation clusters with silica. *Adv Funct Mater* **22**, (2012).

143. Li, L., Kohler, F., Røyne, A. & Dysthe, D. K. Growth of calcite in confinement. *Crystals (Basel)* **7**, (2017).

144. Diao, Y. & Espinosa-Marzal, R. M. Molecular insight into the nanoconfined calcite-solution interface. *Proc Natl Acad Sci U S A* **113**, (2016).

145. Fumagalli, L. *et al.* Anomalously low dielectric constant of confined water. *Science (1979)* **360**, (2018).

146. Yang, H. *et al.* Suppressed terahertz dynamics of water confined in nanometer gaps. *Sci Adv* **10**, (2024).

147. Kožíšek, Z. Crystal nucleation kinetics in confined systems. in *CrystEngComm* vol. 15 (2013).

148. Batys, P., Zhang, Y., Lutkenhaus, J. L. & Sammalkorpi, M. Hydration and Temperature Response of Water Mobility in Poly(diallyldimethylammonium)-Poly(sodium 4-styrenesulfonate) Complexes. *Macromolecules* **51**, (2018).

149. Zeng, M. *et al.* Confinement generates single-crystal aragonite rods at room temperature. *Proc Natl Acad Sci U S A* **115**, (2018).

150. Jani, A. *et al.* Dynamics of water confined in mesopores with variable surface interaction. *Journal of Chemical Physics* **154**, (2021).

151. Zheng, Z.-Y. *et al.* Real-space visualization of intercalated water phases at the hydrophobic graphene interface with atomic force microscopy. *Front Phys (Beijing)* **15**, 23601 (2020).

152. Ferrara, C. G. & Grigera, T. S. Dynamics and structural behavior of water in large confinement with planar amorphous walls. *Journal of Chemical Physics* **147**, (2017).

153. Bülbül, E. *et al.* Confined hydration in nanometer-graded plasma polymer films: Insights from surface-enhanced infrared absorption spectroscopy. *Surfaces and Interfaces* **23**, (2021).

154. Liu, L., Zhao, J., Culligan, P. J., Qiao, Y. & Chen, X. Thermally responsive fluid behaviors in hydrophobic nanopores. *Langmuir* **25**, (2009).

155. David, R., Marchal, P. & Marcant, B. Modelling of agglomeration in industrial crystallization from solution. *Chem Eng Technol* **18**, (1995).

156. David, R., Espitalier, F., Cameirão, A. & Rouleau, L. Developments in the understanding and modeling of the agglomeration of suspended crystals in cr ystallization from solutions. *KONA Powder and Particle Journal* **21**, (2003).

157. Eberl, D. D., Drits, V. A. & Środoń, J. Deducing growth mechanisms for minerals from the shapes of crystal size distributions. *Am J Sci* **298**, (1998).

158. Bauer, B. A., Ou, S., Patel, S. & Siva, K. Dynamics and energetics of hydrophobically confined water. *Phys Rev E Stat Nonlin Soft Matter Phys* **85**, (2012).

159. Rao, P. V. G., Gandhi, K. S. & Ayappa, K. G. Enhancing the hydrophobic effect in confined water nanodrops. *Langmuir* **23**, (2007).

160. Kumar, P. & Han, S. Dynamics of two-dimensional monolayer water confined in hydrophobic and charged environments. *J Chem Phys* **137**, (2012).

161. Tarasevich, Y. I. State and structure of water in vicinity of hydrophobic surfaces. *Colloid Journal* **73**, (2011).

162. Kim, J., Tian, Y. & Wu, J. Thermodynamic and Structural Evidence for Reduced Hydrogen Bonding among Water Molecules near Small Hydrophobic Solutes. *Journal of Physical Chemistry B* **119**, (2015).

163. Grdadolnik, J., Merzel, F. & Avbelj, F. Origin of hydrophobicity and enhanced water hydrogen bond strength near purely hydrophobic solutes. *Proc Natl Acad Sci U S A* **114**, (2017).

164. Galamba, N. Water tetrahedrons, hydrogen-bond dynamics, and the orientational mobility of water around hydrophobic solutes. *Journal of Physical Chemistry B* **118**, (2014).

165. Wawer, J. & Krakowiak, J. Structural changes of water caused by non-electrolytes: Volumetric and compressibility approach for urea-like analogues. *J Mol Liq* **259**, (2018).

166. Osti, N. C., Thapaliya, B. P., Dai, S., Tyagi, M. & Mamontov, E. Strong Enhancement of Nanoconfined Water Mobility by a Structure Breaking Salt. *Journal of Physical Chemistry Letters* **12**, (2021).

167. Zhakiyeva, Z. *et al.* How much water is there within calcium silicate hydrates? Probing water dynamics by inelastic neutron scattering and molecular dynamics simulations. *Cem Concr Res* (2023).

168. Baum, M., Rieutord, F., Juranyi, F., Rey, C. & Rébiscoul, D. Dynamical and Structural Properties of Water in Silica Nanoconfinement: Impact of Pore Size, Ion Nature, and Electrolyte Concentration. *Langmuir* **35**, (2019).

169. Li, H. *et al.* Role of Exchange Cations and Layer Charge on the Dynamics of Confined Water. *Journal of Physical Chemistry A* **128**, (2024).

CHAPTER 5

Deciphering the Mechanisms Governing Calcium Carbonate Phase Selection at Nanoconfined Reactive Silica Interfaces

1. Introduction

Interfacial reaction and mechanism governing carbon mineralization in nanoconfined and reactive environments provides insights into the dynamic interplay between ion transport, phase stability, and reactive mineral-mediated nucleation control that dictate carbonate polymorph selection essential for advancing applications in geochemical carbon sequestration, cementitious material development, and biomineralization process. [1–4] Specifically, the carbonation of natural silicate minerals like wollastonite ($CaSiO_3$), forsterite (Mg_2SiO_4), anorthite ($CaAl_2Si_2O_8$), and olivine (Mg_2SiO_4) provides applications in long-term CO_2 storage forming stable carbonate phases through mineral trapping, involving interfacial reactions, dissolution and crystal growth governing the kinetics and thermodynamics of the process. [5–11]

Notably, exploring the minerology of the mafic and ultramafic rocks indicate the predominant presence of calcium and magnesium, which form a resource base for forming stable carbonates. [3,12,13] Prior studies have extensively investigated the mineral carbonation of the silicate-rich minerals where the overall reaction can be written as,

$$MSiO_3(s) + CO_2\,(g) \rightarrow MCO_3\,(s) + SiO_2(s)$$

Where M represents either Ca^{2+} or Mg^{2+} or other divalent cations. Furthermore, these studies also investigated the preferential carbonate phase formation where wollastonite carbonation at 150 °C and 20 bar display the formation of calcite phase, [14] carbonation of high-calcite wollastonite tailings between 40-60 °C and 20-100 bar indicate the

formation of calcite, [15] carbonation of cement suspension in the presence of alumina-silica gel at 80 ℃ formed aragonite whisker-rich material, [16] carbonation of synthetic alkali-silica reaction gels forming calcite, [17] carbonation of calcium-leached solution from construction and demolition waste forming vaterite, [18] and carbonation reaction of serpentinized peridotite from 155-185 ℃ and 35-50 bar forming magnesite. [19] Based on these studies, it was evident that the mineral composition, carbonation conditions and presence of reactive silica interface influence the carbonate polymorph formation and stabilization. Comprehending the carbonation mechanism involving reactive silica interface was outlined through simulation where in a monocalcium silicate system the breaking of Ca-O bond driven by electrophilic attack from non-bridged oxygen atoms occurs facilitating easier Ca^{2+} dissolution, and enhancing carbonation reactivity, giving insights into the overall mechanism involving several rate-determining steps consisting of chemical reaction mechanisms to diffusion-controlled mechanisms. [20,21]

The ability of controlling the morphology not only depends on the minerology of the surface or the reaction conditions but also taking into consideration the interfacial effects is highly crucial as it can enhance nucleation through collective thermodynamic and kinetic effects. [22,23] Predominantly, the influence of thin water film in mediating the dissolution of CO_2 coupled with dissolution and reprecipitation of carbonate crystals is vital which control the mineral phase formation even in bulk regions. [24] At the reactive silica interface, water becomes more structured slowing the dynamics and altering the free energies across the interface while being highly sensitive to pH change and presence of ions. [25–27] Specifically, water in the interfacial regions of calcium silicate facilitates mineral dissolution and ion exchange through the interaction with interlayer

Ca and O, influencing hydration and structural organization. [28,29] Without this interfacial water, the carbonate complex formation on the surface of wollastonite is restricted to one monolayer whereas water assisted carbonation allows the exchange of Ca^{2+} ions with CO_3^{2-} ions inducing partial delocalization. [30] This dependence on interfacial water is also observed for forsterite where its dissolution and carbonation reaction slows down in the presence of silica-rich water-depleted layer deposition, underscoring the role of water on carbonation. [31]

Based on these observations we can deduce that the carbonation at reactive silica interface follows two step aqueous phase mechanism involving the leaching of Ca^{2+} or Mg^{2+} ions from the silica matrix subsequently reacting with aqueous bicarbonate or carbonate species for nucleation and growth. [14,32,33] A significant characteristic of this process is the formation of passivating silica-rich layer which serves as a diffusion barrier, progressively restricting further cation release impeding carbonation. [14,33] However, in natural conditions, mechanical stresses induced by particle-particle interaction or volume reduction during silica precipitation can disrupt the passivation layer, re-enabling carbonation. [33–35] Although these studies in bulk fluid system provides insights into the reaction mechanisms and interfacial effects, the primary rate-limiting factor is its dependence on temperature where below 150 °C cation leaching is rate-limiting for wollastonite whereas at higher temperatures, carbonate nucleation and growth becomes limiting due to reduced bicarbonate activity. [14]

Aligning with the natural carbonation reactions at reactive silica interfaces require confining the system and performing the reaction at subsurface temperature conditions. Nanoconfinement introduces anomalous physicochemical factors which will influence

the carbonation reaction at the unreactive/reactive silica interface, particularly in terms of nucleation kinetics, phase polymorphism and ion mobility. [36,37] In confined geometries, the energy barrier for carbonate nucleation is reduced due to altered ion hydration and dielectric properties while the silica passivation may get altered because of structural disruption and confined transport bypassing barriers. [32,38,39] Furthermore, the behavior of water deviates vastly from bulk systems exhibiting altered hydrogen bonding, reduced diffusivity and lower dielectric permittivity, modifying the solvation environment and energetics of crystal growth. [40–45] Nanoconfinement parallelly alters the rate limiting steps and shift the reaction from bulk to interfacial mediated while being independent of temperature. [46–48] This anomalous mechanism enables carbonation pathway that otherwise would be kinetically inaccessible. Prior studies have investigated and observed such anomalous characteristics where calcite formation is stabilized when confined in silica nanochannels, [49] or 30 nm KIT-6 mesoporous silica, [50] while vaterite stabilization is observed in 12 nm KIT-6 mesoporous silica, [50] and aragonite is stabilized when dissolved in silica gel. [51] Hydrated calcium carbonate phases which are unstable in bulk solutions is observed to be stable in nanoconfined systems where monohydrocalcitic amorphous calcium carbonate is observed when confined in 24 nm controlled pore glass, [52] while ikaite ($CaCO_3$. $6H_2O$) and monohydrocalcite ($CaCO_3$. H_2O) is stabilized under volume confined nano-liter and pico-liter droplets. [53] Although these studies probed the carbonate nucleation in unreactive silica interface, the primary observation of carbonate nucleation in reactive silica interface is crucial and mimicking subsurface conditions. To test this phenomenon, the current study focuses on the carbonation reaction mechanism confined

in calcium silicate nanochannels. Initiating the carbonate reaction involves the initial synthesis of calcium silicate (Ca-Si) nanochannels in 200 nm anodic alumina membranes as shown in **Figure 42**. During synthesis, calcium nitrate tetrahydrate was used as the calcium source, TEOS was used as the silica source, and to control the morphology CTAB surfactant was utilized. The onset of carbonate reaction is due to the loading of 1M $NaHCO_3$ solution through these nanochannels via aspiration and the evolution of the polymorphs is identified for reactions aged at different temperatures. These observations underscore the critical role of nanoconfinement, temperature and interfacial chemistry in dictating carbonate phase preferential formation, providing foundations into the natural mineralization applicable to CO_2 sequestration strategies.

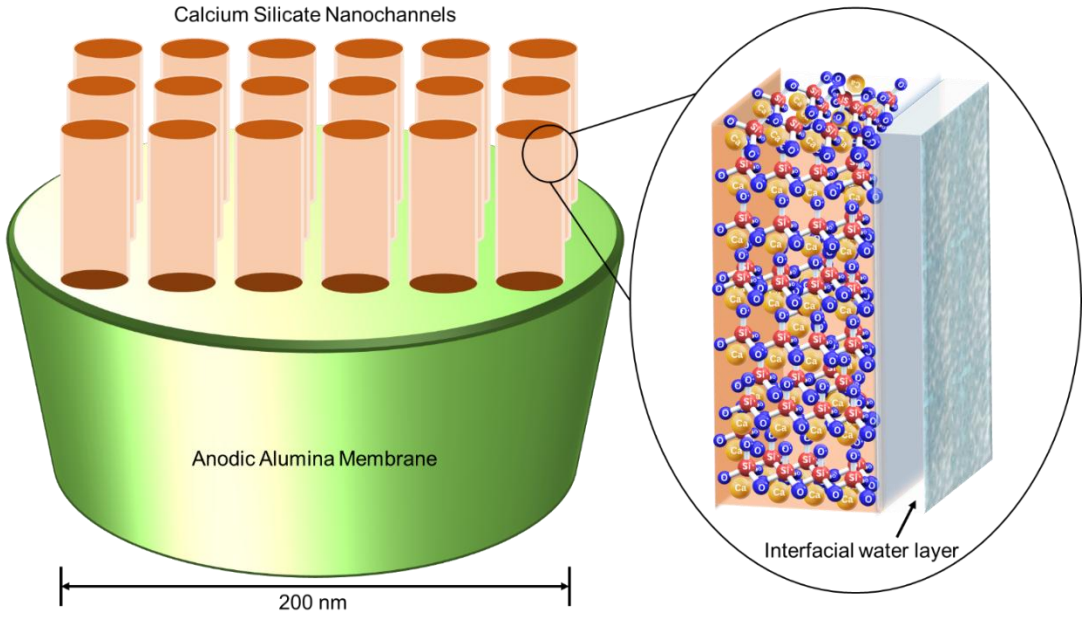

Figure 42 Schematic representation of calcium silicate nanochannels loaded in 200 nm anodic alumina membrane. Within the magnified schematic the calcium ions, silica ions and oxygen ions are represented by yellow, red and blue circles along with the presence on interfacial water layer.

2. Experimental and Methodology

2.1 *Materials*

Whatman™ Anodisc™ having pore size of 200 nm and a length of 60 µm was used as the alumina template which was purchased from Cytiva. To synthesize calcium silicate nanochannels, a precursor solution consisting of Cetyltrimethylammonium bromide (CTAB) surfactant (MP Biomedicals, Molecular biology reagent), hydrochloric acid (HCl) (Sigma Aldrich, 37% ACS reagent), tetraethyl orthosilicate (TEOS) (Sigma Aldrich, 98% reagent grade), deionized (DI) water (18.2 MΩ.cm) from the Milli-Q Q-POD® system, and laboratory grade calcium nitrate tetrahydrate ($Ca(NO_3)_2.\ 4H_2O$) (Sigma Aldrich, BioXtra, ≥ 99%) was utilized. For initiating the carbonation of the calcium silicate nanochannels, sodium bicarbonate ($NaHCO_3$) (Fischer Scientific, ACS reagent 99%) was used. To load both the precursor solution into the empty alumina template or sodium bicarbonate into calcium silicate nanochannels, an aspiration setup was utilized with the membranes being placed on a 25 mm diameter, 50 mL capacity filter funnel which was purchased from Cytiva and used without any modification.

2.2 *Synthesis of Calcium Silicate Nanochannels in Anodic Alumina Membranes*

The approach for the synthesis of Ca-Si nanochannels follows sol-gel method where 1g of CTAB was dissolved in a mixture of 20 mL of 1M HCl and 5 mL of DI water and stirred for 1 hour at 38 °C. In another container, 9 mL of TEOS and 9.46 g of $Ca(NO_3)_2.\ 4H_2O$ was mixed for 30 minutes at room temperature conditions at 700 rpm. Later, the silica rich solution and the surfactant solution were mixed together and stirred for 30

minutes at 700 rpm at room temperature conditions. To obtain Ca-Si nanochannels, 0.3 mL of the final solution was passed through the 200 nm AAM via aspiration and this process was repeated for 5 times. Once the loading is completed, all the excess nanoparticle precipitation on the surface of the membrane were removed by washing with ethanol and ageing for 24 hours. To remove the surfactant, the loaded and aged membrane was calcined at 550 ℃ for 4 hours with a ramp rate of 3 ℃/min in a benchtop muffle furnace (Thermo Scientific Thermolyne).

To determine the formation and morphology of the Ca-Si nanochannels, scanning electron microscope (SEM) (Zeiss Gemini 500) with an accelerating voltage of 3 keV for imaging and 12 keV for energy-dispersive X-ray spectroscopy (EDS) mapping was used.

2.3 *Initiating Calcium Carbonate Formation in Ca-Si Nanochannels*

Initiating the carbon mineralization process in these nanochannels involved the use of 1M $NaHCO_3$ where the synthesized Ca-Si nanochannels were placed in an aspiration setup and 0.5 mL of bicarbonate solution was passed through and this process was repeated 3 times and aged at 25 ℃ as shown in **Figure 43**. To understand the influence of temperature on calcium carbonate phase formation, after loading the membranes were immediately transferred into a vacuum oven (Thermo Scientific Lindberg Blue M) and aged at 50 ℃ and 75 ℃ for 10 minutes. The rest of the ageing is allowed at room temperature conditions to prevent any evaporation of the liquid from the nanochannels. For investigating the phase formation and evolution of calcium carbonate phases in all temperature ageing conditions, X-ray diffraction (XRD) measurements was performed

using Bruker D8 Advance ECO Powder diffractometer having a Cu Kα radiation, operating voltage of 40 kV, and current of 25 mA, from 6 hours to 480 hours after loading.

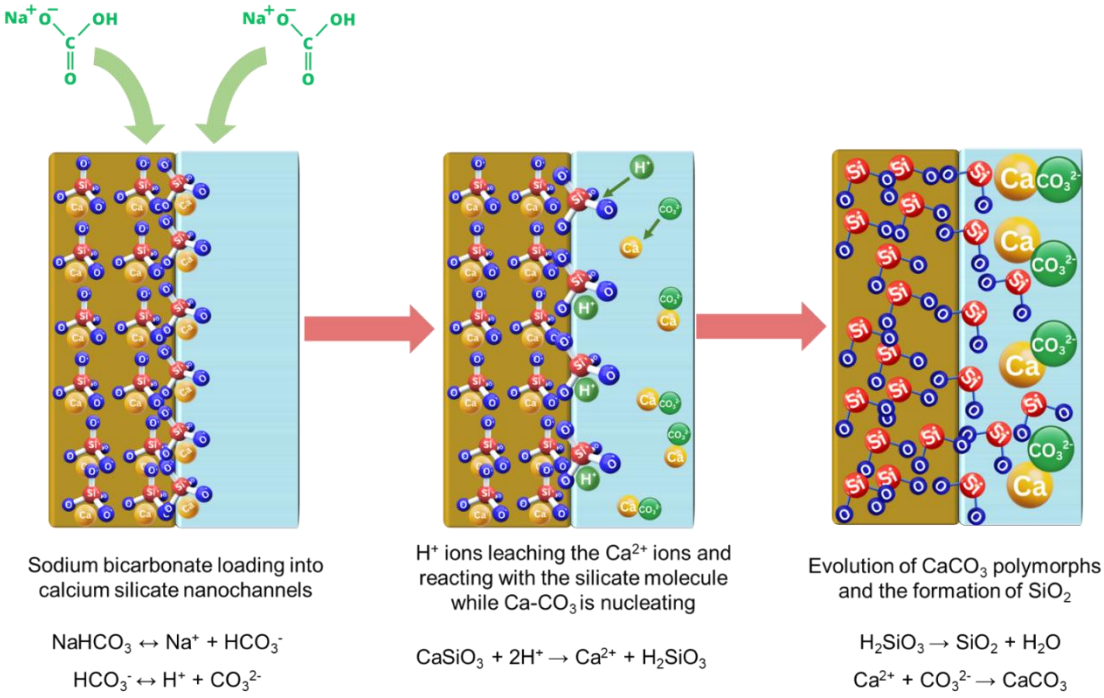

Figure 43 Representation of the reaction mechanism of sodium bicarbonate reacting with calcium silicate nanochannels and the final formation of silicon dioxide (amorphous) and calcium carbonate (s). The chemical reaction occurring at the respective stage is indicated below the write-up. The calcium ions, silica ions and oxygen ions are represented by yellow, red and blue circles while H^+ and CO_3^{2-} ions are represented in green circles.

3. Results and Discussions

3.1 *Surface Morphology of Ca-Si Nanochannels*

The desired outcome from the synthesis of Ca-Si nanochannels is to obtain them in the shape of channels and not as discrete particles. To test this result, the morphology of these nanochannels was observed in a scanning electron microscope. But before any observation is made, the primary step is to dissolve the anodic alumina membrane which

is encapsulating the Ca-Si nanochannels. To achieve this, the loaded AAM is immersed in a solution of 10% H_3PO_4 solution for 24 hours and the nanochannels are obtained via centrifugation. To perform imaging, the acceleration voltage is maintained at 3 keV, and from the SEM images we can confirm that the morphology is indeed in the shape of channels. Further, to identify and quantify the elements in the nanochannels, an EDS mapping was performed for the entire scale of the sample. The EDS peak clearly confirm the presence of high quantities of Si and O while very small peaks correspond to Ca which could be attributed to Ca leaching from the immersion of the membrane in H_3PO_4 solution as shown in **Figure 44**.

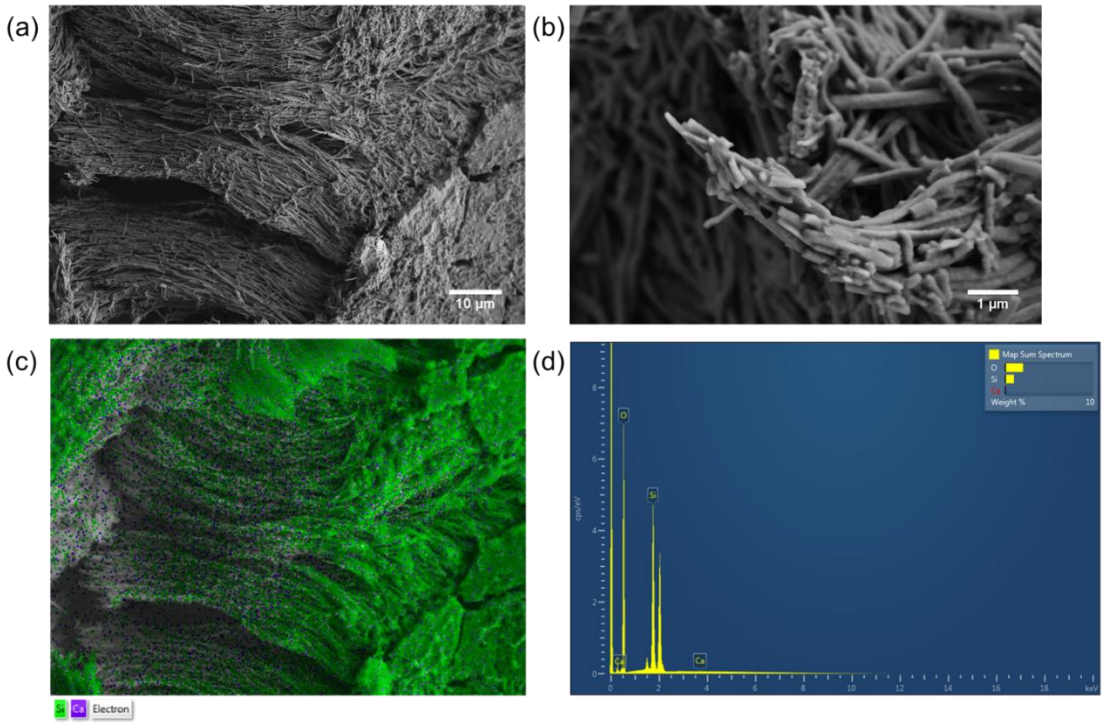

Figure 44 (a,b) Calcium silicate nanochannel formation after etching the alumina membrane with 10% H3PO4 for 24 hours as viewed using a scanning electron microscope, (c,d) EDS measurement to confirm the composition of Ca, Si, and O on the nanochannels.

3.2 *Calcium Carbonate Crystallization and Phase Polymorphism in the Presence of Reactive Silica Interfaces*

Unlike bulk aqueous systems, formation of calcium carbonate in nanoconfinement in the presence of reactive silica interface is enhanced due to nanoscale ion dynamics and lowered energy barrier attributing to the presence of thick interfacial water layer on the surface of the metal-silicate surface. [32,38] To investigate the preferential phase formation and evolution of calcium carbonate at the calcium silicate interface, 1M $NaHCO_3$ solution is passed through the channels via aspiration and X-ray diffraction measurements were carried out as shown in **Figure 45**. From the XRD data, we can deduce that the calcium carbonate formed at 25 ℃ depict the dominant growth of (104) plane of calcite; (222), (115), (202) plane of vaterite; (020), (222) plane of aragonite; and (113) plane of ikaite. The data from XRD from samples aged at 50 ℃ depict the formation of (012) plane of calcite; (202), (104), and (110) plane of vaterite; (111), (222), and (011) plane of aragonite; and (111), (211), (220), and (113) plane of monohydrocalcite. The sample aged at 75 ℃ depict the plane formation of (202), (229), (002), (208), (117) plane of vaterite; (111), (221) plane of aragonite; and (102) plane of monohydrocalcite.

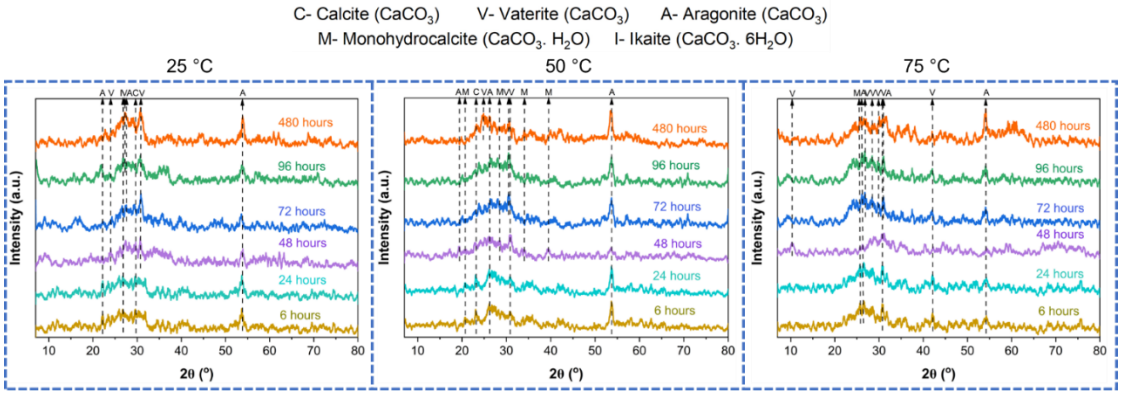

Figure 45 X-ray diffraction (XRD) measurements of calcium carbonate evolution from carbonation of calcium silicate nanochannels from 6 hours to 480 hours after loading investigated at different ageing temperatures.

From the XRD measurements, weight % of each phase is also calculated using the RIR method and the phase evolution over time is investigated. The carbonate phases initially observed when aged at 25 ℃ is anhydrous calcite, aragonite and hydrated ikaite. As the reaction proceeds over time from 6 hours to 480 hours, the key observation of ikaite and calcite dissolution while the formation and stabilization of vaterite and aragonite is observed. The initial formation of ikaite could be attributed to the presence of nm-thick water films while providing a kinetic advantage without involving energy and time-dependent dehydration. [32,54,55] Simultaneously, the role of uncharged $CaCO_3°$ plays a crucial role in the hydrated to anhydrous transition where the uncharged ions could be encapsulated in a localized interfacial water region creating hydrogen bonding and being hydrated. [56] During carbonation, the role of dissolved silica might alter the formation and stability of the polymorphs which could also attribute to the initial hydrated polymorph formation. [57] Within the given reaction, as reaction time increases, another anomalous mechanism observed is calcite dissolution. It is noted that when the bicarbonate ions react with the Ca-Si interface, the silicification reaction occurs influencing the fluid chemistry of calcite dissolution. [58] Furthermore, the growth of calcium carbonate phases is controlled by the deposition of the silica on the carbonate crystals, creating a passivation barrier and reducing the local pH. [59] Other factors which can influence pH is due to the H^+ ions from the bicarbonate solution dissolving Ca^{2+} ions increasing the pH gradient zone in the direction of flow. [60] At the same time, the growth of aragonite and vaterite phases are observed which are consistent with prior

studies indicating aragonite formation after the carbonation of the calcium silicate hydrate (C-S-H) system while vaterite precipitation due to the role of deposited silica or the lowering of pH. [50,61]

Carbonation reaction aged at 50 ℃ indicate the initial formation of anhydrous calcite, vaterite, and aragonite and hydrated monohydrocalcite phase. During ageing, the primary observation is the presence of hydrated phase at high temperatures which could be attributed to the strong interfacial water effects where the hydrogen bonding between the water molecules and the non-bridged oxygen atoms on the silicate layers is strong supporting this stabilization while the divalent Ca^{2+} ions facilitate water sorption in the inter layer space binding to the water whereas the role of dissolved silica in the stabilization and morphological changes of monohydrocalcite is crucial due to the interaction of carbonate and silica solubility vs pH. [62–64] The secondary observation is associated with calcite dissolution which is associated with the role of HCO_3^- ions in leaching Ca^{2+} and the deposited silica restricting the stabilization. [59,60] Lastly, as the reaction proceeds overtime, the stabilization and transition of vaterite and aragonite is noted.

The carbonate phases aged at 75 ℃ exhibit the initial formation of anhydrous vaterite, aragonite and hydrated monohydrocalcite. The presence of hydrated monohydrocalcite phase even at further higher temperatures could be attributed to the strong interfacial hydrogen bonding between the water molecules and the non-bridged oxygen atoms on the silicate layers supporting this stabilization. [62–64] Concurrently, the hydrate phase is accompanied by the formation of vaterite and aragonite and as the reaction time increases, both the anhydrous phases get stabilized due to the preferential formation of

aragonite at the C-S-H and wollastonite system and due to the role of dissolved silica. [8,50,61]

In conclusion, the role of interfacial water and the mechanism of silicification influences which carbonate phase forms first by altering the fluid chemistry, phase stability and morphology. Based on the phase evolution at all temperature conditions, the transition moves from hydrated phase to anhydrous phases. The influence of temperature on the final phase formation is negligible as the interface of calcium silicate clearly prefers the formation of aragonite and vaterite which is shaped by pH shifts, silica dynamics and ion speciation as shown in **Figure 46**.

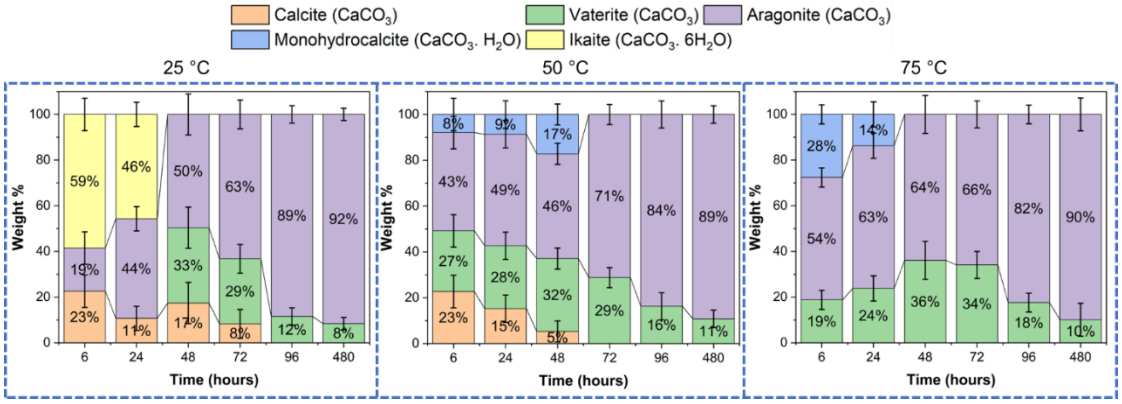

Figure 46 Phase evolution of calcium carbonate polymorphs from calcium silicate carbonation after 6 hours to 480 hours of loading at different reaction ageing temperatures.

4. Conclusion

Unraveling the mechanism of interfacial and confinement-driven dynamics of calcium carbonate crystallization at reactive silica interfaces offers valuable insights into how simultaneous carbonation reaction and dissolved silica influence preferential phase formation occurring in natural and engineered systems, which traditional bulk aqueous systems overlook. Taking this effect into account, the current study investigates the

phase evolution of calcium carbonate crystallization using calcium silicate nanochannels. For initially synthesizing calcium silicate nanochannels, a precursor solution consisting of $Ca(NO_3)_2$. $4H_2O$, TEOS, CTAB and HCl is prepared and the solution is passed through a 200 nm AAM via aspiration. Subsequently, to induce carbonate precipitation, 1M $NaHCO_3$ is passed through the channels and aged at 25, 50 and 75 ℃ investigating the temperature effects, while the phase evolution was measured from 6 hours to 480 hours after loading. The time-resolved XRD data reveal the early stage formation of hydrated polymorphs like ikaite and monohydrocalcite facilitated by interfacial water and hydrogen bonding effects, while subsequent transformation and stabilization favor anhydrous vaterite and aragonite. Dissolution of calcite, despite being the most stable and water insoluble phase, emphasizes the influence of interfacial silica deposition and pH dynamics in altering the nucleation mechanism. Prior studies corroborate that the presence of dissolved silica actively influence the morphology and stability of the calcium carbonate phases while underscoring its role as an active phase modulator. Overall, these findings enhance our understanding of carbonate mineralization in nanoconfined systems under reactive interfaces while offering insights which are applicable to CO_2 mineralization, biomineralization and cement chemistry.

5. Acknowledgments

The authors acknowledge the use of shared facilities at Cornell Center for Materials Research (CCMR) supported through NSF MRFEC program (DMR- 1719875). The authors would also like to acknowledge the NSF CAREER (Grant No- 2144373) for providing the required funding.

6. References

1. Gebauer, D., Kellermeier, M., Gale, J. D., Bergström, L. & Cölfen, H. Pre-nucleation clusters as solute precursors in crystallisation. *Chemical Society Reviews* vol. 43 Preprint at https://doi.org/10.1039/c3cs60451a (2014).

2. Ma, J. *et al.* Drastically Reduced Ion Mobility in a Nanopore Due to Enhanced Pairing and Collisions between Dehydrated Ions. *J Am Chem Soc* 141, (2019).

3. Saleh, M. A., Ryan, M. P., Trusler, J. P. M. & Krevor, S. The interfacial processes controlling carbon dioxide mineralisation in magnesium and calcium silicates. *Fuel* 380, 132969 (2025).

4. De Yoreo, J. J. *et al.* Crystallization by particle attachment in synthetic, biogenic, and geologic environments. *Science* vol. 349 Preprint at https://doi.org/10.1126/science.aaa6760 (2015).

5. Gadikota, G., Matter, J., Kelemen, P. & Park, A. A. Chemical and morphological changes during olivine carbonation for CO2 storage in the presence of NaCl and NaHCO3. *Physical Chemistry Chemical Physics* 16, 4679 (2014).

6. Kelemen, P. B. *et al.* In situ carbon mineralization in ultramafic rocks: Natural processes and possible engineered methods. *Energy Procedia* 146, 92–102 (2018).

7. Miller, Q. R. S. *et al.* Quantitative Review of Olivine Carbonation Kinetics: Reactivity Trends, Mechanistic Insights, and Research Frontiers. *Environ Sci Technol Lett* 6, 431–442 (2019).

8. Svensson, K., Neumann, A., Feitosa Menezes, F., Lempp, C. & Pöllmann, H. Carbonation of natural pure and impure wollastonite. *SN Appl Sci* 1, (2019).

9. Munz, I. A. *et al.* Mechanisms and rates of plagioclase carbonation reactions. *Geochim Cosmochim Acta* 77, 27–51 (2012).

10. Kashim, M. Z., Tsegab, H., Rahmani, O., Abu Bakar, Z. A. & Aminpour, S. M. Reaction Mechanism of Wollastonite In Situ Mineral Carbonation for CO 2 Sequestration: Effects of Saline Conditions, Temperature, and Pressure. *ACS Omega* 5, 28942–28954 (2020).

11. Wang, F. & Dreisinger, D. Acceleration of Iron-Rich Olivine CO2 Mineral Carbonation and Utilization for Simultaneous Critical Nickel and Cobalt Recovery. *Minerals* 14, 766 (2024).

12. Taksavasu, T. Petrographic Analysis of Mafic and Ultramafic Rocks in Northern Thailand: Implications for CO2 Mineralization and Enhanced Rock Weathering Approach. *Geosciences (Basel)* 15, 89 (2025).

13. Katre, S. *et al.* Organic ligands and CO2 unlock the potential for energy relevant metals recovery and carbon mineralization from mafic rocks. *Sci Rep* 15, 10882 (2025).

14. Huijgen, W. J. J., Witkamp, G. J. & Comans, R. N. J. Mechanisms of aqueous wollastonite carbonation as a possible CO2 sequestration process. *Chem Eng Sci* 61, (2006).

15. Ismailov, A., Merilaita, N. & Levänen, E. Accelerated Carbonation of High-Calcite Wollastonite Tailings. *Minerals* 14, 415 (2024).

16. Shen, P. *et al.* Preparation aragonite whisker-rich materials by wet carbonation of cement: Towards yielding micro-fiber reinforced cement and sequestrating CO2. *Cem Concr Res* 159, 106891 (2022).

17. Narneni, S. R. & Panesar, D. K. The Response of Synthetic Alkali-Silica Reaction Products to Carbonation. in *RILEM Bookseries* vol. 33 (2021).

18. Prabhu, S. D. *et al.* Valorization of Construction and Demolition Wastes via Organic Acid Mediated Calcium Recovery and CO 2 Mineralization with Regenerable Sodium Glycinate Solvent: A Pathway toward Circularity in the Construction Industry. *Ind Eng Chem Res* 63, 19359–19374 (2024).

19. Katre, S. *et al.* Mechanistic insights into the co-recovery of nickel and iron via integrated carbon mineralization of serpentinized peridotite by harnessing organic ligands. *Physical Chemistry Chemical Physics* 26, (2024).

20. Zhang, L., Sun, L., Guan, X. & Liu, S. Insight into carbonation reactivity of polycrystalline CS by DFT simulation. *Constr Build Mater* 401, 133008 (2023).

21. Pan, S. Y., Ling, T. C., Park, A. H. A. & Chiang, P. C. An overview: Reaction mechanisms and modelling of CO2 utilization via mineralization. *Aerosol and Air Quality Research* vol. 18 Preprint at https://doi.org/10.4209/aaqr.2018.03.0093 (2018).

22. Armstrong, T., Schmid, J., Niemelä, J., Utke, I. & Schutzius, T. M. Nanostructured Surfaces Enhance Nucleation Rate of Calcium Carbonate. *Small* 20, (2024).

23. Cavanaugh, J., Whittaker, M. L. & Joester, D. Crystallization kinetics of amorphous calcium carbonate in confinement. *Chem Sci* 10, 5039–5043 (2019).

24. Rao, A. *et al.* Nonmonotonic Coupled Dissolution-Precipitation Reactions at the Mineral–Water Interface. *Adv Funct Mater* 31, (2021).

25. Bin Jassar, M., Yao, Q., Siro Brigiano, F., Chen, W. & Pezzotti, S. Chemistry at Oxide/Water Interfaces: The Role of Interfacial Water. *J Phys Chem Lett* 15, 11961–11968 (2024).

26. Dewan, S., Yeganeh, M. S. & Borguet, E. Experimental Correlation Between Interfacial Water Structure and Mineral Reactivity. *J Phys Chem Lett* 4, 1977–1982 (2013).

27. Bouhadja, M. & Skelton, A. A. Dynamical Properties of Water and Ions at the Quartz (101)–Water Interface at a Range of Solution Conditions: A Classical Molecular Dynamics Study. *The Journal of Physical Chemistry C* 122, 1535–1546 (2018).

28. Gaboreau, S. *et al.* Hydration Properties and Interlayer Organization in Synthetic C-S-H. *Langmuir* 36, 9449–9464 (2020).

29. Atmeh, A. R., Chong, E. Z., Richard, G., Festy, F. & Watson, T. F. Dentin-cement Interfacial Interaction. *J Dent Res* 91, 454–459 (2012).

30. Longo, R. C. *et al.* Carbonation of Wollastonite(001) Competing Hydration: Microscopic Insights from Ion Spectroscopy and Density Functional Theory. *ACS Appl Mater Interfaces* 7, 4706–4712 (2015).

31. Mergelsberg, S. T. *et al.* Nanoscale Mg-Depleted Layers Slow Carbonation of Forsterite (Mg 2 SiO 4) When Water Is Limited. *Environ Sci Technol Lett* 10, 98–104 (2023).

32. Abdolhosseini Qomi, M. J. *et al.* Molecular-scale mechanisms of CO2 mineralization in nanoscale interfacial water films. *Nature Reviews Chemistry* Preprint at https://doi.org/10.1038/s41570-022-00418-1 (2022).

33. M.J. McKelvy, H. Bearat, A.V.G. Chizmeshya, R. Nunez & R.W. Carpenter. *UNDERSTANDING OLIVINE CO2 MINERAL SEQUESTRATION MECHANISMS AT THE ATOMIC LEVEL: OPTIMIZING REACTION PROCESS DESIGN*. (2003) doi:10.2172/822896.

34. Monasterio-Guillot, L., Fernandez-Martinez, A., Ruiz-Agudo, E. & Rodriguez-Navarro, C. Carbonation of calcium-magnesium pyroxenes: Physical-chemical controls and effects of reaction-driven fracturing. *Geochim Cosmochim Acta* 304, (2021).

35. Béarat, H. *et al.* Carbon Sequestration via Aqueous Olivine Mineral Carbonation: Role of Passivating Layer Formation. *Environ Sci Technol* 40, 4802–4808 (2006).

36. Jin, D., Wu, N., Zhong, J. & Coasne, B. Phase stability and nucleation kinetics of salts in confinement. *J Mol Liq* 394, (2024).

37. Acharya, D., Abou El Kheir, O., Campi, D. & Bernasconi, M. Crystallization kinetics of nanoconfined GeTe slabs in GeTe/TiTe2-like superlattices for phase change memories. *Sci Rep* 14, (2024).

38. Zare, S., Uddin, K. M. S., Funk, A., Miller, Q. R. S. & Abdolhosseini Qomi, M. J. Nanoconfinement matters in humidified CO2 interaction with metal silicates. *Environ Sci Nano* 9, (2022).

39. Weatherup, R. S. *et al.* Long-Term Passivation of Strongly Interacting Metals with Single-Layer Graphene. *J Am Chem Soc* 137, (2015).

40. Hou, D., Li, Z., Zhao, T. & Zhang, P. Water transport in the nano-pore of the calcium silicate phase: Reactivity, structure and dynamics. *Physical Chemistry Chemical Physics* 17, (2015).

41. Mante, P. A. *et al.* Probing hydrophilic interface of solid/liquid-water by nanoultrasonics. *Sci Rep* 4, (2014).

42. Fumagalli, L. *et al.* Anomalously low dielectric constant of confined water. *Science (1979)* 360, (2018).

43. Reiter, G. F. *et al.* Anomalous ground state of the electrons in nanoconfined water. *Phys Rev Lett* 111, (2013).

44. Le, T. H. H., Morita, A. & Tanaka, T. Refractive index of nanoconfined water reveals its anomalous physical properties. *Nanoscale Horiz* 5, (2020).

45. Fang, F. *et al.* Molecular-Level Insights into Unique Behavior of Water Molecules Confined in the Heterojunction between One- and Two-Dimensional Nanochannels. *Langmuir* 38, (2022).

46. Michell, R. M., Blaszczyk-Lezak, I., Mijangos, C. & Müller, A. J. Confinement effects on polymer crystallization: From droplets to alumina nanopores. *Polymer (Guildf)* 54, 4059–4077 (2013).

47. Gebauer, D., Raiteri, P., Gale, J. D. & Cölfen, H. On classical and non-classical views on nucleation. *Am J Sci* 318, 969–988 (2018).

48. Diaz-Vela, D., Hung, J.-H. & Simmons, D. S. Temperature-Independent Rescaling of the Local Activation Barrier Drives Free Surface Nanoconfinement Effects on Segmental-Scale Translational Dynamics near *T* g. *ACS Macro Lett* 7, 1295–1301 (2018).

49. Asgar, H., Mohammed, S. & Gadikota, G. Confinement induces stable calcium carbonate formation in silica nanopores. *Nanoscale* 14, (2022).

50. Choi, K. M. & Kuroda, K. Polymorph control of calcium carbonate on the surface of mesoporous silica. *Cryst Growth Des* 12, (2012).

51. Zhang, G., Morales, J. & García-Ruiz, J. M. Growth behaviour of silica/carbonate nanocrystalline composites of calcite and aragonite. *J Mater Chem B* 5, (2017).

52. Page, K., Stack, A. G., Chen, S. A. & Wang, H. W. Nanopore facilitated monohydrocalcitic amorphous calcium carbonate precipitation. *Physical Chemistry Chemical Physics* 24, (2022).

53. Rodríguez-Ruiz, I. *et al.* Transient calcium carbonate hexahydrate (ikaite) nucleated and stabilized in confined nano- and picovolumes. *Cryst Growth Des* 14, (2014).

54. Strohm, S. B., Berghofer, S. A., Kaiser, C. & Jordan, G. On the Ephemeral Occurrence of Ikaite in Aqueous Solutions between 0 and 20 °C. *ACS Earth Space Chem* 8, 1725–1736 (2024).

55. Simon, P. *et al.* Nested Formation of Calcium Carbonate Polymorphs in a Bacterial Surface Membrane with a Graded Nanoconfinement: An Evolutionary Strategy to Ensure Bacterial Survival. *ACS Biomater Sci Eng* 8, (2022).

56. Tollefsen, E. *et al.* Ikaite nucleation at 35 °C challenges the use of glendonite as a paleotemperature indicator. *Sci Rep* 10, (2020).

57. Strohm, S. B. *et al.* On the nucleation of ikaite (CaCO3x6H2O) – A comparative study in the presence and absence of mineral surfaces. *Chem Geol* 611, (2022).

58. Liesegang, M., Milke, R., Kranz, C. & Neusser, G. Silica nanoparticle aggregation in calcite replacement reactions. *Sci Rep* 7, (2017).

59. Kellermeier, M. *et al.* Stabilization of amorphous calcium carbonate in inorganic silica-rich environments. *J Am Chem Soc* 132, (2010).

60. Li, L., Steefel, C. I. & Yang, L. Scale dependence of mineral dissolution rates within single pores and fractures. *Geochim Cosmochim Acta* 72, (2008).

61. Bjørge, R., Gawel, K., Chavez Panduro, E. A. & Torsæter, M. Carbonation of silica cement at high-temperature well conditions. *International Journal of Greenhouse Gas Control* 82, (2019).

62. Youssef, M. Y. M. Probing water properties and cationic exchange in calcium-silicate-hydrate : an atomistic modeling study. (2010).

63. Zhang, G., Delgado-López, J. M., Choquesillo-Lazarte, D. & García-Ruiz, J. M. Growth behavior of monohydrocalcite (CaCO3·H2O) in silica-rich alkaline solution. *Cryst Growth Des* 15, (2015).

64. Zhang, G., Delgado-López, J. M., Choquesillo-Lazarte, D. & García-Ruiz, J. M. Crystallization of monohydrocalcite in a silica-rich alkaline solution. *CrystEngComm* 15, (2013).

Chapter 6

Conclusion

Probing the mechanism of mineralization in biological system is vastly investigated but the similar mechanism in the context of carbon sequestration mimicking geological conditions in lacking and the current thesis explores the nanoscale mechanism governing the nucleation, growth and transformation of calcium and magnesium carbonates under confined environments. Th initial approach is to determine the solid interface made up of abundantly available mineral like alumina and silica acting as a confining template. The outcome of using anodic alumina membrane (AAM) and silica nanochannels (SNCs) provides insights into how parameters like surface chemistry, pore size, wettability and temperature fundamentally alter the mineralization behavior compared to bulk systems.

A combination of confining substrates was utilized where anodic alumina membranes had a pore size of 10, 40, and 200 nm whereas the silica nanochannels synthesized and loaded inside the AAMs had a pore size of 10.48, 49.09, 63.23 nm. To alter the surface from hydrophilic to hydrophobic, the AAMs were immersed in a solution of lauric acid in ethanol while the same composition solution was used to alter the surface of silica nanochannels using chemical vapor deposition technique (CVD). To determine the interfacial interaction of water with the solid template, contact angle measurement was performed while the surface charges were determined using Zeta Sizer. The overview of the results is that the contact angle of the membranes decreases as the pore size

increases while the surface covered with lauric acid shows higher negative charge due to the formation of ester bond than hydroxide bond.

Initially, the carbonate nucleation and growth studies were performed for magnesium carbonate loaded in 200 nm AAM while changing the reaction ageing temperature and surface wettability. The crystal evolution was measured using X-ray diffraction which indicate that the hydrated magnesium carbonate phases were predominant in hydrophilic conditions whereas hydrated hydroxyl-based magnesium carbonate phases were predominant in hydrophobic conditions irrespective of temperature. To delineate this observation, molecular dynamics (MD) simulations were performed determining the coordination number, radial distribution functions, and hydrogen bonding between the oxygen from water, bicarbonate and nitrate ions indicating that the structure of water moves from amorphous nature to clatharate-like structure in hydrophilic and hydrophobic conditions.

To further enhance the role of pore size on magnesium carbonate phase evolution, the AAM pore sizes were reduced to 10 and 40 nm whereas the evolution of magnesium carbonate in silica nanochannels is investigated in the following study. The reaction ageing temperature and surface wettability were kept constant and the crystal growth and evolution was studied using XRD. The results indicate that anhydrous $MgCO_3$ phase was observed only in 10 nm AAM while hydrated and hydroxyl-based magnesium carbonate phases are observed in 40 nm AAM and in all pore sizes of silica nanochannels. Understanding the dimensionality of growth and nucleation rate of all the magnesium carbonate phases is measured from the kinetics analysis performed using Avrami equation. The behavior of interfacial water in the presence of magnesium

carbonate is measured using a Quasi-elastic neutron scattering (QENS) measurement indicating that the diffusion of water becomes extremely slow in the presence of magnesium carbonate in hydrophilic conditions whereas there is no change in the diffusion jump rate in hydrophobic conditions with respect to pure water system.

Deducing the nucleation and growth of calcium carbonate follows similar methodology of using AAMs and SNCs having the same pore size, reaction temperature, and surface wettability. The crystal evolution indicates that in AAMs the calcium carbonate phase transition follows bulk pathway which moves from the least stable vaterite phase to stable calcite phase. The formation of hydrated calcium carbonate (ikaite) phase is observed in 200 nm AAM pores and its transition to calcite is noted. Calcium carbonate loaded in silica nanochannels similarly show the formation of stable calcite by the end of 96 hours after loading while the stabilization of hydrated phases or metastable phases is observed for a transitional period. The behavior of interfacial water in the presence of calcium carbonate was determined from QENS measurements where the dynamics of water become slow and the fraction of mobile water molecules decreases in hydrophilic conditions whereas Results from MD simulations correspond with experimental observations where pre-nucleated Ca^{2+} ions indicate the higher probability of formation of anhydrous phases over hydrated phases.

Lastly, to deduce the inherent crystallization of calcium carbonate in reactive silica interface mimicking subsurface conditions involved the synthesis of calcium silicate nanochannels inside AAM template. The carbonation of calcium silicate to calcium carbonate denoted the evolution and stabilization of metastable aragonite and vaterite

phases when aged at 25, 50, and 75 ℃ and the prevalence of calcite dissolution mechanism is observed.

Altogether, the experimental and simulation data provides evidence into the mechanistic insights of carbonate growth in nanoconfined systems establishing a framework for understanding polymorph evolution in geological systems and their control in engineered systems. The findings provide broad implications in carbon capture and sequestration to biomineralization to novel cementitious or composite material development. By tuning confinement dimensions and interfacial chemistries, this work demonstrates the direct mineral phase selection criteria thereby providing precise control of materials at nanoscale.